

**University of Alberta**

**Flare Stack Diameter Scaling and  
Wind Tunnel Ceiling and Floor Effects on Model Flares**

by

Lindsay Howell



A thesis submitted to the Faculty of Graduate Studies and Research in partial fulfillment  
of the requirements for the degree of Master of Science.

Department of Mechanical Engineering

Edmonton, Alberta

Spring 2004



Library and  
Archives Canada

Bibliothèque et  
Archives Canada

Published Heritage  
Branch

Direction du  
Patrimoine de l'édition

395 Wellington Street  
Ottawa ON K1A 0N4  
Canada

395, rue Wellington  
Ottawa ON K1A 0N4  
Canada

*Your file* *Votre référence*  
*ISBN: 0-612-96487-6*  
*Our file* *Notre référence*  
*ISBN: 0-612-96487-6*

The author has granted a non-exclusive license allowing the Library and Archives Canada to reproduce, loan, distribute or sell copies of this thesis in microform, paper or electronic formats.

L'auteur a accordé une licence non exclusive permettant à la Bibliothèque et Archives Canada de reproduire, prêter, distribuer ou vendre des copies de cette thèse sous la forme de microfiche/film, de reproduction sur papier ou sur format électronique.

The author retains ownership of the copyright in this thesis. Neither the thesis nor substantial extracts from it may be printed or otherwise reproduced without the author's permission.

L'auteur conserve la propriété du droit d'auteur qui protège cette thèse. Ni la thèse ni des extraits substantiels de celle-ci ne doivent être imprimés ou autrement reproduits sans son autorisation.

---

In compliance with the Canadian Privacy Act some supporting forms may have been removed from this thesis.

Conformément à la loi canadienne sur la protection de la vie privée, quelques formulaires secondaires ont été enlevés de cette thèse.

While these forms may be included in the document page count, their removal does not represent any loss of content from the thesis.

Bien que ces formulaires aient inclus dans la pagination, il n'y aura aucun contenu manquant.

# Canada

## ABSTRACT

The buoyant plume produced by a flare stack in crosswind was studied experimentally using a wind tunnel. Cross-sectional thermal and compositional ( $\text{CO}_2$ ,  $\text{CO}$ ,  $\text{CH}_4$  and  $\text{O}_2$ ) maps of the plume were generated at varying distances downstream for 0.25- to full-scale flare stacks. It was shown that the plume behaved like a non-reacting buoyant jet. It was verified that the thermal characteristics of plumes from 0.15- to full-scale flare stacks are scalable. Flare stack combustion inefficiency was correlated to a past model, providing the first known confirmation that combustion inefficiency for 0.11- to full-scale flare stacks is scalable.

Experiments and theory confirmed that a wind tunnel's floor and ceiling have negligible effects on the plume rise and combustion inefficiency of a model flare, except when the flare stack exit is near the floor. It was shown that a wind tunnel's ceiling has negligible effects on the approximate angle or length of a flare.

## ACKNOWLEDGEMENTS

The process of completing a M.Sc. thesis is a challenging and at times arduous one. During its realization, the author is rewarded for his determination and perseverance with compelling insights into his chosen field of study as well as into his own character. This ultimate benefit of this accomplishment is not only to make one's unique contribution to the scientific community, but to also improve one's capacity as a scholar and philosopher. I am very thankful to have had the strong support of the following outstanding people during the course of my Master's Degree:

Dr. Larry Kostiuk, my supervisor, for his unflinching trust in my abilities as well as his outstanding support and his knowledge on the subject of combustion. I have been and always will be impressed with his ability to find the good in any situation.

Dr. David Wilson, my co-supervisor, for his extensive experience and helpful insights into the phenomenon of buoyant rising plumes.

Oleg Zastavniuk, for his excellent work as a research engineer throughout this project. His assistance with completing my experiments, as well as his wonderful hospitality during my time in Ottawa, were nothing short of invaluable.

Glen Thomas and Pascal Poudenx for providing me professional advice and assistance with the design, construction and operation of my experimental apparatuses. This research certainly would not have been possible without their contributions.

My good friends in the Combustion and Environment Group, whose company was a strong factor in making my experience as a graduate student a positive and at times humorous one. Thank you for the much-needed stress relief in the form of ping-pong games, squash tournaments, volleyball leagues, Friday lunch at Power Plant, and cocktails at RATT.

The sponsors of the University of Alberta Flare Research Project: The Natural Sciences and Engineering Research Council of Canada (NSERC), Environment Canada, The Government of Alberta, Alberta Energy and Utilities Board (AEUB), Petroleum Technology Alliance Canada (PTAC), Environmental Science and Technology Alliance Canada (ESTAC), Canadian Association of Petroleum Producers (CAPP), and Alberta Innovation and Science.

All those who provided me with financial support in the form of scholarships: NSERC, Luscar Ltd., Walter H. Johns, and Alberta Learning. I am very grateful for the generosity of these organizations.

My friends outside of the academic world who helped put life back into perspective after long days at the lab. Whether it was through sports, music, or casual discussions at the local pub, you all helped contribute to my success.

My parents Darrel and Liz, and my grandmother Molly Howell for always loving and supporting me no matter what path I chose in life.

# TABLE OF CONTENTS

<b>CHAPTER 1 INTRODUCTION</b>	<b>1</b>
1.1 Flaring of Solution Gas in the Oil and Gas Industry	1
1.2 Scale Modeling of Solution Gas Flares	3
1.3 Thesis Research Objectives	4
1.4 Combustion Efficiency of Flaring	5
1.4.1 Local and Global Efficiencies	6
1.5 The University of Alberta Flare Research Project	6
1.6 The U of A Flare Research Project Experimental Facilities	7
1.7 Thesis Outline	8
<b>CHAPTER 2 REVIEW OF RELEVANT LITERATURE</b>	<b>9</b>
2.1 Jets in Crosswind	9
2.1.1 Flow Characterizations	9
2.1.2 Non-reacting Jets	11
2.1.3 Reacting Jets	15
2.2 Flare Combustion Efficiency	19
2.2.1 Flare Plumes in Quiescent Air	19
2.2.2 Flare Plumes in Crosswind	20
2.2.2.1 University of Alberta Flare Research Project Results	23
2.3 Summary of Relevant Literature	23
<b>CHAPTER 3 EXPERIMENTAL METHODS AND ANALYTICAL TECHNIQUES</b>	<b>26</b>
3.1 Theoretical Basis for Scale Modeling of Flares	26
3.1.1 Momentum Flux Ratio	26
3.1.2 Richardson Number	26
3.2 Tracking Plume Dispersion Using Thermal Mappings	28
3.2.1 Overview	28
3.2.2 Plume Dispersion Model	30

<b>3.3 Measuring Flare Combustion Efficiency</b>	<b>33</b>
3.3.1 Fuel Composition and Combustion Chemistry	33
3.3.2 Local Combustion Efficiency	34
3.3.3 Overall Combustion Efficiency	40
<b>CHAPTER 4 FACILITY AND EQUIPMENT</b>	<b>46</b>
<b>4.1 Facility Experimental Systems</b>	<b>46</b>
4.1.1 Wind Tunnel	46
4.1.2 Wind Speed Monitoring and Control	48
4.1.3 Removable False Ceiling	48
4.1.4 Flare Stacks	49
4.1.4.1 Flare Stacks of Varying Diameter and Fixed Height	49
4.1.4.2 Flare Stacks of Fixed Diameter and Adjustable Height	50
4.1.5 Fuel Delivery System	51
<b>4.2 Facility Diagnostic Systems</b>	<b>52</b>
4.2.1 Control Computers and Software	52
4.2.2 Motorized Two-Dimensional Traverse	52
4.2.3 Temperature Measurement	53
4.2.3.1 Radiation Effects	54
4.2.3.2 Total Incurred Error in Calculation of Plume Characteristic Dimension	55
4.2.4 Plume Gas Sampling	55
4.2.5 Digital Camera System	57
<b>4.3 Achieving Steady State Conditions</b>	<b>58</b>
<b>4.4 Summary</b>	<b>60</b>
<b>CHAPTER 5 THERMAL STRUCTURE AND TRAJECTORY OF FLARE PLUMES</b>	<b>71</b>
<b>5.1 Poudenx's Model of Plume Entrainment</b>	<b>71</b>
<b>5.2 Comparison of Current Research with Poudenx's Model</b>	<b>73</b>
5.2.1 Range of Validity of the Plume Entrainment Model	76
<b>5.3 Summary and Conclusions</b>	<b>77</b>
<b>CHAPTER 6 COMPOSITIONAL STRUCTURE OF FLARE PLUMES</b>	<b>83</b>
<b>6.1 Johnson's Combustion Efficiency Correlation</b>	<b>83</b>
<b>6.2 Comparison of Current Research with Johnson's Model</b>	<b>85</b>
6.2.1 Correlations for Combustion Efficiency with $n = 1/3$	86
6.2.2 Correlations for Combustion Efficiency with $n = 1/2$	88
<b>6.3 Summary and Conclusions</b>	<b>89</b>
<b>CHAPTER 7 CEILING AND FLOOR EFFECTS ON THE FLARE, PLUME RISE AND COMBUSTION EFFICIENCY</b>	<b>106</b>

<b>7.1 Wind Tunnel Ceiling Proximity Effects</b>	<b>106</b>
7.1.1 Ceiling Effects on Flame Length and Flame Angle	106
7.1.2 Ceiling Effects on Plume Rise and Dispersion	109
7.1.2.1 Model for Buoyant Plume Rise Under a Ceiling	112
7.1.3 Ceiling Effects on Combustion Efficiency	116
<b>7.2 Wind Tunnel Floor Proximity Effects</b>	<b>116</b>
7.2.1 Floor Effects on Plume Rise and Dispersion	116
7.2.2 Floor Effects on Combustion Efficiency	119
<b>7.3 Summary and Conclusions</b>	<b>120</b>
7.3.1 Ceiling Effects on Flame Length and Flame Angle	120
7.3.2 Ceiling Effects on Plume Rise and Dispersion	121
7.3.3 Ceiling Effects on Combustion Efficiency	122
7.3.4 Floor Effects on Plume Rise and Dispersion	123
7.3.5 Floor Effects on Combustion Efficiency	124
<b>CHAPTER 8 SUMMARY AND CONCLUSIONS</b>	<b>144</b>
<b>8.1 Summary</b>	<b>144</b>
8.1.1 Thermal Structure and Trajectory of Flare Plumes	144
8.1.2 Compositional Structure of Flare Plumes	145
8.1.3 Ceiling and Floor Effects On the Flare, Plume Rise and Combustion Efficiency	146
8.1.3.1 Ceiling Effects on Flame Length and Flame Angle	147
8.1.3.2 Ceiling Effects on Plume Rise and Dispersion	147
8.1.3.3 Ceiling Effects on Combustion Efficiency	148
8.1.3.4 Floor Effects on Plume Rise and Dispersion	148
8.1.3.5 Floor Effects on Combustion Efficiency	149
<b>8.2 Conclusions</b>	<b>149</b>
8.2.1 Thermal Structure and Trajectory of Flare Plumes	149
8.2.2 Compositional Structure of Flare Plumes	149
8.2.3 Ceiling and Floor Effects On the Flare, Plume Rise and Combustion Efficiency	150
8.2.3.1 Ceiling Effects on Flame Length and Flame Angle	150
8.2.3.2 Ceiling Effects on Plume Rise and Dispersion	150
8.2.3.3 Ceiling Effects on Combustion Efficiency	151
8.2.3.4 Floor Effects on Plume Rise and Dispersion	151
8.2.3.5 Floor Effects on Combustion Efficiency	152
<b>8.3 Future Work</b>	<b>153</b>
<b>REFERENCES</b>	<b>154</b>
<b>APPENDIX A: DERIVATION OF THE PLUME ENTRAINMENT MODEL</b>	<b>158</b>
<b>APPENDIX B: SENSITIVITY AND UNCERTAINTY ANALYSIS</b>	<b>163</b>
<b>APPENDIX C: CORRECTED PLUME RISE MODEL</b>	<b>172</b>
<b>APPENDIX D: RADIATION EFFECTS ON TYPE E THERMOCOUPLES</b>	<b>180</b>



## LIST OF TABLES

Table 3.1: Composition of sales grade natural gas.....	33
Table 4.1: NRC open-loop low-speed wind tunnel crosswind steadiness. $u^*_\infty$ = first standard deviation of crosswind speed fluctuations .....	47
Table 4.2: Concentration and accuracy of primary master calibration gases.....	56
Table 4.3: Range, drift, repeatability and uncertainty of each gas analyser .....	57
Table B.1: Case 1, measured values for chemical species' concentrations .....	164
Table B.2: Case 2, measured values for chemical species' concentrations .....	165
Table B.3: Typical concentration values and associated uncertainties for $\eta = 95.5\%$ ..	167

# LIST OF FIGURES

Figure 1.1: Analyses of solution gas at individual oil well sites in Alberta (Johnson et al., 2001a).....	3
Figure 3.1: Entrainment of ambient air into a bent over, non-reacting plume.....	42
Figure 3.2: Mean cross-sectional temperature mapping for a reacting jet in crosswind...	43
Figure 3.3: Idealized model of a non-reacting buoyant plume in crosswind.....	44
Figure 3.4: Mean cross-sectional compositional mapping for a reacting jet in crosswind.....	45
Figure 4.1: Cross-sectional model of NRC open-loop low-speed wind tunnel .....	61
Figure 4.2: Schematic of removable false ceiling in wind tunnel half-section. Removable false ceiling constructed of aluminum sheeting with steel U-channels mounted on top for stiffness and support.....	62
Figure 4.3: Typical velocity profile at stack location in NRC wind tunnel for $U_{\infty} = 8$ m/s using a pitot tube. Horizontal and vertical axis in mm relative to wind tunnel floor and wall, respectively.....	63
Figure 4.4: Cross-sectional schematic of assembled flange adapter and 1" flare stack, mounted to wind tunnel floor.....	64
Figure 4.5: Schematic of fuel delivery system.....	64
Figure 4.6: Cross-sectional schematic of wind tunnel with two-dimensional traverse installed .....	65
Figure 4.7: Schematic of multi-point thermocouple system .....	66
Figure 4.8: Cross-sectional schematic of wind tunnel with thermocouple "rake" attached to traverse probe mount. Note the ceiling cap is removed.....	67
Figure 4.9: Schematic of gas sampling probe .....	68
Figure 4.10: Schematic of gas analysis system.....	69
Figure 4.11: Cross-sectional schematic of wind tunnel with digital camera traverse system installed. Note the ceiling cap is removed .....	70

Figure 5.1: Characteristic dimension of the plume using Poudenx et al. (2004) data. Conditions: $1.5 \text{ m/s} \leq U_{\infty} \leq 8.0 \text{ m/s}$ , $0.5 \text{ m/s} \leq V_j \leq 2.0 \text{ m/s}$ , $16.7 \text{ mm} \leq d_i \leq 33.3 \text{ mm}$ , $0.5 \text{ m} \leq X_o \leq 2.9 \text{ m}$ .....	79
Figure 5.2: Varying modes of temperature profiles for a plume cross-section behind a natural gas flare for constant stack diameter. Conditions: $d_i = 52.6 \text{ mm}$ , $X_o = 2.3 \text{ m}$ ...	80
Figure 5.3: Characteristic dimension of the plume for Poudenx et al. (2004) study and present study. Conditions: $2.0 \text{ m/s} \leq U_{\infty} \leq 8.0 \text{ m/s}$ , $0.5 \text{ m/s} \leq V_j \leq 2.0 \text{ m/s}$ , $26.9 \text{ mm} \leq d_i \leq 102.3 \text{ mm}$ , $0.5 \text{ m} \leq X_o \leq 8.3 \text{ m}$ .....	81
Figure 5.4: Exploded view of Figure 5.3 with Poudenx et al. (2004) data points included. Conditions: Present study's data: $2.0 \text{ m/s} \leq U_{\infty} \leq 8.0 \text{ m/s}$ , $0.5 \text{ m/s} \leq V_j \leq 2.0 \text{ m/s}$ $26.9 \text{ mm} \leq d_i \leq 102.3 \text{ mm}$ , $0.5 \text{ m} \leq X_o \leq 8.3 \text{ m}$ Poudenx et al. (2004) data: $1.5 \text{ m/s} \leq U_{\infty} \leq 8.0 \text{ m/s}$ , $0.5 \text{ m/s} \leq V_j \leq 2.0 \text{ m/s}$ $16.7 \text{ mm} \leq d_i \leq 33.3 \text{ mm}$ , $0.5 \text{ m} \leq X_o \leq 2.9 \text{ m}$ .....	82
Figure 6.1: $\text{CO}_2$ , $\text{CO}$ , $\text{CH}_4$ and $\text{O}_2$ normalized concentrations for kidney shaped plume. Conditions: $U_{\infty} = 4.0 \text{ m/s}$ , $V_j = 0.5 \text{ m/s}$ , $d_o = 114.3 \text{ mm}$ , $X_o = 3.20 \text{ m}$ .....	92
Figure 6.2: Local combustion efficiency profile for kidney shaped plume. Conditions: $U_{\infty} = 4.0 \text{ m/s}$ , $V_j = 0.5 \text{ m/s}$ , $d_o = 114.3 \text{ mm}$ , $X_o = 3.20 \text{ m}$ , $\eta_{ave} = 99.8 \%$ .....	93
Figure 6.3: $\text{CO}_2$ , $\text{CO}$ , $\text{CH}_4$ and $\text{O}_2$ normalized concentrations for circular shaped plume. Conditions: $U_{\infty} = 6.0 \text{ m/s}$ , $V_j = 1.0 \text{ m/s}$ , $d_o = 58.8 \text{ mm}$ , $X_o = 2.60 \text{ m}$ .....	94
Figure 6.4: Local combustion efficiency profile for circular shaped plume. Flare stack wake structures act to create two separate regions of higher combustion efficiency. Conditions: $U_{\infty} = 6.0 \text{ m/s}$ , $V_j = 1.0 \text{ m/s}$ , $d_o = 58.8 \text{ mm}$ , $X_o = 2.60 \text{ m}$ , $\eta_{ave} = 99.5 \%$ .....	95
Figure 6.5: $\text{CO}_2$ , $\text{CO}$ , $\text{CH}_4$ and $\text{O}_2$ normalized concentrations for downwashed plume. Conditions: $U_{\infty} = 8.0 \text{ m/s}$ , $V_j = 1.0 \text{ m/s}$ , $d_o = 30.0 \text{ mm}$ , $X_o = 0.80 \text{ m}$ .....	96
Figure 6.6: Local combustion efficiency profile for downwashed plume. Conditions: $U_{\infty} = 8.0 \text{ m/s}$ , $V_j = 1.0 \text{ m/s}$ , $d_o = 30.0 \text{ mm}$ , $X_o = 0.80 \text{ m}$ , $\eta_{ave} = 88.5 \%$ .....	97

Figure 6.7: Present study's correlation compared with Johnson's correlation for natural gas based flares with $d_o^{1/3}$ dependency. Conditions: $4.0 \text{ m/s} \leq U_\infty \leq 14.0 \text{ m/s}$ , $0.5 \text{ m/s} \leq V_j \leq 2.0 \text{ m/s}$ , $30.0 \text{ mm} \leq d_o \leq 114.3 \text{ mm}$ .....	98
Figure 6.8: Exploded view of Figure 6.7. Conditions: $4.0 \text{ m/s} \leq U_\infty \leq 14.0 \text{ m/s}$ , $0.5 \text{ m/s} \leq V_j \leq 2.0 \text{ m/s}$ , $30.0 \text{ mm} \leq d_o \leq 114.3 \text{ mm}$ .....	99
Figure 6.9: Comparison of scatter between Johnson's data and present study's data for natural gas based flares with $d_o^{1/3}$ dependency. Conditions: Present study's data: $4.0 \text{ m/s} \leq U_\infty \leq 14.0 \text{ m/s}$ , $0.5 \text{ m/s} \leq V_j \leq 2.0 \text{ m/s}$ , $30.0 \text{ mm} \leq d_o \leq 114.3 \text{ mm}$ Johnson and Kostiuk (2002) data: $2.0 \text{ m/s} \leq U_\infty \leq 16.0 \text{ m/s}$ , $0.5 \text{ m/s} \leq V_j \leq 2.0 \text{ m/s}$ , $12.1 \text{ mm} \leq d_o \leq 49.8 \text{ mm}$ .....	100
Figure 6.10: Figure 6.9 shown on semi-log scale. Conditions: Present study's data: $4.0 \text{ m/s} \leq U_\infty \leq 14.0 \text{ m/s}$ , $0.5 \text{ m/s} \leq V_j \leq 2.0 \text{ m/s}$ , $30.0 \text{ mm} \leq d_o \leq 114.3 \text{ mm}$ Johnson and Kostiuk (2002) data: $2.0 \text{ m/s} \leq U_\infty \leq 16.0 \text{ m/s}$ , $0.5 \text{ m/s} \leq V_j \leq 2.0 \text{ m/s}$ , $12.1 \text{ mm} \leq d_o \leq 49.8 \text{ mm}$ .....	101
Figure 6.11: Present study's correlation compared with Johnson's correlation for natural gas based flares with $d_o^{1/2}$ dependency. Conditions: $4.0 \text{ m/s} \leq U_\infty \leq 14.0 \text{ m/s}$ , $0.5 \text{ m/s} \leq V_j \leq 2.0 \text{ m/s}$ , $30.0 \text{ mm} \leq d_o \leq 114.3 \text{ mm}$ .....	102
Figure 6.12: Exploded view of Figure 6.11. Conditions: $4.0 \text{ m/s} \leq U_\infty \leq 14.0 \text{ m/s}$ , $0.5 \text{ m/s} \leq V_j \leq 2.0 \text{ m/s}$ , $30.0 \text{ mm} \leq d_o \leq 114.3 \text{ mm}$ .....	103
Figure 6.13: Comparison of scatter between Johnson's data and present study's data for natural gas based flares with $d_o^{1/2}$ dependency. Conditions: Present study's data: $4.0 \text{ m/s} \leq U_\infty \leq 14.0 \text{ m/s}$ , $0.5 \text{ m/s} \leq V_j \leq 2.0 \text{ m/s}$ , $30.0 \text{ mm} \leq d_o \leq 114.3 \text{ mm}$ Johnson and Kostiuk (2002) data: $2.0 \text{ m/s} \leq U_\infty \leq 16.0 \text{ m/s}$ , $0.5 \text{ m/s} \leq V_j \leq 2.0 \text{ m/s}$ , $12.1 \text{ mm} \leq d_o \leq 49.8 \text{ mm}$ .....	104
Figure 6.14: Figure 6.13 shown on semi-log scale. Conditions: Present study's data: $4.0 \text{ m/s} \leq U_\infty \leq 14.0 \text{ m/s}$ , $0.5 \text{ m/s} \leq V_j \leq 2.0 \text{ m/s}$ , $30.0 \text{ mm} \leq d_o \leq 114.3 \text{ mm}$ Johnson and Kostiuk (2002) data: $2.0 \text{ m/s} \leq U_\infty \leq 16.0 \text{ m/s}$ , $0.5 \text{ m/s} \leq V_j \leq 2.0 \text{ m/s}$ , $12.1 \text{ mm} \leq d_o \leq 49.8 \text{ mm}$ .....	105
Figure 7.1: Schematic depicting concepts of approximate flame length, $L_f$ approximate flame angle, $\theta_f$ , and vertical distance from the flare stack exit to the false ceiling, $Y_c$ ...	126

Figure 7.2: Approximate flame length as affected by vertical distance from flare stack exit to false ceiling. Both axes divided by buoyancy length. Conditions: $U_{\infty} = 4.0$ m/s, $0.5$ m/s $\leq V_j \leq 2.0$ m/s, $d_i = 26.9$ mm .....	127
Figure 7.3: Approximate flame angle as affected by vertical distance from flare stack exit to false ceiling over buoyancy length. Conditions: $U_{\infty} = 4.0$ m/s, $0.5$ m/s $\leq V_j \leq 2.0$ m/s, $d_i = 26.9$ mm .....	128
Figure 7.4: Plume mean thermal cross-sections as flare stack exit is positioned closer to the false ceiling. Conditions: $U_{\infty} = 4.0$ m/s, $V_j = 1.0$ m/s, $d_i = 26.9$ mm, $X_o = 2.13$ m .....	129
Figure 7.5: Plume centroid vertical position as affected by vertical distance from flare stack exit to false ceiling. Both axes divided by buoyancy length. Conditions: $U_{\infty} = 4.0$ m/s, $0.5$ m/s $\leq V_j \leq 2.0$ m/s, $d_i = 26.9$ mm, $X_o = 2.13$ m .....	130
Figure 7.6: Corrected model for a non-reacting buoyant plume in crosswind. Presence of ceiling alters plume trajectory .....	131
Figure 7.7: Corrected and uncorrected real and image plume centerline trajectories .....	132
Figure 7.8: Numerical models for corrected and uncorrected plume rises over buoyancy length varying with downstream distance over flare stack inner diameter. $h_{b, actual}$ predicts slightly higher plume rise than $h_b$ prior to meeting false ceiling because of physics associated with mirror image buoyancy source. Conditions: $U_{\infty} = 4.0$ m/s, $V_j = 0.5$ m/s, $d_i = 26.9$ mm.....	133
Figure 7.9: Numerical models for corrected and uncorrected upward plume speeds over fuel jet speed varying with downstream distance over flare stack inner diameter. Conditions: $U_{\infty} = 4.0$ m/s, $V_j = 0.5$ m/s, $d_i = 26.9$ mm.....	134
Figure 7.10: Numerical models for corrected and uncorrected plume rises over buoyancy length varying with downstream distance over flare stack inner diameter. $h_{b, actual}$ predicts slightly higher plume rise than $h_b$ prior to meeting false ceiling because of physics associated with mirror image buoyancy source. Conditions: $U_{\infty} = 4.0$ m/s, $V_j = 1.0$ m/s, $d_i = 26.9$ mm .....	135
Figure 7.11: Numerical models for corrected and uncorrected upward plume speeds over fuel jet speed varying with downstream distance over flare stack inner diameter. Conditions: $U_{\infty} = 4.0$ m/s, $V_j = 1.0$ m/s, $d_i = 26.9$ mm.....	136

Figure 7.12: Numerical models for corrected and uncorrected plume rises over buoyancy length varying with downstream distance over flare stack inner diameter. $h_{b, actual}$ predicts slightly higher plume rise than $h_b$ prior to meeting false ceiling because of physics associated with mirror image buoyancy source. Conditions: $U_\infty = 4.0$ m/s, $V_j = 2.0$ m/s, $d_i = 26.9$ mm .....	137
Figure 7.13: Numerical models for corrected and uncorrected upward plume speeds over fuel jet speed varying with downstream distance over flare stack inner diameter. Conditions: $U_\infty = 4.0$ m/s, $V_j = 2.0$ m/s, $d_i = 26.9$ mm.....	138
Figure 7.14: Combustion inefficiency as affected by vertical distance from flare stack exit to false ceiling over buoyancy length. Conditions: $U_\infty = 4.0$ m/s, $0.5$ m/s $\leq V_j \leq 2.0$ m/s, $d_i = 26.9$ mm, $X_o = 2.13$ m.....	139
Figure 7.15: Plume mean thermal cross-sections as flare stack exit is positioned closer to the floor. Conditions: $U_\infty = 4.0$ m/s, $V_j = 0.5$ m/s, $d_i = 26.9$ mm, $X_o = 2.13$ m.....	140
Figure 7.16: Plume mean thermal cross-sections as flare stack exit is positioned closer to the floor. Conditions: $U_\infty = 4.0$ m/s, $V_j = 2.0$ m/s, $d_i = 26.9$ mm, $X_o = 2.13$ m.....	141
Figure 7.17: Plume centroid vertical position as affected by vertical distance from flare stack exit to wind tunnel floor. Both axes divided by buoyancy length. Conditions: $U_\infty = 4.0$ m/s, $0.5$ m/s $\leq V_j \leq 2.0$ m/s, $d_i = 26.9$ mm, $X_o = 2.13$ m .....	142
Figure 7.18: Combustion inefficiency as affected by vertical distance from flare stack exit to wind tunnel floor over buoyancy length. Conditions: $U_\infty = 4.0$ m/s, $0.5$ m/s $\leq V_j \leq 2.0$ m/s, $d_i = 26.9$ mm, $X_o = 2.13$ m.....	143
Figure A.1: Model of a non-reacting buoyant plume in crosswind .....	162
Figure B.1: Case 1, sensitivity of Eq. B.6 to a + 5 % change in a variable .....	169
Figure B.2: Case 2, sensitivity of Eq. B.6 to a + 5 % change in a variable .....	170
Figure B.3: Sensitivity of Eq. B.6 to a + 5 % change in a variable with increasing combustion inefficiency .....	171
Figure C.1: Model for a non-reacting buoyant plume in crosswind .....	176
Figure C.2: Comparison between buoyant plume rise models with and without a ceiling .....	177

Figure C.3: Idealized cross-section of buoyant plume structure. Rising cylinder induces velocity  $W$  as a function of  $Y$  ..... 178

Figure C.4: Corrected and uncorrected real and image plume centerline trajectories .... 179

Figure D.1: Position of TC rake relative to flare stack flame for above experimental conditions ..... 184

Figure D.2: One-dimensional convection and radiation heat transfer model for TC1 idealized as a spatially isothermal sphere under steady-state conditions..... 185

## NOMENCLATURE

$a$	number of carbon atoms in the hydrocarbon fuel
$A, B, D, E, F$	coefficients of curve fit
$A_{TC}$	exposed surface area of TC1 ( $m^2$ )
$Area$	area contained within the 50 % temperature contour of a plume's mean cross-sectional thermal structure ( $m^2$ )
ARC	Alberta Research Council
$b$	number of hydrogen atoms in the hydrocarbon fuel
$C_{p\infty}$	specific heat capacity of air (J/kg.K)
$d, e, f, g, i, j$	stoichiometric coefficients
$d_i$	inner diameter of the flare stack (m)
$d_o$	outer diameter of the flare stack (m)
$d_p^*$	characteristic dimension of the plume (m)
EPA	Environmental Protection Agency
EUB	Alberta Energy and Utilities Board
$f_{daf}$	displaced airflow factor
$F_b$	buoyancy flux of combustion products from the flame ( $m^4/s^3$ )
$g$	gravitational constant = 9.81 $m/s^2$
$\bar{h}$	mean convection coefficient ( $W/m^2.K$ )



$h_b$	height of plume centerline above its release point (m)
$h_{b, actual}$	corrected height of plume centerline above its release point (m)
$H_s$	heat release rate at ideal point source of combustion (J/s)
$k$	thermal conductivity of air at 1 atm, 450 K = $37.3 \times 10^{-3}$ W/m.K
$K_h$	upward plume speed coefficient ( $m^2/kg$ ) = $\left(\frac{3}{2\beta^2}\right)^{1/3} \left(\frac{g\bar{R}_\infty}{\pi C_{p\infty} P_\infty}\right)^{1/3}$
$L$	length of false ceiling (m)
$L_b$	buoyancy length = $\frac{F_b}{U_\infty^3}$
$L_c$	characteristic length scale (m)
$L_f$	approximate length of the flame (m)
$LHV_{mass}$	lower heating value by mass (MJ/kg)
$LHV_{mass, CH_4}$	lower heating value by mass of pure methane = 50 MJ/kg
$m$	number of points in the area of integration
$M$	density-weighted velocity ratio = $\left(\frac{\rho_j}{\rho_\infty}\right)^{1/2} \frac{V_j}{U_\infty}$
$n$	coefficient derived from experimental data
$N_A$	number of moles of molecule A
$\overline{Nu}_D$	mean Nusselt number
NRC	National Research Council

$P$	pressure (Pa)
$P_L$	local pressure (Pa)
$P_\infty$	ambient air pressure (Pa)
$Pr$	Prandtl number of air at 1 atm, 450 K = 0.686
$q''$	radiation heat flux ( $\text{W}/\text{m}^2$ )
$q_o$	cold fuel jet initial flow rate ( $\text{m}^3/\text{s}$ )
$q_p$	plume flow rate ( $\text{m}^3/\text{s}$ )
$q_l$	plume flow rate at a single, vertical cross-section ( $\text{m}^3/\text{s}$ )
$Q$	total heat content of flared gas (J/s)
$Q_{hv}$	heating value of the fuel gas (J/kg)
$P_\infty$	ambient air pressure (Pa)
$R$	momentum ratio = $\frac{\rho_j V_j^2}{\rho_\infty U_\infty^2}$
$R_j$	cold fuel jet radius (m)
$R_p$	radius of the plume (m)
$R_s$	radius of TC1 sphere (m)
$R_z$	perpendicular distance from approximate geometric centre of flame to plane of thermocouples (m)
$Re$	Reynolds number
$Re_D$	Reynolds number of a cylinder in cross flow

$Re_L$	Reynolds number of a flat plate in cross flow
$Ri$	Richardson number
$\bar{R}$	specific gas constant (J/kg.K)
$\bar{R}_L$	local specific gas constant (J/kg.K)
$\bar{R}_\infty$	ambient air specific gas constant = 287 J/kg.K
$s_{actual}$	vertical distance from plume centerline to the false ceiling (m) = $Y - h_{b,actual}$
$tot$	total number of variables
$T$	temperature (K)
$T_{background}$	minimum temperature on a thermal map (K)
$T_L$	local temperature (K)
$T_{max}$	maximum temperature on a thermal map (K)
$T_o$	temperature of surroundings (K)
$T_{plume\ core}$	threshold temperature used to define the plume boundary (K) $T_{plume\ core} \geq \frac{T_{background} + T_{max}}{2}$
$T_s$	temperature of the stoichiometric products of combustion originating from the point source (K)
$T_{TC}$	surface temperature of TC1 sphere (K)
$T_\infty$	ambient air temperature (K)
$u_e$	entrainment speed of ambient air (m)

$u_{\infty}^*$	crosswind speed fluctuations (m/s)
$U_{\infty}$	crosswind speed (m/s)
$V_j$	fuel jet speed (m/s)
$w$	number of data points inside the 50 % temperature contour
$W_{image}$	corrected upward plume speed (m/s)
$W_{image\ at\ plume,\ actual}$	speed exerted by the image plume speed upon the real plume (m/s)
$W_p$	upward plume speed (m/s)
$W_{p,\ actual}$	corrected upward plume speed (m/s)
$x_c$	distance downstream from false ceiling leading edge (m)
$x_i$	variable in combustion efficiency equation
X, Y, Z	name of coordinate axis
$X_o$	distance downstream from the flare stack axis (m)
$X_{o1}, X_{o2}$	varying distances downstream of flare stack axis (m)
$y$	vertical component (measured from the wind tunnel floor) of each data point inside the 50 % temperature contour (m)
$y_{centroid}$	vertical component (measured from the wind tunnel floor) of each plume centroid location (m)
$Y_c$	vertical distance from the flare stack exit to the false ceiling (m)
$Y_f$	vertical distance from the flare stack exit to the floor (m)
$Z_{TC}$	perpendicular distance from flare stack axis to plane of thermocouples (m)

$\alpha_{ave}$	average volume fraction of products in the gas sample
$\alpha_L$	local volume fraction of products in the gas sample
$\beta$	entrainment coefficient
$\beta_{avg}$	average entrainment coefficient
$\delta$	turbulent boundary layer thickness (m)
$\epsilon_{ng}$	emissivity of natural gas flame = 0.2
$\epsilon_{TC}$	emissivity of TC1 = 0.9
$\epsilon_{x_i}$	uncertainty of variable $x_i$
$\epsilon_{\Delta T}$	percent error in measured temperature difference (%)
$\epsilon_{\eta}$	uncertainty of combustion efficiency
$\eta$	combustion efficiency (%)
$\eta_{ave}$	overall (global) combustion efficiency for a chosen area (%)
$(1-\eta)$	combustion inefficiency (%)
$\theta_f$	approximate angle of the flame (degrees)
$\rho_s$	density of the stoichiometric products of combustion originating from the point source (kg/m <sup>3</sup> )
$\rho_j$	fuel jet density (kg/m <sup>3</sup> )
$\rho_L$	local fluid density (kg/m <sup>3</sup> )
$\rho_l$	plume density at a single, vertical cross-section (kg/m <sup>3</sup> )

$\rho_{\infty}$	ambient air density (kg/m <sup>3</sup> )
$\Delta t$	time step (s)
$\Delta\rho_o$	initial local density difference (kg/m <sup>3</sup> )
$\Delta\rho_p$	local density difference between plume and ambient air (kg/m <sup>3</sup> )
$\mu$	viscosity of air at 1 atm, 450 K = $250.7 \times 10^{-7}$ N.s/m <sup>2</sup>
$\mu_s$	viscosity of air at surface of TC1 ~ $\mu$
$\nu$	kinematic viscosity of air at 1 atm, 293 K = $1.5 \times 10^{-5}$ m <sup>2</sup> /s
$\sigma$	Stephan-Boltzmann constant = $5.67 \times 10^{-8}$ W/m <sup>2</sup> .K
$(j-1), (j)$	steps in the numerical solution
$[A]_{ave}$	weighted concentration of molecule A (ppm or %)
$[A]_E$	concentration of molecule A in entrained air (ppm or %)
$[A]_G$	concentration of molecule A in flare gas (ppm or %)
$[A]_p$	concentration of molecule A in products of combustion (ppm or %)
	$[A]_p = [A]_s - [A]_G - [A]_R - [A]_E$
$[A]_R$	concentration of molecule A in reacting air (ppm or %)
$[A]_s$	concentration of molecule A in gas sample (ppm or %)

# Chapter 1

## INTRODUCTION

### 1.1 Flaring of Solution Gas in the Oil and Gas Industry

Flaring is a very common practice employed by the oil and gas industry to dispose of unwanted combustible gases. A typical flare is a simple, vertical pipe from which fuel issues into the atmosphere. At the stack exit, the fuel mixes with air where it is ignited and combusts, producing a turbulent flame in crosswind. The ideal products for such a reaction involving a hydrocarbon fuel are carbon dioxide ( $\text{CO}_2$ ) and water vapour. One alternative to flaring is to simply vent unwanted gases straight into the atmosphere. Industry tends to avoid venting this gas, because methane, a gas commonly found in flaring, has a global warming potential 21 times greater than that of  $\text{CO}_2$  by mass (Houghton et al., 1996). Also, if the gas contains hydrogen sulphide ( $\text{H}_2\text{S}$ ), any unburned fuel is potentially toxic, whereas the process of combustion can transform the  $\text{H}_2\text{S}$  into less harmful molecular forms, such as sulphur dioxide ( $\text{SO}_2$ ). The process of flaring aims to consume unwanted flammable or toxic gases in a safe and efficient manner with minimal adverse environmental impact.

Flaring may fall under two basic headings: short term, high flow rate flaring, or continuous, low flow rate flaring. The first mode encompasses all flaring that occurs at refineries during startup/shutdown and the emergency depressurization of process units. Continuous flares are used to destroy gases that leak past relief valves in refineries, as well as to destroy gases that are unwanted byproducts of the refining process. Solution gas flaring, which is the type of flaring most akin to the work described in the present study, falls under the heading of continuous flaring.

Solution gas typically originates in underground reservoirs of crude oil. The gas is found dissolved in the crude oil and water as a result of the high pressure in the reservoir, hence the term solution gas. As the crude oil is extracted and brought to the earth's

surface, the gases come out of solution and a mixture of water, crude oil and solution gas results.

These products of extraction are processed in the field at specialized facilities known as batteries. Battery sites separate the water and solution gas from the crude oil, and then transport the liquid hydrocarbons by pipeline or other means to a refinery for further processing. If it is economically unfeasible to transport the solution gas and if regulations permit, it may be disposed of on site by flaring.

The Energy and Utilities Board reported that in 2001 the Province of Alberta had 3742 batteries with active flare stacks. In total, 20.770 billion cubic metres of solution gas were produced in that year, 624 million cubic metres (3% of total volume) of which were flared (EUB Statistical Series 2002-60B, 2001). A detailed breakdown of the composition of flared and vented solution gas in Alberta in 1999 is presented in a technical paper by Johnson et al. (2001a). Figure 1.1 shows a plot of the mean and maximum percent concentrations of major chemical species found in solution gas at individual oil wells in Alberta. Significant variability exists in the percent concentrations of each of the major components contained in the solution gas, however the collected data indicate the mean percent concentration of CH<sub>4</sub> (C1 hydrocarbons with one carbon atom per molecule) for all wells is significantly larger than any other constituent mean concentration. The mean percent concentrations of C2 hydrocarbons, N<sub>2</sub>, and H<sub>2</sub>S are negligible, although at individual wells their maximum percent concentrations can be significant.



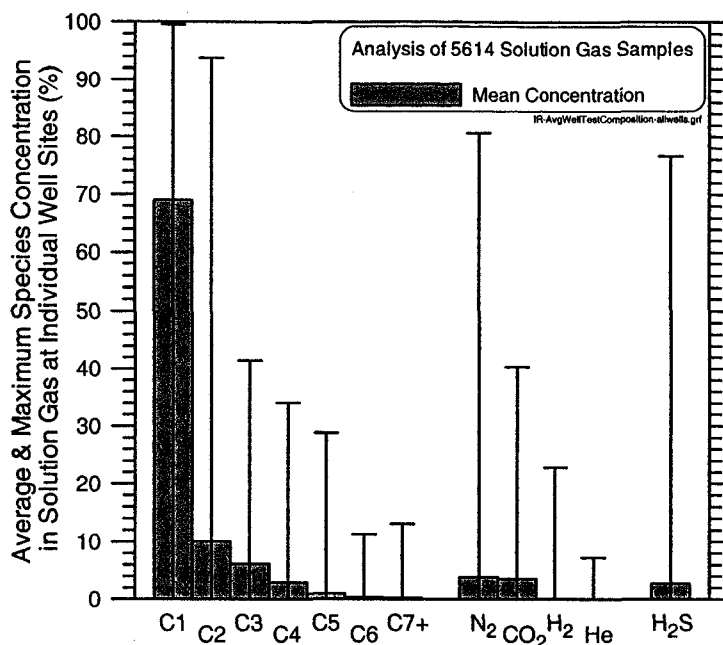


**Figure 1.1: Analyses of solution gas at individual oil well sites in Alberta (Johnson et al., 2001a)**

A typical flare stack installed at a battery site is a vertically mounted 4 inch schedule 40 pipe with an approximate inner diameter of 100 mm. A pilot flame or other device to ensure continuous combustion of the flare gas is mounted at the top of the stack. The fuel gas exits the stack with a turbulent velocity profile. Mean exit velocity typically ranges from one to four metres per second. For the purposes of the present study, a 4 inch schedule 40 pipe with an inner diameter of 102.3 mm and an outer diameter of 114.3 mm is considered to be a full-scale flare stack.

## 1.2 Scale Modeling of Solution Gas Flares

Over the past half-century, researchers have published a considerable amount of literature on flares concerning flame trajectory and stability, the physical and chemical characteristics of the flame, and the thermal radiation associated with a flare. Studies were conducted within and without wind tunnel facilities. Relatively little has been published concerning modeling the combustion efficiency or flare plume dispersion, especially in experimental situations involving a crosswind. Previous studies have claimed that flare combustion efficiency may be 62 % up to 98 % or higher over a wide range of fuel flow rates and fuel compositions, provided the flame is stable. Sample

publications on such findings include reports by the Environmental Protection Agency, or EPA (e.g. Joseph et al., 1983; Pohl and Soelberg, 1985), Romano (1983) and Siegel (1980). However, it is only in the past several years that research has been performed that may be applied to continuous, solution gas flaring (e.g. Strosher, 1996; Johnson and Kostiuk, 2000). From this research, some unresolved engineering issues concerning flare stack plume and combustion efficiency modeling have arisen.

1. A considerable amount of literature exists concerning plume rise and dispersion modeling. However, the vast majority of it addresses non-reacting (or non-burning) flows. Relatively little work exists that investigates and attempts to model the dispersion of flare plumes beyond the boundaries of the flame itself.
2. Scale models to predict the combustion efficiency of solution gas flares have been previously developed for scaled-down flares, but the problem remains that the actual combustion efficiency of full-scale solution gas flares is unknown. Previous studies that have measured combustion efficiency have failed to provide convincing reasons for the observed variations in flare combustion efficiency.
3. Of the studies conducted within the confines of a wind tunnel, no attempt has been made to determine the possible proximity effects of a wind tunnel's ceiling and floor on the flare's physical dimensions, nor the plume's thermal and compositional characteristics.

The current research aims to address these issues as they relate to continuous solution gas flaring.

### **1.3 Thesis Research Objectives**

The overall objective of the present study was to conduct a detailed examination of the scalable characteristics of a flare stack's plume of combustion products over a wide range of flare stack sizes. Using an open-loop wind tunnel facility, thermal and combustion efficiency data were collected on full-scale flare stacks and correlated with data collected on scaled-down flare stacks. Also studied were the proximity effects of a

wind tunnel's ceiling and floor on the flare's physical features and the flare plume's thermal and compositional characteristics.

The specific goals of the present study are

- Verifying that the thermal characteristics of a flare plume's structure are scalable. This was accomplished by collecting a detailed, definitive experimental data set of mean cross-sectional thermal maps at varying distances downstream from 0.25- to full-scale flare stacks and correlating this data with a plume dispersion model validated for 0.15- to 0.33-scale flare stacks.
- Verifying that the compositional characteristics of a flare plume's structure are scalable. This was accomplished by collecting a detailed, definitive experimental data set of mean cross-sectional compositional maps on 0.25- to full-scale flare stacks and correlating this data with a combustion efficiency model validated for 0.11- to 0.44-scale flare stacks.
- Showing that flare stack's plume behaves like a non-reacting buoyant jet in crosswind over the full range of flare stack scales studied
- Demonstrating that a wind tunnel's floor and ceiling have no discernible proximity effects on the plume rise and combustion efficiency of a model flare stack, except for cases where the flare stack is very near the floor. In addition, showing that a wind tunnel's ceiling has no effects on the approximate angle and length of a flare. This was accomplished by collecting a detailed experimental data set of true-color images of the flare, as well as mean cross-sectional thermal and compositional maps when the flare stack is located at varying distances from a wind tunnel floor and ceiling.

#### **1.4 Combustion Efficiency of Flaring**

As stated earlier, when solution gas is flared the ideal products of complete combustion are CO<sub>2</sub> and water vapour. In reality, solution gas combusts incompletely, resulting in CO<sub>2</sub>, water vapour, and some undesirable products such as carbon monoxide

(CO), nitric oxides (NO<sub>x</sub>), unburned hydrocarbons (HC), and soot. By determining where the carbon atoms in the solution gas end up in the various combustion products, one may be able to quantify the performance of a flare. The combustion efficiency ( $\eta$ ) of a flare is defined as the quantity of carbon in the solution gas converted into carbon dioxide, i.e.

$$\eta = \frac{\text{mass of carbon in CO}_2 \text{ produced by flare}}{\text{mass of carbon in fuel}} \quad (1.1)$$

Combustion efficiency is calculated based on the measurement of various chemical species' concentrations in the plume of the flare. Some of the chemical species produced by a combusting flare are already present in the ambient air. Care must be taken to account for these background concentrations (i.e. CO<sub>2</sub>, CO, HC), as ambient air is entrained into a flare plume for both combustion and mixing after combustion. A detailed derivation of Eq. 1.1 into a usable form will be discussed in Chapter 3 of this study.

#### 1.4.1 Local and Global Efficiencies

Using Eq. 1.1, the local efficiency may be calculated for any point in space within the flare plume of gaseous products. The global efficiency refers to the overall combustion efficiency of the entire plume. It has been established by previous research (i.e. Poudenx et al., 2000) that the plume of products coming from a flare stack is not spatially homogeneous, so individual local efficiencies may not be representative of the global or overall efficiency. The global efficiency may be calculated by mass weighting the concentrations of individual chemical species at each point in space, and then applying Eq. 1.1. The present study will focus on the global efficiency of flares.

### 1.5 The University of Alberta Flare Research Project

In 1996 the University of Alberta (U of A) Flare Research Project was initiated mainly in response to a desire by the Alberta petrochemical industry, regulating agencies, and general public to gain a better understanding of the factors that affect flare performance, as well as to determine effective means with which to measure flare combustion efficiency. These concerns stemmed from guidelines set by the Alberta Energy and Utilities Board (EUB) regarding acceptable volumes of solution gas flaring,

as well as regulations relating to minimum flare performance requirements. The enforcement of these regulations has resulted in a 53 % reduction in solution gas flaring in the province of Alberta from 1996 levels, well exceeding the 25 % reduction target set for year-end 2001 by the EUB (EUB Statistical Series 2002-60B, 2001). In addition, results from studies by the U of A Flare Research Project have enabled the EUB to set minimum allowable limits on the energy density of solution gas to be flared in the province of Alberta in an effort to improve the quality of flare stack emissions.

Several research ventures were directed under the heading of the U of A Flare Research Project. Major investigations included research into thermal plume characteristics (Poudenx et al., 2004), parameters affecting combustion efficiency (Johnson and Kostiuk, 2000), flame size and shape (Majeski et al., 2000), and soot production (Prybysh et al., 2000). All of these studies shared the major objective of determining what factors affect the performance of a flare.

These investigations were conducted on scaled-down flare stack models and the results have provided significant evidence that flaring can be an effective, low polluting means of disposing of unwanted combustible gases.

## **1.6 The U of A Flare Research Project Experimental Facilities**

The U of A Flare Research Project currently operates two separate wind tunnel facilities for its research purposes. One facility, a closed-loop wind tunnel, exists at the U of A Mechanical Engineering Department in which scaled-down flare stack models with inner stack diameters ranging from 10.9 mm to 44.6 mm (0.11- to 0.44-scale) are tested. Investigations in this facility by Poudenx et al. (2004) and Johnson and Kostiuk (2000) have developed reliable models with which to predict flare combustion efficiency and thermal plume dispersion for given ranges of gas composition, flare stack diameter, fuel jet speed and crosswind speed. Johnson's work focussed on the combustion efficiency of natural gas and propane fuels, as well as burning natural gas/nitrogen (N<sub>2</sub>), natural gas/CO<sub>2</sub>, propane/N<sub>2</sub>, and propane/CO<sub>2</sub> fuel mixtures. Poudenx's work concerned burning only natural gas.

One major finding was that for a given flare gas fuel speed, combustion efficiency decreases as crosswind speed increases. An extension of this conclusion is that as flare fuel speed increases, the jet of combusting gases is less susceptible to the wind.

A much larger open-loop wind tunnel located at the National Research Council (NRC) in Ottawa, ON is the second facility currently operating under the direction of the Flare Research Project. This facility allows the study of flare stacks up to an inner diameter of 102.3 mm, or nominal 4 inch pipe. Unless stated otherwise, all measurements presented in this study were conducted solely at the NRC facility.

## **1.7 Thesis Outline**

Chapter 2 provides a literature review of relevant works, touching on non-reacting jets, turbulent jet diffusion flames, and the combustion efficiency of scaled-down to full-scale flare stacks in quiescent air and crosswinds.

Chapter 3 explains how data was collected and analysed in this research. The methods used to track plume dispersion using thermal mappings and to measure flare combustion efficiency will be explained.

Chapter 4 describes the NRC facility and its experimental equipment, as well as how the equipment was used to collect data. Chapters 5, 6, and 7 present the results and analysis of all data collected. Chapter 5 focuses on the thermal mapping of a flare stack plume, and validation of a previous model developed to predict dispersion of a full-scale flare stack plume. Chapter 6 deals with the compositional mapping of a flare stack plume, and validation of a previous model developed to predict the combustion efficiency of a full-scale flare stack. Chapter 7 studies the wind tunnel floor and ceiling effects on a scaled-down flare stack's flame and the plume's thermal and compositional characteristics. Chapter 8 provides a summary of the results of this study and the conclusions drawn from the results.

## Chapter 2

### REVIEW OF RELEVANT LITERATURE

This chapter will provide a review of selected relevant studies concerning non-reacting jets, turbulent jet diffusion flames in cross-flow, and the combustion efficiency of model and full-size flare stacks. Topics of interest include modeling plume rise and dispersion, drawing similarities between reacting and non-reacting jets, and the characterization of the structure of diffusion flames.

#### 2.1 Jets in Crosswind

A solution gas flare's bent-over buoyant plume of products is a special case of a buoyant jet in cross-flow. The behaviour of jets in a crosswind has been studied extensively over the past half century. Margason (1993) provides a comprehensive review of over 300 technical papers written on the subject since the 1950s.

##### 2.1.1 Flow Characterizations

A wide variety of characterizations have been developed to describe a non-reacting jet in a crosswind. The velocity ratio,  $V_j/U_\infty$ , can be used to describe any jet in cross-flow based on the jet and crosswind speeds. Momentum-dominated jets are typically described using the density-weighted velocity ratio or the momentum ratio, whereas buoyancy-dominated jets can be described using the Richardson Number. For the purposes of this study, these four flow characterizations will be elaborated on.

The simplest flow characterization uses the velocity ratio, which is the ratio of fuel jet speed over crosswind speed,  $V_j/U_\infty$ . This ratio is widespread in literature concerning jets in cross-flow; however, often it does not allow for direct comparison between varying studies as it does not account for any buoyancy or momentum forces

present in the fuel jet and crosswind. As such, this ratio's usefulness is rather limited, but it still remains a commonly used means of describing a non-reacting jet in cross-flow.

A flow characterization that is more useful than the velocity ratio is the density-weighted velocity ratio,

$$M = \left( \frac{\rho_j}{\rho_\infty} \right)^{1/2} \frac{V_j}{U_\infty} \quad (2.1)$$

where

$\rho_j$  = fuel jet density

$V_j$  = fuel jet speed

$\rho_\infty$  = ambient air density

$U_\infty$  = crosswind speed

This ratio assumes that the dominant forces in the flow are

- the momentum of the fuel jet
- the momentum of the crosswind

This ratio incorporates the densities of the fuel jet and crosswind, making it useful for describing momentum-dominated jets in cross-flow. For the special case of  $\rho_j = \rho_\infty$  (also known as isodensity), the density-weighted velocity ratio then becomes  $M = V_j / U_\infty$ , or equal to the velocity ratio.

The flow characterization known as the momentum ratio is essentially the square of the density-weighted velocity ratio,

$$R = \frac{\rho_j V_j^2}{\rho_\infty U_\infty^2} \quad (2.2)$$

A flow characterization that can be used for describing buoyant jets in cross-flow is the Richardson Number ( $Ri$ ), which is defined as



$$Ri = g \frac{\left( \frac{\Delta\rho_p}{\rho_\infty} \right)}{U_\infty^2} L_c \quad (2.3)$$

where

$g$  = gravitational constant

$L_c$  = characteristic length scale

$\Delta\rho_p$  = local density difference between the plume and ambient air

This equation assumes the dominant forces in the flow are

- the buoyancy of the jet fluid
- the momentum of the crosswind

Richardson Numbers are distinct for non-reacting flows, however in the case of a solution gas flare in crosswind, air is entrained into the both the cold fuel jet and the hot plume of products. This flow characterization is useful for describing buoyancy-dominated jets in cross-flow, and is the basis for Briggs' (1975) well-known buoyant plume rise model, which will be elaborated on later in this chapter.

### 2.1.2 Non-reacting Jets

The major focus of this study as it pertains to jets in cross-flow is the rise, mixing and dispersion of buoyancy-dominated plumes arising from a flare stack in crosswind. To better address this topic, this section will briefly describe the development of momentum- and buoyancy-dominated jet theory, and how these theories were used to develop a buoyant plume rise model.

Bosanquet and Pearson (1936) conducted one of the very first studies on plume dispersion. By studying plume behaviour in the field, their objective was to develop a model of plume spreading for the purpose of predicting ground level concentrations of plume products. Later, theories were developed to describe plume rise. These theories were derived based on the Taylor-Turner hypothesis as developed by Morton et al.

(1956). This hypothesis stated that plume entrainment was linearly proportional to the rate of plume rise,

$$\beta \propto \frac{\partial h_b}{\partial t} \quad (2.4)$$

where

$\beta$  = entrainment coefficient

$h_b$  = height of plume centerline above its release point

From this hypothesis two significant theories were developed to describe plume rise. The first theory, known as the “1/3 power law” profile, was used to describe the trajectory of a momentum-dominated jet that had a density equal to the density of the ambient fluid.

$$h_b \propto X_o^{1/3} \quad (2.5)$$

where

$X_o$  = distance downstream from the stack axis

The second theory, known as the “2/3 power law” profile, was used to describe the trajectory of a buoyancy-dominated jet that had a density much larger or much smaller than the density of the ambient fluid.

$$h_b \propto X_o^{2/3} \quad (2.6)$$

Several researchers (Slawson and Csanady, 1967; Hewett et al., 1971; Shwartz and Tulin, 1972) were successful in fitting experimental data to profiles based on Eq. 2.5. Slawson and Csanady’s work focussed on a full-scale atmospheric study of smoke stack plumes. The measured velocity ratio ( $V_j/U_\infty$ ) ranged from 0.9 to 2.6 and the outer diameter ( $d_o$ ) of the smoke stack was 0.3 m.

Shwartz and Tulin's work accounted for the plume's characteristic rising vortex pair in their plume rise predictions. It was observed that once the plume had lost most of its initial vertical velocity, any further plume rise was governed by the interaction of this vortex pair with the surrounding ambient air. The kidney shape of a bent over plume was directly attributed to the effects of this counter-rotating vortex pair.

In the 1970s the "similarity assumption" began to appear in papers on non-reacting plume rise predictions. The assumption stated that the velocity, temperature and concentration profiles all followed the same distribution (typically Gaussian) over the cross-section of the plume. Using data from sub-scale flare stacks in a wind tunnel and full-scale flare stacks in the field, Ooms (1972) confirmed that this similarity assumption could only be applied after the plume had passed through a zone of flow establishment.

In 1975, Briggs conducted the definitive study in the research area of buoyancy-dominated plume rise. Acknowledging a fundamental lack of agreement amongst the many different plume rise equations formulated before his work, Briggs set out to develop robust, practical equations that would accurately predict plume trajectory, accounting for natural atmospheric density and temperature gradients. Building on the Taylor-Turner hypothesis (Eq. 2.4), Briggs found that the plume entrainment coefficient,  $\beta$ , varied along the length of the plume's boundary. The plume entrainment speed,  $u_e$ , was related to crosswind speed by the following,

$$u_e = \beta U_\infty \quad (2.7)$$

The Taylor-Turner hypothesis also extended to relate the radius of a plume's cross-section ( $R_p$ ) to the plume rise ( $h_b$ ).

$$R_p = \beta h_b \quad (2.8)$$

Using the above, Briggs was able to develop his well-known buoyant plume rise model (as published by Weil, 1977),

$$h_b = \left( \frac{3}{2\beta^2} \right)^{1/3} \frac{F_b^{1/3}}{U_\infty} X_o^{2/3} \quad (2.9)$$

where

$$F_b = \frac{\text{buoyancy force per } m^3 \text{ of plume gas}}{\text{plume gas volumetric flow rate}} \quad (2.10)$$

More dispersion models appeared that combined the 2/3 and 1/3 power laws with other power law variations in an attempt to more accurately predict plume trajectory (Wright, 1977). Even more complex models were developed that accounted for the atmospheric velocity profile (Djurfors and Netterville, 1977). Other studies focussed on developing statistical models for the combustion products' concentration profiles within the plume (Netterville, 1979), and on developing detailed maps of the plume's mean cross-sectional thermal structure (Toften et al, 1993). Toften made an important observation using a flare stack in a wind tunnel that as cross-flow turbulence intensity increased, the strength of the plume's rolled-up longitudinal vortex pair decreased, thereby reducing the plume's maximum attainable rise in height. This effect was also observed to decrease with decreasing velocity ratio.

Recent work by Johnston and Wilson (1997) proposed a plume rise model that used a streamwise vortex pair to produce a downwash velocity to compete with a trajectory centerline plume rise velocity. Johnston's experimental velocity ratio ( $V_j/U_\infty$ ) varied from 0.25 to 8.

In 1998, Smith and Mungal built on work by Ooms (1972) concerning the zone of flow establishment present in a bent-over, non-reacting plume. Smith and Mungal defined the size of this zone based on the velocity ratio  $V_j/U_\infty$  and the diameter of the jet. Smith and Mungal's experiments had velocity ratios between 5 and 25.

A major focus of jet research has been to establish a distinction between buoyant and non-buoyant plumes, and to develop suitable models for plume trajectory and dispersion. Although all these models were proposed for only non-reacting jets in cross-

flow, it was quickly realized that the models could accurately predict the behaviour of a buoyant plume resulting from a reacting jet. The models were inaccurate in predicting certain characteristics of a reacting jet, such as the lateral dispersion of the plume, and these discrepancies were attributed to plume density and temperature changes caused by combustion.

### 2.1.3 Reacting Jets

A large body of literature exists for research on reacting jets; specifically turbulent jet diffusion flames in cross-flow. The majority of the research in this area has dealt with characterizing the structure, size, shape and trajectory of the visible flame close to the stack, and not on the plume's trajectory and thermal and compositional characteristics further downstream. Fuel flammability zones have been of interest, as well as drawing similarities between reacting and non-reacting jets. Limited work has been devoted to studying the combustion efficiency of a reacting jet. Unfortunately, no recently published papers could be found that provide a comprehensive review of these studies.

Gollahalli et al. (1975) studied propane flame size and trajectory for momentum ratios ( $R$ ) ranging from 63 to 1873. The results indicated that a bent over turbulent hydrocarbon diffusion flame exhibited many of the same features of a non-reacting turbulent jet in crosswind. Centerline trajectories of the flames could be accurately predicted using correlations developed for momentum-dominated non-reacting jets (i.e.  $h_b \propto X_o^{1/3}$ ), but the non-reacting jet data could not be used to predict the lateral spreading of the flames.

A study by Botros and Brzustowski (1978) studied the structure of turbulent diffusion flames in cross-flow using a sub-scale flare stack in a wind tunnel. Fuel issued from a 180 mm tall flare stack with an inner diameter of 5 mm, producing a lifted flame. A pitot tube was used to measure the velocity field within the turbulent propane flame arising from a momentum-dominated fuel jet for  $R = 230$  and a flare stack discharge  $Re = 6.2 \times 10^4$ . These conditions produced a high-momentum flame that was lifted from the flare stack tip. In the field on a full-scale battery flare stack with an inner diameter of

approximately 10 cm, this would result in  $V_j = 2.7$  m/s in near-quiescent conditions. It was revealed that a pair of counter-rotating vortices was the principal feature in the flow. A numerical model incorporating turbulence and buoyancy was implemented to predict flame structure and temperature contours.

The ability to predict the size and shape of a turbulent diffusion flame in cross-flow using fuel jet and crosswind speeds ( $V_j$  and  $U_\infty$ , respectively) has been well developed by many researchers since the 1940s. A recent investigation by Kalghatgi (1983) used a video camera to record images of various flames in a wind tunnel issuing from flare stacks whose inner diameters varied from 6 mm up to 22 mm. The velocity ratio ( $V_j/U_\infty$ ) varied from 1.85 to 81.5. Fuels used were propane, ethylene, methane and butane. Kalghatgi was able to describe the shape of the resulting flames using the frustum of a cone defined by five separate parameters, each with its own equation where the independent variables were stack inner diameter, fuel jet speed, crosswind speed, and fuel density. One of his major conclusions was that buoyancy appeared unimportant in terms of predicting flame dimensions, and the more important non-dimensional parameter was  $V_j/U_\infty$ .

Birch et al. (1989) drew similarities between non-reacting and reacting jets, specifically by relating the mean concentration field and ignition characteristics of a non-reacting jet to the temperature and radiation fields associated with the reacting jet. Natural gas was delivered from a 10.26 mm inner diameter pipe in a wind tunnel at a fuel jet speed of 76.2 m/s for the majority of the experiments. Three separate flow regions within the non-reacting jet were identified using balances of jet momentum flux and crosswind momentum flux. Fuel jet flammability zones were identified, along with locations of maximum heat flux below the centerline of the reacting jet. Ultimately, this study lent credence to the theory that reacting and non-reacting jets shared similar physical and fluidic characteristics.

Investigations into fuel jet flammability zones in crosswind also included a study by Hoehne and Luce (1992). Experiments were conducted in a wind tunnel by delivering methane, ethane, butane and heptane gases through a plate jet orifice whose diameter

varied from 1.5 mm up to 9.5 mm.  $V_j/U_\infty$  varied from 10 to 113. Using knowledge of upper and lower flammability limits of the fuels, it was found that the limits of the flammability zones of fuel jets were independent of the fuel used.

More recent publications have explored the possibility of identifying different flame mode shapes as well as characterizing flame structures for turbulent jet diffusion flames in cross-flow. Huang and Chang (1994), Huang and Yang (1996) and Huang and Wang (1999) performed experiments in a wind tunnel on a 5.0 mm inner diameter stack burning propane fuel.  $R$  typically ranged from 0.25 to 5.5. Flame mode shapes were identified and described based on visual observations. The flame was observed to transition from a wake-stabilized diffusion flame with a stack lee side recirculation zone to a downwashed flame shape as the velocity ratio decreased. Temperature distributions and gas concentrations within the flame were also investigated.

Gollahalli and Nanjundappa (1995) conducted a wind tunnel study that investigated the stability and structure of turbulent propane flames in cross-flow. They burned propane fuel on a 20 cm tall flare stack with an inner diameter of 4.7 mm.  $R$  was varied between 0.02 and 0.17. Two flame structures were identified, each with distinct zones. For  $R = 0.17$ , the flame was named “Type 2” and had three zones: a planar recirculation vortex attached to the burner tube, an axisymmetric flame following the recirculation region, and a third junction zone with intense mixing of the jet and cross-flow streams. The “Type 1” flame for  $R = 0.02$  had only two zones: the planar recirculation vortex and intense mixing zone. Using mean cross-sectional temperature and composition profiles of the flames, Gollahalli and Nanjundappa concluded that the “Type 2” flame was akin to a premixed flame and the “Type 1” flame was diffusion controlled.

Majeski et al. (2000) studied the size and shape of jet diffusion flames in cross-flow. Using a closed-loop wind tunnel, he burned propane fuel on flare stacks with inner diameters of 10.8, 16.7, 22.1 and 33.3 mm.  $R$  was varied between 0.014 and 1.3. Using a still camera to capture images of the flame, two distinct flame shapes were observed, one being a buoyancy dominated “rising” plume and the other a cross-flow momentum

dominated “trapped” plume. Majeski also used these captured flame images to develop a model that predicted flame length, and to develop a new parameter separate from  $V_j/U_\infty$ ,  $R$  and  $Ri$  (the Richardson Number) to describe the flame shape.

Studies on turbulent jet diffusion flames in cross-flow have thus far focussed mainly on the areas of flame structure, size, shape and trajectory. Total research in each area is sparse and limited to certain cases of flow regimes, and is by no means a rigorous exploration of the behaviour of turbulent diffusion flames in cross-flow. Studies to date agree on the notion that reacting jets exhibit many of the same physical and fluidic features of non-reacting jets. A wide variety of flame modes, shapes and zones have been identified and described, and there have also been an assortment of non-dimensional parameters proposed to predict flame dimensions. However, a common observation has been that as a reacting jet transitions from buoyancy- to momentum-dominated flow, the flame mode shifts from a rising, “free” plume to a downwashed plume trapped in the wake region of the stack.

A few recent publications (i.e. Poudenx et al., 2004 and Johnson and Kostiuk, 2002) have attempted to cover the subjects of reacting jets and developing reliable methods for calculating and predicting the combustion efficiency of a turbulent jet diffusion flame in cross-flow issuing from a flare stack. But overall, the studies conducted on reacting jets contain very limited work concerning the topic of turbulent jet diffusion flame combustion efficiency. Several studies agree that reacting and non-reacting jets share similar physical and fluidic characteristics, however there is much disagreement over which flow parameters should be used to develop a plume rise equation. Briggs (1975) attempted to address this discord amongst the wide variety of theoretical and empirical plume rise predictions, and authored the definitive study in the area of buoyancy-dominated plume rise research.

The present study aims to further knowledge on this topic of buoyant plume rise and dispersion, as well as the topic of turbulent jet diffusion flame combustion efficiency. Literature addressing the calculation of combustion efficiency of a flare stack through



temperature and compositional mapping of the plume will be discussed in the following section.

## **2.2 Flare Combustion Efficiency**

### **2.2.1 Flare Plumes in Quiescent Air**

In the mid-1980s a significant investigation was performed by the Environmental Protection Agency (EPA) concerning the operation of open-pipe and modified commercial flares, specifically the factors affecting their combustion efficiency and the products of combustion. The first publication in this study (Joseph et al., 1983) detailed the experimental facility and methodology used. The test facility was exposed to the atmosphere. It was used to test flare stacks from 7.6 to 30.5 cm in outer diameter. The scope of the experiment was controlled by a few significant constraints, namely propane/nitrogen mixtures were the only fuel used, a protective screen shielded the flare from crosswind, and tests were limited to dry weather conditions to limit the effects of humidity.

The second publication (Pohl and Soelberg, 1985) presented experimental results from testing at this facility, along with major findings. The report attempted to overcome experimental difficulties encountered in previous researches, such as closing the mass balance, measuring soot emissions, uncertainties from sampling only along the plume centerline, and flame fluctuations due to ambient turbulence. Pohl and Soelberg used two methods for calculating combustion efficiency: collecting the entire plume with a hood, and simultaneous sampling over the cross-section of the plume using five probes.

Overall combustion efficiency of the flare was found to consistently exceed 98 % provided the flame was stable. Unstable flames caused by extremely high fuel gas jet speeds or excessive steam injection yielded efficiencies as low as 55 %. Pohl and Soelberg concluded that the flame became unstable once the fuel jet speed at the stack exit exceeded the flame speed. It should be noted that only the 30.5 cm outer diameter stack was tested using relatively low fuel jet speeds (up to 3 m/s) typical of solution gas flaring in industry.

Some major observations made in this study from the experimental data are as follows.

- Soot accounted for less than 0.5 % of the unburned hydrocarbons emitted by flares, even when pure propane was combusted.
- The size of the flare head did not influence combustion efficiency for the 7.6 cm to 30.5 cm outer diameter flare stacks studied.
- Measurement of local combustion efficiency at a single point could indicate the overall combustion *inefficiency* ( $1 - \eta$ ) with an accuracy of 50 % (i.e.  $1 \% \pm 0.5 \%$  for a 99 % efficient flame).

### 2.2.2 Flare Plumes in Crosswind

The effects of crosswind on the combustion efficiency of a flare have been of considerable interest to industry over the past 30 years. Over this period a wide variety of studies have been conducted in the pursuit of understanding this phenomena.

A prominent study conducted by Siegel (1980) investigated the effects of crosswind using a facility exposed to the atmosphere. Two separate stacks were used in the study, a 5 m tall 70 cm outer diameter stack and a pilot-size 4.6 m tall 20.3 cm outer diameter stack.

The larger stack combusted fuel mixtures containing hydrogen, nitrogen and various hydrocarbons (1-4 carbon atoms per molecule). Fuel jet speed was set to either 0.5 m/s or 2 m/s, and a horizontally mounted fan provided a steady crosswind of 6.7 m/s. Ambient winds produced natural crosswinds of 1.2 to 6 m/s during experiments, significantly affecting the accuracy of the study concerning actual values of crosswind speed. Combustion efficiency was calculated to be 97 % or higher for all conditions.

The smaller stack burned the same fuel mixtures as the large stack. Multi-point downstream sampling of the plume was performed and results indicated that combustion efficiency was above 97 %.

In all of Siegel's experiments, the fan was positioned above the plane of the stack tip, so that the flare stack itself was not exposed to the crosswind. This prevented the creation of a wake and recirculation region downstream of the stack as would occur in the field when the crosswind blows against the entire height of the stack. This wake and recirculation region has been proven to have a significant impact on the performance of a flare in terms of fuel leakage from the flame (Johnson et al., 2001b).

In 1984, Leahey et al. studied the sulphur efficiency of sour gas flares in the field. A technical paper by SKM Consulting Ltd. (1988) provides a summary of his results. The concept of sulphur efficiency is similar to combustion efficiency in that it quantifies the amount of unwanted combustibles (in this case, H<sub>2</sub>S) that are converted into a less toxic substance (i.e. SO<sub>2</sub>). A 24 m tall, 10.2 cm outer diameter flare stack was studied in the field under ambient conditions. Natural crosswind varied between 1.1 m/s and 6.1 m/s. Sulphur efficiency was reported to be 22 %, 89 %, 96 % and 100 % in four separate tests. Unfortunately, details were not provided in the report concerning the measurement technique used nor was there a valid reason presented to explain the great variation in efficiency.

An atmospheric study of flare stacks was conducted by Romano (1983). The heating value of the fuel was varied from 3.1 to 81.4 MJ/m<sup>3</sup>, and fuel delivery rate varied from 1.7 x 10<sup>-4</sup> to 0.33 m<sup>3</sup>/s. Using single-point sampling downstream of the plume, the overall combustion efficiency of the flare was reported to be above 98 %. No details on flare stack dimensions or crosswind speeds were given.

In 1996, the Alberta Research Council (ARC) considered laboratory scale and field studies of flare stack efficiency measurements (Stroscher, 1996). Single-point sampling and multi-point sampling techniques were evaluated in the laboratory setting, along with collection of the entire plume using a hood. The study also conducted experiments on two separate flare stacks in the field, one burning sweet solution gas (less than 1 % H<sub>2</sub>S) and the other burning sour gas (20-25 % H<sub>2</sub>S). Both fuels were composed primarily of C1 to C6 hydrocarbons. Single-point sampling was the sole measurement technique used in the field tests.

The sweet solution gas flare stack was 12 m tall and 20 cm in outer diameter. Combustion efficiency was calculated along several vertical planes downstream of the stack. Efficiency was reported to be as low as 62 %. Strosher concluded that as the amount of liquid droplets of fuel and water in the liquid knockout system increased, the combustion efficiency decreased. Evidence of incomplete combustion was discovered in the form of various toxic substances such as volatile organic compounds and polynuclear aromatic hydrocarbons.

The sour gas flare stack was 15 m tall and 7.6 cm in outer diameter. Combustion efficiency was reported to be 82 %. Incompletely oxidized products of combustion were also detected in this case.

This ARC work revealed the presence of numerous toxic chemical species in the flare plume. Unfortunately, inadequate detail was provided concerning the measurement techniques. Specifically, Strosher does not mention how he accounted for the background concentration of CO<sub>2</sub> in the entrained ambient air when making his combustion efficiency calculations.

These past studies concerning the combustion efficiency of flare stacks in crosswind are sparse and do not represent a comprehensive analysis of flare stack performance. Sampling techniques have varied from hood collection to single- and multi-point sampling, and combustion efficiencies have been reported to be as low as 22 % and as high as 100 %. In some cases, insufficient reasons are given for such great variations in combustion efficiency. Flare stack sizes have ranged from 7.6 cm to 70 cm, but there have been few attempts at making substantial connections between small-scale stacks in the laboratory and full-scale stacks that exist in the field. In addition, some studies did not even report fuel jet speeds, stack diameters, or even the sampling technique used. One of the goals of this study is to demonstrate correlations between small-scale and full-scale stacks in terms of their plumes' thermal and compositional characteristics. Recent literature, which adds credibility to the theory that a flare stack's plume dispersion and combustion efficiency are scalable, will be discussed in the following section.

### 2.2.2.1 University of Alberta Flare Research Project Results

Poudenx et al. (2004) performed experiments on scaled-down flares in a closed-loop wind tunnel. The flare stacks used had inner diameters ( $d_i$ ) ranging from 16.7 mm to 33.3 mm. Fuel jet speeds ( $V_j$ ) ranged from 0.5 m/s to 2 m/s and crosswind speeds ( $U_\infty$ ) from 1.5 m/s to 8 m/s. The fuel used was sales grade natural gas. Multi-point sampling was used to create thermal and compositional maps of the flare plume. Poudenx was able to determine that the characteristics of the mean cross-sectional structure of the thermal plume were scalable over the range of stack sizes tested. Namely, Poudenx was able to collapse his data using a derivation of Briggs' buoyant plume rise model (Eq. 2.9). Estimation of the overall efficiency from single-point sampling was found to be very sensitive to probe position due to the non-homogeneous local composition in the plume.

Johnson and Kostiuk (2000) performed combustion efficiency experiments in the same facility as Poudenx with flare stack outer diameters ( $d_o$ ) ranging from 12.1 mm to 49.8 mm. Fuel jet speeds ( $V_j$ ) ranged up to 4 m/s and crosswind speeds ( $U_\infty$ ) up to 17 m/s. Natural gas or propane was used as the combusting fuel. Diluents in the form of nitrogen and carbon dioxide were added to both fuels. It was found that the addition of inert diluents had a profound, adverse effect on the combustion efficiency. Johnson and Kostiuk developed correlations between efficiency and crosswind speed that could enable one to make predictions about the performance of full-scale flares in the field.

## 2.3 Summary of Relevant Literature

One of the objectives of this study is to verify that a flare stack plume disperses in a manner suitable for scaling. A corollary to this is to prove that a flare stack plume, which is in essence a reacting jet in crosswind, behaves like a non-reacting buoyant jet. The dispersion and trajectory of non-reacting buoyant jets have been well described by a wide variety of studies, but the same has not been done for reacting (or burning) buoyant jets. Investigations into reacting buoyant jets have focused mainly on characterizing the structure, size, shape and trajectory of the flames, and not the plume beyond the boundaries of the reacting jet. It has been indicated in a few studies that a non-reacting jet trajectory model may be used to accurately predict the trajectory of a reacting jet, but

little evidence exists to support this theory. Poudenx et al. (2004) expanded on this theory by showing that the buoyant plume resulting from a low momentum reacting jet closely resembles the plume of a buoyant non-reacting jet. This study endeavours to build on the research conducted by Poudenx by providing further evidence of the similarity in behaviour between non-reacting and reacting jets in crosswind, and by developing a scalable plume dispersion model for sub-scale to full-scale flare stacks.

Another objective of this study is to verify that a flare stack's combustion efficiency is a scalable characteristic. The combustion efficiency of solution gas flaring has been studied for a better part of the past thirty years, but considerable disagreement exists amongst the calculated combustion efficiencies stated by various investigations. As well, measurement techniques are widely varied and at times inadequate detail is given on the exact positioning of aspirating probes or on the equipment dimensions (i.e. stack diameter) and operating conditions (i.e. crosswind speeds, fuel jet speeds).

Few of these studies, such as Gollahalli et al. (1975), have attempted to make substantial connections between small-scale stacks in the laboratory and full-scale stacks that exist in the field. Theory has been developed that shows a flare stack's plume disperses in a scalable manner, but scant physical evidence of this theory has been presented nor has much research been conducted that proves or disproves scaling theory for overall combustion efficiency. No research has been conducted on reacting jets in crosswind on flare stacks with an outer diameter larger than 5 cm, which is smaller than the range of interest in this study, as a full-scale flare stack has an outer diameter of approximately 10 cm. Researchers have acknowledged that more data on full-scale flare stacks are required in order to develop a reliable scaling method. By collecting combustion efficiency data on sub-scale to full-scale flare stacks, this study aims to build on recent work by Johnson and Kostiuik (2002) to develop a scalable combustion efficiency model for sub- to full-scale flare stacks.

The last objective of this study is to demonstrate that a wind tunnel's floor and ceiling have no discernible proximity effects on the plume rise and combustion efficiency of a model flare stack, except for cases where the flare stack is very near the floor. In

addition, this study intends to show that a wind tunnel's ceiling has no effects on the approximate angle and length of a flare. Of the various studies that have used wind tunnels to conduct research on reacting jets and flare plumes in cross-flow (i.e. Gollahalli et al., 1975, Birch et al., 1989, Johnson and Kostiuk, 2000), none have made attempts to ascertain the effects, if any, of the wind tunnel floor and ceiling on the combustion efficiency of the flame or the dispersion of the plume downstream of the flare stack.

In summation, the present research aims to contribute to the topics of flare stack diameter scaling as it relates to plume dispersion and combustion efficiency. It also aims to study the use of non-reacting jet behaviour to model reacting jet trajectory and investigate possible wind tunnel ceiling and floor modeling effects on a flare stack flame and plume.

## Chapter 3

### EXPERIMENTAL METHODS AND ANALYTICAL TECHNIQUES

This chapter is devoted to the explanation of the experimental techniques used in this research, as well as the procedures used concerning data analysis. The theoretical background for scale modeling of flares will be discussed, and the Richardson Number will be recast in another form that aids in explaining the behaviour of a jet in cross-flow. Included is a detailed description of the method in which combustion efficiency of the flare was calculated.

#### 3.1 Theoretical Basis for Scale Modeling of Flares

Past researchers have made effective use of the ratios of momentum and buoyancy to momentum to describe the behaviour of jets in cross-flow.

##### 3.1.1 Momentum Ratio

The relative influence of vertical momentum of a jet to the crosswind momentum that will act to bend the jet over is the fuel jet to cross-flow momentum ratio ( $R$ ).

Recalling from section 2.1.1,

$$R = \frac{\rho_j V_j^2}{\rho_\infty U_\infty^2} \quad (3.1)$$

Note that Eq. (3.1) places equal emphasis on the magnitudes of  $V_j$  and  $U_\infty$ .

##### 3.1.2 Richardson Number

Another force balance that must be considered for explaining buoyant jets in cross-flow is the Richardson Number ( $Ri$ ). Recalling from section 2.1.1,



$$Ri = g \frac{\left( \frac{\Delta\rho_p}{\rho_\infty} \right)}{U_\infty^2} L_c \quad (3.2)$$

To make  $Ri$  more useful,  $\Delta\rho_p$  in Eq. (3.2) needs to be replaced by a relationship between the fuel jet and cross-flow speeds. This can be accomplished by performing an excess mass balance on the fluid flows associated with a bent over, non-reacting plume (Figure 3.1).

A bent-over buoyant plume entrains ambient air as it is advected downstream, thereby continuously reducing the density difference between the plume and the ambient air, as well as cooling it. Briggs (1975) found that the entrainment coefficient,  $\beta$ , varied along the length of the bent-over buoyant plume, resulting in  $\beta = 0.6 \pm 0.2$  for  $1 \leq R \leq 1000$ . This naturally results in a plume whose cross-sectional area increases with downstream distance. The initial flow rate of the cold fuel jet may be defined as  $q_o = \pi V_j R_j^2$  with an initial local density difference,  $\Delta\rho_o$ . At a downstream location where the plume has become completely bent-over, one may assume that the cold fuel jet speed,  $V_j$ , is equal to the crosswind speed,  $U_\infty$ . Now the flow rate may be defined as  $q_p = \pi U_\infty R_p^2$  where the density difference is denoted by  $\Delta\rho_p$ . Using conservation of buoyancy flux for a plume rising in a constant pressure environment with a constant ambient density,  $g(\rho_1 - \rho_\infty)q_1$  remains constant at every vertical cross-section "1" through the plume. Since gravity is constant, this buoyancy flux conservation is just a conservation of "excess mass." Note that the excess mass balance in a plume does not come from mass flux conservation, but rather from buoyancy flux conservation. It can be said that  $q_o\Delta\rho_o = q_p\Delta\rho_p$ , a relationship that allows one to replace  $\Delta\rho_p$  in Eq. 3.2 and redefine the Richardson Number as

$$Ri = g \frac{V_j}{U_\infty^3} \frac{\Delta\rho_o}{\rho_\infty} \left( \frac{R_j}{R_p} \right)^2 \quad (3.3)$$

This form of  $Ri$  has an explicit relationship between fuel jet speed and crosswind speed. The terms  $R_j$ ,  $R_p$  and  $L_c$  provide information on how the physical dimensions of the plume are affected by the combustion process. However, this research is most concerned with the velocity dependency indicated by the ratio of buoyancy to momentum forces. The reader should take note of the relationship between  $U_\infty$  and  $V_j$ , specifically the strong influence of  $U_\infty^3$  in the definition of  $Ri$ . If one assumes that the combustion efficiency is strongly dependent on the interaction of buoyancy and momentum,

$$\eta = f\left(\frac{U_\infty}{V_j^{1/3}}\right) \quad (3.4)$$

Using the above reasoning, Johnson and Kostiuk (2002) were able to develop correlations between efficiency and crosswind speed to collapse data collected on natural gas and propane flares.

$$(1 - \eta) = f\left(\frac{U_\infty}{(gV_j)^{1/3} d_o^n}\right) \quad (3.5)$$

where

$d_o$  = outer diameter of flare stack

$n$  = coefficient derived from experimental data

Later, variations of this equation will be used to collapse efficiency data from natural gas flare stacks.

## 3.2 Tracking Plume Dispersion Using Thermal Mappings

### 3.2.1 Overview

The first objective of this research was to map the mean cross-sectional thermal structure of the plume near the flare stack flame for the purposes of expanding knowledge on the dispersion of the plume of products. Little information is available on this subject

in published literature, save for the work by Poudenx et al. (2004) that the current research aims to build on.

Visualization of the plume's thermal cross-section was determined by generating mean temperature maps in much the same manner as Poudenx et al. (2004). Combustion products leaving the flare are typically much hotter than the surrounding ambient air; therefore the mean cross-sectional structure of the plume can be identified by its mean temperature contours generated at various positions downstream. Figure 3.2 demonstrates this experimental method.

A vertically oriented array of thermocouples was used to create mean cross-sectional thermal maps of the plume's structure. Chapter 4 elaborates on this temperature measurement apparatus, along with the associated data sampling and data analysis.

The definition of the plume's 50 % temperature contour at an individual cross-section is central to determining a characteristic dimension of the plume ( $d_p^*$ , which will be discussed shortly). For the purposes of this research, the 50 % temperature contour is taken to represent the plume's core, which contains a significant amount of combustion products. Poudenx et al. (2004) chose to define this core as a region that has a temperature equal to or greater than 50 % of the temperature difference between the hottest and coldest points in a cross-section.

$$T_{plume\ core} \geq \frac{T_{background} + T_{max}}{2} \quad (3.6)$$

For the sake of consistency and ease of comparison, this definition is applied to the current research. Chapter 5 will present some typical plume shapes and correlate the characteristic dimension of plume cross-sections with the buoyant plume model.

Maps of the mean cross-sectional thermal structure were generated for varying outer stack diameters ( $d_o$ ), crosswind speeds ( $U_\infty$ ), fuel jet speeds ( $V_j$ ) and distances downstream from the flare stack axis ( $X_o$ ). For each cross-sectional thermal map, the plume's 50 % temperature contour was used to define the mean plume cross-sectional

area. These cross-sectional areas were then compared to an existing buoyant plume model derived by Briggs (1975). This model is known to accurately predict the behaviour of non-reacting plumes in general, as well as the behaviour of reacting jets at large distances downstream.

### 3.2.2 Plume Dispersion Model

As stated above, the model used in this study was originally developed to predict the dispersion of a non-reacting plume. Briggs derived it based on the Richardson Number, which assumes that the buoyancy of the fuel jet and the momentum of the crosswind are the dominant forces in the flow. The present research intends to apply this model to a reacting jet. A significant characteristic of a reacting jet is that from the flare stack exit to the flame tip the buoyancy of the jet is steadily increasing because the combustion dramatically increases the jet temperature, thereby decreasing plume density. Gollahalli and Brzustowski (1975) confirmed that a non-reacting jet model could accurately predict the centerline trajectory of the flames present in a reacting jet, however their theoretical model could not account for lateral spreading of the flames caused by dramatic increases in jet temperature due to combustion.

Figure 3.3 presents an idealized model of the present situation, where the stoichiometric products of combustion are concentrated in a single point source located at the exit of the flare stack. As the plume of products is advected downstream it behaves like a non-reacting buoyant plume. Briggs buoyant plume model, modified to account for heat release due to combustion, can then be applied.

This model gives the height of the buoyant plume centerline ( $h_b$ ) for a given crosswind speed ( $U_\infty$ ), fuel jet speed ( $V_j$ ), inner stack diameter ( $d_i$ ), and distance downstream from the flare stack axis ( $X_o$ ).

$$h_b = \left( \frac{3}{2\beta^2} \right)^{1/3} \frac{g^{1/3} Q_{hv}^{1/3} R_j^{2/3} V_j^{1/3}}{T_s^{1/3} C_{p\infty}^{1/3} U_\infty} X_o^{2/3} \quad (3.7)$$

where

$\beta$  = entrainment coefficient

$Q_{hv}$  = heating value of the gas

$R_j$  = radius of fuel jet =  $d_i / 2$

$C_{p\infty}$  = heat capacity of air

$T_s$  = temperature of stoichiometric products of combustion

The derivation of Eq. 3.7 is found in Appendix A.

The Taylor-Turner hypothesis, developed by Morton et al. (1956), states that

$$\beta \propto \frac{\partial h_b}{\partial t} \quad (3.8)$$

This theory extends to relate the radius of a plume's cross-section to the plume rise,

$$R_p = \beta h_b \quad (3.9)$$

Using Eq. 3.9, Eq. 3.7 then becomes

$$R_p = \left( \frac{3\beta Q_{hv}}{2T_s C_{p\infty}} \right)^{1/3} g^{1/3} R_j^{2/3} \frac{V_j^{1/3}}{U_\infty} X_o^{2/3} \quad (3.10)$$

$R_p$  is the conventional characteristic dimension used to describe a non-reacting plume's cross-section. However, Poudenx et al. (2004) found that flare stack plumes are typically not circular and actually showed dramatically different shapes over his range of experimental conditions. For this reason a new characteristic dimension,  $d_p^*$ , was

introduced to describe a plume's cross-sectional structure.  $d_p^*$  is physically defined by the following equation.

$$d_p^* = \sqrt{Area} \quad (3.11)$$

where

$Area$  = area contained within the 50 % temperature contour of a plume's mean cross-sectional thermal structure

Now the non-reacting plume model may be defined as

$$d_p^* = (\pi)^{1/2} \left( \frac{3\beta Q_{hv}}{2T_s C_{p\infty}} \right)^{1/3} g^{1/3} d_i^{2/3} \frac{V_j^{1/3}}{U_\infty} X_o^{2/3} \quad (3.12)$$

The collection of terms  $(\pi)^{1/2} \left( 3\beta Q_{hv} / 2T_s C_{p\infty} \right)^{1/3}$  is a constant for the following conditions.

- fuel composition remains the same for all experiments
- combustion is almost complete ( $\eta \approx 100$  %)
- ambient pressure remains relatively constant

The final form of the plume rise model is

$$d_p^* \propto g^{1/3} \frac{V_j^{1/3}}{U_\infty} X_o^{2/3} d_i^{2/3} \quad (3.13)$$

Note that the above equation depends on the plume trajectory being well represented by a single value of the entrainment coefficient,  $\beta$ . Recall that Briggs (1975) observed  $\beta$  could vary between 0.4 and 0.8 along the length of a bent-over buoyant plume for the conditions  $1 \leq R \leq 1000$ . Fortunately, Johnston and Wilson (1997) showed that a single value of  $\beta = 0.6$  provides a good approximation for  $2 \leq R \leq 100$ .

### 3.3 Measuring Flare Combustion Efficiency

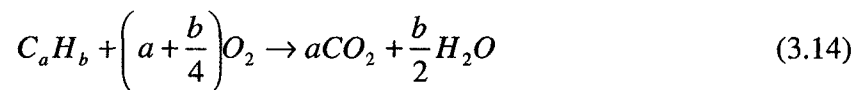
#### 3.3.1 Fuel Composition and Combustion Chemistry

The research presented used sales grade natural gas as the combusting fuel. Natural gas is composed primarily of methane (CH<sub>4</sub>). Several additional chemical species consisting of hydrocarbons (such as ethane, C<sub>2</sub>H<sub>6</sub> and propane, C<sub>3</sub>H<sub>8</sub>) and non-combustible molecules (such as CO<sub>2</sub> and N<sub>2</sub>) comprise the remainder of the gas. Table 3.1 lists the constituents of sales grade natural gas.

Chemical Species	CH <sub>4</sub>	C <sub>2</sub> H <sub>6</sub>	N <sub>2</sub>	CO <sub>2</sub>	Other
Mean % Concentration	95.2	2.1	1.7	0.8	0.2

**Table 3.1: Composition of sales grade natural gas**

In an ideal situation, all of the hydrocarbon fuel exiting a flare stack would combust to produce CO<sub>2</sub> and H<sub>2</sub>O (water vapour). Such an oxidation reaction is as follows.



where

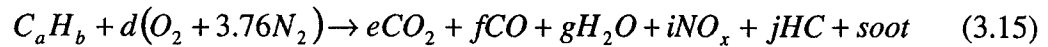
$a$  = number of carbon atoms in the hydrocarbon fuel

$b$  = number of hydrogen atoms in the hydrocarbon fuel

Atmospheric nitrogen (N<sub>2</sub>) has been neglected from the above equation and it is assumed that adequate amounts of oxygen are immediately available to react with the hydrocarbon fuel, resulting in complete combustion. When the hydrocarbon fuel is completely oxidized, the combustion reaction is considered to be 100 % efficient.

Unfortunately, such an ideal reaction is not realistic. Oxygen in the atmosphere does not mix perfectly with the hydrocarbon fuel emitted from a flare stack, resulting in incomplete combustion and the formation of chemical species other than CO<sub>2</sub> and H<sub>2</sub>O.

Atmospheric nitrogen should also be included, yielding a more realistic oxidation reaction as shown in Eq. 3.15.



where

$HC$  = unburned hydrocarbons

$NO_x$  = nitric oxides

$d, e, f, g, i, j$  = stoichiometric coefficients

Although nitrogen and nitric oxides have been included in Eq. 3.15, they will be neglected from flare combustion efficiency calculations. The reason for this is that nitrogen does not react with carbon, the element that is of greatest concern when calculating flare combustion efficiency. The role carbon plays in the overall calculation of combustion efficiency will be discussed shortly.

If there is an insufficient amount of oxygen, if reacting substances do not reside in the flame long enough, or if the flame temperature is too low, the incomplete oxidation reaction such as Eq. 3.15 can occur. The result is the production of undesirable, toxic molecules that may include carbon monoxide and a wide variety of hydrocarbons, denoted by HC. Some of these hydrocarbons are part of the fuel stream that were unaffected by the flame and some are in the form of toxic and carcinogenic compounds formed by combustion. Examples of these hazardous substances are volatile organic compounds, such as those found in solvents and cleaners, and polynuclear aromatic hydrocarbons (i.e. hydrocarbons with multiple benzene rings), which are typical components of asphalts, fuels and oils.

### 3.3.2 Local Combustion Efficiency

The second objective of this research was to map the mean cross-sectional compositional structure of the plume near the flare stack for the purposes of calculating flare combustion efficiency. It has been established in past studies (i.e. Pohl et al., 1986,



and Poudenx et al., 2000) that the products of combustion are not distributed uniformly throughout the flare plume. This means that a local value of combustion efficiency, or efficiency at a single point in space, is not uniform throughout the entire plume. Therefore, it is necessary that the local efficiency be calculated at many different points in a plume cross-section in order to arrive at an estimate of overall combustion efficiency.

A single-point gas sampling system was devised to make time-averaged measurements of gas concentrations at individual points in space. Details of the components of this system and its operation are given in Chapter 4.

Concentration maps were generated for CO<sub>2</sub>, CO, HC and O<sub>2</sub> at various cross-sections downstream of the flare. Figure 3.4 demonstrates this experimental technique.

The efficiency of a flare may be defined as the quantity of carbon as hydrocarbons in the flare gas that is converted into carbon dioxide. Local efficiency for a natural gas flare is calculated based on this definition.

$$\eta = \frac{\text{mass of carbon as CO}_2 \text{ produced by flare}}{\text{mass of carbon in C}_a\text{H}_b \text{ in flare gas}} \quad (3.16)$$

By conservation of atomic species, all carbon in the fuel will finish the reaction as CO<sub>2</sub>, CO, H<sub>2</sub>O, HC and soot. In a study conducted by the EPA (Pohl and Soelberg, 1985), it was found when burning propane that soot production accounted for less than 0.5 % of the HC and could be neglected from efficiency calculations provided the fuel being combusted was natural gas. Recent work by Prybysh et al. (2000) measured no soot production on scaled-down flare stacks in a closed-loop wind tunnel. Poudenx used a gas chromatograph analysis of the fuel stream to conclude that the HC in the plume of products emitted by a natural gas flare stack are the same relative mixture of hydrocarbons as the fuel stream. The gas analysers used in Poudenx's research and in the current research were both calibrated with methane (CH<sub>4</sub>), so that all airborne hydrocarbons were interpreted as C1 (one carbon atom per carbon-based molecule in the fuel). Hence, all unburned hydrocarbons (HC) will be represented as C<sub>1</sub>H<sub>4</sub> (whereas the

actual chemical formula for natural gas is  $C_1H_{3.96}$ ) for the purposes of the present study, given the mixture of fuels in sales grade natural gas.

Building on Eq. 3.16, local combustion efficiency can be found using the concentrations of  $CO_2$ ,  $CO$ , and  $CH_4$  produced by the process of combustion (based on Eq. 3.14).

$$\eta = \frac{[CO_2]_p}{[CO_2]_p + [CO]_p + [CH_4]_p} \quad (3.17)$$

where

$[A]_p$  = concentration of molecule A in products of combustion

Since the majority of carbon-based molecules in sales grade natural gas (see Table 3.1) and the combustion products have only one carbon atom per molecule, the addition and ratios of concentrations can be considered accurate in terms of mass conservation.

However, the current form of this equation is valid only in a closed volume with no mass transfer. This is not the case for a natural gas flare, as it is an open system characterized by the following points.

- The flare and plume of products are surrounded by a cross-flow of ambient air that reacts with the flame and then air is further entrained along the length of the plume.
- The entrained air naturally contains molecules of the same chemical form as those that are produced by combustion in the flare. These background concentrations must be accounted for in the calculation of efficiency, otherwise substantial errors will result.
- The natural gas fuel stream may contain  $CO_2$ . This means that even in a closed system there will be a certain amount of  $CO_2$  present that is not resulting from combustion and must not be included in efficiency calculations.

The foregoing points complicate the combustion efficiency calculation of Eq. 3.17. Another problem with Eq. 3.17 is that the concentration of any molecule A that results from combustion cannot be measured directly from a gas sample. The situation may be idealized by assuming that a single-point gas sample contains 1 kmol of gases, composed of CO<sub>2</sub>, CO, CH<sub>4</sub>, and O<sub>2</sub>. The number of moles (N) of each molecule in the 1 kmol sample may be calculated as follows.

$$N_{CO_2S} = [CO_2]_S (1kmol) = N_{CO_2P} + N_{CO_2E} + N_{CO_2G} + N_{CO_2R} \quad (3.18)$$

$$N_{COS} = [CO]_S (1kmol) = N_{COP} + N_{COE} + N_{COR} \quad (3.19)$$

$$N_{CH_4S} = [CH_4]_S (1kmol) = N_{CH_4P} + N_{CH_4E} + N_{CH_4R} \quad (3.20)$$

$$N_{O_2S} = [O_2]_S (1kmol) = N_{O_2P} + N_{O_2E} + N_{O_2R} \quad (3.21)$$

where the subscripts S, P, E G, and R denote molecules found in the gas sample, products of combustion, entrained air, flare gas, and reacting air, respectively.

Hence, Eq. 3.17 may be rewritten as

$$\eta = \frac{N_{CO_2P}}{N_{CO_2P} + N_{COP} + N_{CH_4P}} \quad (3.22)$$

The above equations must be simplified to determine the concentrations of the products of combustion, and hence estimate the flare combustion efficiency. Poudenx et al. (2004) performed an order of magnitude analysis to determine the relative importance of each variable in the equation. A summary of the reasoning follows.

As shown in Table 3.1, natural gas typically contains less than 1 % CO<sub>2G</sub>. When methane burns completely in air, nearly 10 moles of air and 1 mole of methane are used to produce 1 mole of CO<sub>2P</sub>. Assuming a dilution of the combustion products with the entrained air of 100:1, 1000 moles of entrained air are present for every 10 moles of products. The ambient air that reacts with the flame and is entrained in the plume typically contains about 400 ppm of carbon dioxide (CO<sub>2R</sub> and CO<sub>2E</sub>). This means that

$CO_{2R}$  and  $CO_{2G}$  can be neglected because they represent about 0.04 % and 1 %, respectively, of the carbon dioxide found in the sample. This also means that  $CO_{2E}$  may represent about 40 % of  $CO_{2S}$ , so it cannot be neglected from calculations. Using Eq. 3.18,

$$N_{CO_2P} = [CO_2]_S - N_{CO_2E} \quad (3.23)$$

Similar arguments may be made for carbon monoxide, CO, and hydrocarbons,  $CH_4$ . It is estimated that a realistic combustion process produces about 1 %  $CO_P$  and 1 %  $CH_4P$ . The ambient air that reacts with the flame and is entrained in the plume typically contains about 2 ppm each of carbon monoxide and methane. This means that  $CO_R$  and  $CH_4R$  are insignificant because they each represent about 0.02 % of the carbon monoxide and hydrocarbons found in the sample.

$$N_{CO_P} = [CO]_S - N_{CO_E} \quad (3.24)$$

$$N_{CH_4P} = [CH_4]_S - N_{CH_4E} \quad (3.25)$$

Assuming a hypothetical state of pure products without any extra air involved other than that used in combustion, Eq. 3.21 can be simplified by neglecting  $O_{2R}$ . Therefore,

$$N_{O_2P} = [O_2]_S - N_{O_2E} \quad (3.26)$$

For the above equations to be useful, the number of moles of each molecule in the entrained air must be evaluated. A means to solve this problem is to define a local volume fraction of products,  $\alpha_L$ , in the gas sample. The concentrations of  $O_{2E}$ ,  $O_{2S}$  and  $O_{2P}$  can be related by the following.

$$[O_2]_S = \alpha_L [O_2]_P + (1 - \alpha_L) [O_2]_E \quad (3.27)$$

If one assumes complete combustion occurs in the flame, then no oxygen would exist in the products of combustion, so  $O_{2P}$  can also be neglected. The volume fraction,  $\alpha_L$ , may now be defined as

$$\alpha_L = 1 - \frac{[O_2]_S}{[O_2]_E} \quad (3.28)$$

The concept in Eq. 3.26 may be used to calculate the number of moles of dioxide in the products of combustion.

$$N_{CO_{2P}} = [CO_2]_P (1kmol) = \frac{[CO_2]_S - (1 - \alpha_L)[CO_2]_E}{\alpha_L} \quad (3.29)$$

Similarly,

$$N_{CO_P} = [CO]_P (1kmol) = \frac{[CO]_S - (1 - \alpha_L)[CO]_E}{\alpha_L} \quad (3.30)$$

$$N_{CH_{4P}} = [CH_4]_P (1kmol) = \frac{[CH_4]_S - (1 - \alpha_L)[CH_4]_E}{\alpha_L} \quad (3.31)$$

Now, using Eq. 3.29 to 3.31, the calculation of the local combustion efficiency calculation may be performed,

$$\eta = \frac{N_{CO_{2P}}}{N_{CO_{2P}} + N_{CO_P} + N_{CH_{4P}}} \quad (3.32)$$

Equivalently,

$$\eta = \frac{[CO_2]_P}{[CO_2]_P + [CO]_P + [CH_4]_P} \quad (3.33)$$

A sensitivity and uncertainty analysis for the above calculations is presented in Appendix B.

### 3.3.3 Overall Combustion Efficiency

Once the local combustion efficiency at each point in the plume's cross-section is calculated using Eq. 3.33, the overall combustion efficiency of the flare may be estimated. This is accomplished by integrating all calculated local efficiencies within a prescribed plume boundary. The process of integration and estimation of overall efficiency is as follows.

The boundaries of integration must first be defined. This is accomplished by setting a limit on the extent that the plume is diluted, or the amount of entrained ambient air. For the purposes of this research, a contour encompassing O<sub>2</sub> concentrations which are above 10 % of the difference between the background and maximum [O<sub>2</sub>] defines this boundary.

Next, local density must be calculated for each point in the area of integration. The plume's temperature is non-uniform throughout its cross-section, leading to variations in local density. Local densities may be calculated using the ideal gas law.

$$\rho_L = \frac{P_L}{\bar{R}_L T_L} \quad (3.34)$$

where

$\bar{R}_L$  = local specific gas constant

$P_L$  = local pressure

$T_L$  = local temperature

The weighted concentration of each chemical species,  $[A]_{ave}$ , is now calculated by multiplying the chemical concentration at each point by its local density, adding all these values and dividing by the sum of all local densities. This is done for species concentrations in both the sample (S) and entrained (E) air.

$$[A]_{S/E\ ave} = \frac{\sum (\rho_L [A]_{S/E})}{\sum_m \rho_L} \quad (3.35)$$

where

$m$  = number of points in the area of integration

Next the average volume fraction of products in the gas sample,  $\alpha_{ave}$ , is calculated for the area of integration. This value determines average dilution in the plume cross-section.

$$\alpha_{ave} = \frac{\sum_m \alpha_L}{m} \quad (3.36)$$

Using the above values for weighted concentrations and average dilution, average concentrations may now be found for each chemical species in the entrained air over the entire area of integration.

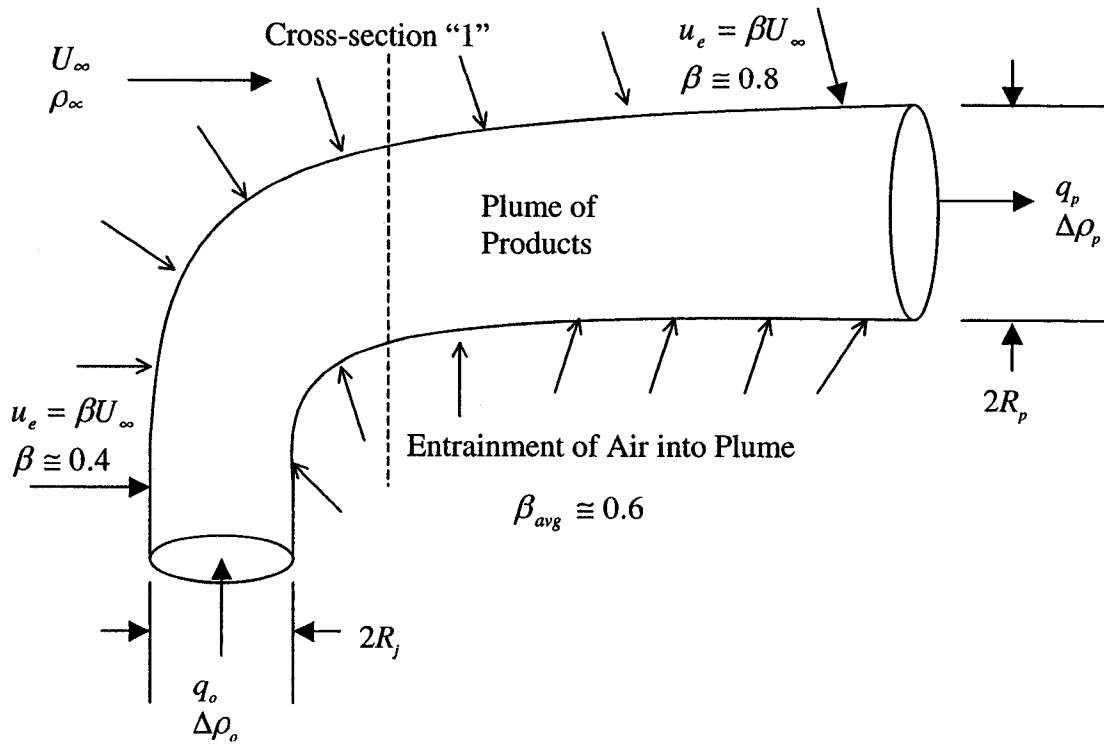
$$[CO_2]_{P\ ave} = \frac{[CO_2]_{S\ ave} - (1 - \alpha_{ave}) [CO_2]_{E\ ave}}{\alpha_{ave}} \quad (3.37)$$

$$[CO]_{P\ ave} = \frac{[CO]_{S\ ave} - (1 - \alpha_{ave}) [CO]_{E\ ave}}{\alpha_{ave}} \quad (3.38)$$

$$[CH_4]_{P\ ave} = \frac{[CH_4]_{S\ ave} - (1 - \alpha_{ave}) [CH_4]_{E\ ave}}{\alpha_{ave}} \quad (3.39)$$

Finally, the overall combustion efficiency of the flare may be calculated.

$$\eta_{ave} = \frac{[CO_2]_{P\ ave}}{[CO_2]_{P\ ave} + [CO]_{P\ ave} + [CH_4]_{P\ ave}} \quad (3.40)$$



$q_o$  = cold fuel jet initial flow rate       $q_p$  = plume flow rate

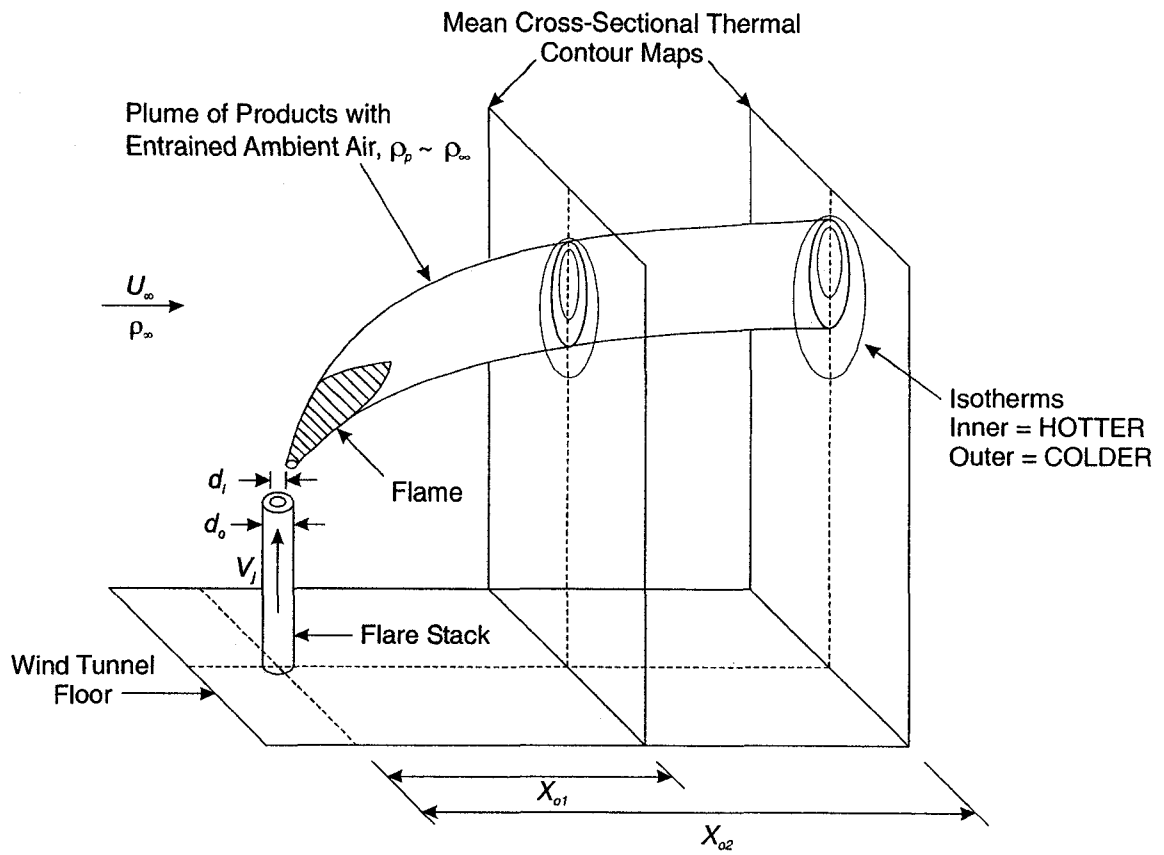
$\beta_{avg}$  = average entrainment coefficient       $u_e$  = entrainment speed of ambient air

$R_j$  = cold fuel jet radius       $R_p$  = plume radius

$\Delta\rho_o$  = initial local density difference

**Figure 3.1: Entrainment of ambient air into a bent over, non-reacting plume**

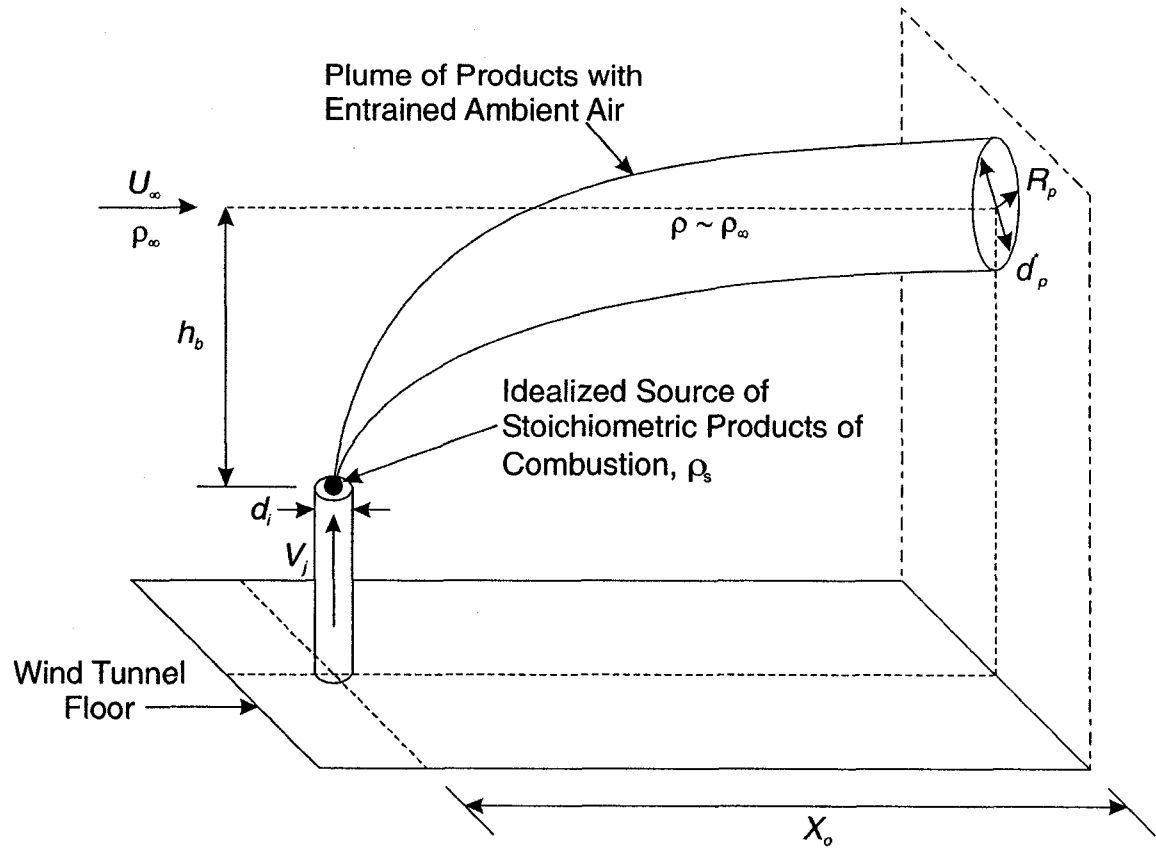




$d_i$  = inner stack diameter

$X_{o1}$ ,  $X_{o2}$  = varying distances downstream of flare stack axis

**Figure 3.2: Mean cross-sectional temperature mapping for a reacting jet in crosswind**



$d_p^*$  = characteristic dimension of the plume

**Figure 3.3: Idealized model of a non-reacting buoyant plume in crosswind**

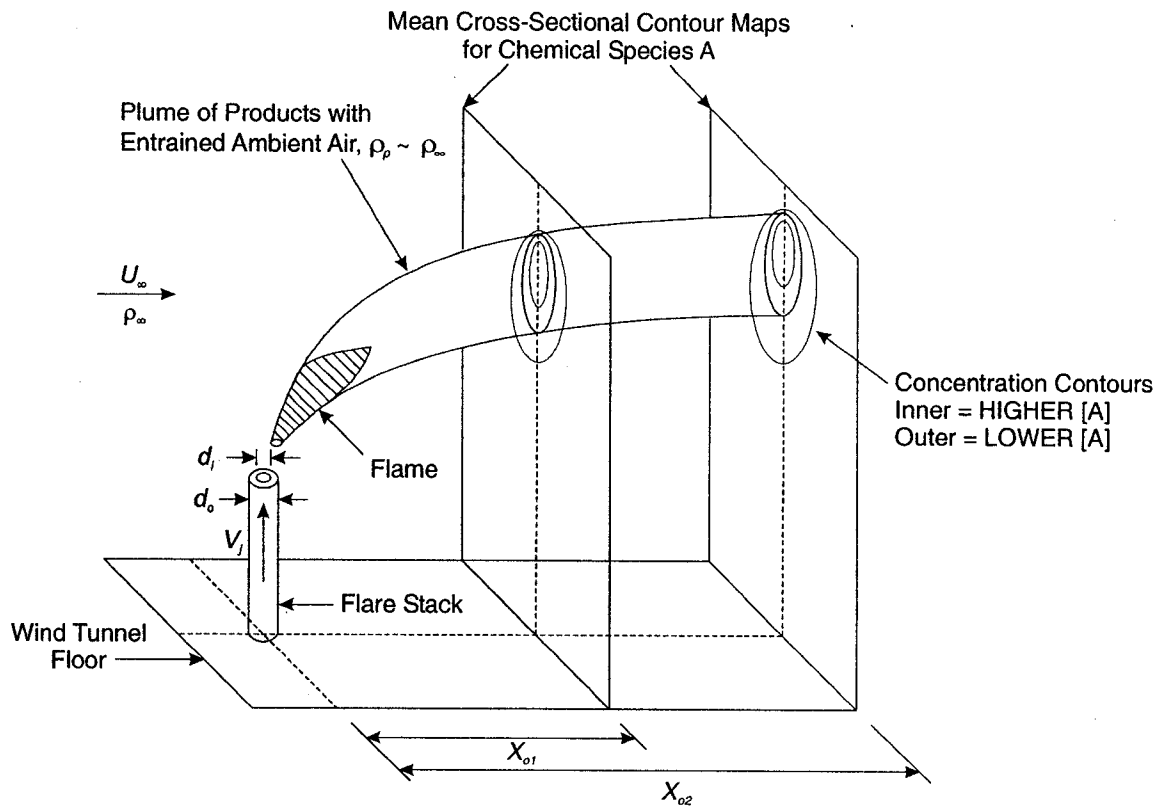


**Figure 3.4: Mean cross-sectional compositional mapping for a reacting jet in crosswind**

## Chapter 4

### FACILITY AND EQUIPMENT

This chapter is divided into three sections that describe the experimental and diagnostic systems used in this research. The first section, concerning experimental systems, will discuss the wind tunnel, the methods used to monitor and control wind speed, the variety of flare stacks used, and the fuel delivery system. The second section will describe the facility's diagnostic systems: the control computers, the motorized two-dimensional traverse, the temperature measurement apparatus, the plume sampling system and gas analysers, and the digital camera for capturing flame images. The final section will provide the steps followed for achieving steady state experimental conditions under which data were collected in the wind tunnel facility.

#### 4.1 Facility Experimental Systems

##### 4.1.1 Wind Tunnel

All experiments were performed under steady state conditions at the National Research Council (NRC) open-loop low-speed wind tunnel facility in Ottawa, ON, a cross-sectional model of which is displayed in Figure 4.1. This wind tunnel is a single-pass facility that continuously draws fresh air into the test section from the outside, effectively avoiding recirculation of any flare combustion products that may leave the facility's exhaust. The test section of the facility measured 3.05 m wide by 6.10 m tall by 8 m long and was housed within a 3-storey building. Steel I-beams were mounted along both walls of the test section to act as guide rails for a motorized traverse system and to act as a mounting surface for a removable false ceiling, both of which will be discussed in later sections. The tunnel featured corner fillets at the edges of the ceiling and floor that gradually decreased in size along the length of the test section to recede into the tunnel corners. These corner fillets are visible in Figure 4.2. This design accounted for boundary layer growth and ensured that the mean velocity of the test section's core flow

remained constant along the length of the test section. The wind tunnel also featured a removable ceiling cap that allowed for insertion and removal of wind tunnel equipment.

The tunnel had a 6 m diameter fan that was powered by a 1050 kW DC motor, continuously providing fresh ambient air to the test section at crosswind speeds up to 39 m/s. The facility was used for lower crosswind speeds however ( $U_{\infty} \leq 14$  m/s), and was tested for stability and velocity profile uniformity over the speed range required for the experiments. To measure velocity stability, a pitot tube was positioned in the centre of the test section at the location of the tip of a 3.05 m tall flare stack. The probe was maintained at this position for several hours while crosswind speed was sampled at 5 Hz for three data sets at  $U_{\infty} = 2, 5,$  and 8 m/s. The mean crosswind speed and speed fluctuations were found for each data set. Table 4.1 presents the results.

Set Crosswind Speed, $U_{\infty}$ (m/s)	Measured Mean Crosswind Speed (m/s)	Fluctuations, $u^*_{\infty}$ (m/s)	Fluctuations Intensity, $u^*_{\infty} / U_{\infty} \times 100\%$ (%)
2	2.39	0.23	9.6
5	5.13	0.21	4.2
8	8.23	0.15	1.8

**Table 4.1: NRC open-loop low-speed wind tunnel crosswind steadiness.  $u^*_{\infty}$  = first standard deviation of crosswind speed fluctuations**

The speed fluctuations for  $U_{\infty} \geq 5$  m/s tests were deemed to be within an acceptable range (less than 5 %). As  $U_{\infty}$  approached 2 m/s, crosswind speed fluctuations became large and potentially problematic. Fluctuations in crosswind speed were attributed to unsteady outdoor winds blowing into the wind tunnel inlet. Mean cross-sectional thermal mappings were generated at  $U_{\infty} = 2$  m/s, but these crosswind speed fluctuations need to be considered when interpreting the data.

Figure 4.3 displays a typical velocity profile at the stack location in the wind tunnel. Data were recorded using a pitot tube. Wind tunnel velocity profile uniformity throughout the test section was judged to be acceptable for this research, as effects of non-uniformity in the cross-flow were filtered out as the plume entrained ambient air from differing heights and downstream positions.

Solid-state analog temperature sensors with a measuring accuracy of  $\pm 0.5$  °C monitored the tunnel intake air temperature and gas detectors mounted outside the test section monitored hydrocarbon and carbon monoxide concentrations.

#### 4.1.2 Wind Speed Monitoring and Control

Wind speed was measured with 2 pitot tubes that were mounted on both wind tunnel walls and protruded into the airflow at the inlet of the test section. The tubes were connected to independent pressure transducers that were monitored by two separate computers, one being the master control computer and the other a computer operated by an NRC technical officer. The master control computer was used to collect and display  $U_\infty$  data, and the other computer was used to set the desired  $U_\infty$ . Wind speed was set manually by using a pair of analog potentiometers (for coarse and fine adjustments) to control the current delivered to the wind tunnel's 1050 kW DC motor.

#### 4.1.3 Removable False Ceiling

A removable false ceiling was constructed for the NRC facility for the purpose of testing the proximity effects a wind tunnel's ceiling on flare combustion efficiency and plume rise, as well as the flame length and angle. The removable false ceiling was mounted in the wind tunnel 2.74 m above the floor, as shown in Figure 4.2. It measured 3.02 m wide by 2.44 m long and sat on top of the rails mounted on the wind tunnel walls, spanning the width of the tunnel.

The removable false ceiling was used for ceiling effects experiments as opposed to the NRC facility's actual ceiling

- to avoid inflicting permanent heat damage to the NRC wind tunnel ceiling through flame impingement.
- to prevent excessive flare stack oscillations. It was observed that a  $d_f = 26.9$  mm flare stack in crosswind oscillated considerably and required additional support in the form of steel wires securing the flare stack to the wind tunnel walls. It was

decided that a shorter, more stable flare stack would be a better choice than an ungainly, 6 m tall flare stack that reached to the NRC wind tunnel's actual ceiling.

The removable false ceiling was constructed from aluminum sheeting with steel U-channels mounted on top for stiffness and support. Flare stacks of fixed diameter but adjustable height, which will be discussed in the next section, were used to flare natural gas at varying distances from the removable false ceiling and floor.

#### 4.1.4 Flare Stacks

##### 4.1.4.1 Flare Stacks of Varying Diameter and Fixed Height

One aspect of this research was devoted to determining if the dispersion of the plume from a flare and its combustion efficiency were scalable. For these experiments three flare stack sizes were tested. Inner diameters ( $d_i$ ) of the stacks were 26.9 mm, 52.6 mm and 102.3 mm, corresponding to 1, 2 and 4 inch schedule 40 steel pipes. The ratio of inner diameter over outer diameter for a standard 4 inch schedule 40 steel pipe is 0.9. The outside surfaces of the 1 and 2 inch stacks were machined to match this ratio, so the outside diameters ( $d_o$ ) of the 1, 2 and 4 inch stacks were 30.0 mm, 58.8 mm, and 114.3 mm. This was done in order to preserve geometric similarity. Each stack was 3.05 m tall.

A full-scale battery flare stack is considered to be a standard 4 inch schedule 40 steel pipe. Battery sites separate the water and solution gas from the crude oil, and then transport the liquid hydrocarbons by pipeline or other means to a refinery for further processing. Under typical atmospheric conditions, crosswind speed ( $U_\infty$ ) may vary from near quiescent up to 15 m/s, resulting in a laminar boundary layer on the outer surface of a full-scale flare stack. The external cross-flow Reynolds ( $Re_D$ ) number for  $30.0 \text{ mm} \leq d_o \leq 114.3 \text{ mm}$  model flare stacks ranges from 4000 to  $1.143 \times 10^5$  as the crosswind speed is increased from 1 m/s to 15 m/s, which is in the regime where a laminar boundary layer separation would be expected for the cross-flow on the outside surface of the stack. A scaled-down flare stack should be in the same flow regime to ensure that the characteristics of its boundary layer separation, vortex shedding and

downstream recirculation vortex are similar to those of a full-scale stack. Visual observation confirmed this by inspecting soot deposition on each of the stacks. For each of the three stack diameters, soot was found on the backside of the stack's cylindrical surface in the wake region, between 90 and 270 degrees from the forward stagnation point. If boundary layer separation had been turbulent, soot would have been found on the backside of the stack's cylindrical surface between 120 and 240 degrees from the forward stagnation point.

A change in the external flow regime does not occur until  $Re_D \sim 5 \times 10^5$  where the stack boundary layer becomes turbulent. As an example, this transition occurs at  $U_\infty = 15$  m/s when  $d_o = 0.5$  m and hence places full-scale battery flare stacks in the same external flow regime as scaled-down flare stacks.

#### 4.1.4.2 Flare Stacks of Fixed Diameter and Adjustable Height

The second part of this study dealt with the proximity effects of a wind tunnel's ceiling and floor on a flare stack plume's trajectory and combustion efficiency. It also examined the ceiling's effects on flame length and angle. Two separate 1 inch schedule 40 steel pipes with  $d_i = 26.9$  mm were used, one being 2.74 m tall and the other 1.52 m tall. Both pipes' outside surfaces were machined to  $d_o = 30.0$  mm. Again, the ratio of inner diameter over outer diameter was held at 0.9 to maintain geometric similarity with a full-scale flare stack.

The 2.74 m tall stack was used in conjunction with the removable false ceiling to study ceiling proximity effects on flare plume trajectory, combustion efficiency, flame length and flame angle. Using a friction fit facilitated by a Teflon ferrule and steel nut, a flange adapter mounted to the wind tunnel floor allowed the distance that the stack extended above the wind tunnel floor to be adjusted to place the stack tip at varying distances from the removable false ceiling. The stack was able to traverse anywhere between the bottom surface of the removable false ceiling to 1.52 m below it. The length of stack that extended below the floor resided in a  $d_i = 102.3$  mm (4" schedule 40 pipe) plenum. Figure 4.4 is a cross-sectional schematic of the flange adapter and flare stack assembled and mounted to the wind tunnel floor.



The 1.52 m tall stack was used to study floor proximity effects on flare plume trajectory and combustion efficiency. The same flange adapter was used to adjust the stack's height from 0.30 m to 1.22 m above the floor.

#### **4.1.5 Fuel Delivery System**

The fuel delivery system was designed so that the flare could burn natural gas, propane, or a mixture of the two fuels that could include carbon dioxide or nitrogen. All of the experiments conducted in this research were done with only natural gas. Figure 4.5 displays the corresponding gas supply schematic for this fuel. Fuel was delivered to the system via a sales grade natural gas source. The gas traveled through metal coils in a water bath to stabilize the gas temperature at approximately  $293\text{ K} \pm 1\text{ K}$  as the mass flow controllers were calibrated to deliver sales grade natural gas at this temperature. After this step the fuel passed through one of seven computer-controlled mass flow controllers, each calibrated for specific ranges of flow rates between 0 and 3000 slpm. Each of the mass flow controllers provided an accuracy of  $\pm 1.0\%$  of full scale. Gas temperature was measured with a solid-state analog temperature sensor before being piped to the base of the flare stack. Flow of the fuel was controlled using two (2) two-way solenoid valves, as shown in Figure 4.5.

A retractable hydrogen flame ignitor that used a manual sparking system for ignition facilitated combustion of the fuel. As shown in Figure 4.5, the hydrogen flame ignitor consisted of a rigid steel tube connected to flexible Teflon tubing that led to a compressed hydrogen fuel cylinder. Attached to the tip of the steel tube was a sparking tip, whose wires led back through the steel tube to a powered, manual sparking system. To ignite the natural gas fuel jet coming from the flare stack, first the steel tube was extended into the center of the wind tunnel through an access port in the wind tunnel wall. Upon positioning the tip of the steel tube above the flare stack tip, hydrogen fuel was delivered through the Teflon and steel tubing via a regulator on the compressed cylinder. Then, using the manual sparking system, the hydrogen fuel was ignited, producing a hydrogen flame that in turn ignited the flare stack's natural gas fuel jet. The regulator on the hydrogen fuel cylinder was then closed and the steel tube was retracted

back to the wind tunnel wall so that it would not cause any flow disturbances at or near the flare stack tip.

## **4.2 Facility Diagnostic Systems**

### **4.2.1 Control Computers and Software**

Three computers controlled all aspects of experimentation and data acquisition at the NRC facility. Slave computer # 1, a Celeron 733 MHz, was dedicated to receiving data from the mass flow controllers and was connected to all valves in the fuel delivery system. Slave computer # 2, a Dell 1.1 GHz, was devoted to acquiring data from the temperature measurement apparatus, discussed in section 4.2.3. The third computer, an AMD Athlon 1.67 GHz, acted as the master control computer. This machine controlled all aspects of the fuel delivery system and the motorized traverse, and monitored the tunnel wind speed, ambient temperature and ambient pressure. It collected data from the plume sampling system (described in section 4.2.4), the digital camera (section 4.2.5) and all experimental data acquired by the two slave computers for the purposes of processing and storage.

All three computers operated on Windows 2000 / NT platforms and were connected via a local area network. Data acquisition and control software was developed exclusively with LabVIEW (National Instruments) computer code. The master control computer generated a master file for each test that contained important parameters such as ambient temperature, ambient pressure, tunnel wind speed, set and actual fuel flow rates, and gas analyser readings. Grapher and Surfer (Golden Software Inc.) programs were used for all plotting of data.

### **4.2.2 Motorized Two-Dimensional Traverse**

Figure 4.6 displays the motorized two-dimensional traverse installed in the test section downstream of the flare stack. The traverse was computer-controlled and could be programmed to follow a predetermined two-dimensional grid pattern behind the flare stack, pausing at each grid node to either collect a gas sample or thermocouple data,

depending on the nature of the experiment. Servomotors facilitated movement of the traverse probe mount plate in the X- and Y-directions (horizontal and vertical directions, respectively) with a spatial accuracy of  $\pm 5$  mm in both directions. Either the single-point gas sampling probe or the multi-point thermocouple system (the thermocouple “rake”) could be attached to the traverse probe mount plate; both systems will be described in later sections.

The traverse system I-beam included side-supports that had wheels installed on both ends. These wheels were set in rails that were mounted on the wind tunnel walls for manual position of the traverse in the Z-direction (streamwise direction). The traverse could be positioned anywhere between the stack location and up to 8 m downstream. The traverse was locked in position using four hydraulic pistons. One piston was mounted on each corner of the traverse, and upon pressurization each piston extended until it made contact with the wind tunnel wall, thereby securing the traverse’s streamwise position.

#### 4.2.3 Temperature Measurement

A multi-point thermocouple-based system was used for collected temperature data on the thermal plume. The thermocouple (TC) system (or thermocouple “rake”) is displayed in Figure 4.7. Figure 4.8 shows the thermocouple “rake” installed on the traverse probe mount. Also note in Figure 4.8 that the ceiling cap has been removed; this ceiling cap allowed for insertion and removal of wind tunnel equipment. The “rake” was an aluminum box-beam on which 29 type E (nickel-chromium / copper-nickel) thermocouples were mounted, each of which was housed in a 30.5 cm long steel tube with a diameter of 6 mm. The steel tubes were used to extend the tips of the thermocouples from the rest of the system so that the thermocouples were isolated upstream from any flow disturbances that the aluminum box-beams and TC terminal boxes may have caused. In addition, extending the thermocouples away from the rest of the system helped the TC terminal boxes and their associated wires avoid heat damage from the flare. The thermocouple wires themselves extended 4 cm from the tips of the steel tubes and their junctions measured approximately 2 mm in diameter. Positions of the thermocouples could be adjusted manually along the box-beam and were spaced at

intervals of 95 mm or 50 mm, based on the size of the plume to be mapped. Accuracy of the type E thermocouples was  $\pm 3$  K based on the error limits of the thermocouple wire and the calibration of the temperature measurement system. The smallest difference in temperature that was detected was 1 K. A data acquisition system with cold-junction compensation was used to measure thermocouple outputs. The traverse followed a predetermined grid pattern, moving the thermocouples laterally from one side of the plume to the other. At each point, temperatures were sampled at 25 Hz and time-averaged over a 20 s period to calculate mean temperatures. Complete two-dimensional thermal maps required between 7 to 20 minutes depending on the plume size.

#### 4.2.3.1 Radiation Effects

A natural gas flame is a predominantly blue flame and as such does not radiate significant amounts of energy. Simple heat transfer calculations for the variety of testing conditions concluded that the maximum expected incident radiation on a thermocouple on the TC rake was approximately  $2000 \text{ W/m}^2$ . The most extreme testing situation encountered in the wind tunnel in terms of radiation heat transfer was for the following conditions.

- Fuel: sales grade natural gas (see Table 3.1), energy density is  $37.5 \text{ MJ/m}^3$
- $d_i = 102.3 \text{ mm}$  (full-scale)
- $V_j = 2.0 \text{ m/s}$ , corresponding to a fuel flow rate of  $920 \text{ l/min}$  ( $0.0153 \text{ m}^3/\text{s}$ )
- $U_\infty = 4 \text{ m/s}$
- $T_{max} = 450 \text{ K}$  ( $\sim 175 \text{ }^\circ\text{C}$ )
- $T_\infty = 293 \text{ K}$  ( $20 \text{ }^\circ\text{C}$ )

An energy balance calculation concluded that the type E thermocouple sensed a 4 K temperature increase due to the natural gas flame radiation alone. See Appendix D for details on energy balance calculations. Considering the maximum plume temperature measured in this situation was approximately 450 K, an incurred error of 4 K was

considered to be acceptable. One can conclude that for all other thermal plume mappings, heat flux resulting from flare radiation incurred an error in temperature measurements of less than 4 K.

#### 4.2.3.2 Total Incurred Error in Calculation of the Plume Characteristic Dimension

Considering that the type E thermocouples used in this study had an accuracy of  $\pm 3$  K and that flare radiation could incur a maximum error in temperature measurement of 4 K, a mean cross-sectional thermal plume map could have a maximum error of 7 K for a typical temperature measurement. In a worst-case scenario, all data points along or near the 50 % temperature contour would be 7 K higher than actual. Several mean cross-sectional thermal plume maps collected in this study were examined to determine the effect of this error upon the calculation of the area captured within the 50 % temperature contour, and hence the calculation of the plume characteristic dimension,  $d_p^*$ . It was found that the maximum expected error in the calculation of  $d_p^*$  because of flare radiation effects and thermocouple accuracy was approximately 7 %.

#### 4.2.4 Plume Gas Sampling

Single-point sampling was used for gas analysis of the flare plume, focussing on concentrations of CO<sub>2</sub>, CO, CH<sub>4</sub>, and O<sub>2</sub> (as discussed in Chapter 3). The single-point gas sampling probe developed for this research is shown in Figure 4.9. It was a 1/4" diameter stainless steel inner tube housed within a 3/8" diameter stainless steel outer tube that was attached to an aluminum support arm which connected to the traverse's probe mount plate. The inner tube was connected to 21.4 m of Teflon tubing that ran to 4 separate gas analysers. The sampling system was isokinetic, in that suction pressure on the gas sampling probe line was adjusted so that the speed of the gas sample inside the line matched the crosswind speed ( $U_\infty$ ) in the wind tunnel.

The sampling system could measure the mean concentrations of CO<sub>2</sub>, CO, CH<sub>4</sub>, and O<sub>2</sub>. Using a carbon mass balance as described by Eq. 3.33 the local combustion efficiency could be calculated at the sample point. The length of the Teflon tube incurred

a sampling delay of approximately 15 s, which was incorporated into the data acquisition technique. Data was sampled at 2 Hz and time-averaged over 30 s periods.

Figure 4.10 provides an overview of the entire gas analysis system. Independent lines with gas flow meters delivered samples to each of the four analysers at their required flow rates (approximately 0.5 l/min for the CH<sub>4</sub> analyser, 1.0 l/min for the CO<sub>2</sub>, CO, and O<sub>2</sub> analysers). The analysers used consisted of a Siemens Ultramat 6E (CO<sub>2</sub> and CO), a Siemens Oxymat 6E (O<sub>2</sub>), and a Horiba FIA-510 (CH<sub>4</sub>). Each analyser was calibrated at the beginning of each day of experiments. Gravimetrically prepared primary master calibration gases balanced with nitrogen were used. Table 4.2 lists the calibration gases used and their reported accuracies.

Calibration Gas	Concentration	Accuracy
CO <sub>2</sub>	500 ppm	± 25 ppm
CO <sub>2</sub>	1500 ppm	± 75 ppm
CO	10 ppm	± 0.5 ppm
CO	40 ppm	± 2 ppm
CH <sub>4</sub>	10 ppm	± 0.5 ppm
CH <sub>4</sub>	100 ppm	± 5 ppm
O <sub>2</sub>	20.9%	± 0.4 %

**Table 4.2: Concentration and accuracy of primary master calibration gases**

The Siemens Ultramat 6E uses two separate non-dispersive infrared detectors that measure concentrations of CO<sub>2</sub> and CO. In each analyser, an infrared beam is fired through 2 separate test cells, one housing a reference gas and the other housing the gas sample to be analysed. After the beams exit the 2 test cells, the beams are compared for difference in energy intensity. This energy difference between the two beams is caused by absorption of the beam by the gas sample, and is used to generate an electric signal proportional to the concentration of CO<sub>2</sub> or CO.

The Siemens Oxymat 6E is a paramagnetic detector. This detector makes use of the paramagnetic properties of O<sub>2</sub> for detection purposes. O<sub>2</sub> molecules from the gas sample are placed in an inhomogeneous magnetic field that draws the molecules in the

direction of increased field strength. This process induces a pressure differential across a test cell that produces an electrical signal proportional to the pressure differential. The concentration of O<sub>2</sub> is then calculated based on this signal.

The Horiba FIA-510 is a flame ionization detector. Within the unit a hydrogen flame is used to combust the gas sample, causing carbon atoms in the sample to emit ions. This process produces a trace ionization current across 2 electrodes near the flame, which is directly proportional to the number of carbon atoms as hydrocarbons burned in the sample.

The non-dispersive infrared and paramagnetic detectors produced outputs of 0-20 mA, which were converted to 0-10 V DC signals using resistors. The ionization detector produced a 0-10 V DC output. All outputs were relayed to data acquisition cards installed in the master control computer. Table 4.3 lists the range, drift, repeatability and uncertainty of each gas analyser.

Detector		Range	Drift	Repeatability	Uncertainty
Name	Type				
Ultramat 6E	CO <sub>2</sub>	0-10 <sup>4</sup> ppm	< ±1% of range / week	< 1% of range	100 ppm
Ultramat 6E	CO	0-200 ppm	< ±1% of range / week	< 1% of range	2 ppm
FIA-510	CH <sub>4</sub>	0-500 ppm	< ±1% of range / day	< 0.5% of range	2.5 ppm
Oxymat 6E	O <sub>2</sub>	0-25 %	< ±0.5% of range / 3 months	< 1% of range	0.25%

**Table 4.3: Range, drift, repeatability and uncertainty of each gas analyser**

#### 4.2.5 Digital Camera System

A Nikon D100 digital still camera was used to capture images of flare stack flames for the portion of this research concerned with investigating ceiling effects. Images were captured with an 18 mm lens under ISO 1000 equivalent conditions. Aperture was set to  $f = 2.8$  and shutter speed varied between 1/13 s and 1/2.5 s depending on the luminosity of the natural gas flames. Captured images had a spatial resolution of 3000 pixels horizontally and 2000 vertically. The camera's field of view was approximately 1.7 m wide by 1.2 m tall in the plane of the flare stack axis, so that the

resolution was approximately 300 pixels/cm<sup>2</sup>. The camera was focussed using a chequered target placed in the plane of the flare stack axis.

The camera was housed in a protective plywood box and was located normal to the crosswind using a simple traverse system that allowed for positioning of the camera in the Y- and Z-directions (vertical and streamwise directions, respectively). The traverse system consisted of aluminum tubing and pillow blocks. Four pillow blocks secured the system to the wind tunnel wall, two blocks connected the two vertical aluminum tubes to the single streamwise one, and one block served as a hard point for the camera's plywood box. All camera positioning was performed manually and the aluminum tubes were secured by inserting them into the pillow blocks and forming friction fits.

The system was mounted on the inside of the wind tunnel wall at the edge of the entrance to the test section. Figure 4.11 displays this traverse system inside the tunnel with the ceiling section removed. The master control computer handled all camera functions remotely.

### **4.3 Achieving Steady State Conditions**

All experiments were performed under steady state conditions at the National Research Council (NRC) open-loop low-speed wind tunnel facility. Steady state conditions were achieved for temperature measurement and gas analysis experiments through the following steps.

1. Install temperature measurement apparatus or plume sampling system on motorized traverse.
2. If performing plume sampling experiment, bring gas analysers online and initiate "warm-up" cycles. Allow 1.5 hours for "warm-up" and calibration.
3. Install removable false ceiling if desired.
4. Install desired flare stack.



- a. 1.52 m or 2.74 m tall  $d_i = 26.9$  mm adjustable height flare stack (for use with removable false ceiling or floor proximity experiments) or
  - b. 2.74 m tall  $d_i = 26.9, 52.6$  or 102.3 mm fixed height flare stack
5. Manually position traverse in wind tunnel along Z-direction. Lock traverse in position with hydraulic pistons.
  6. Record ambient pressure and temperature.
  7. Activate wind tunnel fan and set wind speed. Wait for wind speed measurement on master control computer to settle on constant value.
  8. If performing plume sampling experiment, record gas analyser data to obtain background concentrations of CO<sub>2</sub>, CO, CH<sub>4</sub>, and O<sub>2</sub>.
  9. Open manual shut-off valve in fuel delivery system.
  10. Using master control computer,
    - a. open master valve and two-way solenoid valve # 1 in fuel delivery system (Figure 4.5).
    - b. activate one of seven mass flow controllers and set desired flow rate.
    - c. open two-way solenoid valve # 2 leading to flare stack (Figure 4.5).
  11. Insert hydrogen flame ignitor into wind tunnel to ignite flare. Retract upon ignition of flare.
  12. Using master control computer,
    - a. program two-dimensional grid pattern for traverse operation.
    - b. position traverse at starting point of two-dimensional grid pattern. Activate grid program. Collect temperature or gas analysis data.

13. Upon completion of experiment, using master control computer, close two-way solenoid valve # 1 in fuel delivery system.
14. Allow flare to extinguish. Connect separate compressed nitrogen source to fuel line and purge fuel delivery system with nitrogen gas.
15. Using master control computer, deactivate mass flow controllers and close two-way solenoid valve # 2.
16. Set wind speed to zero and deactivate wind tunnel fan.

#### 4.4 Summary

The need to verify the scalable thermal and compositional characteristics of a flare plume has required the use of an open-loop low-speed wind tunnel facility that is sufficiently large enough to accommodate the flare plumes produced by model flare stacks of up to  $d_o = 114.3$  mm (4 inch schedule 40 pipe). The facility is single-pass and does not allow for recirculation or accumulation of flare combustion products in the test section.

The temperature and gas sampling apparatuses developed specifically for this study will be used to gather mean thermal and compositional data in this tunnel on  $30.0 \text{ mm} \leq d_o \leq 114.3$  model flare stacks burning natural gas. These data will be used to validate past results gathered at the smaller University of Alberta wind tunnel on  $10.8 \text{ mm} \leq d_o \leq 49.8$  mm model flare stacks burning natural gas, as well as show how smaller wind tunnels can be operated to minimize scale flare stack model sizing effects.

Making use of a removable false ceiling, it will also be demonstrated that a wind tunnel's floor and ceiling have no discernible proximity effects on the plume rise and combustion efficiency of a model flare stack, except for cases where the flare stack is very near the floor. In addition, by using a digital camera to capture still true-color images of the flare it will be shown that a wind tunnel's ceiling has no effects on the physical dimensions of a flare.

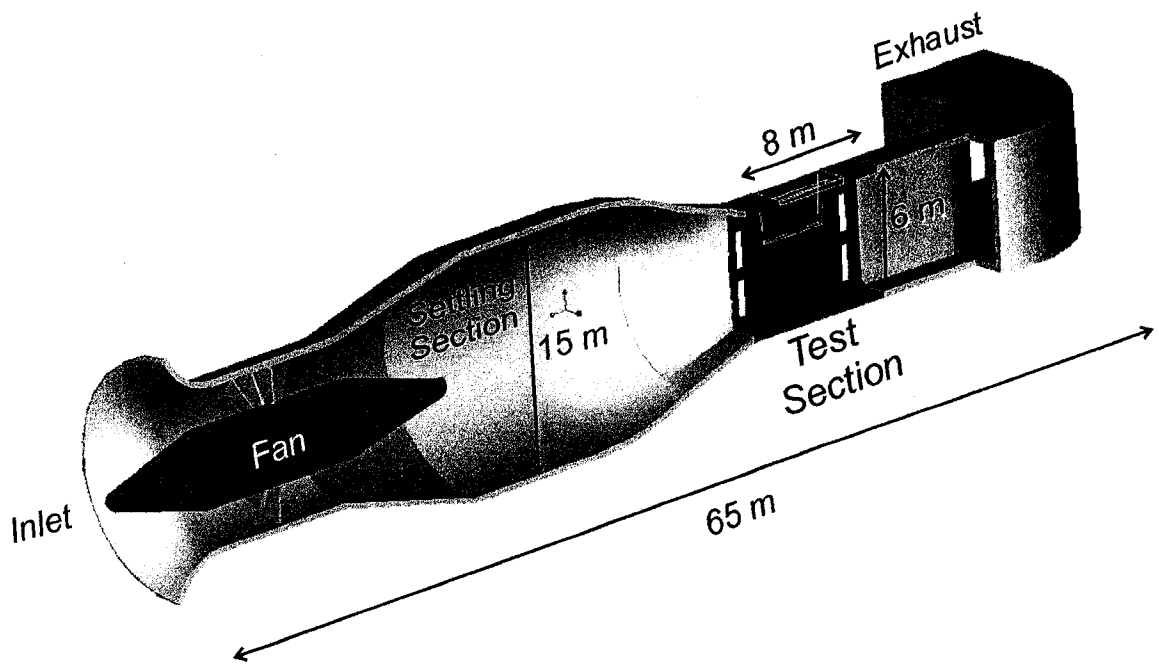


**Figure 4.1: Cross-sectional model of NRC open-loop low-speed wind tunnel**

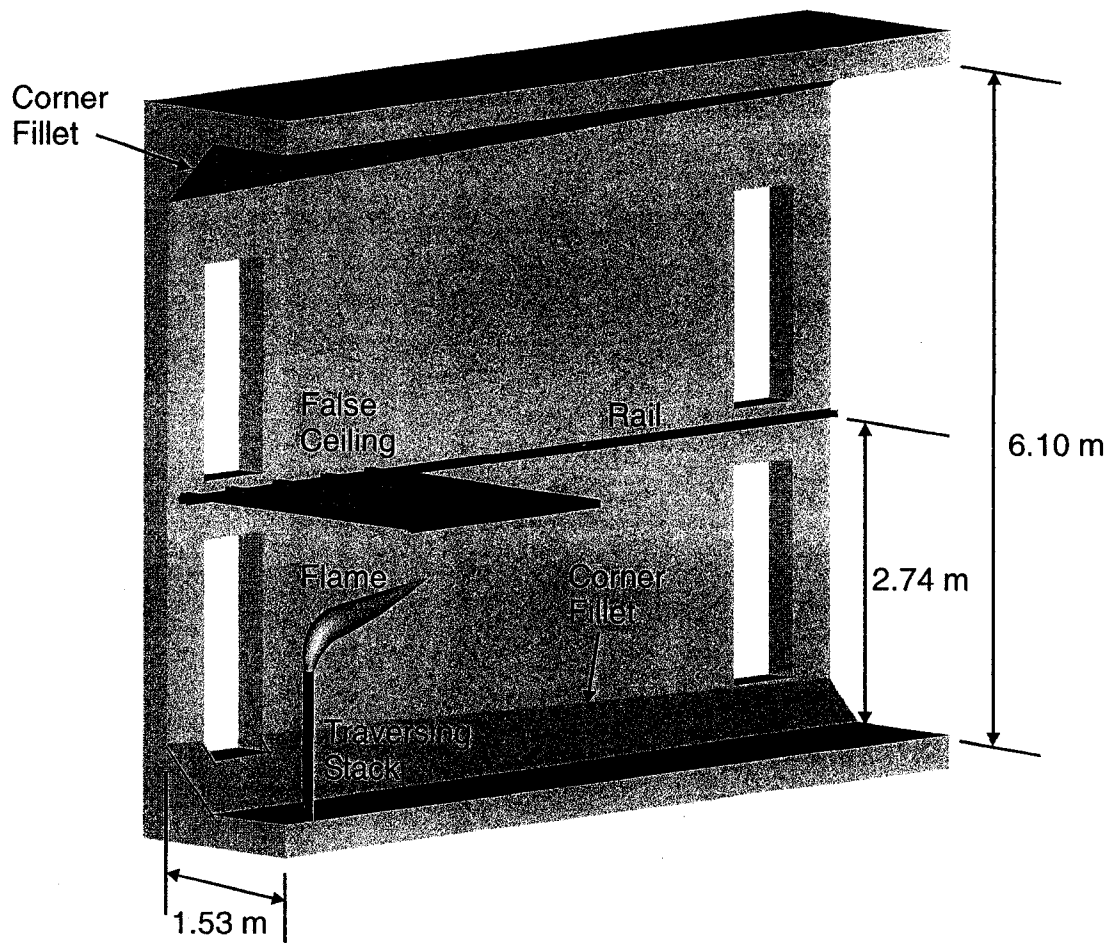


**Figure 4.2: Schematic of removable false ceiling in wind tunnel half-section. Removable false ceiling constructed of aluminum sheeting with steel U-channels mounted on top for stiffness and support**

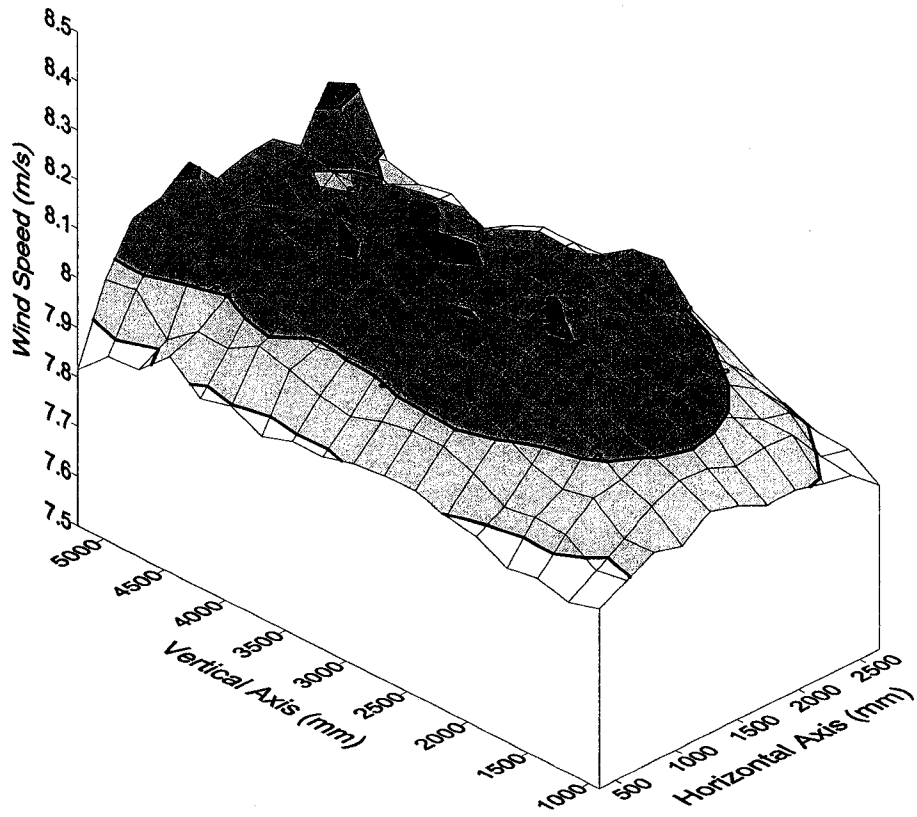


**Figure 4.3: Typical velocity profile at stack location in NRC wind tunnel for  $U_{\infty} = 8$  m/s using a pitot tube. Horizontal and vertical axis in mm relative to wind tunnel floor and wall, respectively**

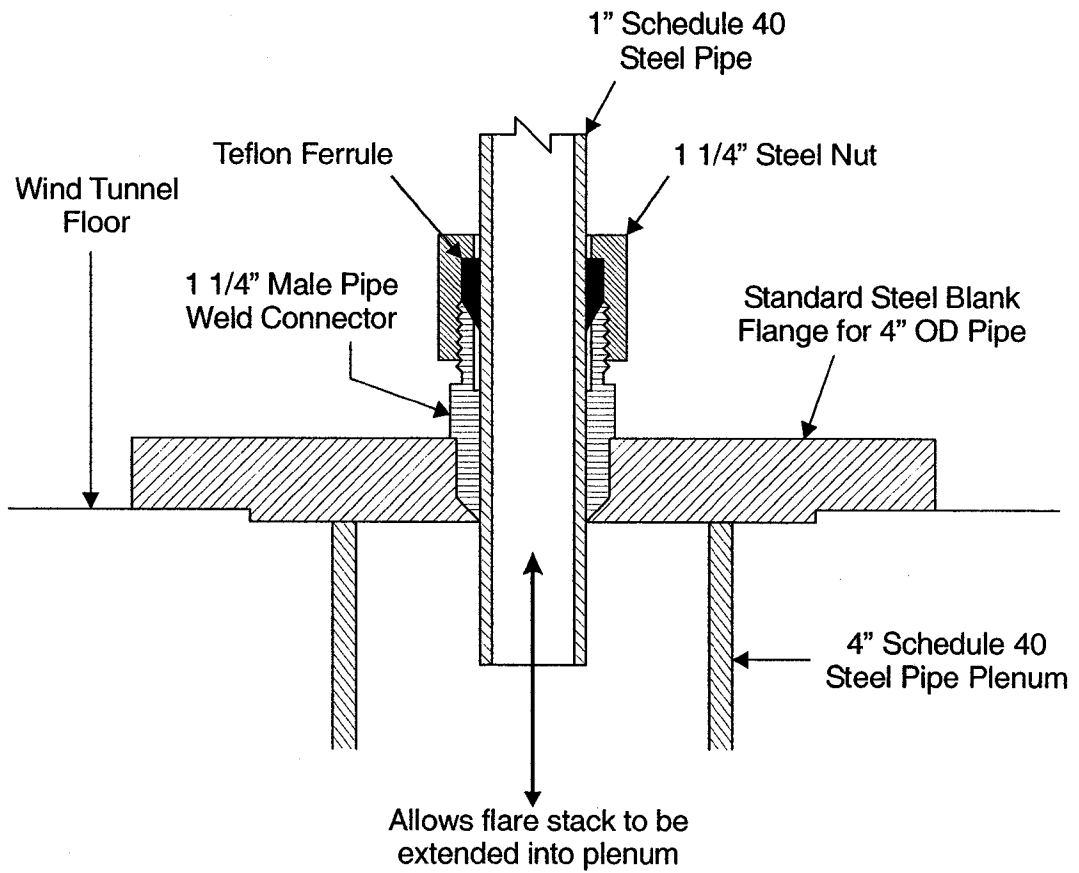


**Figure 4.4: Cross-sectional schematic of assembled flange adapter and 1" flare stack, mounted to wind tunnel floor**

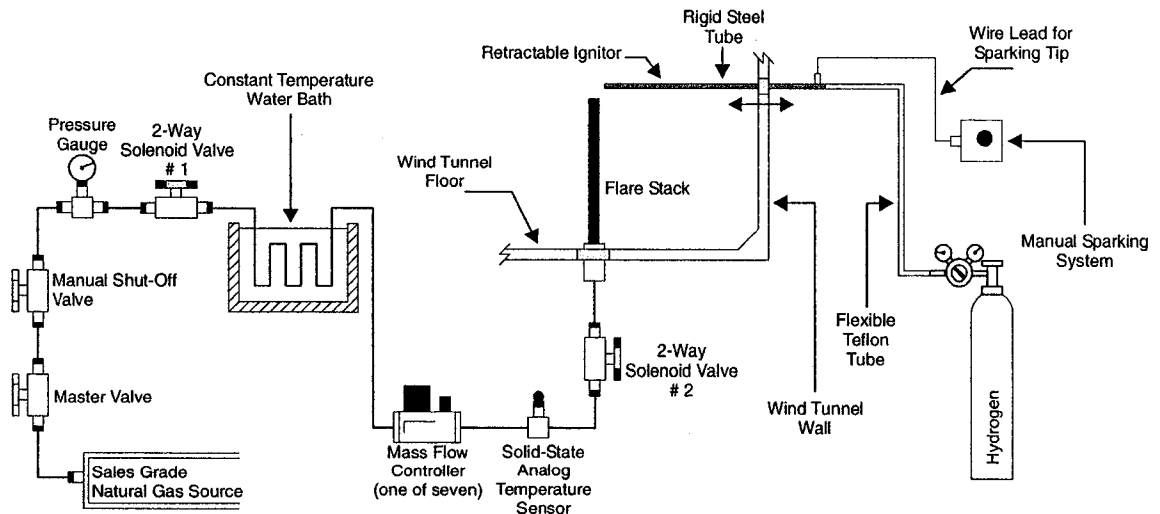


**Figure 4.5: Schematic of fuel delivery system**

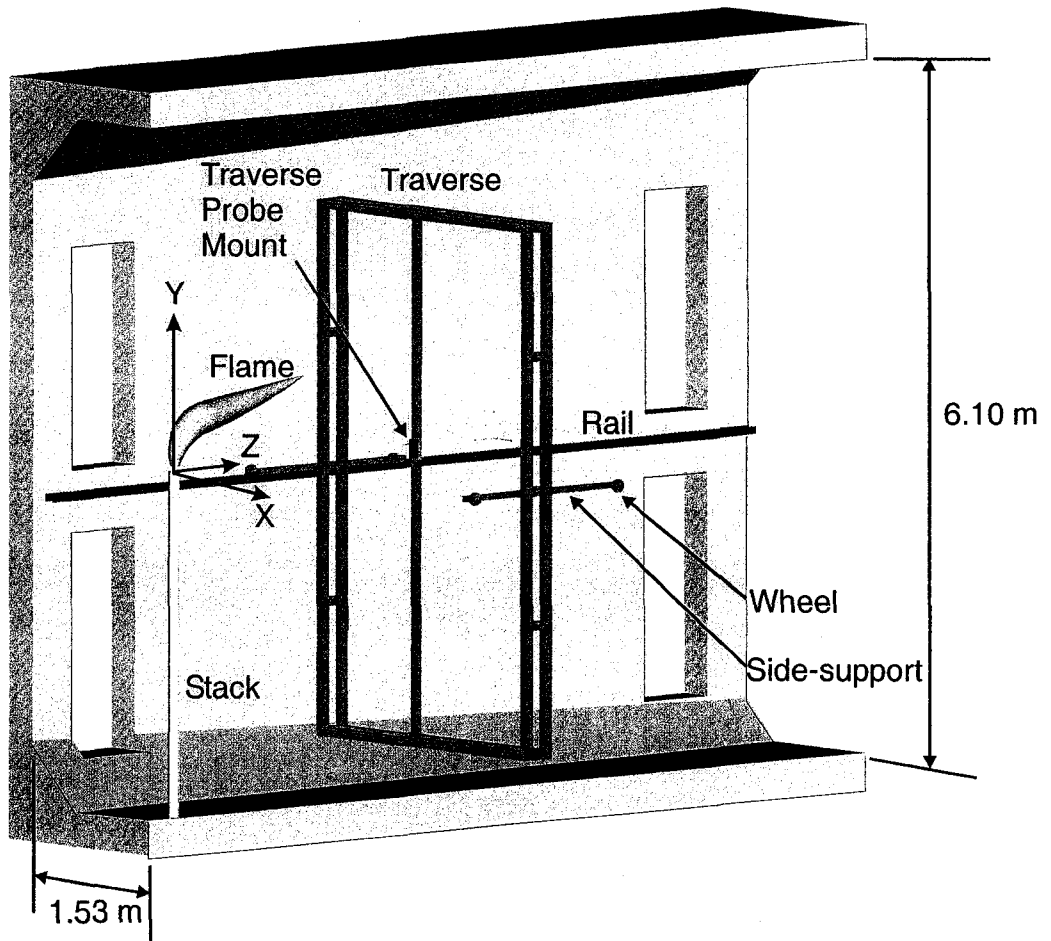


**Figure 4.6: Cross-sectional schematic of wind tunnel with two-dimensional traverse installed**

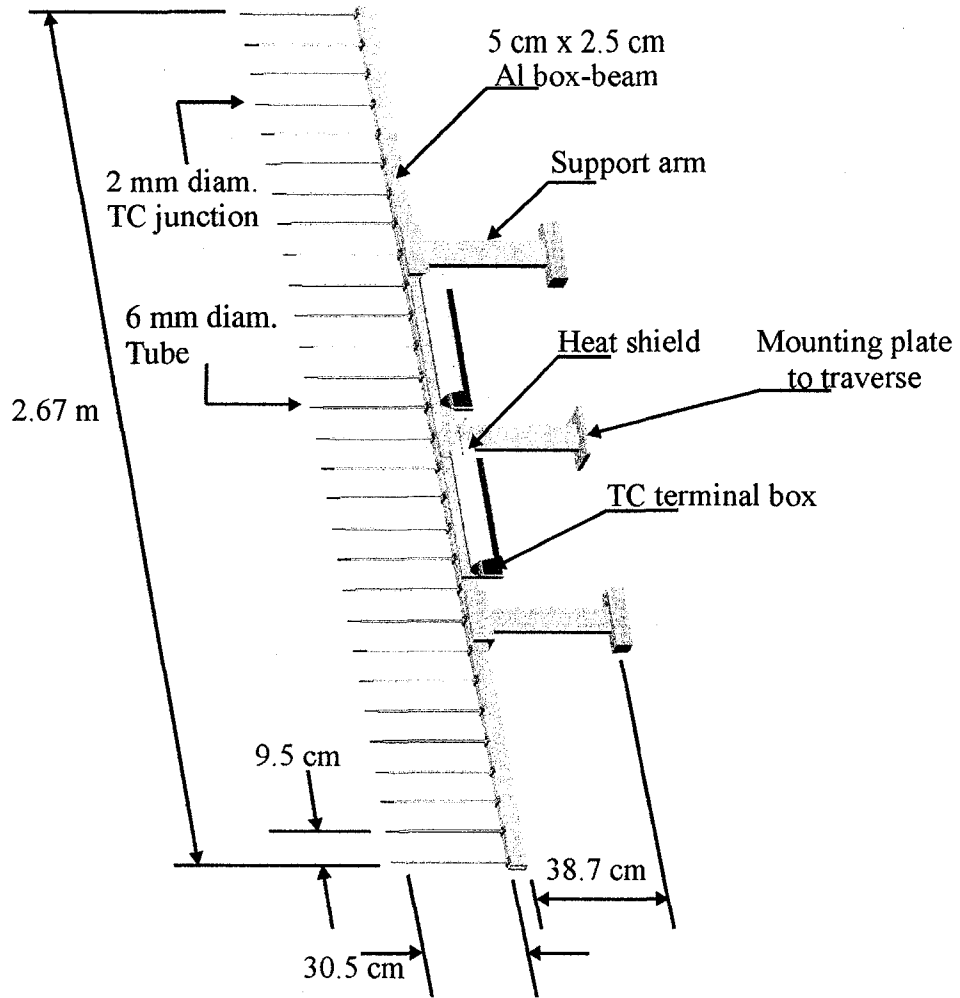


**Figure 4.7: Schematic of multi-point thermocouple system**



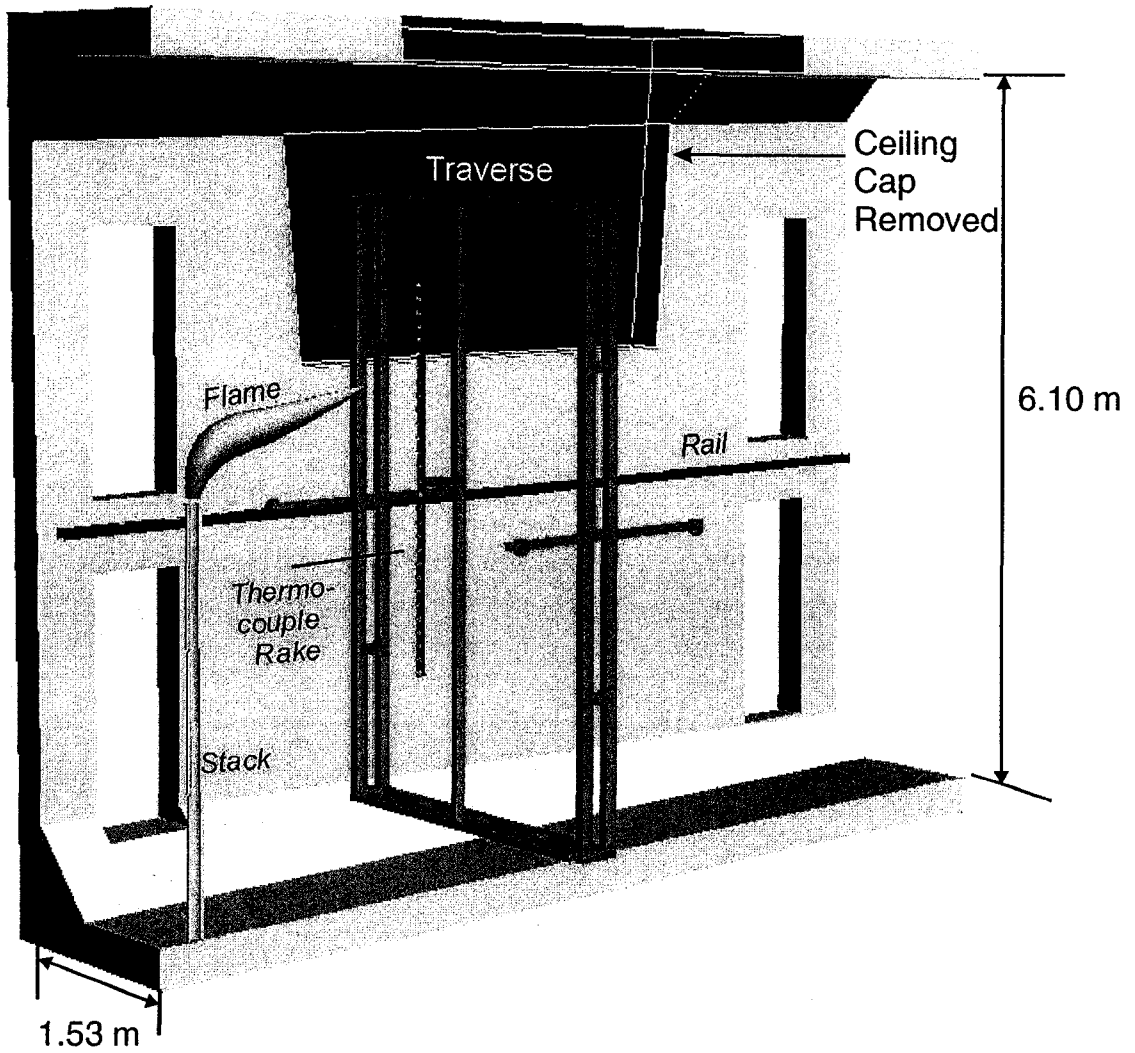


**Figure 4.8: Cross-sectional schematic of wind tunnel with thermocouple “rake” attached to traverse probe mount. Note the ceiling cap is removed**

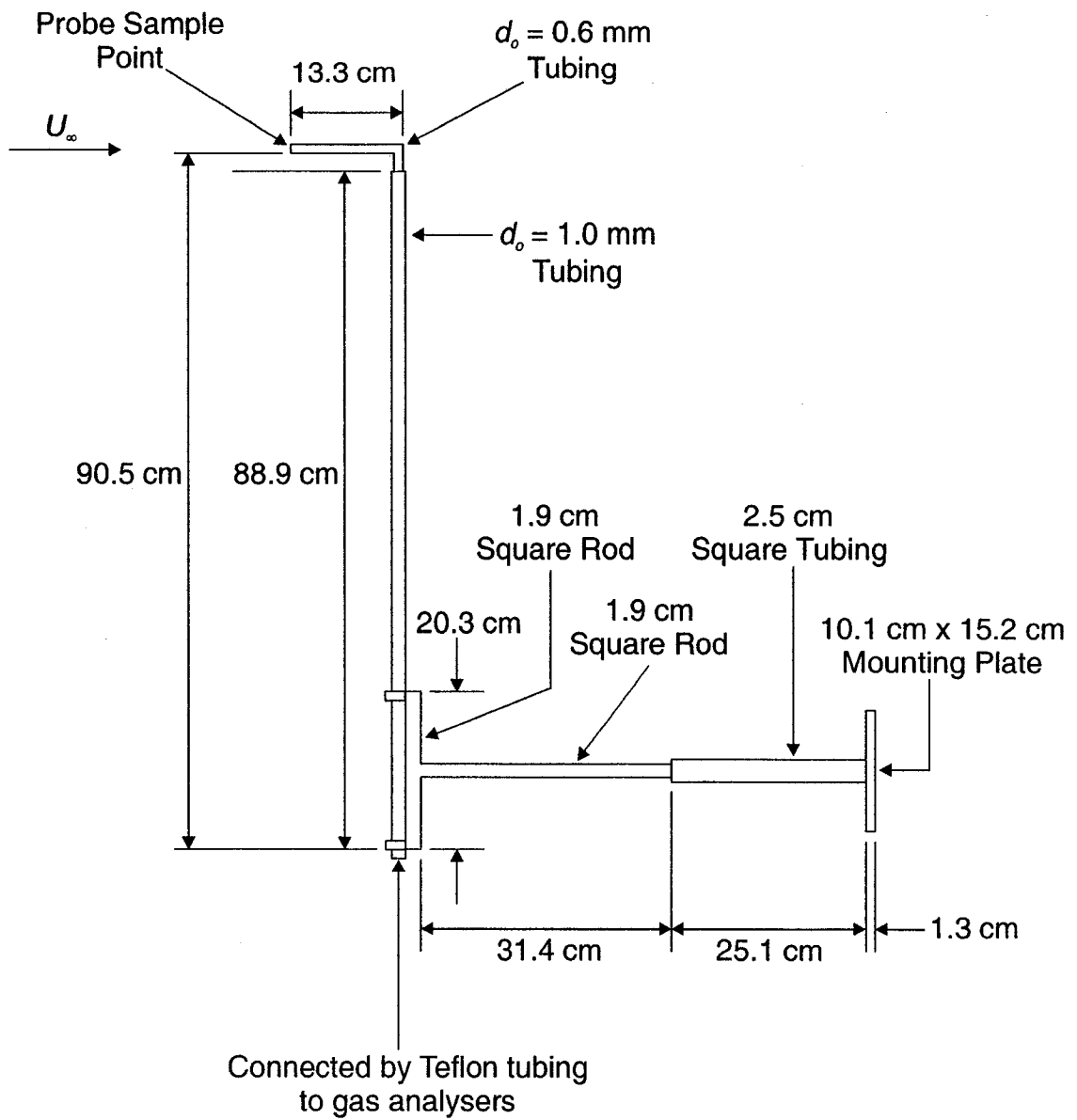


**Figure 4.9: Schematic of gas sampling probe**

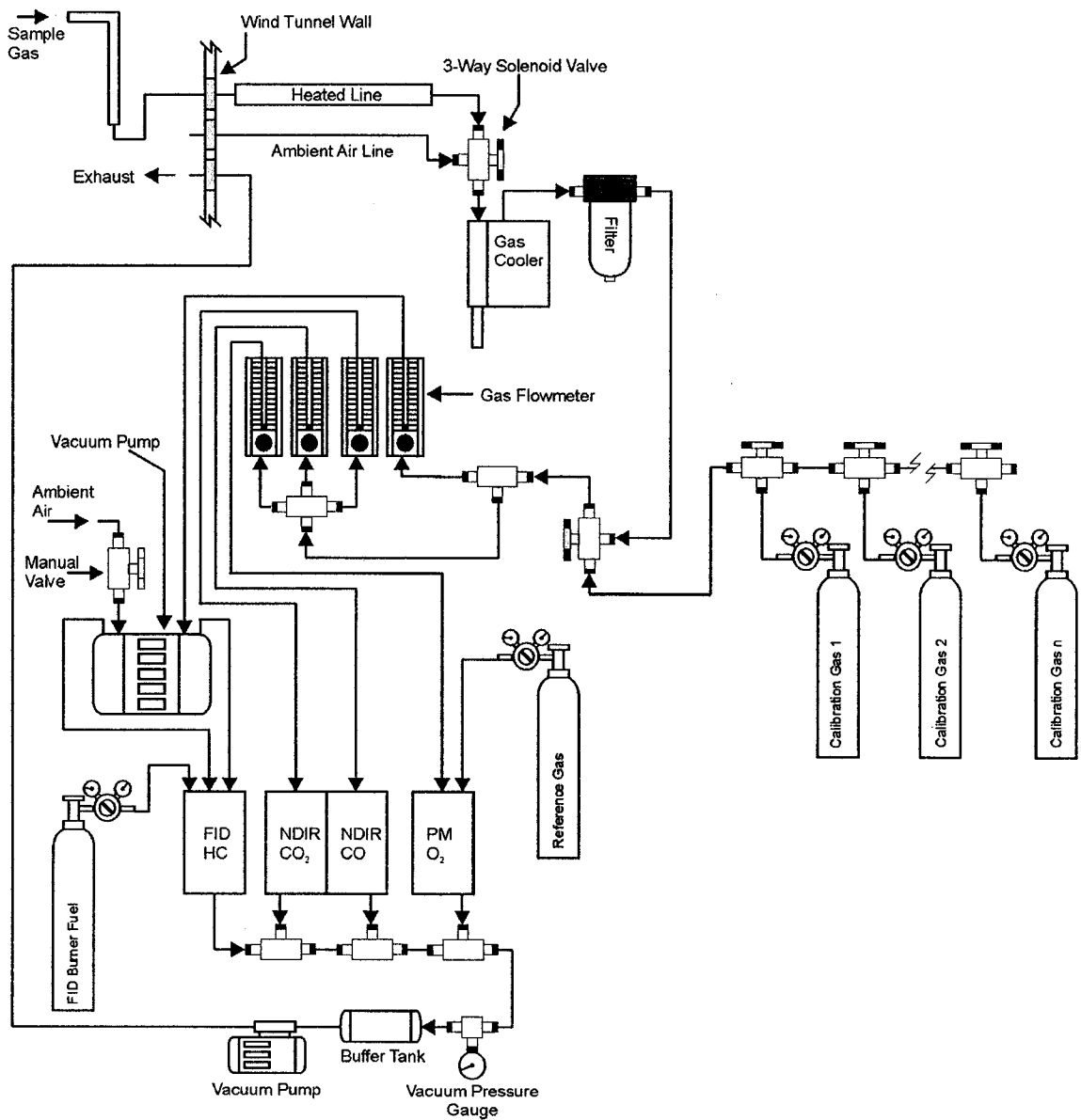


**Figure 4.10: Schematic of gas analysis system**

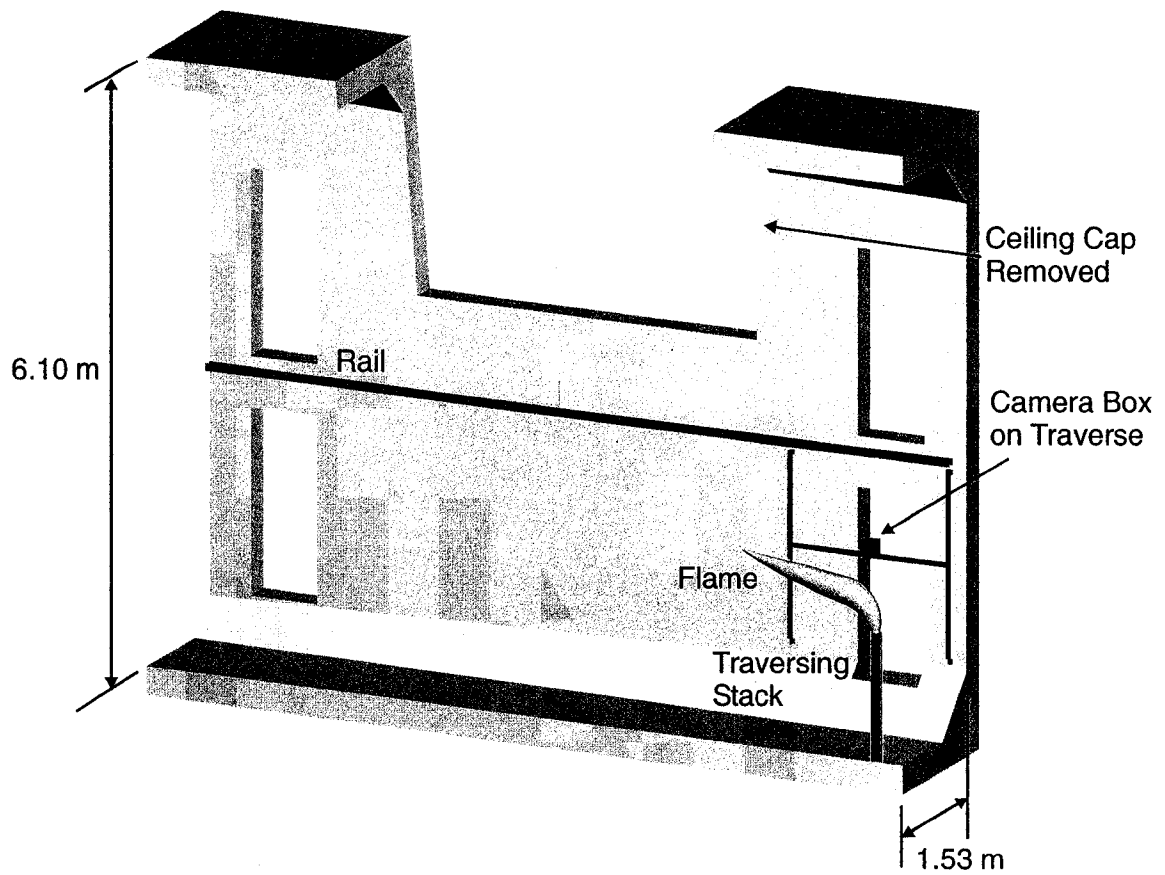


**Figure 4.11: Cross-sectional schematic of wind tunnel with digital camera traverse system installed. Note the ceiling cap is removed**

## Chapter 5

### THERMAL STRUCTURE AND TRAJECTORY OF FLARE PLUMES

The experimental research presented in this chapter focuses on the mean cross-sectional thermal structure of the plume. Two-dimensional thermal mappings of the flare stack plume were examined for scaled-down to full-scale flare stacks. These mappings were used to study the dispersion of the flare stack plume as it was advected downstream, and experimental results were compared against a plume dispersion model developed by Poudenx et al. (2004) for scaled-down flare stacks.

#### 5.1 Poudenx's Model of Plume Entrainment

Studies have been conducted in the past concerning the thermal structure of the flame and the plume behind the flare stack (i.e. Hewett et al., 1971, Toften et al., 1993). Experimental results were studied to observe the effects of crosswind speed and fuel jet speed on plume trajectory and dispersion, and to attempt to model the plume trajectory. The study by Poudenx et al. (2004) furthered this previous work by developing a correlation that could predict with reasonable accuracy how the mean cross-sectional area of a plume changes as a flare's plume of products is advected downstream.

A wide variety of plume rise predictions have been formulated over the past 50 years, some of the most prominent being developed by Briggs (1975) which were expanded on by Weil (1977). Physical parameters shown to be of importance are crosswind speed ( $U_{\infty}$ ), fuel jet speed ( $V_j$ ), distance downstream from the flare stack axis ( $X_o$ ), and the flare stack inner diameter ( $d_i$ ). Flare stack inner diameter rather than outer diameter is significant in predicting plume rise because it determines the jet velocity of a given fuel flow rate. The outer diameter determines the size of the wake recirculation region immediately downstream from the stack.

Poudenx's study developed a correlation to predict the dispersion of a plume as it was advected downstream which accounts for entrainment of ambient air. It is given by

$$d_p^* = Ag^{1/3} \frac{V_j^{1/3}}{U_\infty} X_o^{2/3} d_i^{2/3} - B \quad (5.1)$$

In this equation  $A$  and  $B$  are coefficients which depend on the fuel type, and  $g$  is the gravitational constant.  $d_p^*$  is the characteristic dimension of the plume, which has the dimension of metres (m). It is physically defined as the square root of the area contained within the 50 % temperature contour of a plume's mean cross-sectional structure.

However, the coefficient  $B$  in Eq. 5.1 was later deemed to not have any physical significance. The reasoning was that as  $X_o$  goes to zero, the diameter of a flare stack plume (and thus the characteristic dimension,  $d_p^*$ ) should ideally go to zero and not to some constant non-zero  $B$ . This concept was demonstrated in section 3.2.2 with an idealized point source of combustion products (with diameter equal to zero) above the flare stack tip (see Figure 3.3). Hence, a new correlation with  $B = 0$  was developed to reflect this reasoning.

$$d_p^* = Ag^{1/3} \frac{V_j^{1/3}}{U_\infty} X_o^{2/3} d_i^{2/3} \quad (5.2)$$

The model in Eq. 5.2 was confirmed by Poudenx's data, which consisted of 129 plume cross-sectional thermal maps generated under the following experimental conditions in a closed-loop wind tunnel.

- Fuel: sales grade natural gas (see Table 3.1)
- $1.5 \text{ m/s} \leq U_\infty \leq 8.0 \text{ m/s}$
- $0.5 \text{ m/s} \leq V_j \leq 2.0 \text{ m/s}$
- $16.7 \text{ mm} \leq d_i \leq 33.3 \text{ mm}$  (0.15- to 0.33-scale)

- $0.50 \text{ m} \leq X_o \leq 2.90 \text{ m}$

All physical quantities were measured and  $A$  was calculated from a least squares fit of these data, given by the following correlation.

$$d_p^* = 2.22 g^{1/3} \frac{V_j^{1/3}}{U_\infty} X_o^{2/3} d_i^{2/3} \quad (5.3)$$

Figure 5.1 displays a plot of Eq. 5.3 for the 129 thermal maps as studied by Poudenx et al. (2004). Eq. 5.2 applies to flare stacks of 0.15- to 0.33-scale, but in principle it may be extrapolated to predict plume dispersion for full-scale flares. However, no physical evidence existed at the time to support this extrapolation. However, strong evidence exists (Poudenx et al., 2004, Johnson and Kostiuk, 2000) that flare stacks of 0.15- to full-scale are all part of the same external cold flow regime and gives validity to performing scaled-down flare stack testing. One of the main goals of this research is to show that characteristics of the mean cross-sectional structure of the thermal plume can be scaled up to full-size flare stacks. That is, to show that the current data follow Poudenx's correlation for  $d_p^*$ , proving that Eq. 5.2 is applicable to flare stacks of 0.15- to full-scale for natural gas flares.

## 5.2 Comparison of Current Research with Poudenx's Model

The research presented in this dissertation concerns 93 plume cross-sectional thermal maps generated under the following experimental conditions in an open-loop wind tunnel. The multi-point thermocouple-based system described in section 4.2.3 was used to generate the mean cross-sectional thermal plume mappings. Maps were created immediately downstream of the flame tip and at two regular distance intervals downstream of each stack – 30 cm intervals for the 26.9 mm stack, and 60 cm intervals for the 52.6 mm and 102.3 mm stacks.

- Fuel: sales grade natural gas (see Table 3.1)
- $2.0 \text{ m/s} \leq U_\infty \leq 8.0 \text{ m/s}$

- $0.5 \text{ m/s} \leq V_j \leq 2.0 \text{ m/s}$
- $26.9 \text{ mm} \leq d_i \leq 102.3 \text{ mm}$  (0.25- to full-scale)
- $0.50 \text{ m} \leq X_o \leq 8.30 \text{ m}$

Figure 5.2 shows thermal maps of a plume's cross-sectional structure for  $d_i = 52.6 \text{ mm}$  and  $X_o = 2.3 \text{ m}$ , while  $V_j$  and  $U_\infty$  are varied to provide a variety of plume shapes. Dimensions are indicated in millimetres relative to the flare stack tip. In this figure, the plume's shape gradually evolves through 3 distinct modes: kidney shape (a) and (b), circular shape (c), and downwashed shape (d) and (e).

At low crosswind speeds, the dominant flow structure in a kidney shaped plume is a pair of counter-rotating vortices that are associated with bending over the jet in the direction of the crosswind (Smith and Mungal, 1998). A maximum temperature peak exists at each vortex core, and since the flame is located above the flare stack, it is not significantly affected by any wake flow structures that exist downstream of the flare stack.

The circular shaped plume arises at higher crosswind speeds, when the flame trajectory becomes more horizontal and the kidney shape shrinks and transitions into a more circular shape. The plume of combustion products are found closer to the region of wake flow structures created by the stack, which traps a portion of the products and results in a slightly downwashed portion below the circular plume shape.

At even higher values of crosswind speed, a second temperature peak manifests itself below the flare stack tip height. More of the flame and its associated combustion products become trapped in the flare stack's wake, resulting in a downwashed profile. In Figure 5.2 (e), the majority of the flame is caught in the flare stack's recirculation zone and the upper temperature peak has almost completely disappeared.



This evolution of plume shapes has been well documented by Poudenx et al. (2004), who showed that plumes downstream of flare stacks  $16.7 \text{ mm} \leq d_i \leq 33.3 \text{ mm}$  (0.15- to 0.33-scale) evolve in a manner proper for scaling.

The use of isotherms is central to the calculation of the characteristic plume dimension. Isotherms are drawn on thermal maps to indicate contours of constant temperature. The 50 % temperature contour (drawn as a heavy line in the thermal maps) is defined as the mean temperature between the lowest and highest temperatures recorded. The lowest recorded temperature is that of the ambient air. The 50% temperature contour is used to define the limit of the hot plume's "core."

Using the same analytical approach of Poudenx, 50 % temperature contours were calculated for each of the 93 plumes collected. The computer program Surfer (Golden Software, Inc.) was used to calculate the area captured within the 50 % temperature contour for each plume. The vertical and horizontal dimensions of each plume cross-section were calculated based on the known spacing between the thermocouples mounted on the temperature measurement apparatus (described in section 4.2.3). Figure 5.3 displays a plot of the characteristic dimension for the plumes collected in this study with respect to the experimental conditions. A curve fit to the data in the present study gives the following correlation.

$$d_p^* = 2.34 g^{1/3} \frac{V_j^{1/3}}{U_\infty} X_o^{2/3} d_i^{2/3} \quad (5.4)$$

This linear trendline fits the data well, indicating that the plume characteristic dimension,  $d_p^*$ , is scalable with the experimental variables  $U_\infty$ ,  $V_j$ ,  $X_o$ , and  $d_i$  for flare stacks of 0.25- to full-scale. The previous curve fit to Poudenx's data defined by Eq. 5.3, which was confirmed for  $g^{1/3} V_j^{1/3} X_o^{2/3} d_i^{2/3} / U_\infty \leq 0.17 \text{ m}$  (limit is shown on Figure 5.3), is included for comparison. Figure 5.4 is an exploded view of Figure 5.3 for  $g^{1/3} V_j^{1/3} X_o^{2/3} d_i^{2/3} / U_\infty \leq 0.24 \text{ m}$  with Poudenx et al. (2004) data points included. The present study's data overlap well with the past study's data. It is also observed that the

curve fit to the current research compares well with the past curve fit. This demonstrates that the characteristics of the mean cross-sectional structure of the thermal plume are scalable over the full range of flare stack scales investigated,  $16.7 \text{ mm} \leq d_i \leq 102.3 \text{ mm}$  (0.15- to full-scale). Note that the origin for the variable  $X_o$  is at the flare stack exit, aligned with the axis of the flare stack.

Regardless of the shape of the plume,  $d_p^*$ , defined by the area contained with a plume's hot core, remains the correct choice for characterizing downstream dispersion of the flare stack plume.

The self-similar shape of a plume produced by a non-reacting buoyant jet as it is advected downstream has been well studied by past researchers such as Smith and Mungal (1998). However, the current research concerns a reacting plume. The plume entrainment model represented by Eq. 5.2 was derived based on the Richardson Number (Eq. 3.2), which assumes that the buoyancy of the fuel jet and the momentum of the crosswind are the dominant forces in the flow. Richardson Numbers are well defined for non-reacting flows, and the results presented here indicate that a flare stack's reacting plume behaves similarly to a non-reacting buoyant jet over the full range of scales investigated.

### 5.2.1 Range of Validity of the Plume Entrainment Model

A total of 108 mean cross-sectional thermal maps were collected during experimentation, but only 93 were used to generate the model shown by Eq 5.4. There are two reasons for this. Firstly, it was observed that some plume mappings had very low maximum temperatures (below 70 °C), resulting in high uncertainty when determining the characteristic plume dimension. This is attributed to the small difference in temperature between the plume's hottest point and the ambient air temperature. High uncertainty in calculating  $d_p^*$  was encountered for  $V_j/U_\infty \leq 0.125$  on the  $d_i = 26.9 \text{ mm}$  stack and for  $V_j/U_\infty \leq 0.0625$  on the  $d_i = 52.6 \text{ mm}$  stack. For this reason these plumes were not included in the plume entrainment model.

Secondly, some plumes were so large that the walls of the wind tunnel restricted their growth. These plumes were prevented from dispersing naturally, and portions of them became trapped in the wind tunnel walls' and ceiling's boundary layers. Hence, these plumes were not included in the plume entrainment model. This occurred for  $V_j/U_\infty \geq 1.0$  on the  $d_i = 102.3$  mm stack

Note that the purpose of Eq. 5.2 is to provide a characteristic length, not an actual physical dimension, for a flare stack plume with the following operating conditions:

- Fuel: sales grade natural gas (see Table 3.1)
- $1.5 \text{ m/s} \leq U_\infty \leq 8.0 \text{ m/s}$
- $0.5 \text{ m/s} \leq V_j \leq 2.0 \text{ m/s}$
- $16.7 \text{ mm} \leq d_i \leq 102.3 \text{ mm}$  (0.15- to full-scale)
- $0.50 \text{ m} \leq X_o \leq 8.30 \text{ m}$

Nevertheless, this model shows remarkable self-consistency over the wide range of plume sizes studied.

### 5.3 Summary and Conclusions

Using a multi-point thermocouple-based system, the mean cross-sectional thermal structure of a natural gas flare plume was mapped as it dispersed downstream of a flare stack. The present study was conducted under the following experimental conditions:  $2.0 \text{ m/s} \leq U_\infty \leq 8.0 \text{ m/s}$ ,  $0.5 \text{ m/s} \leq V_j \leq 2.0 \text{ m/s}$ ,  $26.9 \text{ mm} \leq d_i \leq 102.3 \text{ mm}$  (0.25- to full-scale),  $0.50 \text{ m} \leq X_o \leq 8.30 \text{ m}$ .

A buoyant plume rise model (derived in Appendix A) was used to scale the characteristic dimension of the flare plume,  $d_p^*$ , against the physical parameters crosswind speed ( $U_\infty$ ), fuel jet speed ( $V_j$ ), distance downstream from the flare stack axis

( $X_o$ ), and the flare stack inner diameter ( $d_i$ ).  $d_p^*$  was physically defined as the diameter of an ideal circular plume cross-section whose area is equal to the area contained within the 50 % temperature contour of a plume's mean cross-sectional structure.

The correlation was defined as

$$d_p^* = Ag^{1/3} \frac{V_j^{1/3}}{U_\infty} X_o^{2/3} d_i^{2/3} \quad (5.5)$$

For the present study, it was found that  $A = 2.34$ . This result was compared with past research conducted by Poudenx et al. (2004). A curve fit to Poudenx's data resulted in  $A = 2.22$ . The coefficient  $A$  in the present study varied by 0.12 (5 %) with the past study by Poudenx.

The curve fits applied to both sets of data compare well with each other, showing that the characteristic dimension ( $d_p^*$ ) of the mean cross-sectional thermal structure of the plume is scalable over the full range of flare stack scales investigated,  $16.7 \text{ mm} \leq d_i \leq 102.3 \text{ mm}$  (0.15- to full-scale).

The equation describing the characteristic dimension of the plume was derived based on the Richardson Number, which assumes that the buoyancy of the combustion products and the momentum of the crosswind are the dominant forces in the flow. Richardson Numbers are well-defined for non-reacting flows, and the results presented here indicate that a flare stack plume behaves similarly to a non-reacting buoyant jet over the wide range of flare stack scales investigated in the present study.

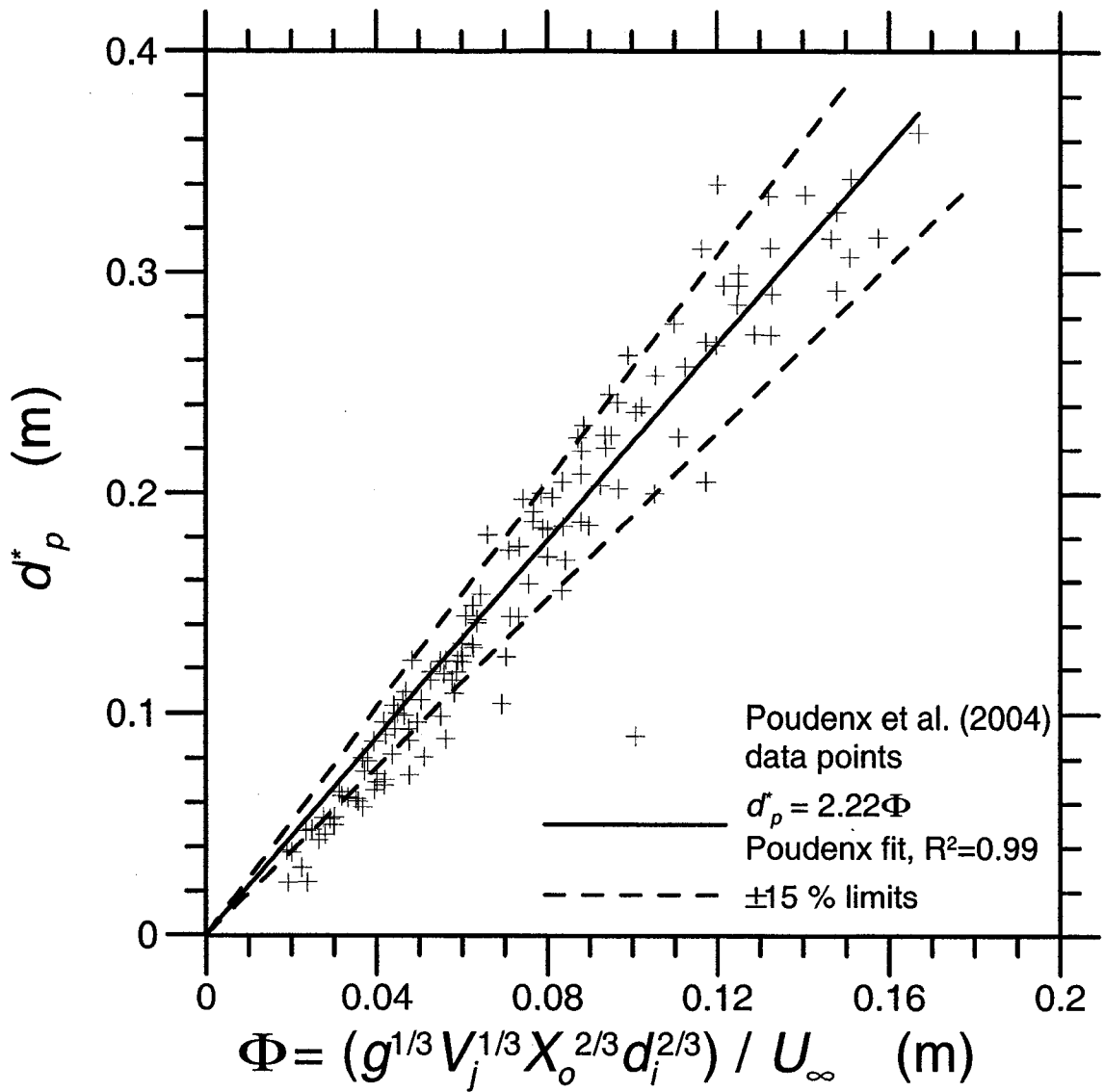
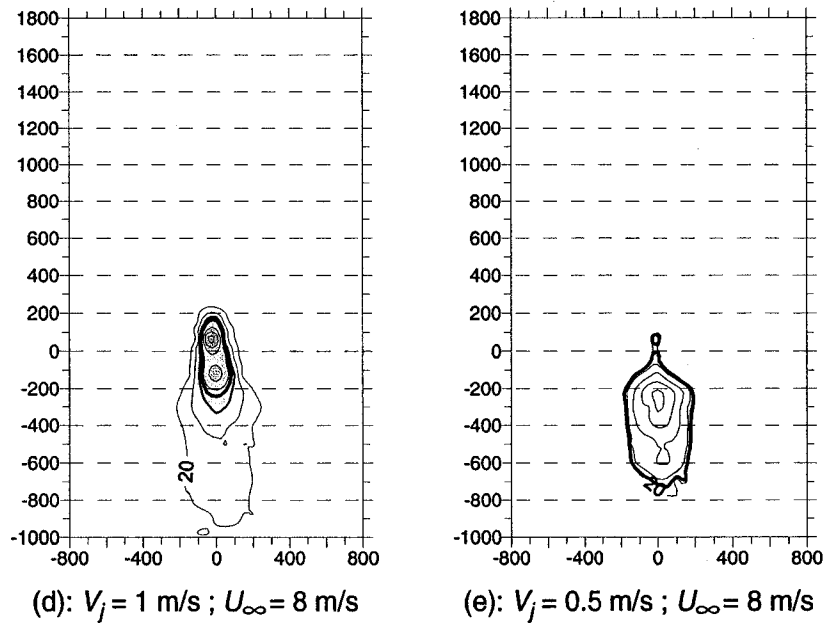
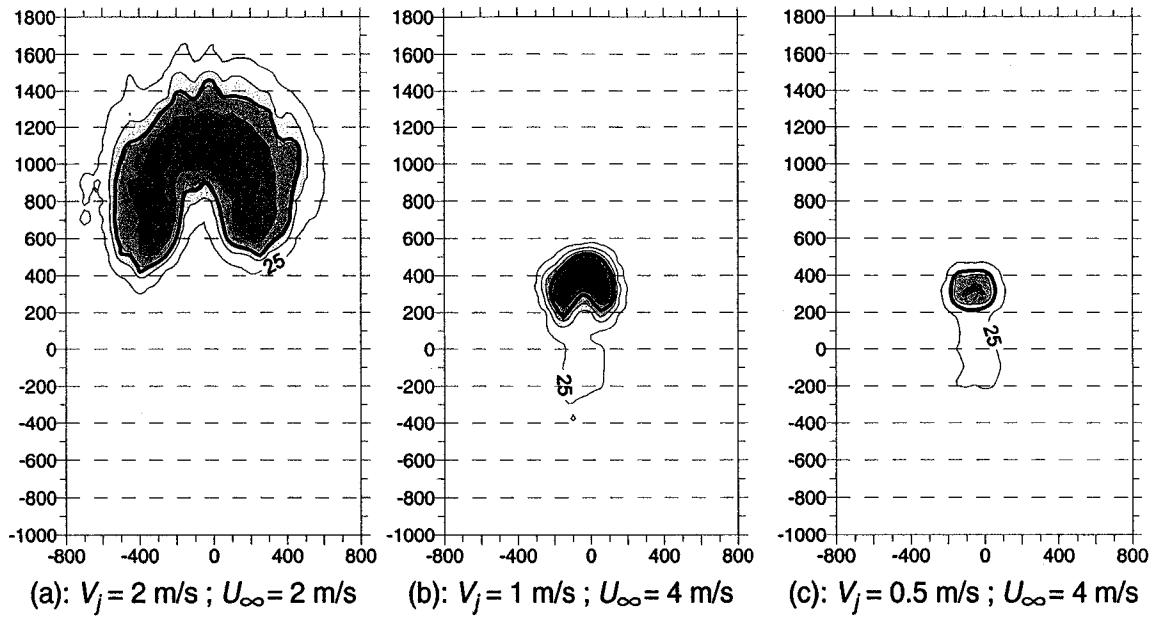


**Figure 5.1: Characteristic dimension of the plume using Poudenx et al. (2004) data.**

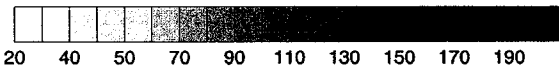
**Conditions:**

$$1.5 \text{ m/s} \leq U_\infty \leq 8.0 \text{ m/s}, 0.5 \text{ m/s} \leq V_j \leq 2.0 \text{ m/s}$$

$$16.7 \text{ mm} \leq d_i \leq 33.3 \text{ mm}, 0.5 \text{ m} \leq X_o \leq 2.9 \text{ m}$$



Temperature Scale (deg. C)



— : 50% Temperature contour

NOTE: X and Y axis in mm relative to flare stack tip

**Figure 5.2: Varying modes of temperature profiles for a plume cross-section behind a natural gas flare for constant stack diameter.**

**Conditions:**

$$d_i = 52.6 \text{ mm}, X_o = 2.3 \text{ m}$$

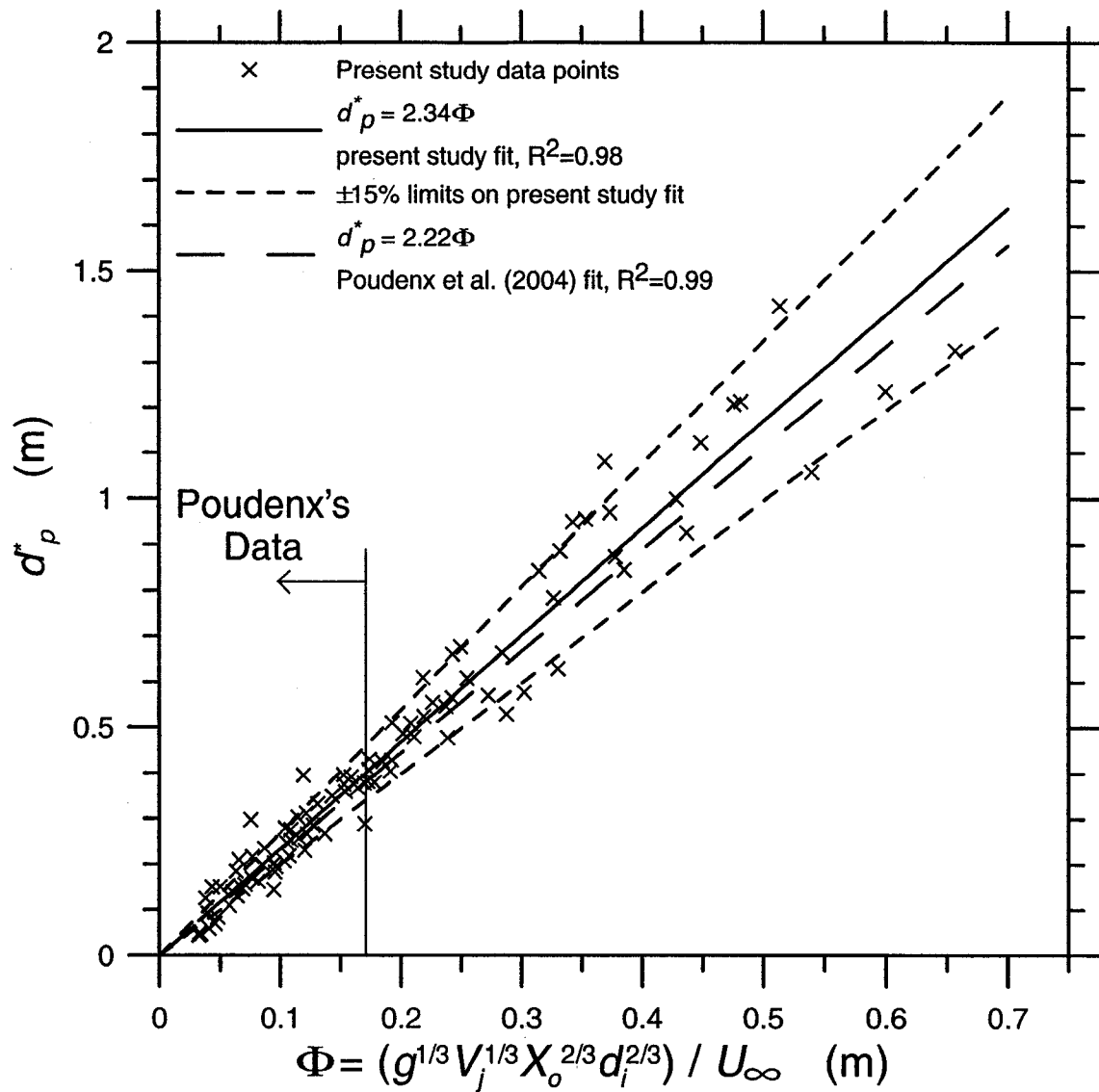


**Figure 5.3: Characteristic dimension of the plume for Poudenx et al. (2004) study and present study.**

**Conditions:**

$$2.0 \text{ m/s} \leq U_\infty \leq 8.0 \text{ m/s}, 0.5 \text{ m/s} \leq V_j \leq 2.0 \text{ m/s}$$

$$26.9 \text{ mm} \leq d_i \leq 102.3 \text{ mm}, 0.5 \text{ m} \leq X_o \leq 8.3 \text{ m}$$

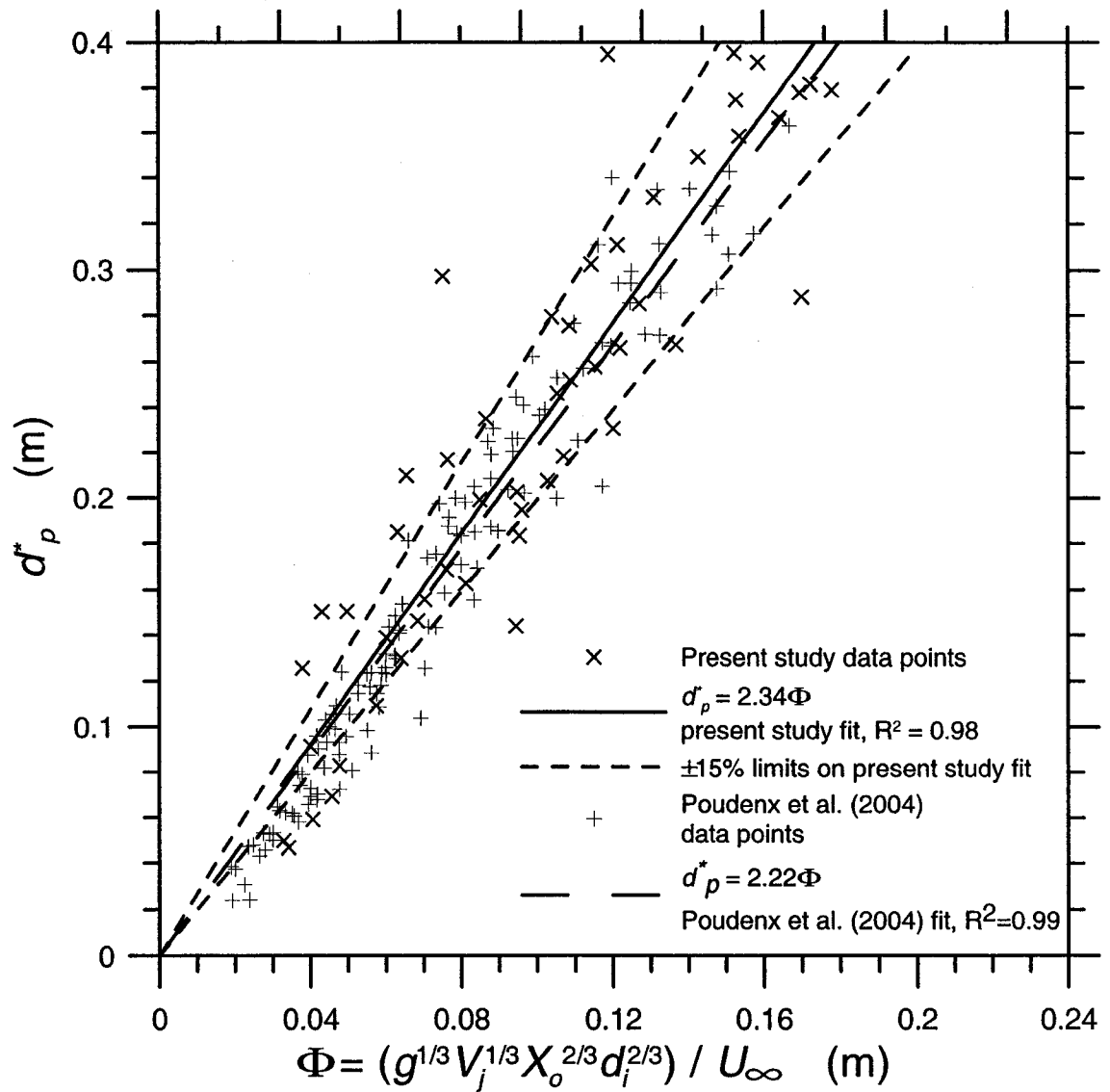


**Figure 5.4: Exploded view of Figure 5.3 with Poudenx et al. (2004) data points included.**

**Conditions:**

**Present study's data:  $2.0 \text{ m/s} \leq U_\infty \leq 8.0 \text{ m/s}$ ,  $0.5 \text{ m/s} \leq V_j \leq 2.0 \text{ m/s}$**

**$26.9 \text{ mm} \leq d_i \leq 102.3 \text{ mm}$ ,  $0.5 \text{ m} \leq X_o \leq 8.3 \text{ m}$**

**Poudenx et al. (2004) data:  $1.5 \text{ m/s} \leq U_\infty \leq 8.0 \text{ m/s}$ ,  $0.5 \text{ m/s} \leq V_j \leq 2.0 \text{ m/s}$**

**$16.7 \text{ mm} \leq d_i \leq 33.3 \text{ mm}$ ,  $0.5 \text{ m} \leq X_o \leq 2.9 \text{ m}$**



## Chapter 6

### COMPOSITIONAL STRUCTURE OF FLARE PLUMES

This chapter investigates the mean cross-sectional compositional structure of the plume. Local and overall combustion efficiencies are calculated based on compositional measurements, and the experimental results are compared against combustion efficiency correlations established by Johnson and Kostiuk (2002) for scaled-down flares in crosswind.

#### 6.1 Johnson's Combustion Efficiency Correlation

The combustion efficiency of a flare stack has been a topic of increasing interest for the past 25 years. Data collected during field researches by Leahey et al. (1984), Romano (1983), and Strosher (1996) have indicated that flare combustion efficiency can vary from as low as 22 % to 98 % and higher. Unfortunately, trends within these data are difficult to interpret and there is a lack of description of the measurement and analysis techniques used.

Studies conducted by Poudenx et al. (2004) and Johnson and Kostiuk (2002) attempted to address these problems by studying the combustion efficiency of scaled-down flares in a closed-loop wind tunnel environment. Physical parameters shown to be of importance are crosswind speed ( $U_{\infty}$ ), fuel jet speed ( $V_j$ ), flare stack outer diameter ( $d_o$ ), and lower heating value of the fuel by mass ( $LHV_{mass}$ ). In Johnson's study, a combustion efficiency correlation was developed using the Richardson Number (Eq. 3.2), which is based on the ratio of fuel jet buoyancy to crosswind momentum. The correlation was of the form

$$(1 - \eta)(LHV_{mass})^3 = D \exp \left( E \frac{U_{\infty}}{(gV_j)^{1/3} d_o^n} \right) \quad (6.1)$$

In this equation  $D$ ,  $E$ , and  $n$  are coefficients,  $g$  is the gravitational constant, and  $\eta$  is the overall combustion efficiency.  $E$  is dimensionless, whereas  $D$  and  $(LHV_{mass})^3$  have the units of  $(\text{MJ/kg})^3$ . This correlation can be made dimensionless by dividing both sides by  $(LHV_{mass,CH_4})^3$ , where  $LHV_{mass,CH_4}$  is the lower heating value by mass of pure methane, 50 MJ/kg. The dimensionless correlation is then

$$(1 - \eta) \left( \frac{LHV_{mass}}{LHV_{mass,CH_4}} \right)^3 = F \exp \left( E \frac{U_\infty}{(gV_j)^{1/3} d_o^n} \right) \quad (6.2)$$

where

$$F = \frac{D}{(LHV_{mass,CH_4})^3}$$

Johnson's model was developed from data collected under the following experimental conditions in a closed-loop tunnel:

- Fuel: sales grade natural gas (see Table 3.1) diluted with
  - 0% – 60% CO<sub>2</sub> or
  - 0% – 80% N<sub>2</sub>
- $7.0 \text{ MJ/kg} \leq LHV_{mass} \leq 43.5 \text{ MJ/kg}$
- $2.0 \text{ m/s} \leq U_\infty \leq 16.0 \text{ m/s}$
- $0.5 \text{ m/s} \leq V_j \leq 2.0 \text{ m/s}$
- $12.1 \text{ mm} \leq d_o \leq 49.8 \text{ mm}$  (0.11- to 0.44-scale)

All physical parameters in Eq. 6.2 were measured and  $E$  and  $F$  were calculated based on a least squares fit of these data. The portion of Johnson's work that is of interest in this study concerned burning natural gas fuel diluted with varying percentages of inert

gases (nitrogen and carbon dioxide).  $LHV_{mass}$  was incorporated into his correlation to reflect the variations in fuel heating values due to mixing of the fuel stream with  $CO_2$  or  $N_2$ .

A curve fit to these data with  $n = 1/3$  yielded the following correlation.

$$(1 - \eta) \left( \frac{LHV_{mass}}{LHV_{mass, CH_4}} \right)^3 = 1.25 \times 10^{-3} \exp \left( 0.317 \frac{U_\infty}{(gV_j)^{1/3} d^{1/3}} \right) \quad (6.3)$$

Johnson realized that combustion efficiency results from a natural gas based flare stack could collapsed better with  $n = 1/2$ . This yielded the following empirical curve fit.

$$(1 - \eta) \left( \frac{LHV_{mass}}{LHV_{mass, CH_4}} \right)^3 = 1.17 \times 10^{-3} \exp \left( 0.175 \frac{U_\infty}{(gV_j)^{1/3} d_o^{1/2}} \right) \quad (6.4)$$

Eq. 6.3 uses the correct value of  $n = 1/3$  to provide a dimensionless correlation, whereas Eq. 6.4 is an empirical curve fit that uses  $n = 1/2$  and has the units of  $m^{-1/6}$ . Eq. 6.3 and 6.4 apply to flare stacks of 0.11- to 0.44-scale, but in principle they may be extrapolated to predict combustion efficiency for full-scale flares. One of the main goals of this research is to show that the characteristics of the mean cross-sectional compositional structure of the flare plume are scalable for all flare stack diameters tested. Specifically, that the data collected in this study follow Johnson's correlations combustion efficiency, proving that Eq. 6.2 is applicable to flare stacks of 0.11- to full-scale.

## 6.2 Comparison of Current Research with Johnson's Model

This section will compare curve fits of the form Eq. 6.2 made on past and present combustion efficiency data using  $n = 1/3$  and  $n = 1/2$ . It will be shown that present curve fits match well with past curve fits. Most importantly, it will be demonstrated that the data collected in the present study provide the first known scientific confirmation that the overall combustion inefficiency of a flare stack is scalable over the wide range of flare stack sizes studied for  $n = 1/3$ .

### 6.2.1 Correlations for Combustion Efficiency with $n = 1/3$

The research presented in this dissertation concerns 62 plume cross-sectional compositional maps generated in an open-loop wind tunnel under the following experimental conditions. Maps were created immediately downstream of the flame tip.

- Fuel: sales grade natural gas (see Table 3.1)
- $LHV_{mass} = 47.5 \text{ MJ/kg}$
- $4.0 \text{ m/s} \leq U_{\infty} \leq 14.0 \text{ m/s}$
- $0.5 \text{ m/s} \leq V_j \leq 2.0 \text{ m/s}$
- $30.0 \text{ mm} \leq d_o \leq 114.3 \text{ mm}$  (0.25- to full-scale)

Concentrations of  $\text{CO}_2$ ,  $\text{CO}$ ,  $\text{CH}_4$  and  $\text{O}_2$  were measured for each of the 62 plume cross-sections, and from these concentrations local and overall combustion efficiencies ( $\eta$  and  $\eta_{ave}$ , respectively) of the flare were calculated using the equations derived in section 3.3.

Figure 6.1 shows normalized concentrations of  $\text{CO}_2$ ,  $\text{CO}$ ,  $\text{CH}_4$  and  $\text{O}_2$  for the case  $U_{\infty} = 4.0 \text{ m/s}$ ,  $V_j = 0.5 \text{ m/s}$ ,  $d_o = 114.3 \text{ mm}$ ,  $X_o = 2.30 \text{ m}$ , which produces a kidney shaped plume. For these normalizations the background species concentration is set to zero and the maximum species concentration is set to 1. Dimensions are in millimetres relative to the flare stack tip. Figure 6.2 shows the local combustion efficiency profile for this case, where  $\eta_{ave} = 99.8 \%$ . Recall that the overall combustion efficiency of the flare is determined by integrating all calculated local efficiencies within a prescribed plume boundary. The plume boundary of integration is defined by a contour encompassing  $\text{O}_2$  concentrations which are above 10 % of the difference between the background and maximum  $[\text{O}_2]$ .

Figure 6.3 shows normalized concentrations of CO<sub>2</sub>, CO, CH<sub>4</sub> and O<sub>2</sub> for the case  $U_{\infty} = 6.0$  m/s,  $V_j = 1.0$  m/s,  $d_o = 58.8$  mm,  $X_o = 2.60$  m, which produces a circular shaped plume. Figure 6.4 shows the local combustion efficiency profile for this case, where  $\eta_{ave} = 99.5$  %. Two separate regions of higher combustion efficiency are present. This can be attributed to the wake flow structures downstream of the flare stack, which are trapping a portion of the combustion products in the hot core of the plume and downwashing them.

Figure 6.5 shows normalized concentrations of CO<sub>2</sub>, CO, CH<sub>4</sub> and O<sub>2</sub> for the case  $U_{\infty} = 8.0$  m/s,  $V_j = 1.0$  m/s,  $d_o = 30.0$  mm,  $X_o = 0.80$  m, which produces a downwashed plume. Note that the majority of the combustion products are concentrated below the flare stack tip, indicating they are trapped within the flare stack wake flow structures. Figure 6.6 shows the local combustion efficiency profile for this case, where  $\eta_{ave} = 88.5$  %. The majority of the flare stack flame and plume are now trapped in the flare stack's recirculation zone, downwashing the region of highest combustion efficiency.

Figure 6.7 shows a plot of the overall combustion efficiency correlation for all plumes sampled in this study. A curve fit to these data using  $n = 1/3$  gives the following dimensionless equation.

$$(1 - \eta) \left( \frac{LHV_{mass}}{LHV_{mass, CH_4}} \right)^3 = 5.73 \times 10^{-4} \exp \left( 0.330 \frac{U_{\infty}}{(gV_j)^{1/3} d_o^{1/3}} \right) \quad (6.5)$$

Figure 6.8 is an exploded view of Figure 6.7 for

$0 \leq (1 - \eta) \left( LHV_{mass} / LHV_{mass, CH_4} \right)^3 \leq 0.06$ . Johnson's curve fit to the data he collected in his study is included in both figures for comparison.

It is observed that the present curve fit compares reasonably well with Johnson's fit. Figure 6.9 provides a comparison of the data scatter found in Johnson's study and in the present study. Figure 6.10 shows the same data as in Figure 6.9 but plotted on a semi-

logarithmic scale. This figure is useful in determining the accuracy of the correlation at differing values of  $U_\infty / (gV_j d_o)^{1/3}$ . The data show that the uncertainty of the correlation is greater at lower values of  $U_\infty / (gV_j d_o)^{1/3}$  or alternatively at lower values of  $(1 - \eta) \left( LHV_{mass} / LHV_{mass, CH_4} \right)^3$ . It is also observed that the scatter in the data collected for this study overlaps reasonably well with the data collected by Johnson, yielding parallel curve fits.

The correlation in Eq. 6.5 provides a reasonable fit to the data collected in this study, and comparison with Johnson's fit to his data indicates that the correlation applies to the full range of flare stacks tested (0.11- to full-scale). Most importantly, the data collected in this study provide the first known scientific confirmation that the overall combustion inefficiency of a flare stack is scalable over the wide range of flare stack sizes studied for  $n = 1/3$ .

However, considerable scatter exists in the data, suggesting that there may be other mechanisms at work besides the crosswind momentum and fuel jet buoyancy that are causing combustion inefficiency.

### 6.2.2 Correlations for Combustion Efficiency with $n = 1/2$

Figure 6.11 displays a plot of the combustion efficiency correlation for all plumes sampled in this study, with an empirical curve fit using  $n = 1/2$ . The empirical fit is as follows.

$$(1 - \eta) \left( \frac{LHV_{mass}}{LHV_{mass, CH_4}} \right)^3 = 5.38 \times 10^{-4} \exp \left( 0.210 \frac{U_\infty}{(gV_j)^{1/3} d_o^{1/2}} \right) \quad (6.6)$$

The right side of Eq. 6.6 has the units  $m^{-1/6}$ . Figure 6.12 is an exploded view of Figure 6.11 for  $0 \leq (1 - \eta) \left( LHV_{mass} / LHV_{mass, CH_4} \right)^3 \leq 0.06$ . Johnson's empirical curve fit to the data he collected in his study is included in both figures for comparison.

In this case the new empirical curve fit compares even better with Johnson's empirical fit. The data collapse better with  $n = 1/2$ , an observation that Johnson also made in his study. This result shows that one is partly successful in accounting for any unconsidered (and unknown) mechanisms causing combustion inefficiency by adjusting the exponent  $n$ . However, adjusting  $n$  results in an empirical correlation that does not have physical meaning or practical application, as the dimension  $m^{-1/6}$  now appears on the x-axis.

Figure 6.13 provides a comparison of the data scatter found in Johnson's research and in this research. Figure 6.14 shows the same data as in Figure 6.13 but plotted on a semi-logarithmic scale. Data scatter for this study and Johnson's study is reduced noticeably upon comparison with Figures 6.9 and 9.10. Again, the data show that the uncertainty of the empirical curve fit is greater at lower values of  $U_\infty / ((gV_j)^{1/3} d_o^{1/2})$  or alternatively at lower values of  $(1 - \eta) (LHV_{mass} / LHV_{mass, CH_4})^3$ . However, in this case both sets of data collapse and overlap even better than for the  $n = 1/2$  case, yielding intersecting empirical curve fits.

### 6.3 Summary and Conclusions

Using a single-point gas sampling system, 62 plume mean cross-sectional compositional maps were generated downstream of model flare stacks burning natural gas. The study was conducted under the following experimental conditions:

$$LHV_{mass} = 47.5 \text{ MJ/kg}, 4.0 \text{ m/s} \leq U_\infty \leq 14.0 \text{ m/s}, 0.5 \text{ m/s} \leq V_j \leq 2.0 \text{ m/s}, \\ 30.0 \text{ mm} \leq d_o \leq 114.3 \text{ mm} \text{ (0.25- to full-scale).}$$

A correlation was developed that scaled combustion inefficiency  $(1 - \eta)$  against the physical parameters crosswind speed ( $U_\infty$ ), fuel jet speed ( $V_j$ ), flare stack outer diameter ( $d_o$ ), and lower heating value of the fuel by mass ( $LHV_{mass}$ ). The correlation was made dimensionless using the lower heating value by mass of pure methane ( $LHV_{mass, CH_4}$ ).

The dimensionless correlation was defined as

$$(1 - \eta) \left( \frac{LHV_{mass}}{LHV_{mass, CH_4}} \right)^3 = 5.73 \times 10^{-4} \exp \left( 0.330 \frac{U_\infty}{(gV_j)^{1/3} d_o^{1/3}} \right) \quad (6.7)$$

This curve fit was compared with research conducted by Johnson and Kostiuk (2002). Johnson's dimensionless curve fit was defined as

$$(1 - \eta) \left( \frac{LHV_{mass}}{LHV_{mass, CH_4}} \right)^3 = 1.25 \times 10^{-3} \exp \left( 0.317 \frac{U_\infty}{(gV_j)^{1/3} d_o^{1/3}} \right) \quad (6.8)$$

The correlation in Eq. 6.7 provides a reasonable fit to the data collected in this study, and comparison with Johnson's fit to his data indicates that the correlation applies to the full range of flare stacks tested in both studies (0.11- to full-scale).

The exponent 1/3 on the parameter  $d_o$  is the correct value to make Eq. 6.7 dimensionless. However, Johnson observed that if the exponent was adjusted to 1/2 the natural gas based data collapsed slightly better. His empirical curve fit with  $d_o^{1/2}$  dependence was defined as

$$(1 - \eta) \left( \frac{LHV_{mass}}{LHV_{mass, CH_4}} \right)^3 = 1.17 \times 10^{-3} \exp \left( 0.175 \frac{U_\infty}{(gV_j)^{1/3} d_o^{1/2}} \right) \quad (6.9)$$

The right side of Eq. 6.9 has the units  $m^{-1/6}$ . An empirical curve fit was made to the present data with  $d_o^{1/2}$  dependence to facilitate direct comparison to Johnson's work. It was defined as

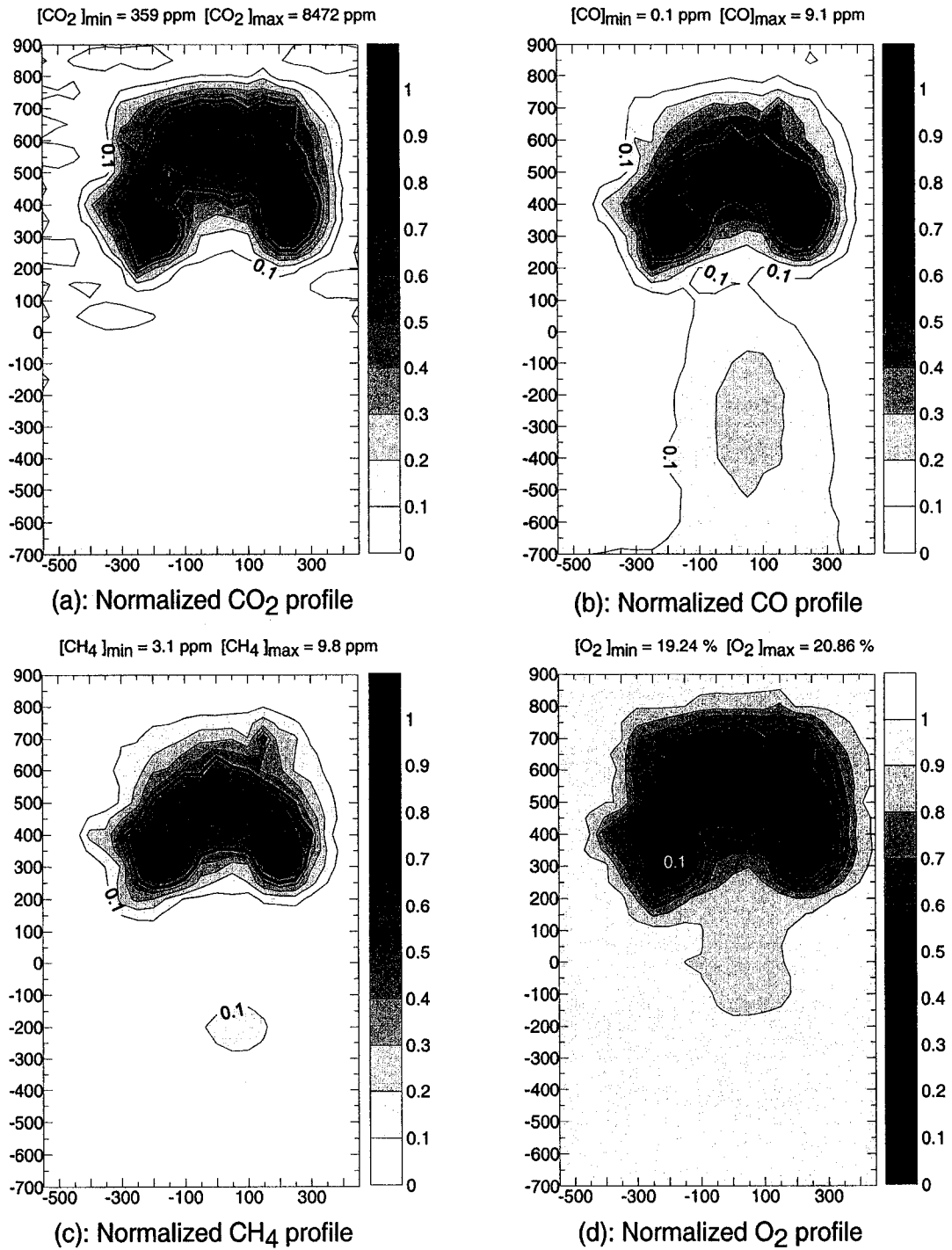
$$(1 - \eta) \left( \frac{LHV_{mass}}{LHV_{mass, CH_4}} \right)^3 = 5.38 \times 10^{-4} \exp \left( 0.210 \frac{U_\infty}{(gV_j)^{1/3} d_o^{1/2}} \right) \quad (6.10)$$

Curve fits made on Johnson's data and the present data for  $d_o^n$  with  $n = 1/3$  and  $n = 1/2$  dependence indicate that the overall combustion inefficiency of a flare plume is



scalable over the full range of flare stack scales investigated,  $12.1 \text{ mm} \leq d_o \leq 114.3 \text{ mm}$  (0.11- to full-scale). The coefficient  $n = 1/3$  is the correct value to be used, as this results in a dimensionless correlation. The present study is significant in that it provides the first known scientific confirmation that the overall combustion inefficiency of a flare stack is scalable over the wide stack sizes studied for  $n = 1/3$ .

It was observed that current and past data collapsed slightly better for  $n = 1/2$ , resulting in the dimension  $\text{m}^{-1/6}$  on the right hand side of the empirical curve fit. This suggests that there may be underlying mechanisms influencing inefficiencies in combustion other than the crosswind momentum flux and jet buoyancy that require further study. One proposed method, a fuel stripping mechanism for wake-stabilized jet diffusion flames in crosswind, has been discussed and studied by Johnson et al. (2001b).

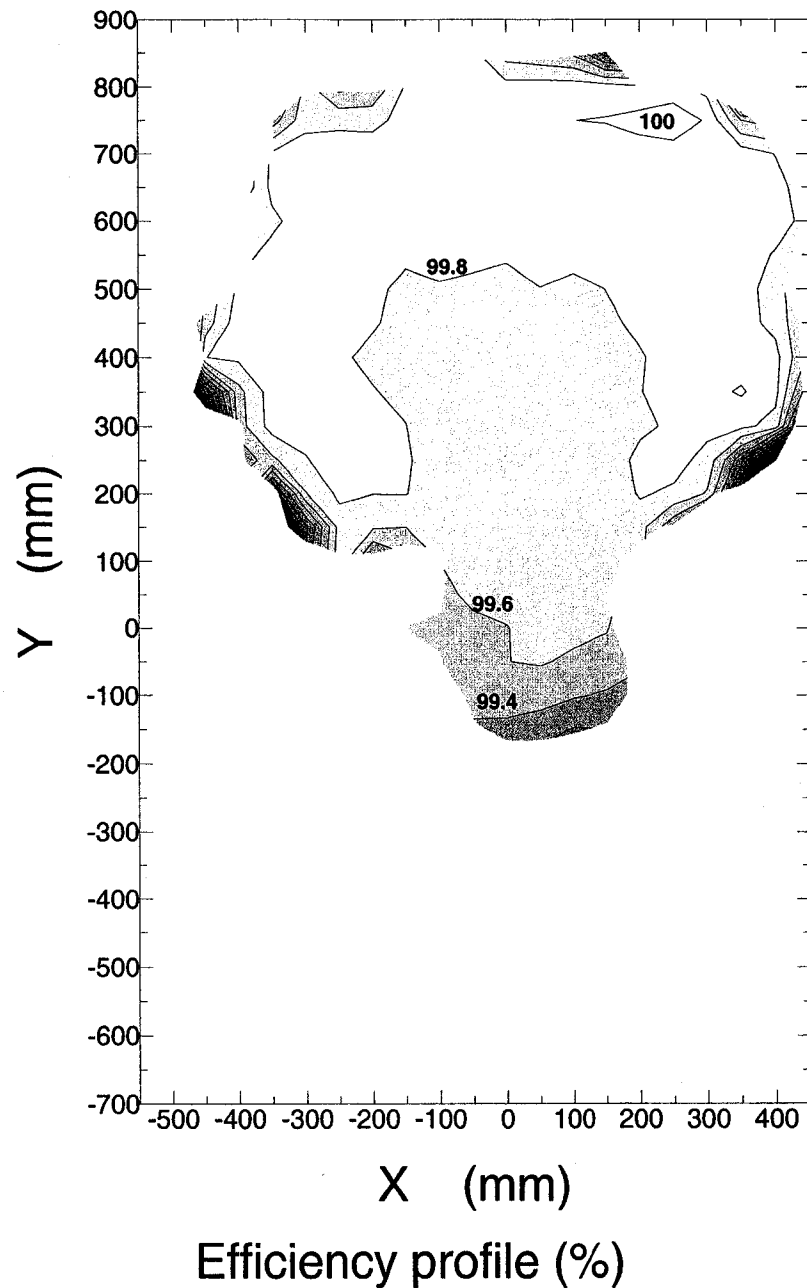


NOTE: X and Y axis in mm relative to flare stack tip

**Figure 6.1: CO<sub>2</sub>, CO, CH<sub>4</sub> and O<sub>2</sub> normalized concentrations for kidney shaped plume.**

**Conditions:**

$$U_{\infty} = 4.0 \text{ m/s}, V_j = 0.5 \text{ m/s}, d_o = 114.3 \text{ mm}, X_o = 3.20 \text{ m}$$



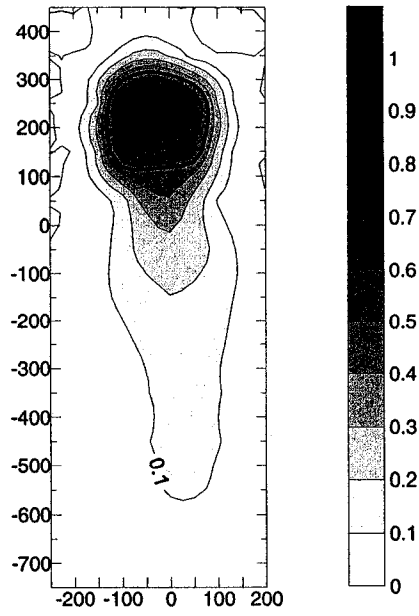
NOTE: X and Y axis in mm relative to flare stack tip

**Figure 6.2: Local combustion efficiency profile for kidney shaped plume.**

**Conditions:**

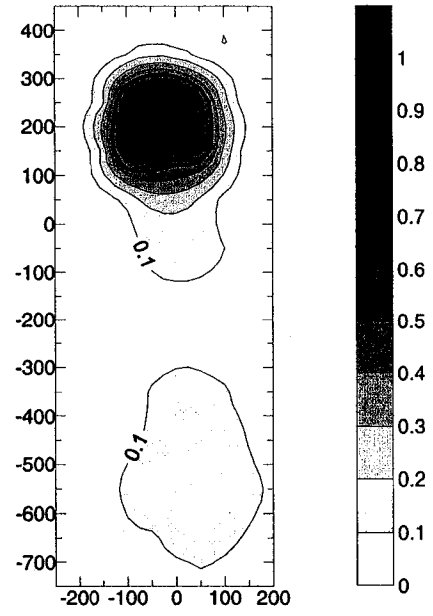
$$U_{\infty} = 4.0 \text{ m/s}, V_j = 0.5 \text{ m/s}, d_o = 114.3 \text{ mm}, X_o = 3.20 \text{ m}, \eta_{ave} = 99.8 \%$$

[CO<sub>2</sub>]<sub>min</sub> = 347 ppm [CO<sub>2</sub>]<sub>max</sub> = 5446 ppm



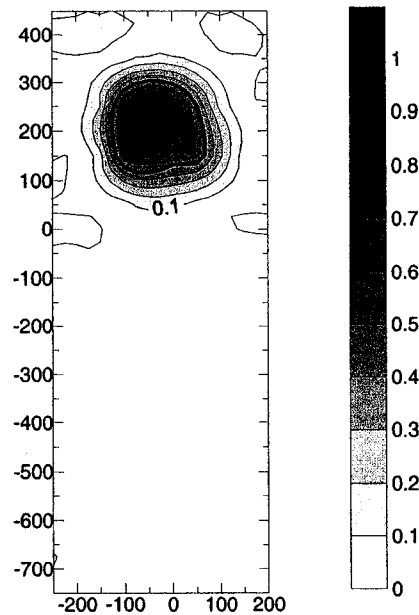
(a): Normalized CO<sub>2</sub> profile

[CO]<sub>min</sub> = 0.0 ppm [CO]<sub>max</sub> = 16.1 ppm



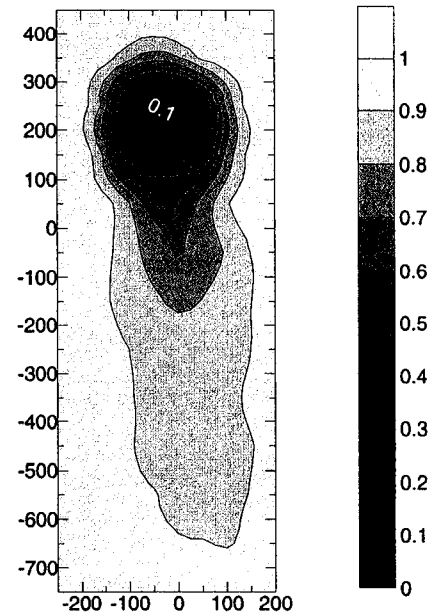
(b): Normalized CO profile

[CH<sub>4</sub>]<sub>min</sub> = 3.1 ppm [CH<sub>4</sub>]<sub>max</sub> = 23.7 ppm



(c): Normalized CH<sub>4</sub> profile

[O<sub>2</sub>]<sub>min</sub> = 19.56 % [O<sub>2</sub>]<sub>max</sub> = 20.54 %



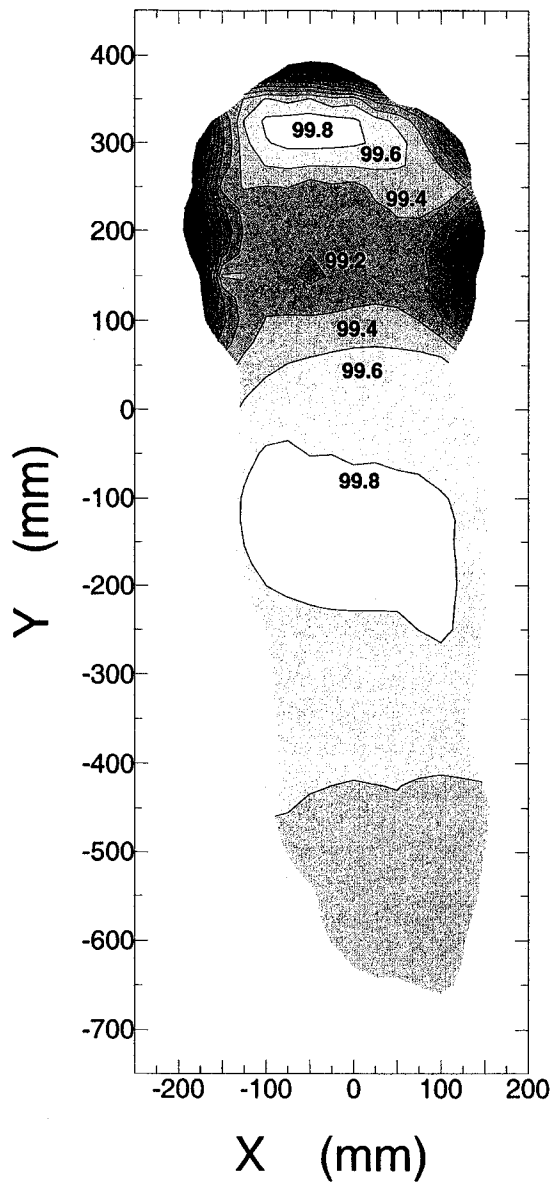
(d): Normalized O<sub>2</sub> profile

NOTE: X and Y axis in mm relative to flare stack tip

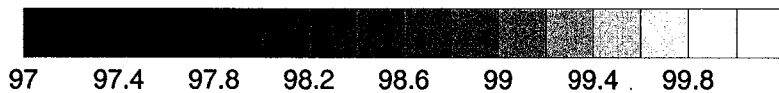
**Figure 6.3: CO<sub>2</sub>, CO, CH<sub>4</sub> and O<sub>2</sub> normalized concentrations for circular shaped plume.**

**Conditions:**

$$U_{\infty} = 6.0 \text{ m/s}, V_j = 1.0 \text{ m/s}, d_o = 58.8 \text{ mm}, X_o = 2.60 \text{ m}$$



Efficiency profile (%)



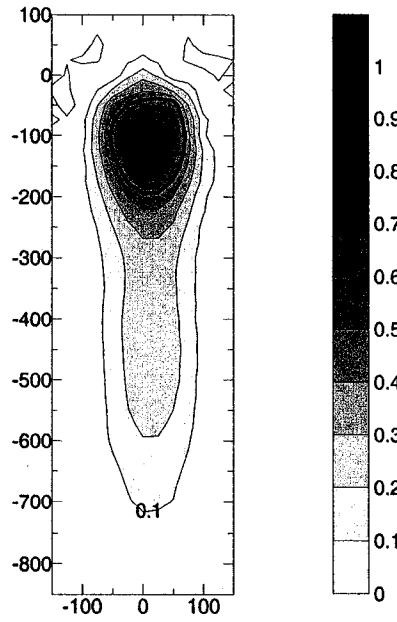
NOTE: X and Y axis in mm relative to flare stack tip

**Figure 6.4: Local combustion efficiency profile for circular shaped plume. Flare stack wake structures act to create two separate regions of higher combustion efficiency.**

**Conditions:**

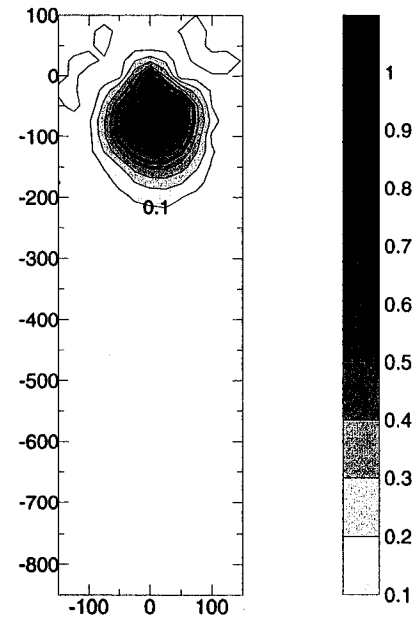
$$U_{\infty} = 6.0 \text{ m/s}, V_j = 1.0 \text{ m/s}, d_o = 58.8 \text{ mm}, X_o = 2.60 \text{ m}, \eta_{ave} = 99.5 \%$$

[CO<sub>2</sub>]<sub>min</sub> = 342 ppm [CO<sub>2</sub>]<sub>max</sub> = 1988 ppm



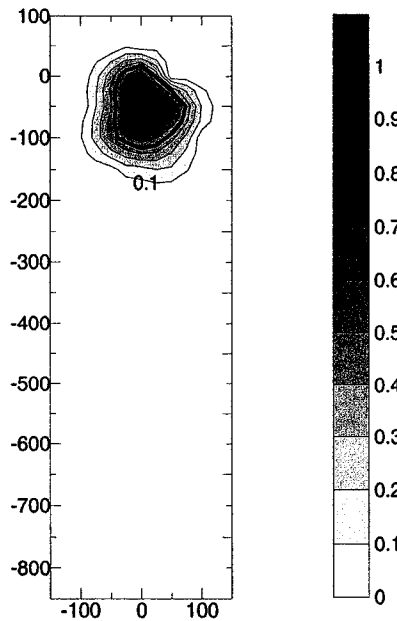
(a): Normalized CO<sub>2</sub> profile

[CO]<sub>min</sub> = 0.1 ppm [CO]<sub>max</sub> = 48.4 ppm



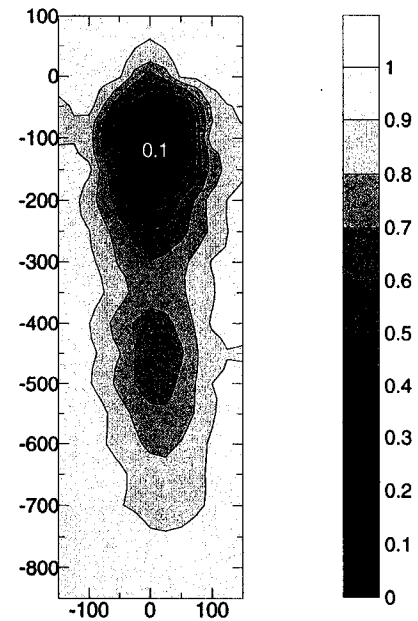
(b): Normalized CO profile

[CH<sub>4</sub>]<sub>min</sub> = 2.6 ppm [CH<sub>4</sub>]<sub>max</sub> = 466.0 ppm



(c): Normalized CH<sub>4</sub> profile

[O<sub>2</sub>]<sub>min</sub> = 20.40 % [O<sub>2</sub>]<sub>max</sub> = 20.75 %



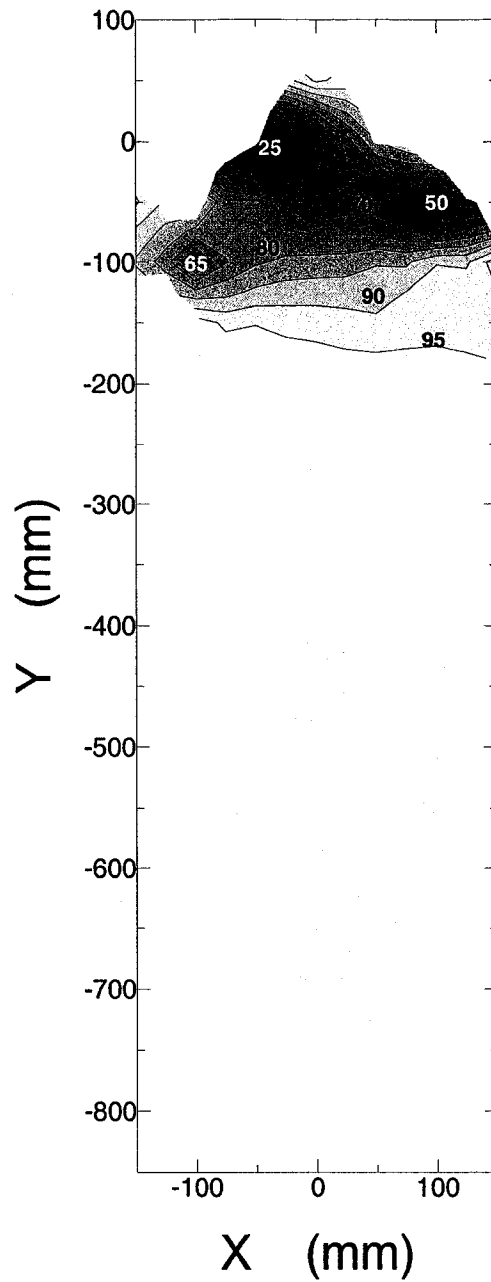
(d): Normalized O<sub>2</sub> profile

NOTE: X and Y axis in mm relative to flare stack tip

**Figure 6.5: CO<sub>2</sub>, CO, CH<sub>4</sub> and O<sub>2</sub> normalized concentrations for downwashed plume.**

**Conditions:**

$$U_{\infty} = 8.0 \text{ m/s}, V_j = 1.0 \text{ m/s}, d_o = 30.0 \text{ mm}, X_o = 0.80 \text{ m}$$



Efficiency profile (%)



NOTE: X and Y axis in mm relative to flare stack tip

Figure 6.6: Local combustion efficiency profile for downwashed plume.

Conditions:

$$U_{\infty} = 8.0 \text{ m/s}, V_j = 1.0 \text{ m/s}, d_o = 30.0 \text{ mm}, X_o = 0.80 \text{ m}, \eta_{ave} = 88.5 \%$$

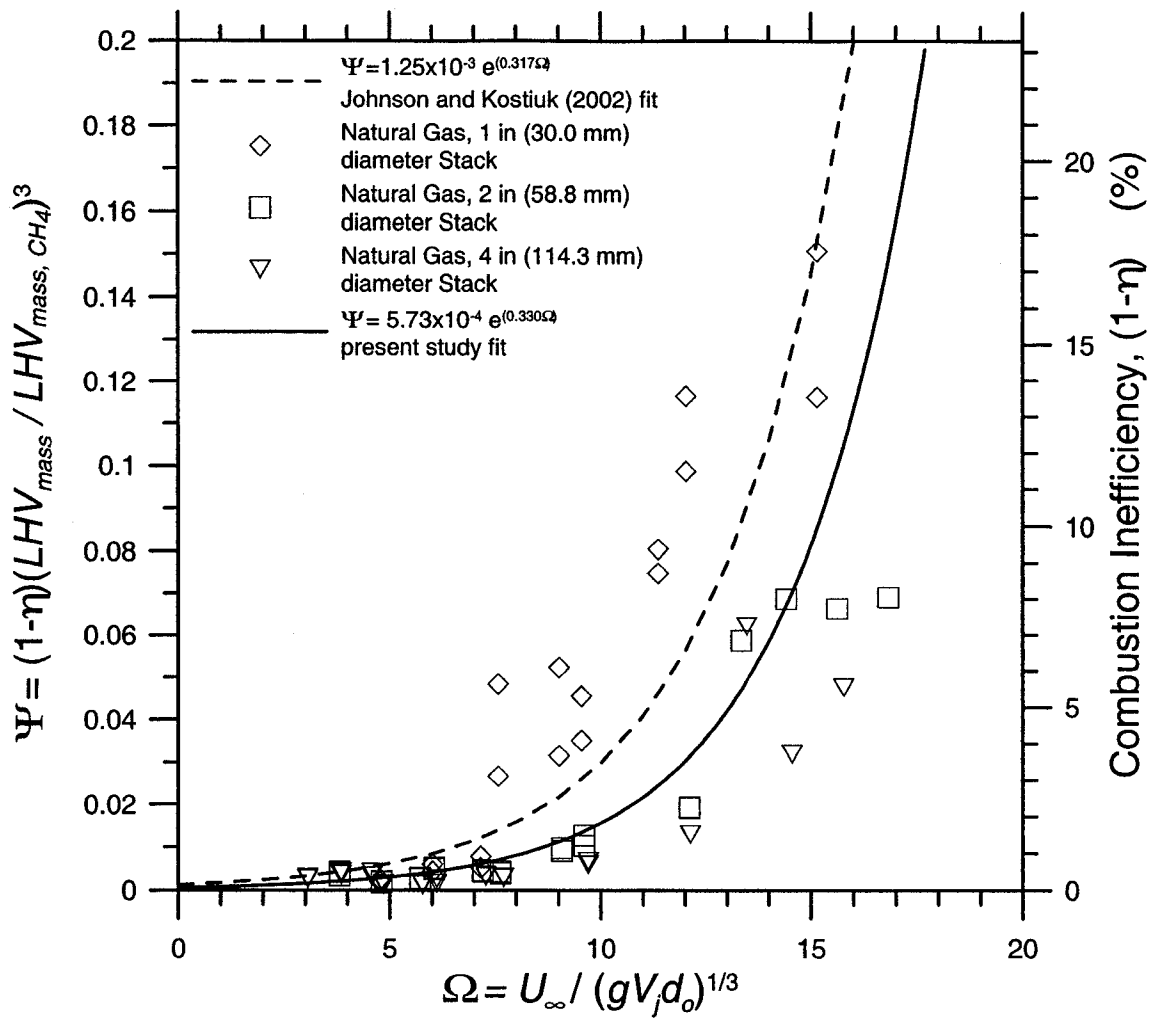


**Figure 6.7: Present study's correlation compared with Johnson's correlation for natural gas based flares with  $d_o^{1/3}$  dependency.**

**Conditions:**

$$4.0 \text{ m/s} \leq U_\infty \leq 14.0 \text{ m/s}, 0.5 \text{ m/s} \leq V_j \leq 2.0 \text{ m/s}$$

$$30.0 \text{ mm} \leq d_o \leq 114.3 \text{ mm}$$



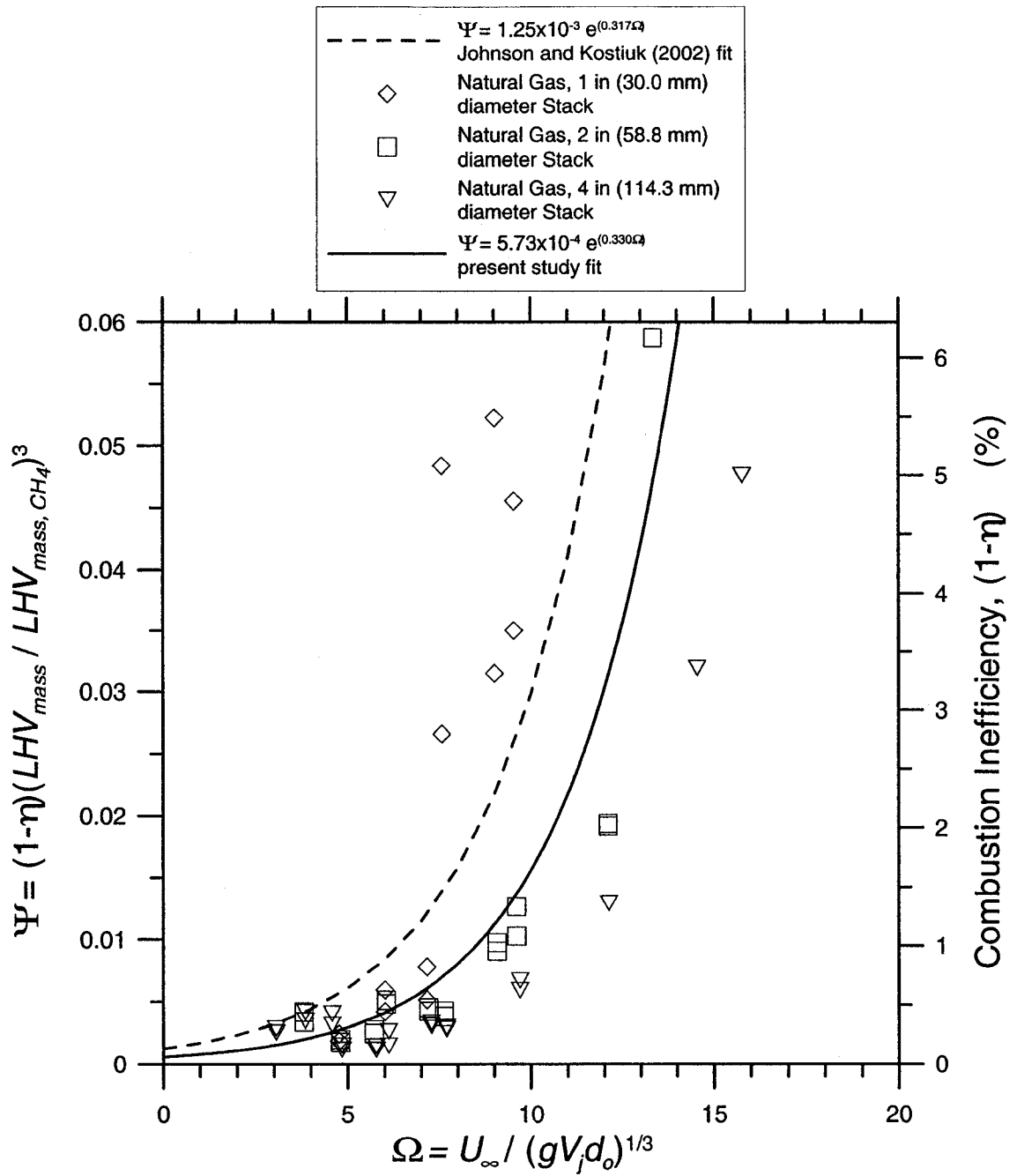
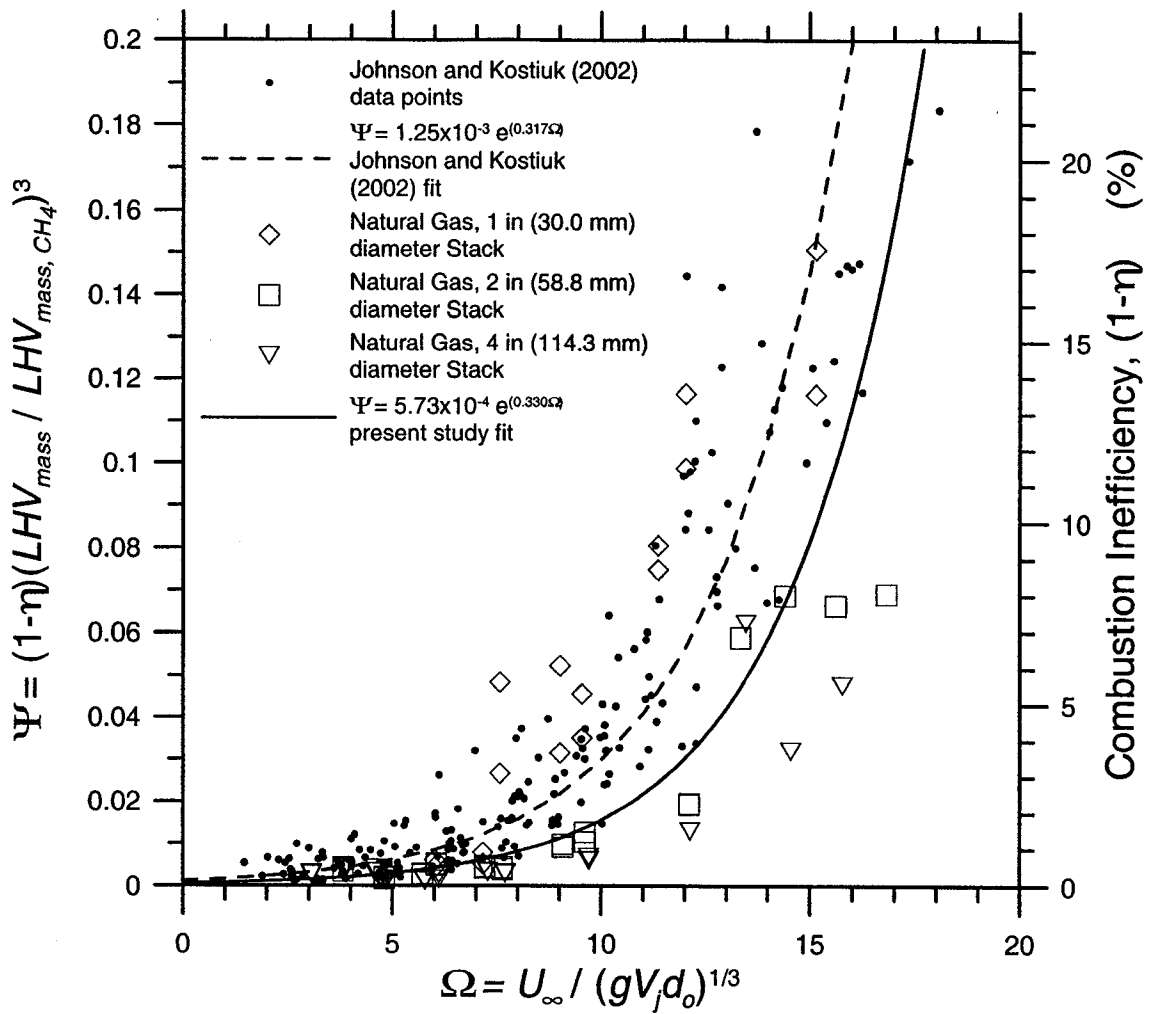


Figure 6.8: Exploded view of Figure 6.7.

Conditions:

$$4.0 \text{ m/s} \leq U_{\infty} \leq 14.0 \text{ m/s}, 0.5 \text{ m/s} \leq V_j \leq 2.0 \text{ m/s}$$

$$30.0 \text{ mm} \leq d_o \leq 114.3 \text{ mm}$$



**Figure 6.9: Comparison of scatter between Johnson's data and present study's data for natural gas based flares with  $d_o^{1/3}$  dependency.**

**Conditions:**

**Present study's data:  $4.0 \text{ m/s} \leq U_\infty \leq 14.0 \text{ m/s}$ ,  $0.5 \text{ m/s} \leq V_j \leq 2.0 \text{ m/s}$**

**$30.0 \text{ mm} \leq d_o \leq 114.3 \text{ mm}$**

**Johnson and Kostiuk (2002) data:  $2.0 \text{ m/s} \leq U_\infty \leq 16.0 \text{ m/s}$ ,  $0.5 \text{ m/s} \leq V_j \leq 2.0 \text{ m/s}$**

**$12.1 \text{ mm} \leq d_o \leq 49.8 \text{ mm}$**

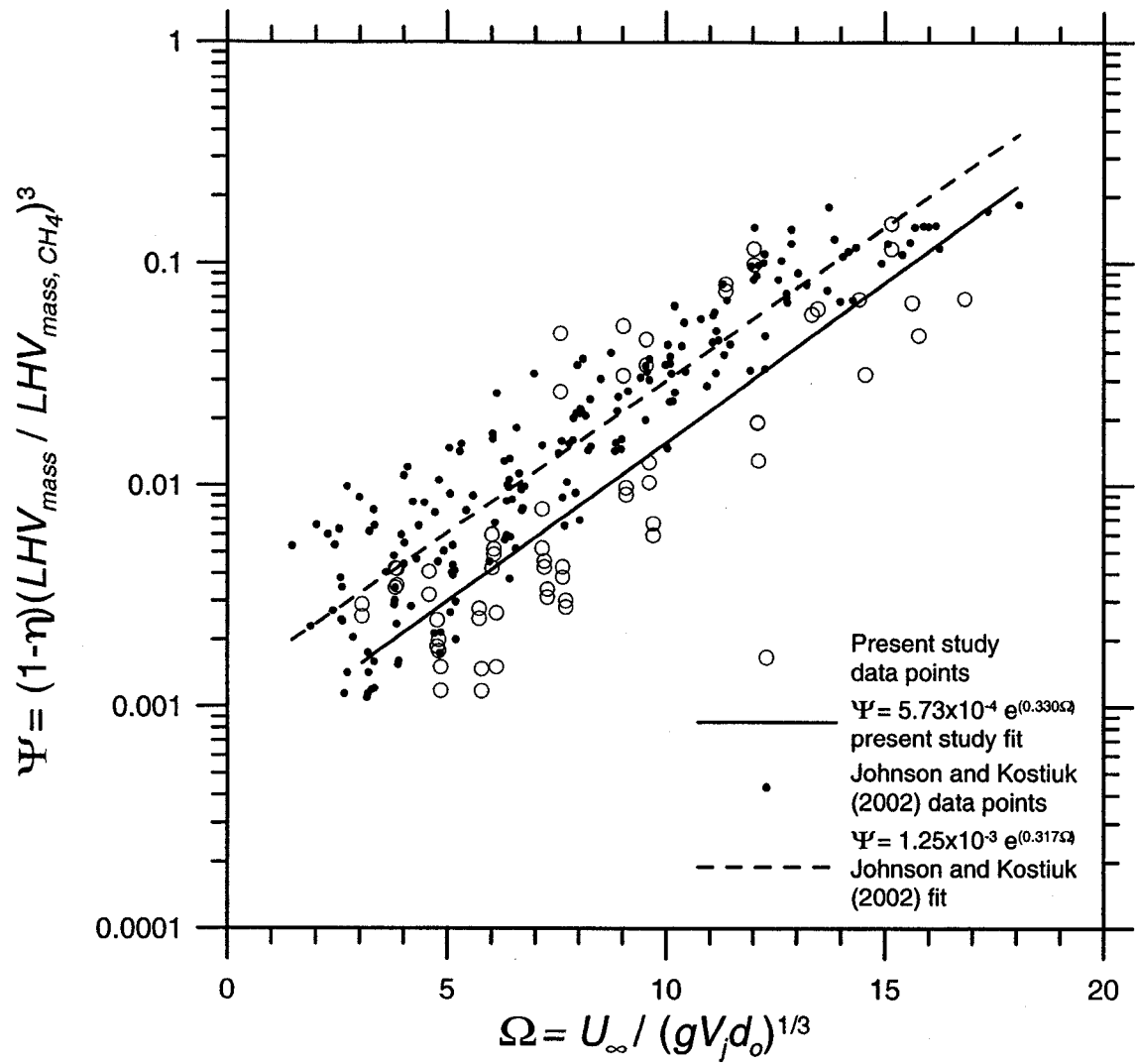


Figure 6.10: Figure 6.9 shown on semi-log scale.

Conditions:

Present study's data:  $4.0 \text{ m/s} \leq U_\infty \leq 14.0 \text{ m/s}$ ,  $0.5 \text{ m/s} \leq V_j \leq 2.0 \text{ m/s}$

$30.0 \text{ mm} \leq d_o \leq 114.3 \text{ mm}$

Johnson and Kostiuik (2002) data:  $2.0 \text{ m/s} \leq U_\infty \leq 16.0 \text{ m/s}$ ,  $0.5 \text{ m/s} \leq V_j \leq 2.0 \text{ m/s}$

$12.1 \text{ mm} \leq d_o \leq 49.8 \text{ mm}$

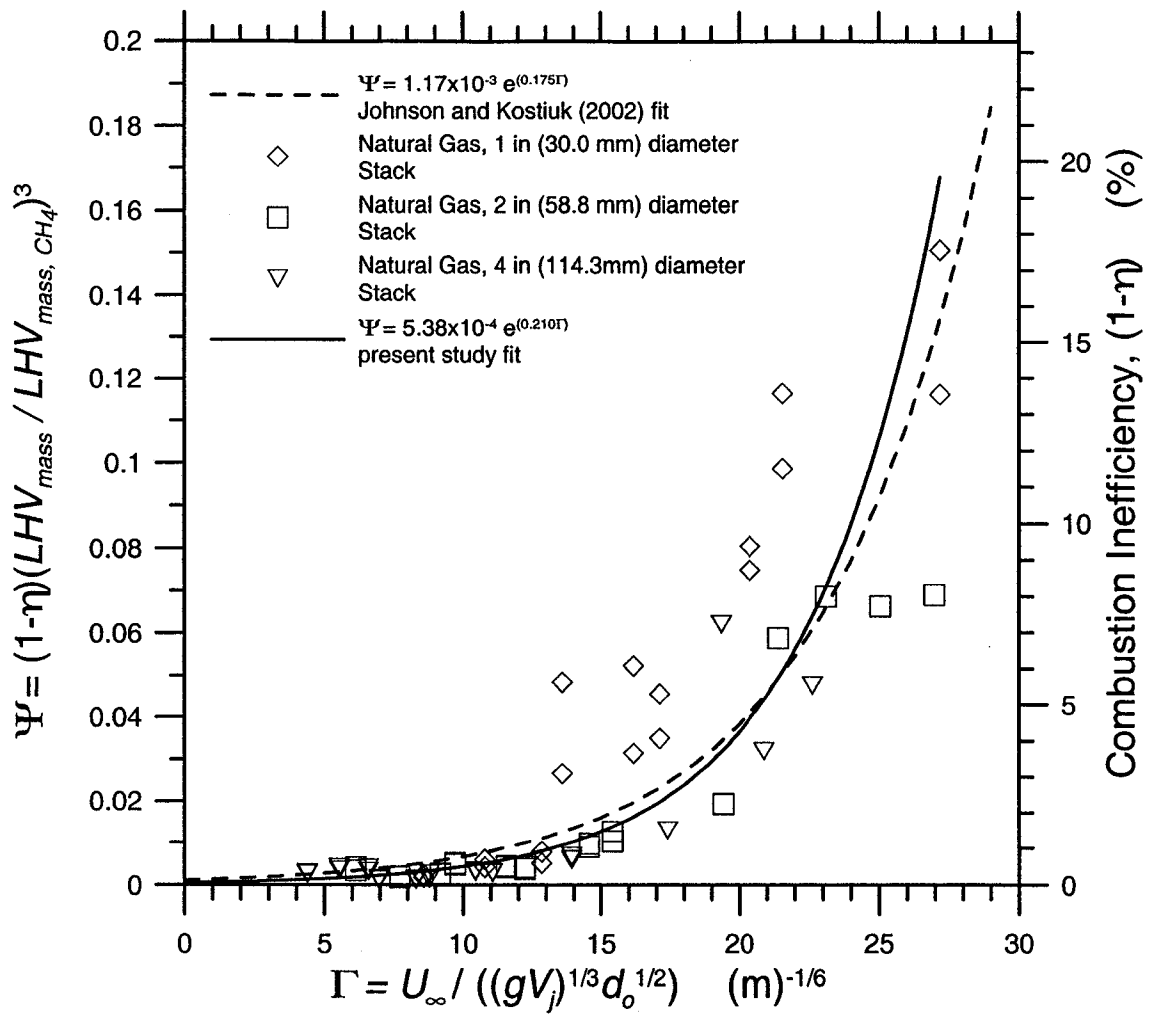


**Figure 6.11: Present study's correlation compared with Johnson's correlation for natural gas based flares with  $d_o^{1/2}$  dependency.**

**Conditions:**

$4.0 \text{ m/s} \leq U_\infty \leq 14.0 \text{ m/s}$ ,  $0.5 \text{ m/s} \leq V_j \leq 2.0 \text{ m/s}$

$30.0 \text{ mm} \leq d_o \leq 114.3 \text{ mm}$

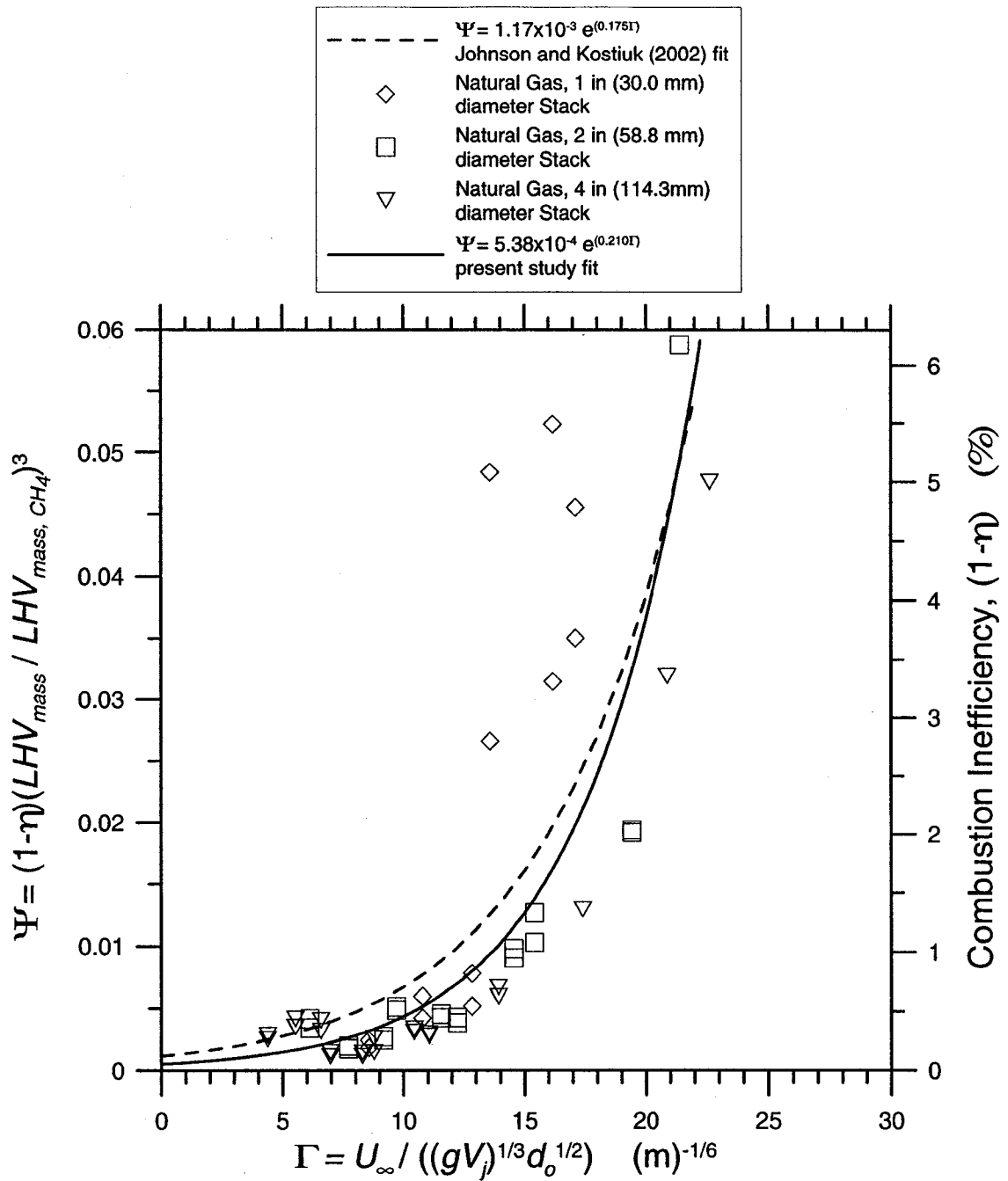
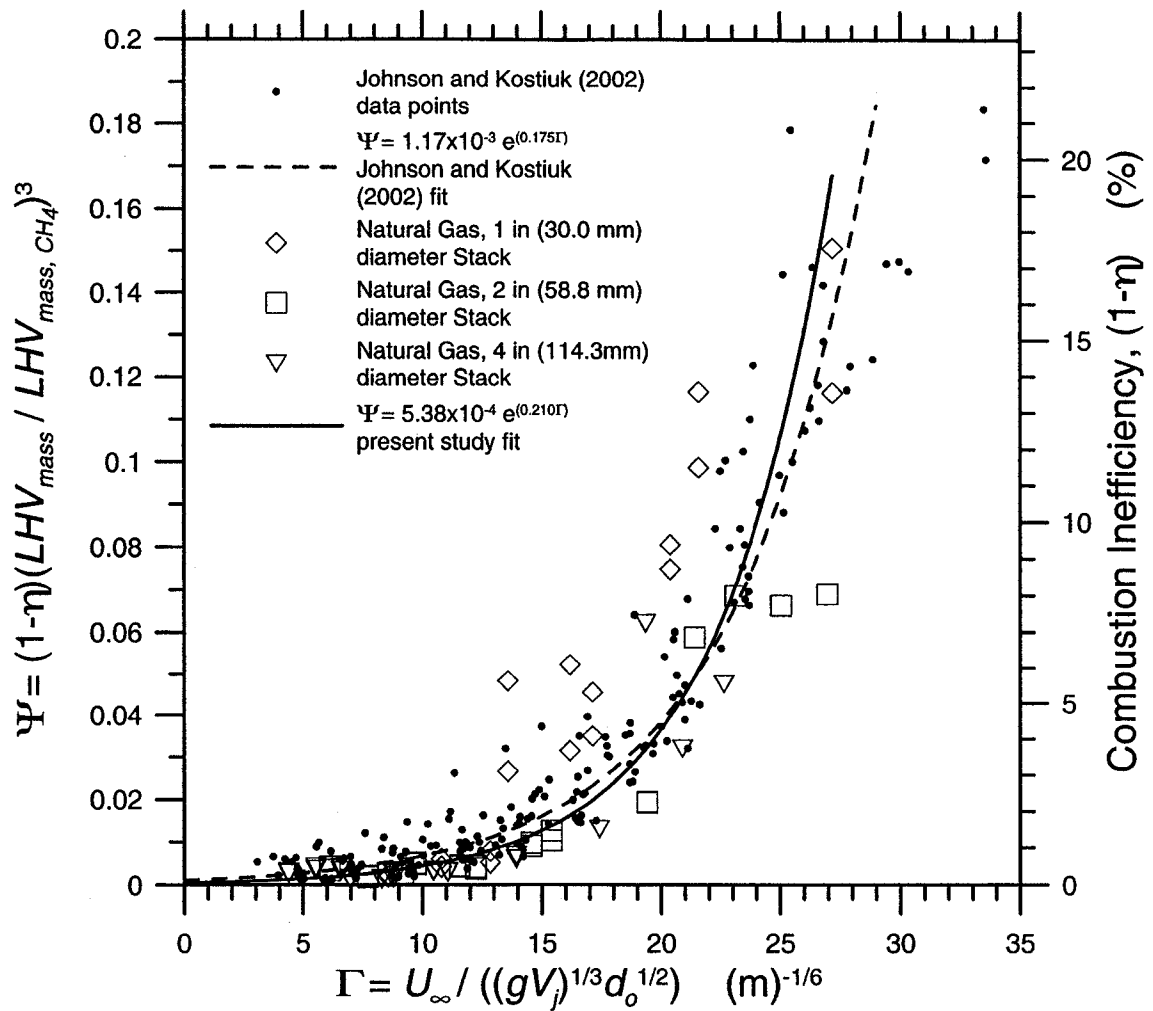


Figure 6.12: Exploded view of Figure 6.11.

Conditions:

$4.0 \text{ m/s} \leq U_\infty \leq 14.0 \text{ m/s}$ ,  $0.5 \text{ m/s} \leq V_j \leq 2.0 \text{ m/s}$

$30.0 \text{ mm} \leq d_o \leq 114.3 \text{ mm}$



**Figure 6.13: Comparison of scatter between Johnson's data and present study's data for natural gas based flares with  $d_o^{1/2}$  dependency.**

**Conditions:**

**Present study's data:  $4.0 \text{ m/s} \leq U_\infty \leq 14.0 \text{ m/s}$ ,  $0.5 \text{ m/s} \leq V_j \leq 2.0 \text{ m/s}$**

**$30.0 \text{ mm} \leq d_o \leq 114.3 \text{ mm}$**

**Johnson and Kostiuk (2002) data:  $2.0 \text{ m/s} \leq U_\infty \leq 16.0 \text{ m/s}$ ,  $0.5 \text{ m/s} \leq V_j \leq 2.0 \text{ m/s}$**

**$12.1 \text{ mm} \leq d_o \leq 49.8 \text{ mm}$**

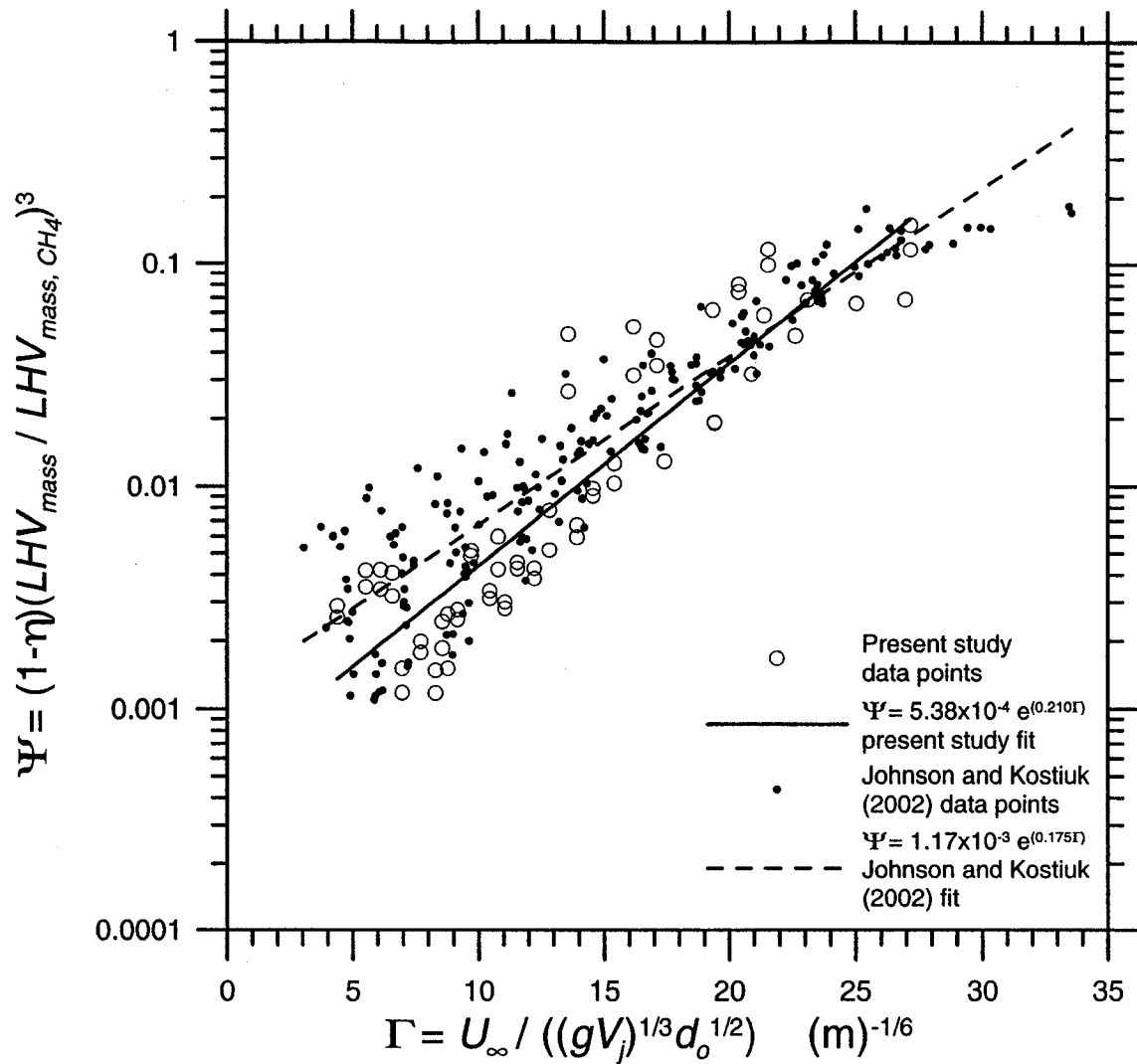


Figure 6.14: Figure 6.13 shown on semi-log scale.

Conditions:

Present study's data:  $4.0 \text{ m/s} \leq U_\infty \leq 14.0 \text{ m/s}$ ,  $0.5 \text{ m/s} \leq V_j \leq 2.0 \text{ m/s}$

$30.0 \text{ mm} \leq d_o \leq 114.3 \text{ mm}$

Johnson and Kostiuik (2002) data:  $2.0 \text{ m/s} \leq U_\infty \leq 16.0 \text{ m/s}$ ,  $0.5 \text{ m/s} \leq V_j \leq 2.0 \text{ m/s}$

$12.1 \text{ mm} \leq d_o \leq 49.8 \text{ mm}$

## Chapter 7

### CEILING AND FLOOR EFFECTS ON THE FLARE, PLUME RISE AND COMBUSTION EFFICIENCY

The objective of this chapter is to measure the effect of the proximity of the wind tunnel ceiling and floor on a model flare. It will be shown that ceiling and floor effects on plume trajectory and combustion efficiency are insignificant, except in cases where the stack exit is very close to the floor.

The model flare stack height was adjusted to bring the stack tip incrementally closer to the ceiling or floor; at each increment, mean cross-sectional compositional and thermal maps were generated. Results were compared to determine possible ceiling and floor effects on plume trajectory and dispersion and flare combustion efficiency. True color images of the flame were captured to investigate ceiling effects on the flame length and angle. Experimental results for plume trajectory were compared against a plume rise model that incorporated the effect of a wind tunnel ceiling through a mirror image buoyancy source that forced plume rise to stop at the ceiling.

#### 7.1 Wind Tunnel Ceiling Proximity Effects

##### 7.1.1 Ceiling Effects on Flame Length and Flame Angle

A digital camera (described in Chapter 4) was used to capture images of the flames issuing from the 2.74 m tall adjustable height flare stack (described in section 4.1.4.2) with the false ceiling installed at 9 ft (2.74 m) above the tunnel floor.

Experiments were conducted under the following conditions:

- Fuel: sales grade natural gas (see Table 3.1)
- $U_{\infty} = 4.0$  m/s



- $0.5 \text{ m/s} \leq V_j \leq 2.0 \text{ m/s}$ 
  - $V_j = 0.5 \text{ m/s}, 0.15 \text{ m} \leq Y_c \leq 0.61 \text{ m}$
  - $V_j = 1.0 \text{ m/s}, 0.23 \text{ m} \leq Y_c \leq 0.76 \text{ m}$
  - $V_j = 2.0 \text{ m/s}, 0.30 \text{ m} \leq Y_c \leq 0.76 \text{ m}$
- $d_i = 26.9 \text{ mm}$  (0.25-scale)

where  $Y_c$  is the vertical distance from the flare stack exit to the false ceiling (shown in Figure 7.1). Minimum  $Y_c$  values were set by impingement of the flame on the false ceiling. Images were captured at 7.6 cm (3 in) increments of  $Y_c$ .

Several images were collected for each value of  $Y_c$ . Shutter speed was varied between 1/13 s and 1/2.5 s to accommodate for flame fluctuations and generate a mean flame image. The approximate length and angle of the flame,  $L_f$  and  $\theta_f$  respectively, were determined for each image taken at a set  $Y_c$ , then values of  $L_f$  and  $\theta_f$  were averaged for all flame images collected at a set  $Y_c$ .

$L_f$  is defined as the distance from the intersection of the flare stack axis with the stack exit to the tip of the approximate core of the flame.  $\theta_f$  is defined as the angle the flame length makes with the horizontal. The approximate core of the flame was defined using a color intensity filter in the graphic viewing program PhotoImpact (Ulead Systems Inc.). PhotoImpact assigns an intensity value between 0 and 255 points to the red, blue and green colour components of each pixel. The color intensity filter selected all pixels within the flame that had intensity points between 255 and 155 for each of the colour components (a color intensity similarity of 100 points), effectively collecting the most luminous part of the flame (i.e. bright yellow). Figure 7.1 demonstrates the concept of  $L_f$ ,  $\theta_f$  and  $Y_c$ .

A new normalization parameter, buoyancy length ( $L_b$ ), is introduced so that plots of approximate flame length and flame angle can make use of non-dimensional variables. Buoyancy length is defined as

$$L_b = \frac{F_b}{U_\infty^3} \quad (7.1)$$

where

$$F_b = g \frac{\bar{R}_\infty H_s}{\pi C_{p\infty} P_\infty} = \text{buoyancy flux of combustion products from the flame}$$

$g$  = gravitational constant

$H_s$  = heat release rate at ideal point source of combustion (Eq. A.3)

$C_{p\infty}$  = constant specific heat of the ambient air

$P_\infty$  = ambient air pressure                       $\bar{R}_\infty$  = ambient air specific gas constant

Figure 7.2 displays a plot of  $L_f / L_b$ , approximate flame length over buoyancy length, with respect to  $Y_c / L_b$ , vertical distance from the flare stack exit to the false ceiling over buoyancy length. Data is presented for  $V_j = 0.5$  m/s, 1.0 m/s and 2.0 m/s. The flame length over buoyancy length without any ceiling and floor effects is indicated by a horizontal solid or dashed line for each case. These flame lengths were recorded at  $Y_c / L_b = 508$ .

It was assumed that at  $Y_c / L_b = 508$ , midway between the wind tunnel floor and false ceiling, there were no ceiling or floor effects acting on the flame. These effects encompass the ceiling and floor boundary layers and pressure effects. This assumption was made based on the fact that at this location the flame was positioned far outside the floor and ceiling boundary layers. Also, at this location the flame is assumed to be unchanged by pressure effects caused by the ceiling and floor.

Figure 7.2 shows the approximate flame length remains relatively constant as the flare stack exit is moved closer and closer to the false ceiling. This indicates that the proximity of the false ceiling has no discernible effect on the approximate flame length.

Figure 7.3 shows a plot of  $\theta_f$ , approximate flame angle, with respect to  $Y_c / L_b$ , vertical distance from the flare stack exit to the false ceiling over buoyancy length for the cases  $V_j = 0.5$  m/s, 1.0 m/s and 2.0 m/s. The flame angle without any ceiling and floor effects is indicated by a horizontal solid or dashed line for each case. These flame angles were recorded at  $Y_c / L_b = 508$ .

It can be seen that considerable scatter exists in the data recorded for the approximate flame angle. This scatter, which appears to be largest at distances furthest from the false ceiling, could be attributed to the presence of large-scale turbulent eddies in the crosswind above the flare stack. It was observed that the data converged on the approximate flame angle measured without any ceiling or floor effects as the flare stack exit was moved closer to the false ceiling (i.e. as  $Y_c / L_b$  decreases). The reason for this may be that near the false ceiling the large-scale crosswind turbulence breaks down into smaller-scale eddies that cause less fluctuations in the approximate flame angle.

### 7.1.2 Ceiling Effects on Plume Rise and Dispersion

For this portion of the research, the 2.74 m tall adjustable height flare stack was used with the false ceiling installed at 9 ft (2.74 m) above the wind tunnel floor. 20 plume cross-sectional thermal maps generated under the following experimental conditions:

- Fuel: sales grade natural gas (see Table 3.1)
- $U_\infty = 4.0$  m/s
- $0.5$  m/s  $\leq V_j \leq 2.0$  m/s
  - $V_j = 0.5$  m/s,  $0.31$  m  $\leq Y_c \leq 1.22$  m

- $V_j = 1.0 \text{ m/s}, 0.38 \text{ m} \leq Y_c \leq 1.22 \text{ m}$
- $V_j = 2.0 \text{ m/s}, 0.46 \text{ m} \leq Y_c \leq 1.22 \text{ m}$
- $d_i = 26.9 \text{ mm (0.25-scale)}$
- $X_o = 2.13 \text{ m}$

Assuming a turbulent boundary layer profile, it was calculated using Eq. 7.2 for a flat plate (White, 1999, p. 428) that the ceiling boundary layer was approximately 6 cm tall at  $X_o = 2.13 \text{ m}$  (downstream location of false ceiling trailing edge).

$$\frac{\delta}{x_c} \approx \frac{0.16}{\text{Re}_L^{1/7}} \quad (7.2)$$

where

$$\text{Re}_L = \frac{U_\infty L}{\nu}$$

$\delta$  = turbulent boundary layer thickness

$x_c$  = distance downstream from false ceiling leading edge

$L$  = length of false ceiling = 2.44 m

$\nu$  = kinematic viscosity of air at 1 atm, 293 K =  $1.5 \times 10^{-5} \text{ m}^2/\text{s}$

Minimum  $Y_c$  values were set based on the presence of this boundary layer, as thermal maps that showed a plume core (50 % temperature contour) inside the layer were not included in the study. This was done to ensure that all thermal plumes were isolated from the added mixing present in the turbulent boundary layer. Thermal maps were generated at 7.6 cm increments of  $Y_c$ .

Figure 7.4 displays the mean thermal cross-sections of the plume as it approaches the ceiling for the case  $V_j = 1.0$  m/s and  $U_\infty = 4$  m/s. Note that ambient temperature was approximately  $-20$  deg. C for all plumes in this case. The proximity of the ceiling does not appear to have a quantifiable impact on the shape of the plume mean thermal cross-section, nor does it appear to deflect the plume downwards. Note that Figure 7.4 (f) plots data only up to the position of the ceiling for  $Y_c / L_b = 140$ , because lower values of  $Y_c / L_b$  showed flare plume cores inside the false ceiling boundary layer.

The centroids of all 20 plume cross-sections were calculated for the purpose of determining the ceiling's effects on plume rise at  $X_o / d_i = 79.2$ . Using data points found within the 50 % temperature contour of each thermal plume, the vertical component (measured from the wind tunnel floor) of each centroid location was determined using the following equation.

$$y_{centroid} = \frac{\sum_w (\rho_L y)}{\sum_w \rho_L} \quad (7.3)$$

where

$w$  = number of data points inside the 50 % temperature contour

$\rho_L$  = local density at each data point, defined by Eq. 3.24

$y$  = vertical component of each data point inside the 50 % temperature contour (measured from wind tunnel floor)

Figure 7.5 displays a plot of  $y_{centroid} / L_b$ , plume centroid vertical position over buoyancy length, with respect to  $Y_c / L_b$ , vertical distance from the flare stack exit to the false ceiling over buoyancy length for  $X_o / d_i = 79.2$ . The cases  $V_j = 0.5$  m/s, 1.0 m/s and 2.0 m/s are presented. The value of  $y_{centroid} / L_b$  without any ceiling effects is indicated by a horizontal solid or dashed line for each case.

In this research, the vertical component of the centroid location was assumed to represent the centerline of the plume and hence could be used to investigate the ceiling's effect on the rise of the plume. The aforementioned figure shows that for  $X_o / d_i = 79.2$ , the plume centroid vertical position remains relatively constant in each case as the flare stack exit is moved closer and closer to the false ceiling. This indicates that for plumes whose cores are not found in the false ceiling's turbulent boundary layer, the proximity of the ceiling to the plume has no significant impact on plume rise.

#### 7.1.2.1 Model for Buoyant Plume Rise Under a Ceiling

The buoyant plume rise model shown in Eq. (3.7) was derived for a reacting plume whose rise was uninhibited by physical obstacles. The purpose of this section is to derive a new plume rise model that incorporates the effects of a ceiling. Although data presented in section 7.1.2 shows that the ceiling does not significantly affect plume rise, it is of scientific interest to determine if a theoretical model agrees with reality.

Figure 7.6 presents an idealized model of the situation, showing how the presence of the ceiling may alter the plume's trajectory. An idealized point reaction is placed at the exit of the stack; complete combustion ( $\eta = 100\%$ ) is assumed to occur. The need arises to find define a corrected plume rise,  $h_{b,actual}$  and a corrected upward plume speed,

$$W_{p,actual}.$$

Using buoyant non-reacting plume models and theory developed by Briggs (1975) and Weil (1977), one may derive expressions for buoyant plume rise ( $h_b$ ) and upward plume speed ( $W_p$ ) without the presence of a ceiling.

$$h_b = K_h \frac{H_s^{1/3} X_o^{2/3}}{U_\infty} \quad (7.4)$$

$$W_p = \frac{\partial h_b}{\partial t} = \frac{\partial h_b}{\partial X_o} \frac{\partial X_o}{\partial t} = U_\infty \frac{\partial h_b}{\partial X_o}$$

$$W_p = \frac{2}{3} K_h \left( \frac{H_s}{X_o} \right)^{1/3} \quad (7.5)$$

where

$$K_h = \left( \frac{3}{2\beta^2} \right)^{1/3} \left( \frac{g\bar{R}_\infty}{\pi C_{p\infty} P_\infty} \right)^{1/3}$$

$$H_s = \pi R_j^2 V_j \rho_s C_{p\infty} (T_s - T_\infty) = \text{heat release rate at the point source}$$

The presence of the ceiling was modeled by adding a mirror image plume opposite the real plume, and then using a backward difference method (subscript  $j$ ) to find the corrected plume rise trajectory ( $h_{b,actual}$ ) and corrected upward plume speed ( $W_{p,actual}$ ). Figure 7.7 demonstrates the implementation of the model.

$$h_{b,actual}(j) = h_{b,actual}(j-1) + (W_{p,actual}(j-1) - W_{image\ at\ plume,actual}(j-1)) \frac{\Delta X_o}{U_\infty} \quad (7.6)$$

$$W_{p,actual}(j-1) = W_{p,actual}(j-2) + \left( \frac{\partial W_{p(j-1)}}{\partial t} \right) \frac{\Delta X_o}{U_\infty} \quad (7.7)$$

In this model the image plume is idealized as a solid rising cylinder. Ambient air must be pushed out of the rising cylinder's path; hence a velocity gradient is created with the ambient air that works to "push" down the real plume. This velocity exerted by the image plume velocity on the real plume is defined as

$$W_{image\ at\ plume,actual}(j-1) = f_{daf} W_{p,actual}(j-1) \left( \frac{R_{p(j-1)}}{2S_{actual}(j-1)} \right)^2 \quad (7.8)$$

where

$$R_{p(j-1)} = \text{radius of the plume at point (j-1)}$$

$f_{dat}$  = displaced airflow factor

There are two types of ambient airflow around a buoyant plume. One type of airflow is the air that passes around the top of the plume and gets entrained at on the plume's underside. The other type of airflow is the non-entrained flow that is displaced by the plume and pushed out of the way as the plume rises. The displaced airflow factor accounts for the ambient air inertia that must be overcome and "pushed aside" in order to clear the image plume rising cylinder's path. Appendix C provides derivations of Eq. 7.4 to 7.8.

Numerical models for  $h_{b,actual}$  and  $W_{p,actual}$  were created for the following cases at  $U_{\infty} = 4.0$  m/s,  $d_i = 26.9$  mm and  $Y_c = 30.5$  cm. These models were compared against the traditional models for  $h_b$  and  $W_p$  as defined by Eq. 7.4 and 7.5.

- $V_j = 0.5$  m/s,  $Y_c / L_b = 225$
- $V_j = 1.0$  m/s,  $Y_c / L_b = 112$
- $V_j = 2.0$  m/s,  $Y_c / L_b = 56$

The position  $Y_c = 30.5$  cm was chosen as it was an extreme situation for each of the above three cases of fuel speeds. In each case the flame is almost impinging on the ceiling, so it was assumed that this extreme proximity to the ceiling would result in the strongest ceiling effects on the flare and thus, the greatest deflection of the plume rise.

Figure 7.8 displays a plot of  $h_b / L_b$  and  $h_{b,actual} / L_b$  with respect to  $X_o / d_i$  for the case  $V_j = 0.5$  m/s. Note that the horizontal dashed line defines the position of the ceiling. It is observed that the plot for  $h_{b,actual} / L_b$  closely follows that of  $h_b / L_b$  until the plume "sees" the false ceiling at  $X_o / d_i \approx 70$ , whereupon the corrected plume trajectory gradually flattens until  $X_o / d_i \approx 90$  where it makes a sharp decrease in slope to follow the surface of the ceiling. The model for  $h_{b,actual}$  in this case converged for  $f_{daf} = 0.006$ .



Figure 7.9 shows a plot of  $W_p / V_j$  and  $W_{p,actual} / V_j$  with respect to  $X_o / d_i$  for  $V_j = 0.5$  m/s.  $W_{p,actual}$  closely follows  $W_p$  until, as expected, it drops off around  $X_o / d_i \approx 70$  and quickly goes to zero at  $X_o / d_i \approx 90$ , indicating the plume is following the surface of the false ceiling.

Figures 7.10 to 7.13 display plots of  $h_b / L_b$  and  $h_{b,actual} / L_b$  with respect to  $X_o / d_i$ , and  $W_p / V_j$  and  $W_{p,actual} / V_j$  with respect to  $X_o / d_i$  for the cases  $V_j = 1.0$  and  $2.0$  m/s. In both cases,  $h_{b,actual} / L_b$  closely follows  $h_b / L_b$  until a certain value of  $X_o / d_i$  ( $\approx 50$  for  $V_j = 1.0$  m/s,  $\approx 35$  for  $V_j = 2.0$  m/s) where it senses the false ceiling, then gradually flattens until it makes a sharp decrease in slope ( $X_o / d_i \approx 65$   $V_j = 1.0$  m/s,  $X_o / d_i \approx 45$  for  $V_j = 2.0$  m/s) to follow the surface of the ceiling. The model for  $h_{b,actual}$  converged at  $f_{daf} = 0.007$  for the case  $V_j = 1.0$  m/s and at  $f_{daf} = 0.008$  for the case  $V_j = 2.0$  m/s.

All the cases presented were considered extreme in that the flame was nearly impinging on the ceiling, and one may assume that the extreme proximity to the ceiling would result in the strongest ceiling effects on the plume rise. The corrected buoyant plume rise model ( $h_{b,actual}$ ) shows that the presence of the ceiling does not have a significant effect on the rise of the reacting plume until very near the ceiling, which is to be expected as the plume trajectory is physically forced to follow the ceiling surface. However, the presence of the ceiling does have a significant effect upon the local rate of plume rise,  $W_{p,actual}$ . In all cases the theoretical model agrees with physical data presented in section 7.1.2 concerning the vertical component of plume centroids.

Although  $f_{daf}$  varied between 0.006 and 0.008 for the cases presented in this study, it was found that setting  $f_{daf}$  to 0.007 incurred errors of less than 1 % in the maximum attained plume rise,  $h_{b,actual}$ , for the cases  $V_j = 0.5$  and  $2.0$  m/s. Based on these

negligible errors,  $f_{daf}$  can be considered a constant with a value of 0.007 for cases presented in this study.

### 7.1.3 Ceiling Effects on Combustion Efficiency

In this section, 16 plume cross-sectional compositional maps were generated under the same experimental conditions as in section 7.1.2. Again, minimum  $Y_c$  values were set based on the presence of the ceiling's turbulent boundary layer. Maps were generated at 7.6 cm (3 in) increments of  $Y_c$ .

Figure 7.14 displays a plot of  $(1 - \eta)$ , combustion inefficiency, with respect to  $Y_c / L_b$ , vertical distance from the flare stack exit to the false ceiling over buoyancy length. The cases  $V_j = 0.5$  m/s, 1.0 m/s and 2.0 m/s are presented. The flare stack inefficiency without any ceiling and floor effects is indicated by a horizontal solid or dashed line for each case.

Figure 7.14 shows that flare stack combustion inefficiency remains relatively constant as the flare stack exit is moved closer to the false ceiling. This indicates that the proximity of the false ceiling has no significant impact on combustion inefficiency of the flare stack.

## 7.2 Wind Tunnel Floor Proximity Effects

### 7.2.1 Floor Effects on Plume Rise and Dispersion

In this section, 18 plume cross-sectional compositional maps were generated using the 1.52 m tall adjustable height flare stack. Data was collected under the following experimental conditions:

- Fuel: sales grade natural gas (see Table 3.1)
- $U_\infty = 4.0$  m/s
- $0.5$  m/s  $\leq V_j \leq 2.0$  m/s

- $31 \text{ cm} \leq Y_f \leq 69 \text{ cm}$
- $d_i = 26.9 \text{ mm}$  (0.25-scale)
- $X_o = 2.13 \text{ m}$

where  $Y_f$  is the vertical distance from the flare stack exit to the wind tunnel floor. Maps were generated at 7.6 cm (3 in) increments of  $Y_f$ .

Figure 7.15 shows the mean thermal cross-sections of the plume as it approaches the floor for the case  $V_j = 0.5 \text{ m/s}$  and  $U_\infty = 4 \text{ m/s}$ . Note that ambient temperature was approximately - 20 deg. C for all plumes in this case. This case produces a downwashed plume cross-section. As the plume nears the floor, its downwashed profile shrinks in the vertical direction. As would be expected, the floor is preventing the plume from downwashing. Figure 7.16 shows the effect of the floor on the physical dimensions of the plume for the case  $V_j = 2.0 \text{ m/s}$  at  $U_\infty = 4 \text{ m/s}$ . Note that the ambient temperature was approximately - 10 deg. C for all plumes in this case. In this case there is no downwash and little change is seen in the shape of the plume as it nears the floor.

Using the same analytical technique discussed in section 7.1.2, the centroids of each plume cross-section collected for  $0.5 \text{ m/s} \leq V_j \leq 2.0 \text{ m/s}$  were calculated for the purpose of determining the floor's effects on plume rise at  $X_o = 2.13 \text{ m}$ .

Figure 7.17 displays a plot of  $y_{centroid} / L_b$ , plume centroid vertical position over buoyancy length, with respect to  $Y_f / L_b$ , vertical distance from the flare stack exit to the floor over buoyancy length. The cases  $V_j = 0.5, 1.0$  and  $2.0 \text{ m/s}$  are presented. A horizontal solid or dashed line for each case indicates the value of  $y_{centroid} / L_b$  without any floor effects.

Again, it is assumed that the vertical component of the centroid location represents the centerline of a thermal plume. Figure 7.17 shows that the plume centroid vertical position is affected by the proximity of the floor, especially for the case

$V_j = 0.5$  m/s. It appears that as the flare stack exit moves closer to the floor, the buoyant plume trajectory is deflected downwards. This effect is strongest on downwashed, less-buoyant plumes.

The fluid dynamics near the floor could be visualized theoretically by positioning a counter-rotating mirror image recirculation region “under” the floor (similar to the image plume concept employed in section 7.1.2.1), which would act to increase overall circulation observed near the flare stack. However, this image source does not adequately simulate how the real, solid stack alters the floor’s turbulent boundary layer. In reality there is a complex interaction between the vortices oriented perpendicular to the crosswind in the floor’s turbulent boundary layer and the solid flare stack. As these vortices meet the flare stack, they must bend and distort themselves around the stack’s shape, resulting in very complicated and chaotic flow structures.

Examining a plume’s entrainment of ambient air at a fixed position downstream can provide an alternate and simpler explanation. The pair of counter-rotating vortices in a bent-over buoyant plume act to entrain ambient air from the plume’s underside at an entrainment speed  $u_e = \beta U_\infty$ . The entrainment coefficient  $\beta$  can be considered to be a constant, which also means that the flux of ambient air into the plume’s underside at that position is a constant. This produces a low-pressure region below the buoyant plume, as air is rushing to that location to enter the plume’s volume. As a plume nears the floor, there becomes less air between the underside of the plume and the floor, and since the rate of air entrainment is a constant, ambient air must move faster to the underside of the plume in order to maintain the rate of flux of entrained air. This causes the pressure on the underside of the plume to drop.

Assuming the above explanation holds true for all positions downstream of the flare stack, pressure beneath the length of the plume will be lower than for a plume that is far above the floor, and since a higher, unchanged pressure still exists on the top side of the plume, the buoyant plume’s centerline trajectory will be deflected downwards.

## 7.2.2 Floor Effects on Combustion Efficiency

18 plume cross-sectional compositional maps were generated under the same experimental conditions as in section 7.2.1. Maps were generated at 7.6 cm (3 in) increments of  $Y_f$ .

Figure 7.18 displays a plot of  $(1 - \eta)$ , combustion inefficiency, with respect to  $Y_f / L_b$ , vertical distance from the flare stack exit to the floor over buoyancy length. The cases  $V_j = 0.5, 1.0$  and  $2.0$  m/s are presented. The flare stack inefficiency without any ceiling and floor effects is indicated by a horizontal solid or dashed line for each case.

This figure shows that for the cases  $V_j = 1.0$  and  $2.0$  m/s, flare stack combustion inefficiency remains relatively constant as the flare stack exit is moved closer to the floor. However, for the case  $V_j = 0.5$  m/s, flare stack combustion inefficiency decreases noticeably for lower values of  $Y_f / L_b$ .

An explanation for this can be made using the fuel stripping mechanism identified by Johnson et al. (2001b) and how it may interact with the floor. This mechanism consists of the flare stack's downstream recirculation region and the vortices shedding from the flare stack, and how they affect the flare. The coherent, shedding vortices act to open intermittent holes in the flame, allowing bursts of unburned hydrocarbons to be pulled from the flame by the downstream recirculation region. These bursts of unburned hydrocarbons are then ejected from the reacting jet, resulting in combustion inefficiency.

The floor's turbulent boundary layer may be interfering with the formation of coherent vortices shedding from the flare stack, essentially reducing the frequency of holes in the flame, and thus increasing the combustion efficiency of the flare. Combining this argument with the one presented in section 7.2.1 concerning plume rise, it may be concluded that by increasing flare downwash (or reducing a plume's buoyancy) and moving a flare stack exit closer to the floor of a wind tunnel, plume rise is deflected downwards and the flame burns more efficiently.

## 7.3 Summary and Conclusions

### 7.3.1 Ceiling Effects on Flame Length and Flame Angle

Using a digital camera (described in section 4.2.5), true color images were captured of natural gas flares issuing from the 2.74 m tall adjustable height flare stack (described in section 4.1.4.2) with the false ceiling installed at 2.74 m above the tunnel floor. Experiments were conducted under the following conditions:

- $U_{\infty} = 4.0$  m/s
- $0.5$  m/s  $\leq V_j \leq 2.0$  m/s
  - $V_j = 0.5$  m/s,  $0.15$  m  $\leq Y_c \leq 0.61$  m
  - $V_j = 1.0$  m/s,  $0.23$  m  $\leq Y_c \leq 0.76$  m
  - $V_j = 2.0$  m/s,  $0.30$  m  $\leq Y_c \leq 0.76$  m
- $d_i = 26.9$  mm (0.25-scale)

where  $Y_c$  is the vertical distance from the flare stack exit to the false ceiling (shown in Figure 7.1). Minimum  $Y_c$  values were set by impingement of the flame on the false ceiling. Images were captured at 7.6 cm (3 in) increments of  $Y_c$ .

It was determined that for the given experimental conditions, the proximity of the false ceiling had no discernible effect on the approximate flame length,  $L_f$ , or flame angle,  $\theta_f$ . However, considerable scatter was found in the data collected for the approximate flame angle; scatter was largest at distances furthest from the ceiling, which was attributed to turbulence-induced fluctuations in the flame position. As  $Y_c / L_b$  was decreased (where  $L_b$  is buoyancy length, defined by Eq. 7.1), the presence of the ceiling seemed to cause the data to converge on the approximate flame angle measured without any ceiling or floor effects. This could be attributed to the fact that the presence of the

false ceiling was causing the large-scale crosswind turbulence to break down into smaller-scale eddies that had less effect on the approximate flame angle.

### 7.3.2 Ceiling Effects on Plume Rise and Dispersion

Using a multi-point thermocouple-based system, the 2.74 m tall adjustable height flare stack, and the false ceiling (installed at 2.74 m above the wind tunnel floor), the mean cross-sectional thermal structure of a natural gas flare plume was mapped as it dispersed downstream of the flare stack. 20 plume cross-sectional thermal maps were generated under the following experimental conditions:

- $U_{\infty} = 4.0 \text{ m/s}$
- $0.5 \text{ m/s} \leq V_j \leq 2.0 \text{ m/s}$ 
  - $V_j = 0.5 \text{ m/s}, 0.31 \text{ m} \leq Y_c \leq 1.22 \text{ m}$
  - $V_j = 1.0 \text{ m/s}, 0.38 \text{ m} \leq Y_c \leq 1.22 \text{ m}$
  - $V_j = 2.0 \text{ m/s}, 0.46 \text{ m} \leq Y_c \leq 1.22 \text{ m}$
- $d_i = 26.9 \text{ mm}$  (0.25-scale)
- $X_o = 2.13 \text{ m}$

Thermal maps were generated at 7.6 cm increments of  $Y_c$ . No thermal maps were included in the study that showed a plume core (50 % temperature contour) inside the ceiling's turbulent boundary layer.

Centroids were calculated for each of the 20 plumes collected. The vertical component of the centroid location was used to represent the plume centerline. It was determined for plumes whose cores were not found in the false ceiling's turbulent boundary layer, the proximity of the ceiling to the plume had no important effects on

plume rise. However, the ceiling did have a significant impact on the local rate of plume rise.

A corrected buoyant plume rise model, based on Eq. 3.7, was developed to incorporate the effects of a ceiling. The presence of the ceiling was modeled by adding a mirror image buoyant plume opposite the real plume. Then, the buoyant mirror plume was idealized as a solid rising cylinder that induced a velocity gradient in the air that was in its path. The resulting model was solved numerically for the cases  $V_j = 0.5, 1.0,$  and  $2.0$  m/s at  $Y_c / L_b = 225, 112,$  and  $56,$  respectively. In all cases the theoretical plume rise model agreed with physical data presented in section 7.1.2 concerning the vertical component of plume centroids.

The model made use of a constant known as the displaced airflow factor,  $f_{daf}$ . Although  $f_{daf}$  varied between 0.006 and 0.008 for the cases presented, it was found that setting  $f_{daf}$  to 0.007 incurred errors of less than 1 % in the maximum attained plume rise,  $h_{b,actual}$ , for the cases  $V_j = 0.5$  and  $2.0$  m/s. Hence,  $f_{daf}$  can be considered a constant with the value 0.007 for the cases presented in this study,  $V_j = 0.5, 1.0$  and  $2.0$  m/s.

### 7.3.3 Ceiling Effects on Combustion Efficiency

Using a single-point gas sampling system, 16 plume cross-sectional compositional maps were generated under the same experimental conditions as in section 7.1.2. Maps were generated at 7.6 cm increments of  $Y_c$ . Compositional maps that showed a plume core (50 % temperature contour) inside the ceiling's turbulent boundary layer were not included in the study.

It was found that combustion inefficiency of the  $d_o = 26.9$  mm flare stack remained relatively constant as the stack exit was moved closer to the false ceiling, indicating that the proximity of the false ceiling had no significant impact on combustion inefficiency of the flare stack.



### 7.3.4 Floor Effects on Plume Rise and Dispersion

In this section, 18 plume cross-sectional compositional maps were generated using a multi-point thermocouple-based system and the 1.52 m tall adjustable height flare stack (described in section 4.1.4.2) burning natural gas. Data was collected under the following experimental conditions:

- $U_{\infty} = 4.0$  m/s
- $0.5$  m/s  $\leq V_j \leq 2.0$  m/s
  - $31$  cm  $\leq Y_f \leq 69$  cm
- $d_i = 26.9$  mm (0.25-scale), 1.52 m traversing flare stack
- $X_o = 2.13$  m

where  $Y_f$  is the vertical distance from the flare stack exit to the floor. Maps were generated at 7.6 cm (3 in) increments of  $Y_f$ .

Using the analysis technique in section 7.1.2, the vertical component of the centroid location represented the centerline of the plume. It was determined for the given experimental conditions that as the flare stack exit moved closer to the floor, the plume trajectory was deflected downwards (see Figure 7.17). The effect appeared strongest for downwashed plumes with a strong recirculation region downstream of the flare stack, such as for  $V_j = 0.5$  m/s.

The fluid dynamics near the floor can be visualized theoretically by positioning a counter-rotating mirror image recirculation region “under” the floor (similar to the image plume concept employed in section 7.1.2.1), which would act to increase overall circulation observed near the flare stack. However, this image source does not adequately simulate the complex interaction between the vortices oriented perpendicular to the crosswind in the floor’s turbulent boundary layer and the solid flare stack. As these

vortices meet the flare stack, they bend and distort themselves around the stack's shape to produce very complicated and chaotic flow structures.

Examining a plume's entrainment of ambient air at a fixed position downstream can provide an alternate and simpler explanation. The pair of counter-rotating vortices in a bent-over buoyant plume act to entrain ambient air from the plume's underside at an entrainment speed  $u_e = \beta U_\infty$ . The entrainment coefficient  $\beta$  can be considered to be a constant, which also means that the flux of ambient air into the plume's underside at that position is a constant. This produces a low-pressure region below the buoyant plume, as air is rushing to that location to enter the plume's volume. As a plume nears the floor, there becomes less air between the underside of the plume and the floor, and since the rate of air entrainment is a constant, ambient air must move faster to the underside of the plume in order to maintain the rate of flux of entrained air. This causes the pressure on the underside of the plume to drop.

Assuming the above explanation holds true for all positions downstream of the flare stack, pressure beneath the length of the plume will be lower than for a plume that is far above the floor, and since a higher, unchanged pressure still exists on the topside of the plume, the buoyant plume's centerline trajectory will be deflected downwards.

### 7.3.5 Floor Effects on Combustion Efficiency

Using a single-point gas sampling system, 18 plume cross-sectional compositional maps were generated under the same experimental conditions as in section 7.2.1. Maps were generated at 7.6 cm increments of  $Y_f$ .

As can be seen in Figure 7.18, it was found that for the cases  $V_j = 1.0$  and 2.0 m/s, combustion inefficiency of the  $d_o = 26.9$  mm flare stack remained relatively constant as the stack exit was moved closer to the floor. However, for the case  $V_j = 0.5$  m/s, flare stack combustion inefficiency was observed to decrease as  $Y_f / L_b$  was decreased.

An explanation for this can be made using the fuel stripping mechanism identified by Johnson et al. (2001b) and how it may interact with the floor. This mechanism consists of the flare stack's downstream recirculation region and the vortices shedding from the flare stack, and how they affect the flare. The coherent, shedding vortices act to open intermittent holes in the flame, allowing bursts of unburned hydrocarbons to be pulled from the flame by the downstream recirculation region. These bursts of unburned hydrocarbons are then ejected from the reacting jet, resulting in combustion inefficiency.

The floor's turbulent boundary layer may be interfering with the formation of coherent vortices shedding from the flare stack, essentially reducing the frequency of holes in the flame, and thus increasing the combustion efficiency of the flare. Combining this argument with the one presented in section 7.2.1 concerning plume rise, it may be concluded that by increasing flare downwash (or reducing a plume's buoyancy) and moving a flare stack exit closer to the floor of a wind tunnel, plume rise is deflected downwards and the flame burns more efficiently.

In closing, the data collected in this study and the theory developed in this chapter demonstrate the following:

1. Wind tunnel ceiling effects on the approximate angle and length of the flame issuing from a flare stack are insignificant.
2. Wind tunnel ceiling effects on plume rise and dispersion are insignificant. A numerical model for buoyant plume rise under a ceiling was developed and agreed with data collected.
3. Wind tunnel ceiling effects on combustion efficiency are insignificant.
4. Wind tunnel floor effects act to deflect the plume trajectory downwards and increase combustion efficiency, especially when the flare stack tip is near the floor and the plume is heavily downwashed.

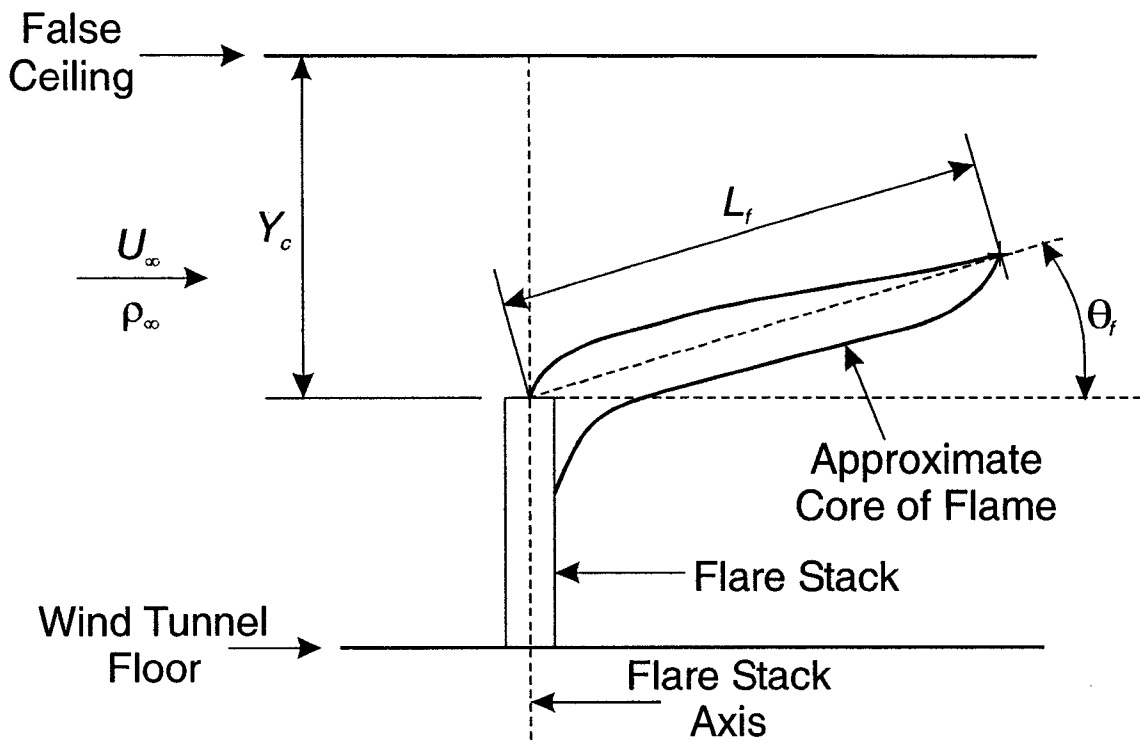


**Figure 7.1: Schematic depicting concepts of approximate flame length,  $L_f$  approximate flame angle,  $\theta_f$ , and vertical distance from the flare stack exit to the false ceiling,  $Y_c$**

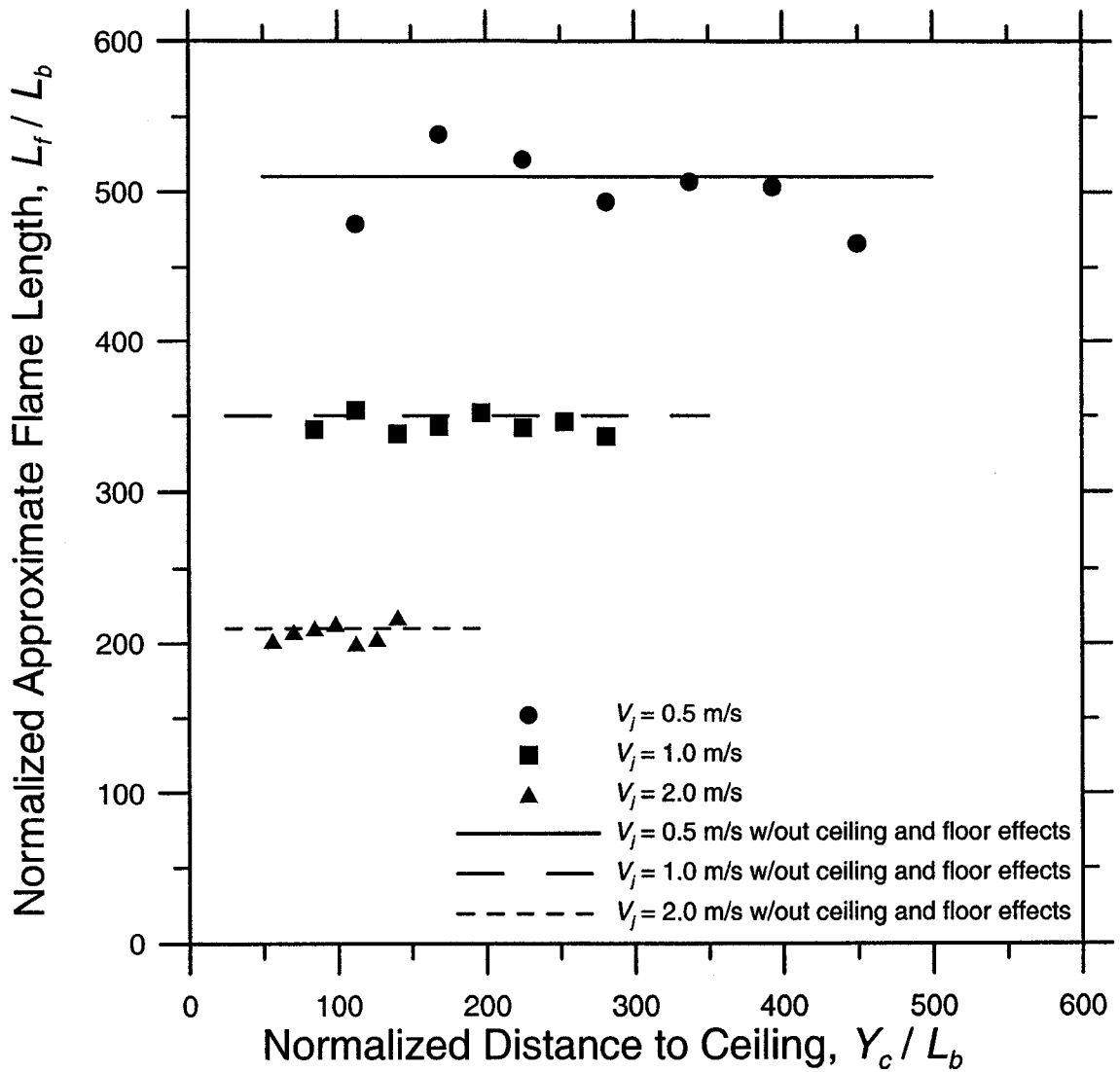


**Figure 7.2: Approximate flame length as affected by vertical distance from flare stack exit to false ceiling. Both axes divided by buoyancy length.**

**Conditions:**

$$U_\infty = 4.0 \text{ m/s}, 0.5 \text{ m/s} \leq V_j \leq 2.0 \text{ m/s}, d_i = 26.9 \text{ mm}$$

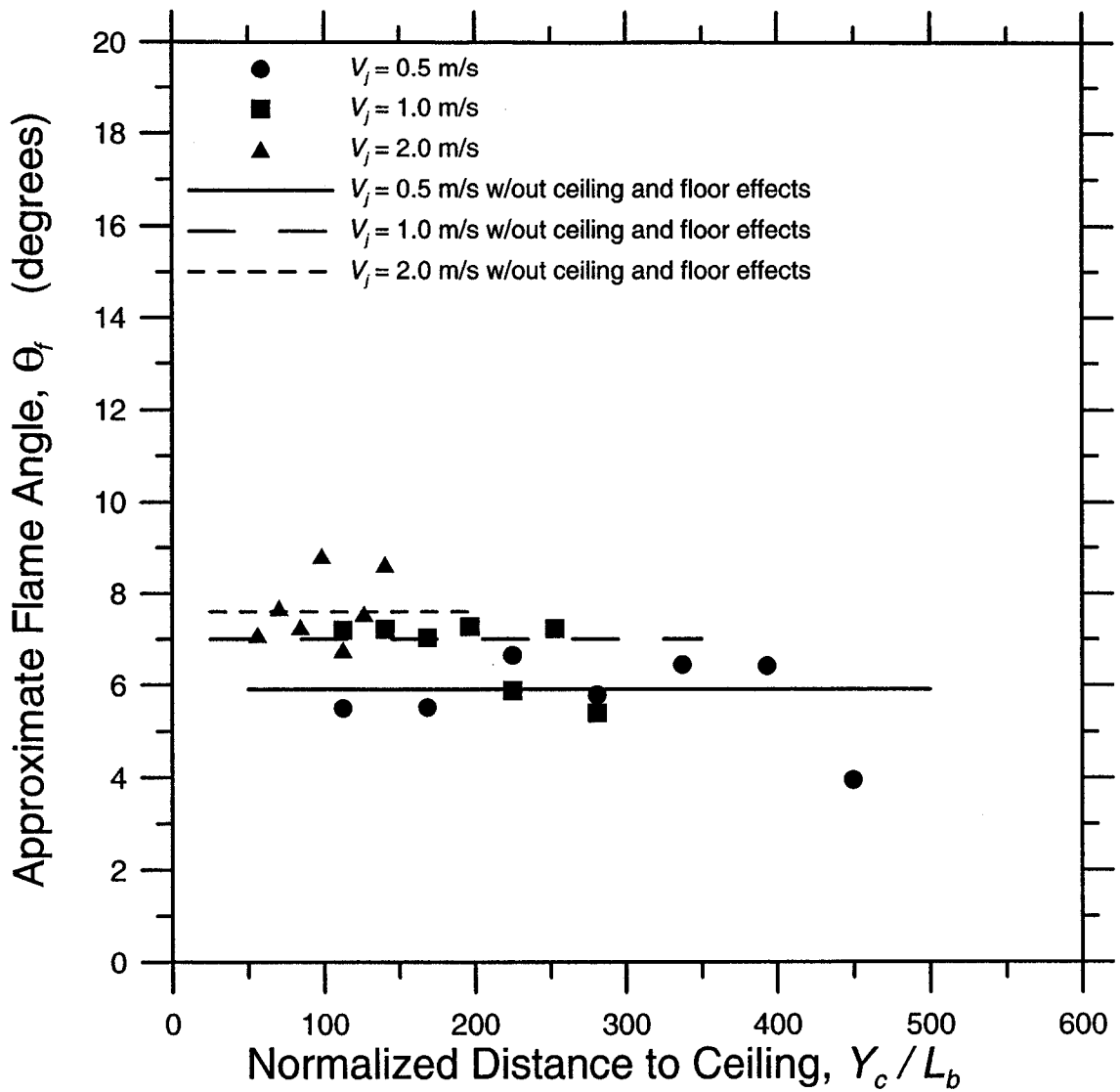
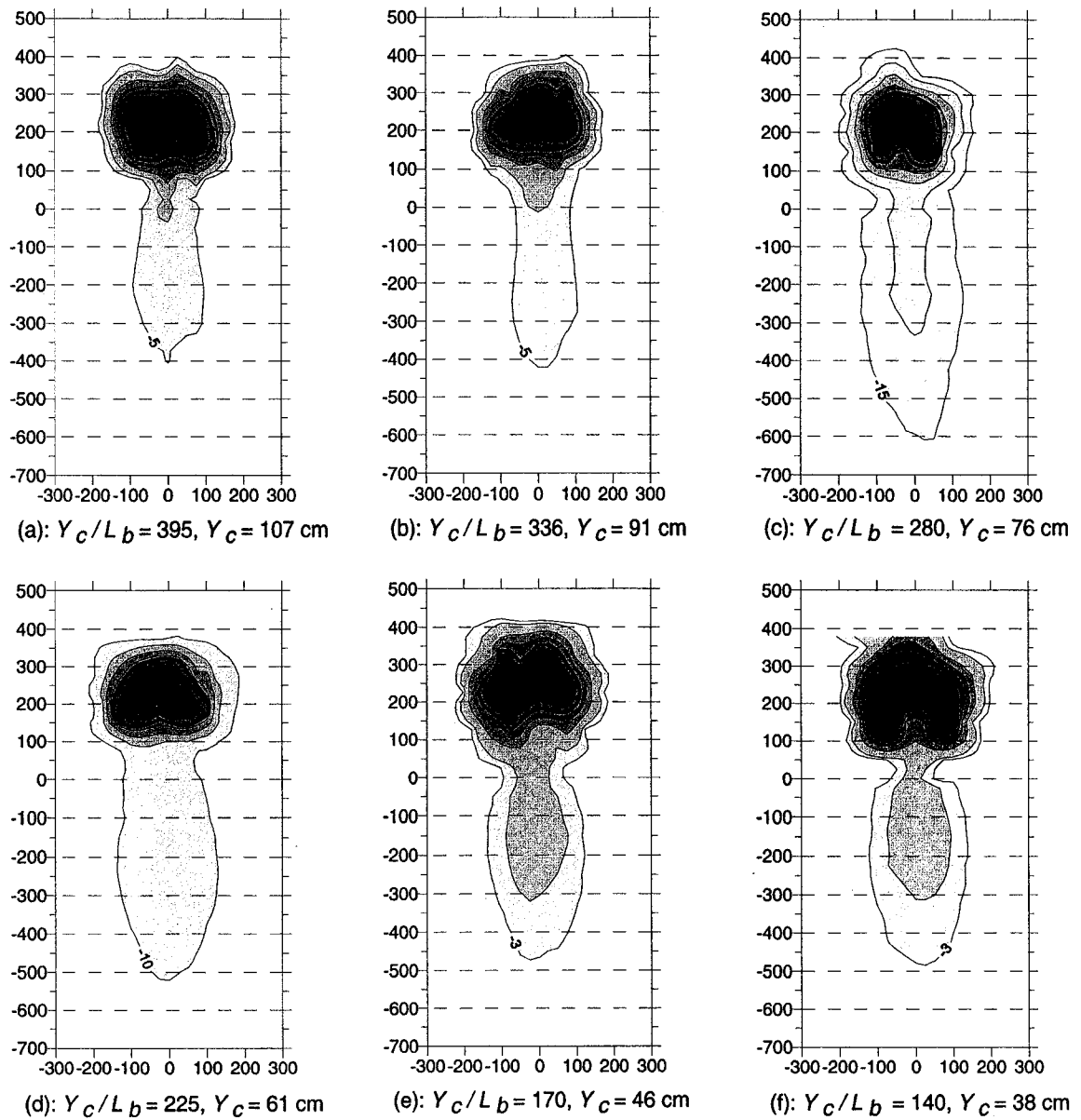


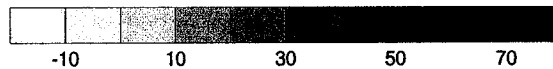
**Figure 7.3: Approximate flame angle as affected by vertical distance from flare stack exit to false ceiling over buoyancy length.**

**Conditions:**

$$U_\infty = 4.0 \text{ m/s}, 0.5 \text{ m/s} \leq V_j \leq 2.0 \text{ m/s}, d_i = 26.9 \text{ mm}$$



Temperature Scale (deg. C)



— : 50% Temperature contour

NOTE: X and Y axis in mm relative to flare stack tip

**Figure 7.4: Plume mean thermal cross-sections as flare stack exit is positioned closer to the false ceiling.**

**Conditions:**

$$U_{\infty} = 4.0 \text{ m/s}, V_j = 1.0 \text{ m/s}, d_i = 26.9 \text{ mm}, X_o = 2.13 \text{ m}$$

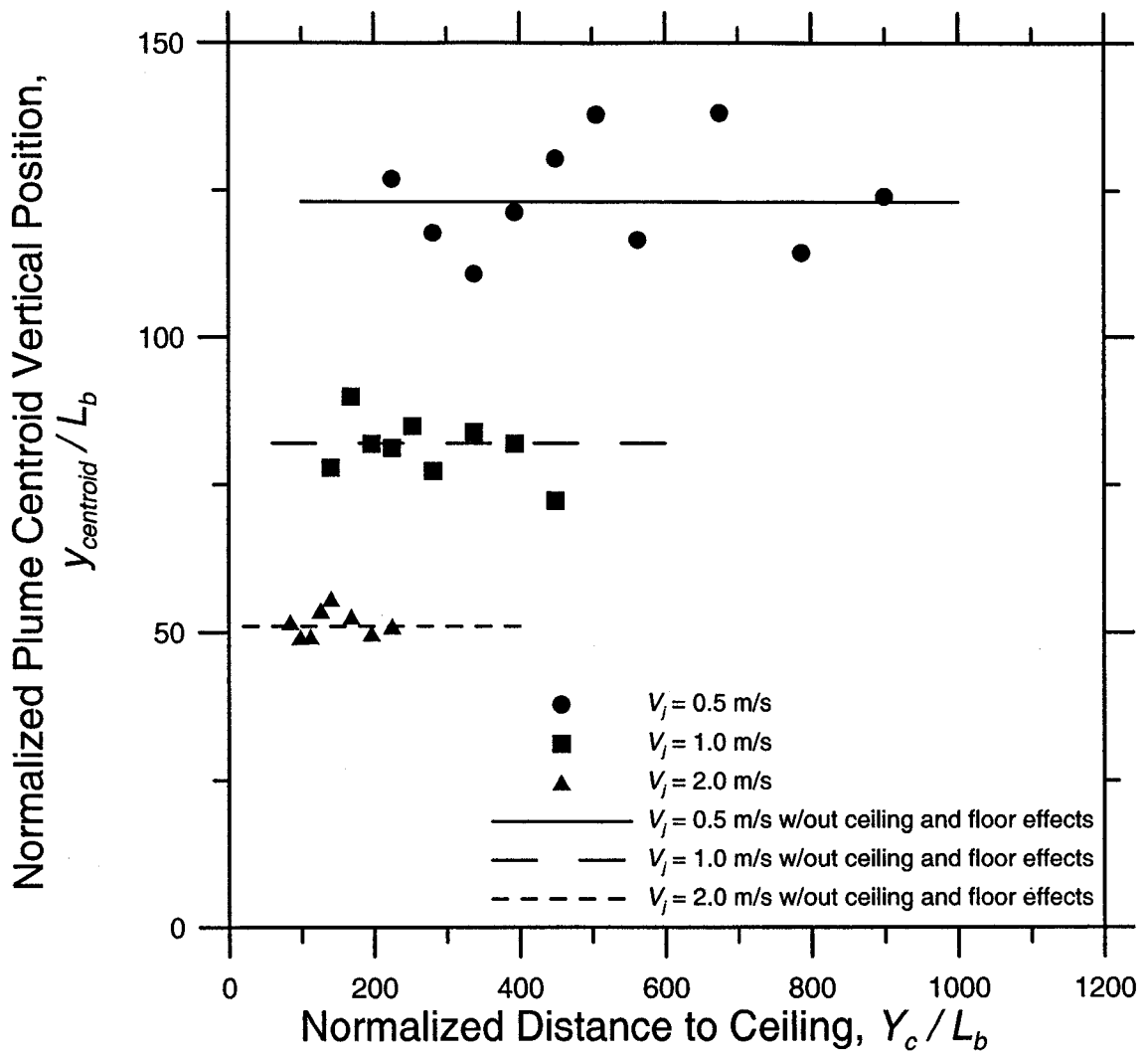


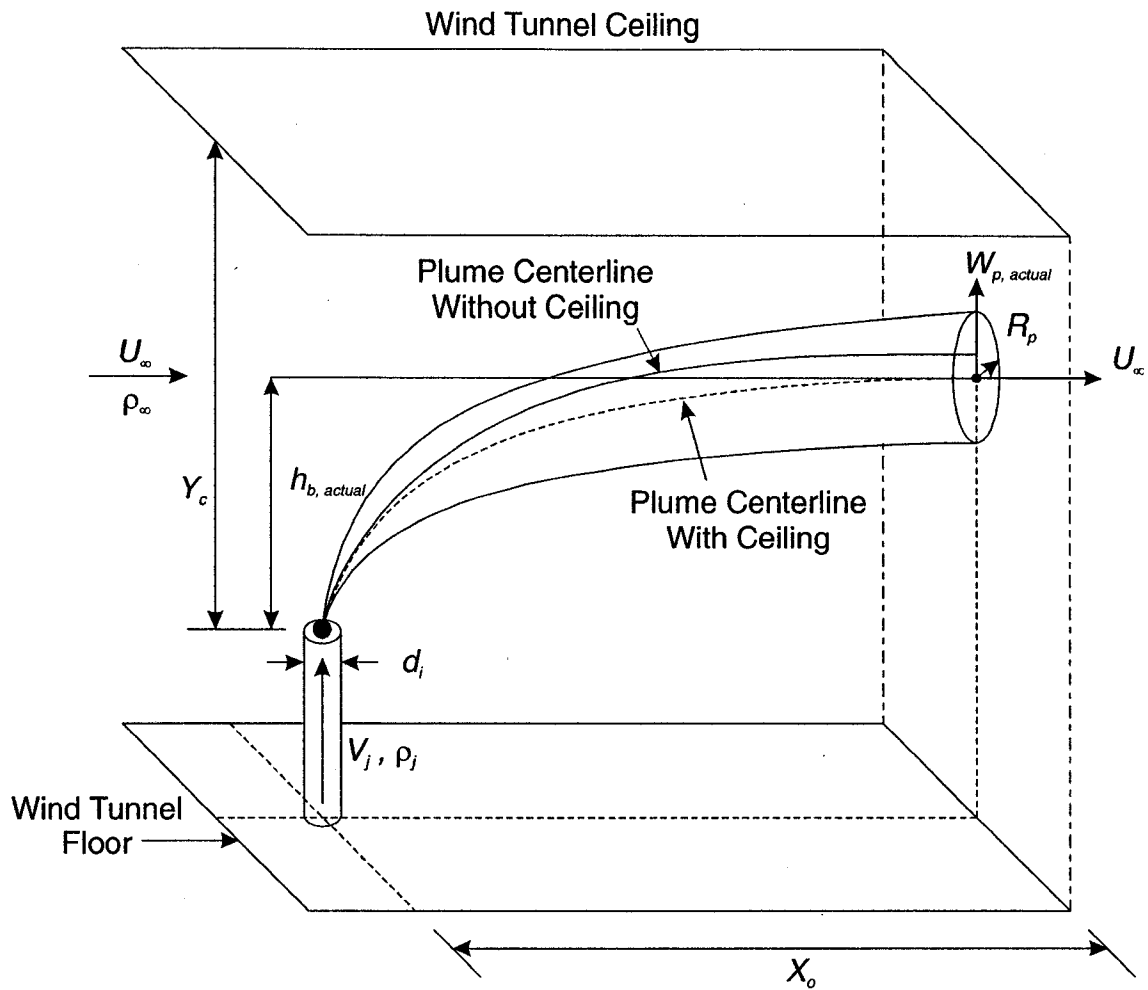
**Figure 7.5: Plume centroid vertical position as affected by vertical distance from flare stack exit to false ceiling. Both axes divided by buoyancy length.**

**Conditions:**

$$U_{\infty} = 4.0 \text{ m/s}, 0.5 \text{ m/s} \leq V_j \leq 2.0 \text{ m/s}$$

$$d_i = 26.9 \text{ mm}, X_o = 2.13 \text{ m}$$





$\rho_\infty$  = ambient air density

$\rho_j$  = fuel jet density

$d_i$  = inner stack diameter

$R_p$  = radius of plume

$Y_c$  = distance from flare stack exit to ceiling

$X_o$  = distance downstream of flare stack axis

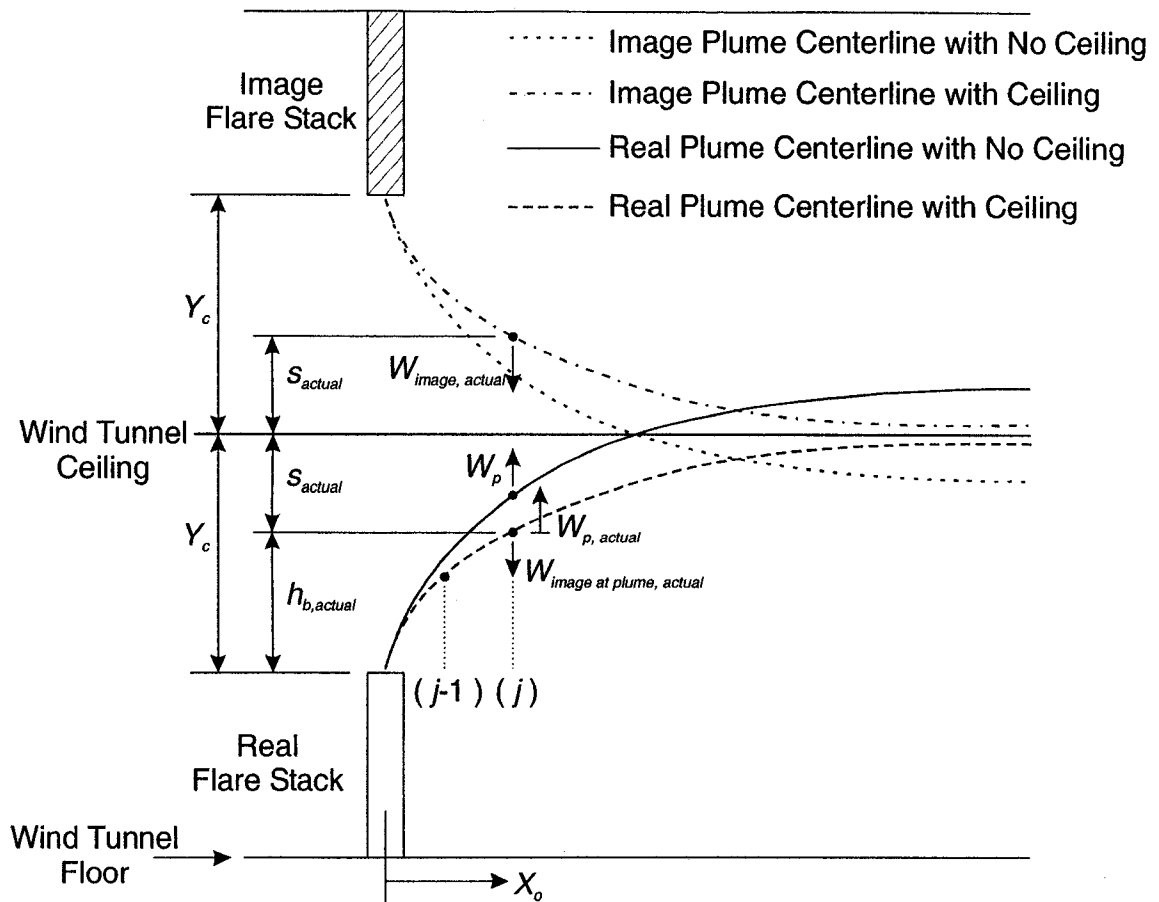
$h_{b, actual}$  = corrected plume rise

$W_{p, actual}$  = corrected upward plume speed

$V_j$  = fuel jet speed

$U_\infty$  = crosswind speed

**Figure 7.6: Corrected model for a non-reacting buoyant plume in crosswind. Presence of ceiling alters plume trajectory**



$Y_c$  = distance from flare stack exit to ceiling

$(j-1), (j)$  = steps in the numerical solution

$X_o$  = distance downstream of flare stack axis

$h_{b,actual}$  = corrected plume rise

$$s_{actual} = Y_c - h_{b,actual}$$

$W_p$  = uncorrected upward plume speed

$W_{p,actual}$  = corrected upward plume speed

$W_{image,actual}$  = corrected upward image plume speed

$W_{image at plume,actual}$  = corrected upward image plume speed seen by real plume

**Figure 7.7: Corrected and uncorrected real and image plume centerline trajectories**

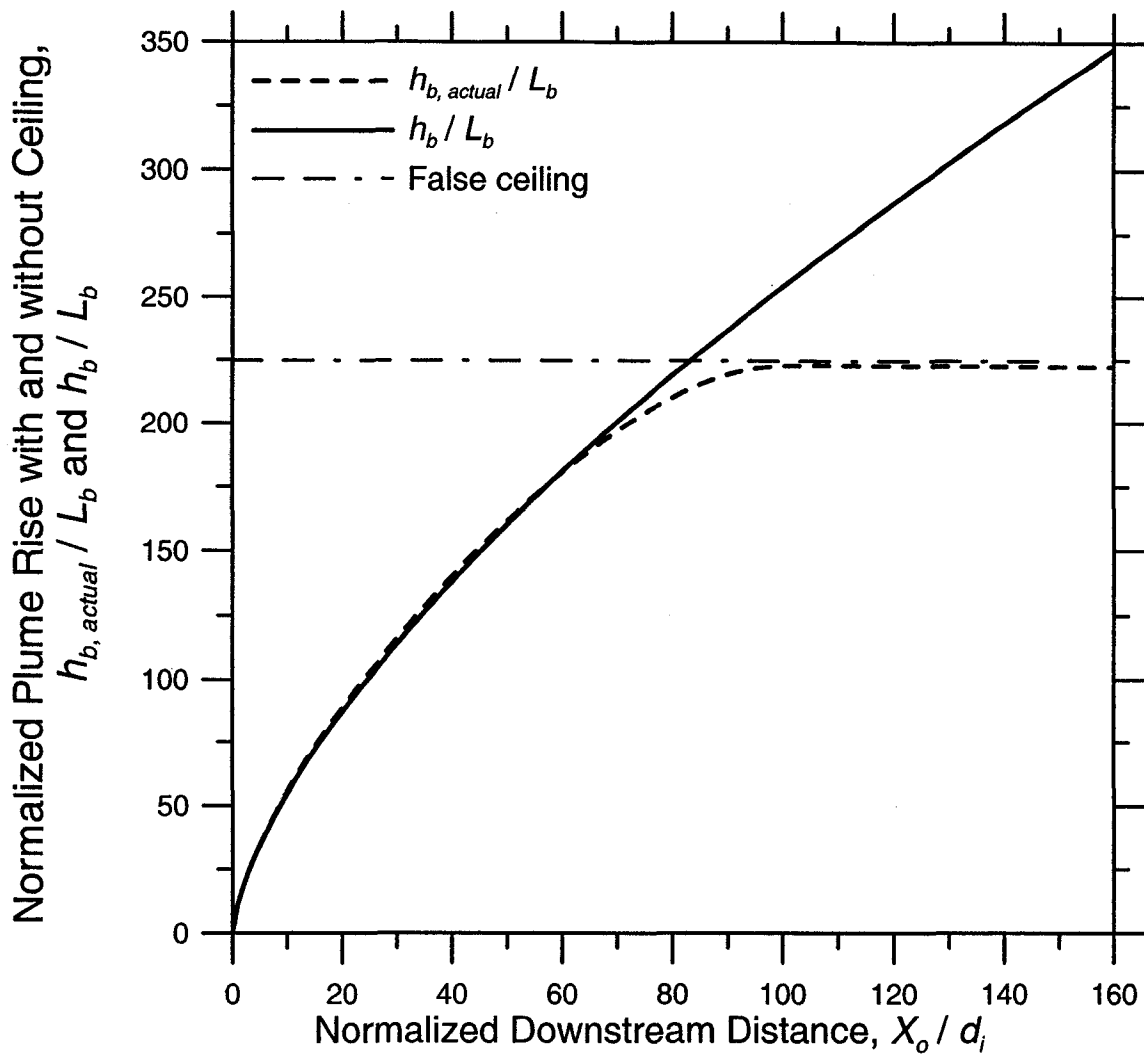


**Figure 7.8: Numerical models for corrected and uncorrected plume rises over buoyancy length varying with downstream distance over flare stack inner diameter.  $h_{b, actual}$  predicts slightly higher plume rise than  $h_b$  prior to meeting false ceiling because of physics associated with mirror image buoyancy source.**

**Conditions:**

$$U_{\infty} = 4.0 \text{ m/s}, V_j = 0.5 \text{ m/s}$$

$$d_i = 26.9 \text{ mm}$$

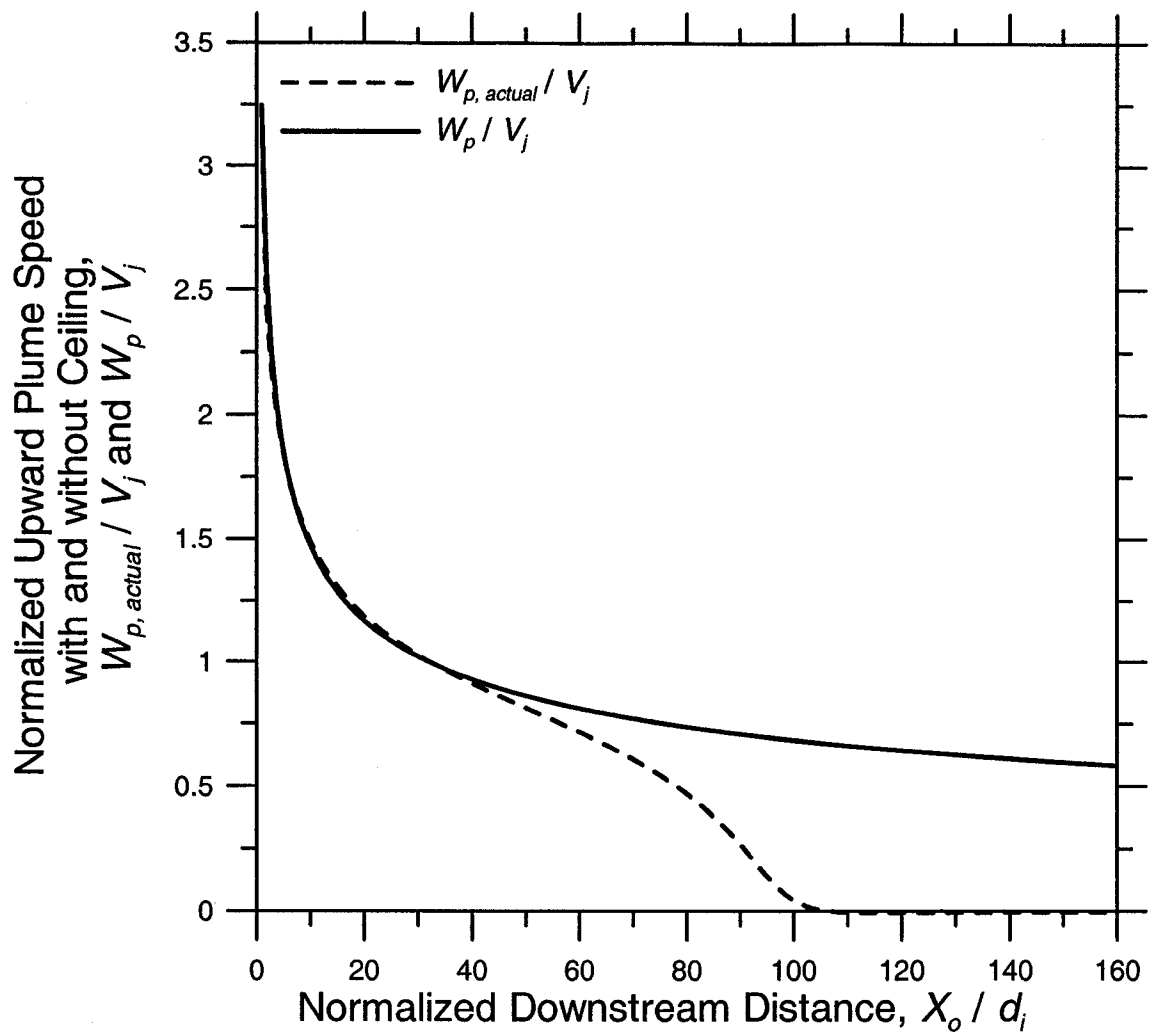


**Figure 7.9: Numerical models for corrected and uncorrected upward plume speeds over fuel jet speed varying with downstream distance over flare stack inner diameter.**

**Conditions:**

$$U_{\infty} = 4.0 \text{ m/s}, V_j = 0.5 \text{ m/s}$$

$$d_i = 26.9 \text{ mm}$$

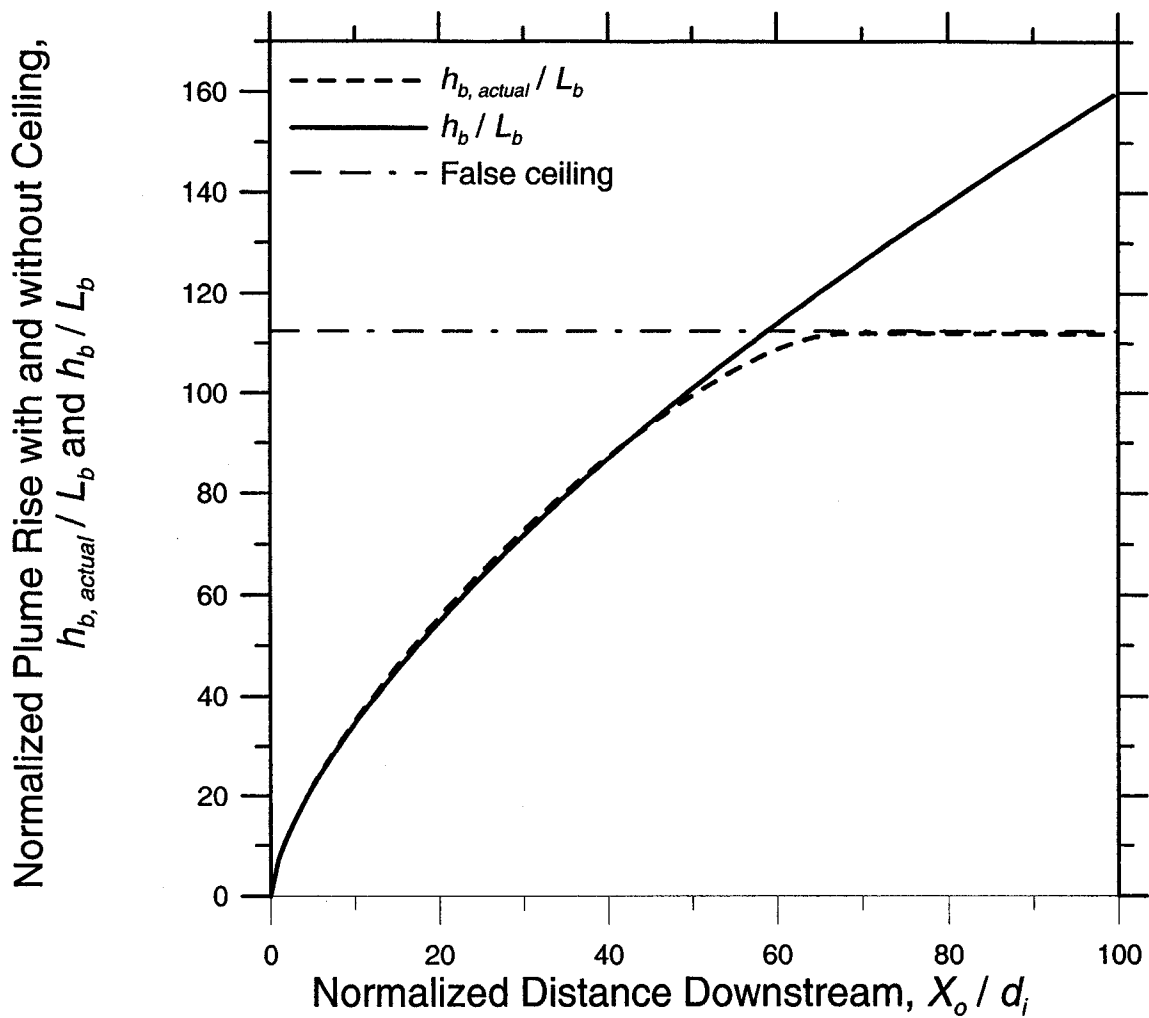


**Figure 7.10: Numerical models for corrected and uncorrected plume rises over buoyancy length varying with downstream distance over flare stack inner diameter.  $h_{b, actual}$  predicts slightly higher plume rise than  $h_b$  prior to meeting false ceiling because of physics associated with mirror image buoyancy source.**

**Conditions:**

$$U_{\infty} = 4.0 \text{ m/s}, V_j = 1.0 \text{ m/s}$$

$$d_i = 26.9 \text{ mm}$$

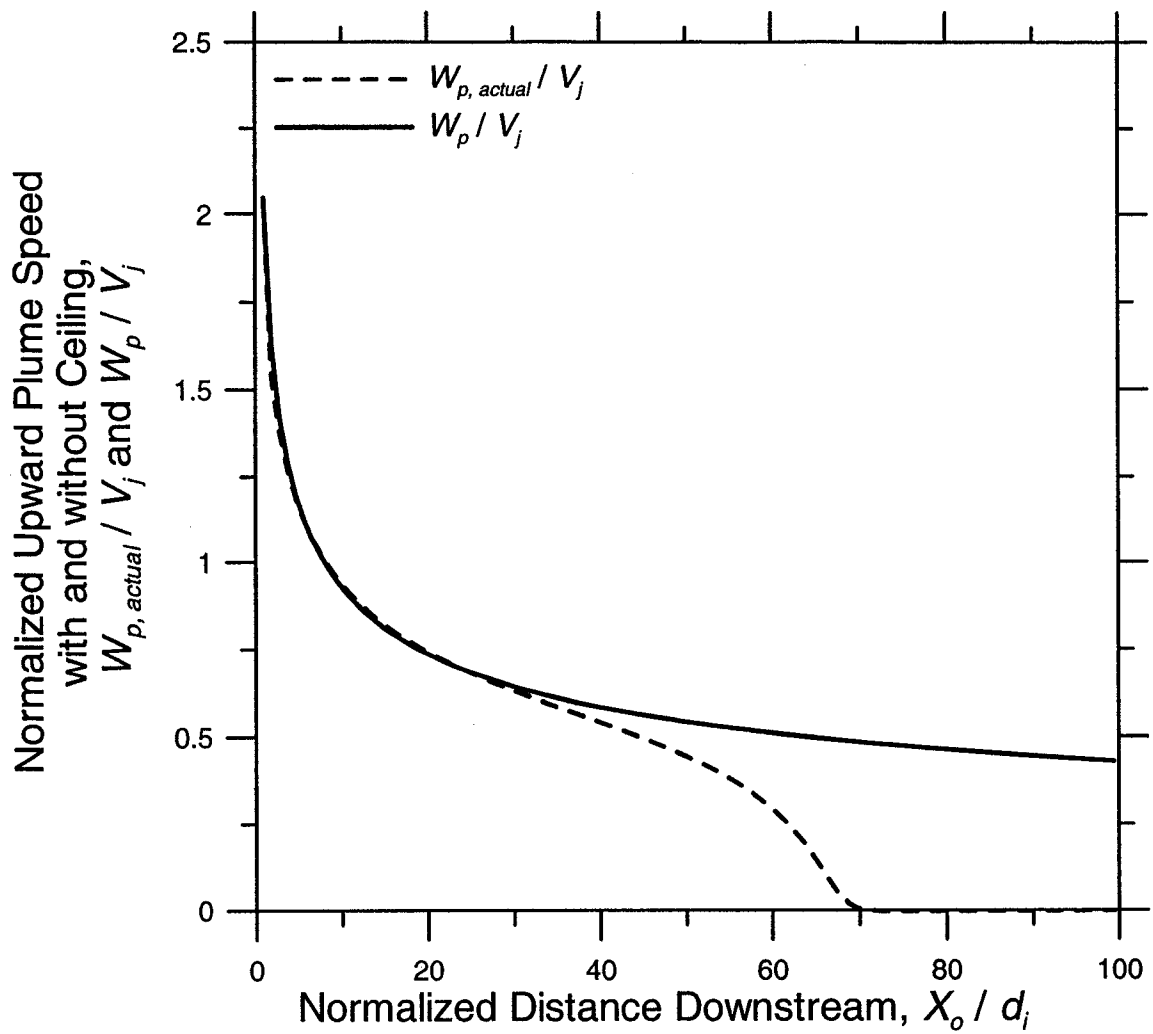


**Figure 7.11: Numerical models for corrected and uncorrected upward plume speeds over fuel jet speed varying with downstream distance over flare stack inner diameter.**

**Conditions:**

$$U_{\infty} = 4.0 \text{ m/s}, V_j = 1.0 \text{ m/s}$$

$$d_i = 26.9 \text{ mm}$$

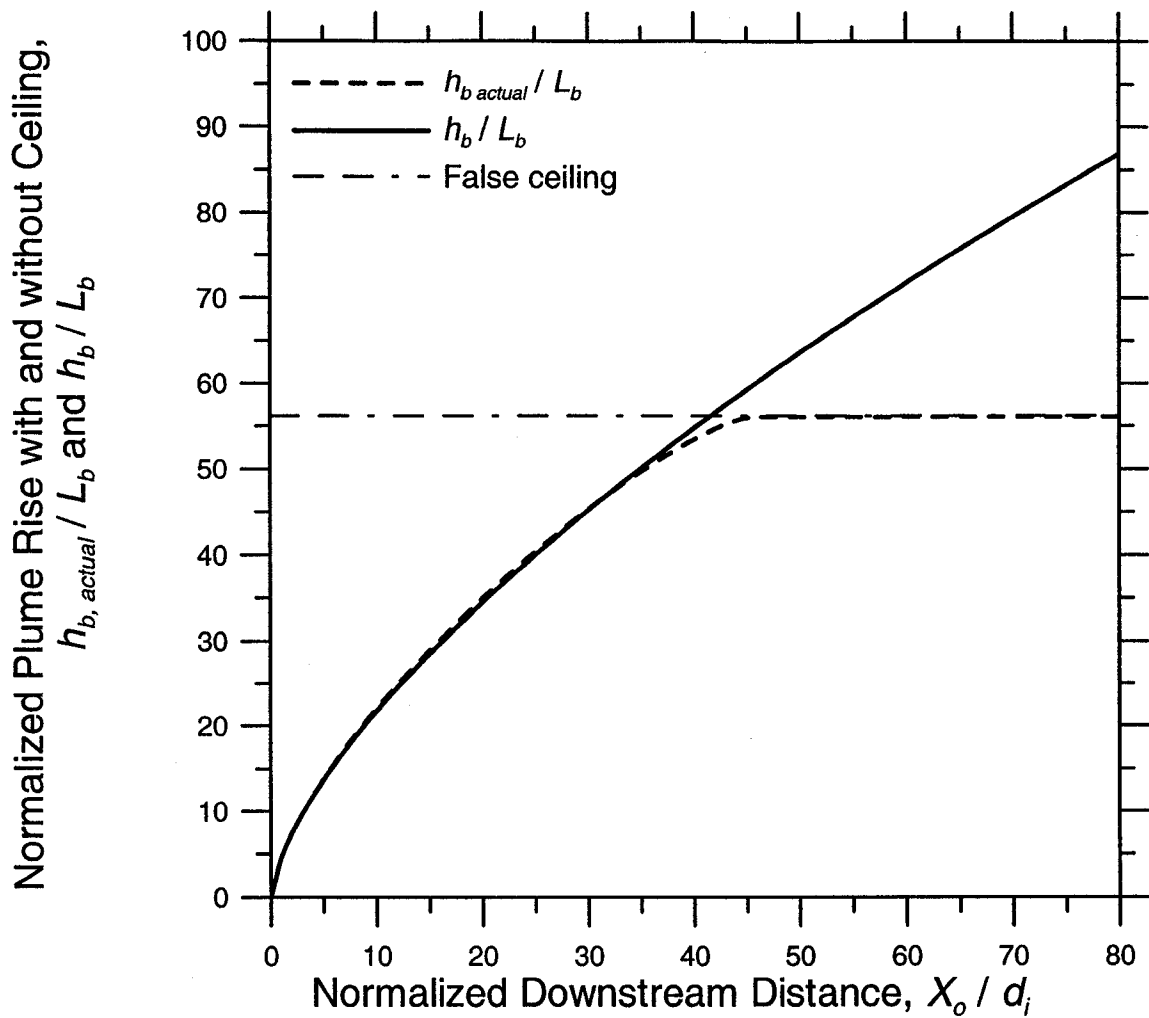


**Figure 7.12: Numerical models for corrected and uncorrected plume rises over buoyancy length varying with downstream distance over flare stack inner diameter.  $h_{b, actual}$  predicts slightly higher plume rise than  $h_b$  prior to meeting false ceiling because of physics associated with mirror image buoyancy source.**

**Conditions:**

$$U_{\infty} = 4.0 \text{ m/s}, V_j = 2.0 \text{ m/s}$$

$$d_i = 26.9 \text{ mm}$$

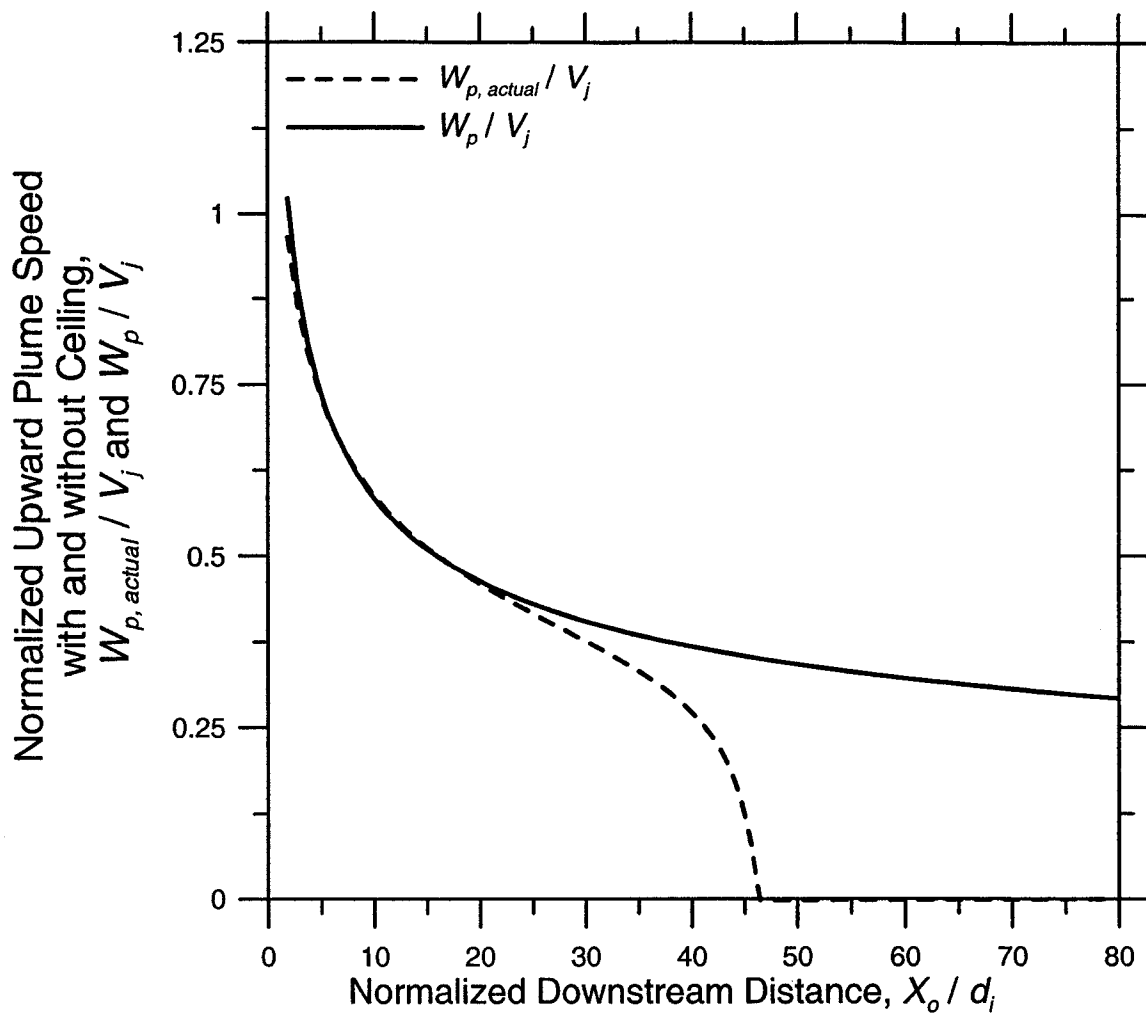


**Figure 7.13: Numerical models for corrected and uncorrected upward plume speeds over fuel jet speed varying with downstream distance over flare stack inner diameter.**

**Conditions:**

$$U_{\infty} = 4.0 \text{ m/s}, V_j = 2.0 \text{ m/s}$$

$$d_i = 26.9 \text{ mm}$$



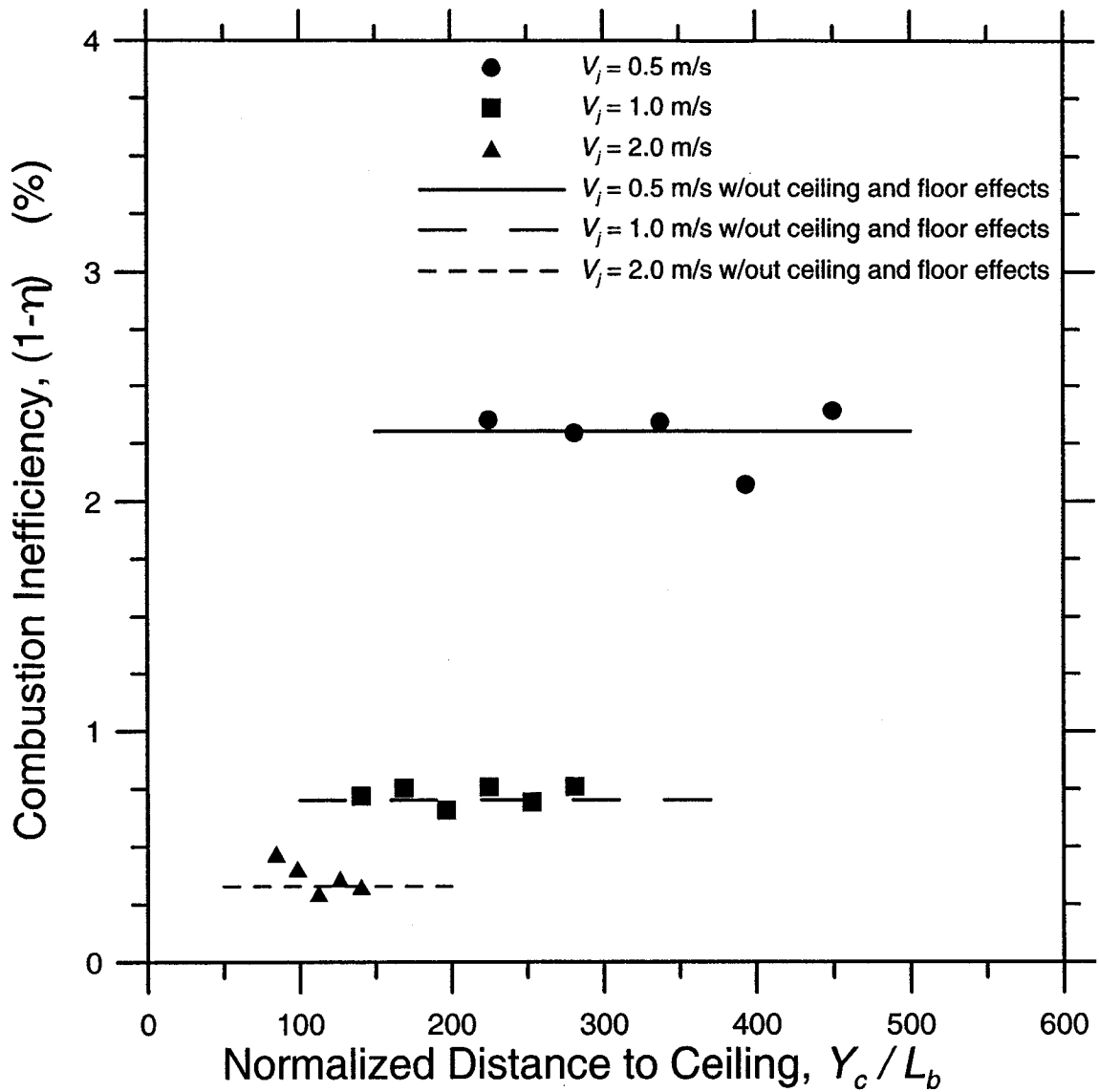


**Figure 7.14: Combustion inefficiency as affected by vertical distance from flare stack exit to false ceiling over buoyancy length.**

**Conditions:**

$$U_{\infty} = 4.0 \text{ m/s}, 0.5 \text{ m/s} \leq V_j \leq 2.0 \text{ m/s}$$

$$d_i = 26.9 \text{ mm}, X_o = 2.13 \text{ m}$$

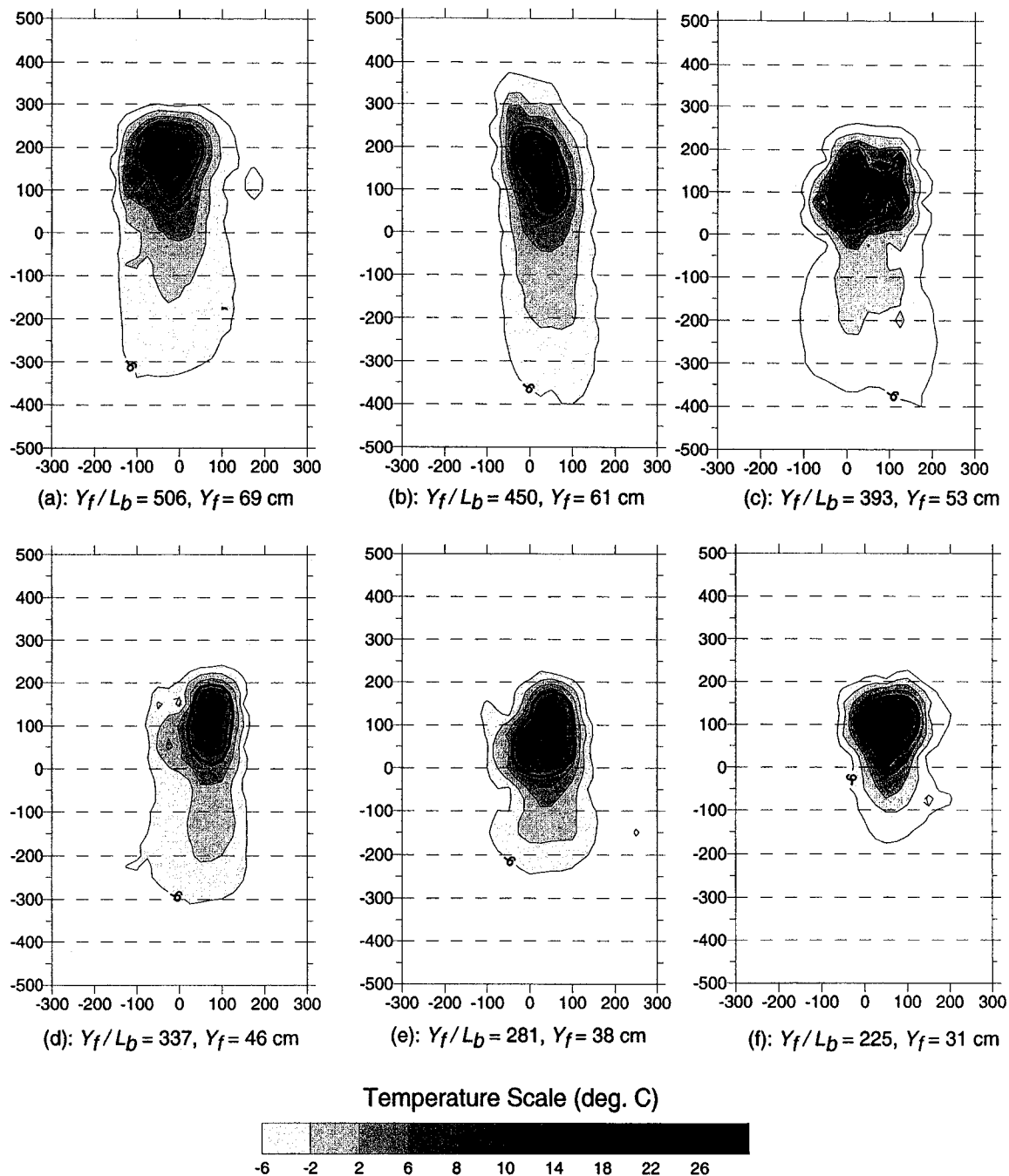


**Figure 7.15: Plume mean thermal cross-sections as flare stack exit is positioned closer to the floor.**

**Conditions:**

$$U_\infty = 4.0 \text{ m/s}, V_j = 0.5 \text{ m/s}, d_i = 26.9 \text{ mm}, X_o = 2.13 \text{ m}$$

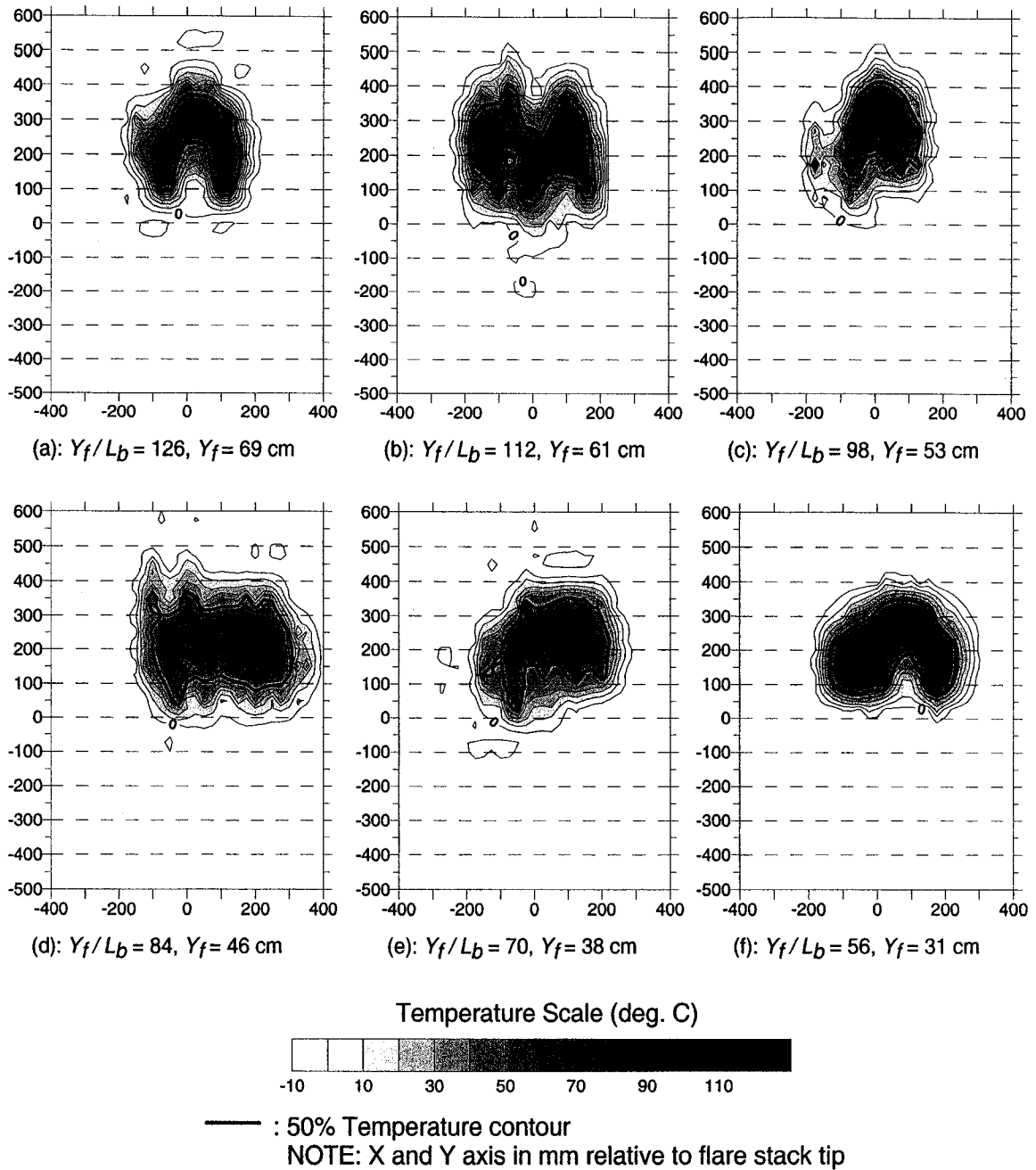


**Figure 7.16: Plume mean thermal cross-sections as flare stack exit is positioned closer to the floor.**

**Conditions:**

$$U_\infty = 4.0 \text{ m/s}, V_j = 2.0 \text{ m/s}, d_i = 26.9 \text{ mm}, X_o = 2.13 \text{ m}$$

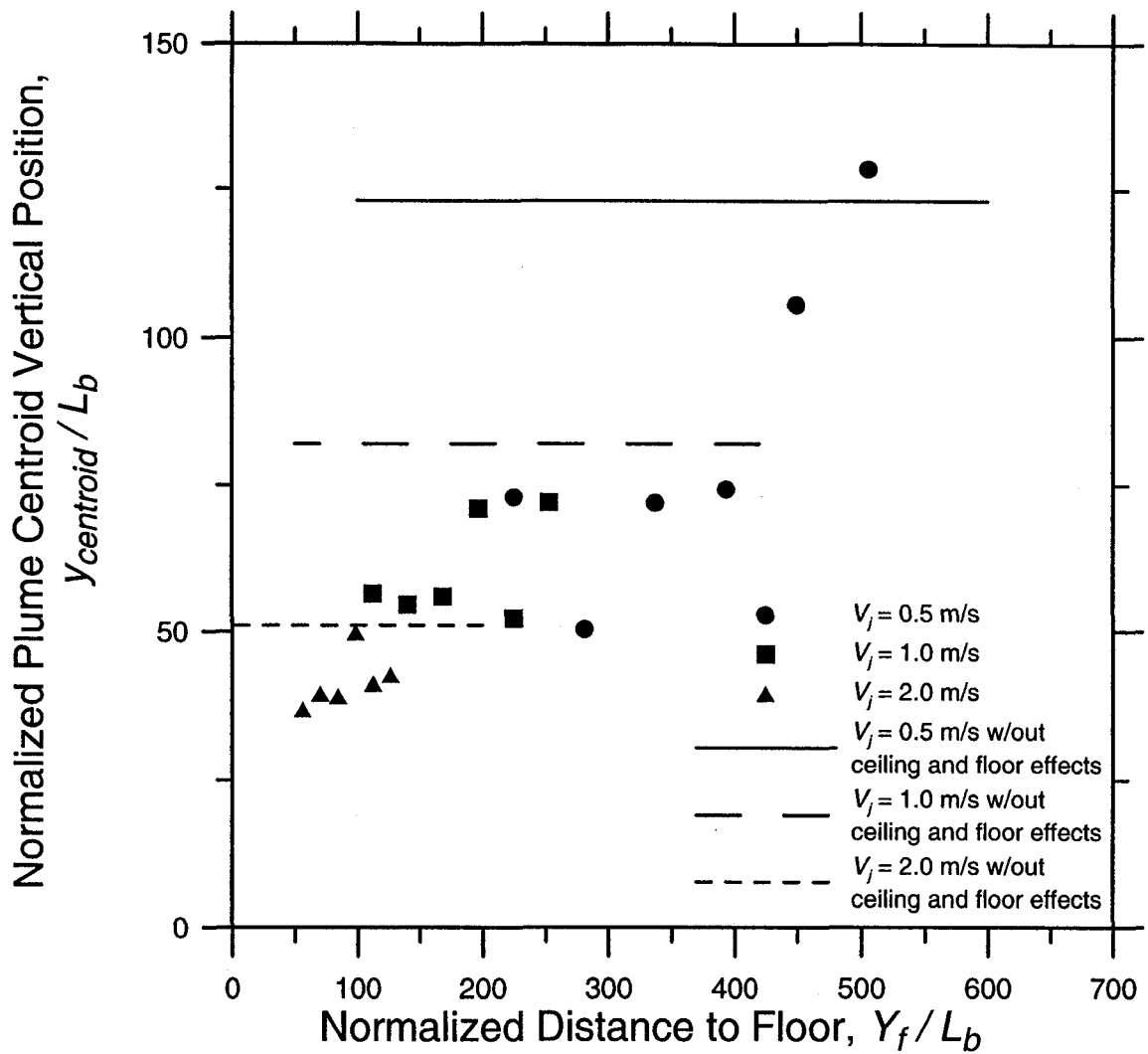


**Figure 7.17: Plume centroid vertical position as affected by vertical distance from flare stack exit to wind tunnel floor. Both axes divided by buoyancy length.**

**Conditions:**

$$U_{\infty} = 4.0 \text{ m/s}, 0.5 \text{ m/s} \leq V_j \leq 2.0 \text{ m/s}$$

$$d_i = 26.9 \text{ mm}, X_o = 2.13 \text{ m}$$

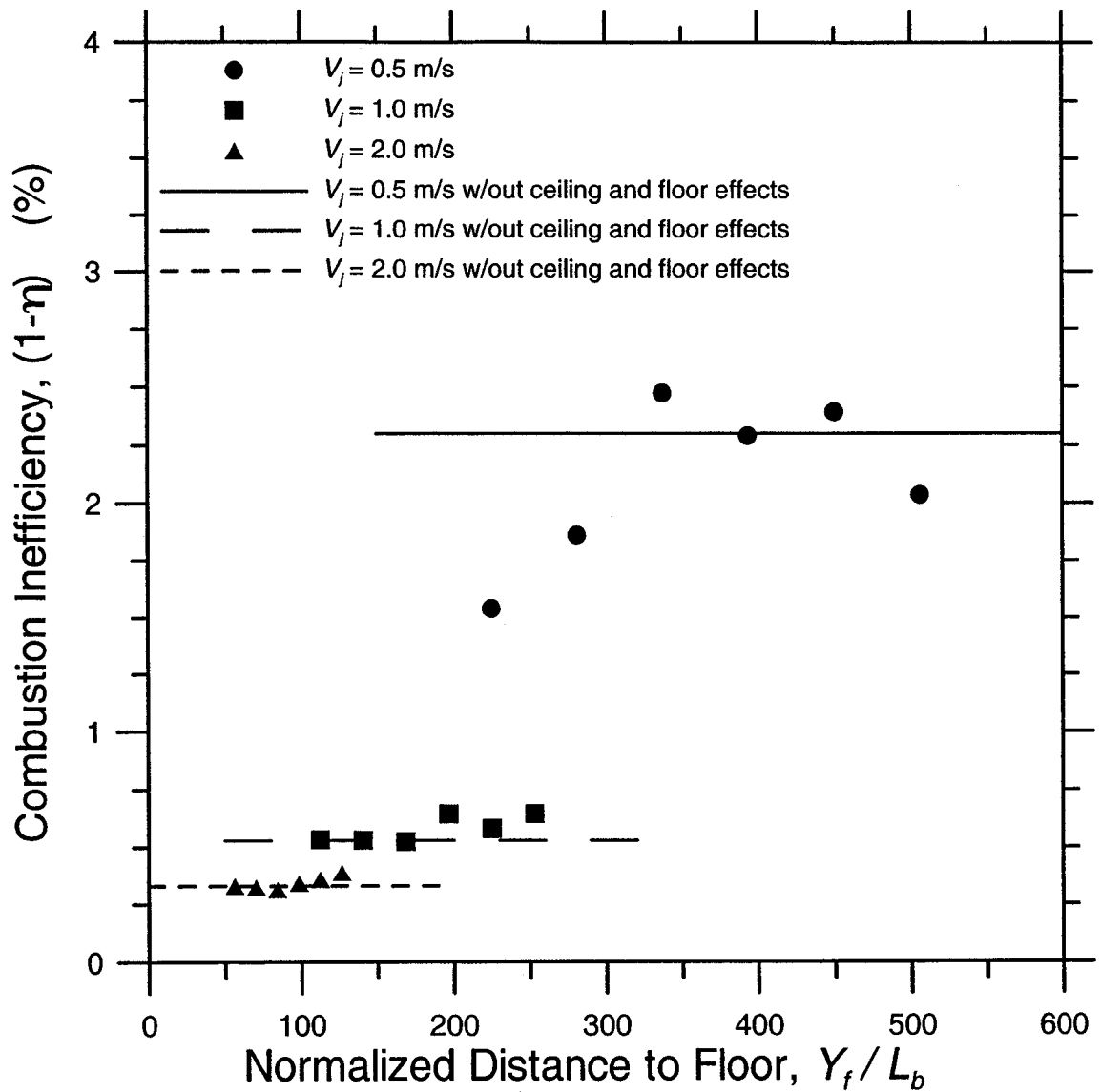


**Figure 7.18: Combustion inefficiency as affected by vertical distance from flare stack exit to wind tunnel floor over buoyancy length.**

**Conditions:**

$$U_\infty = 4.0 \text{ m/s}, 0.5 \text{ m/s} \leq V_j \leq 2.0 \text{ m/s}$$

$$d_i = 26.9 \text{ mm}, X_o = 2.13 \text{ m}$$

## Chapter 8

### SUMMARY AND CONCLUSIONS

#### 8.1 Summary

##### 8.1.1 Thermal Structure and Trajectory of Flare Plumes

The mean cross-sectional thermal structure of a flare stack plume was investigated experimentally using an open-loop, low-speed, single-pass wind tunnel. A multi-point thermocouple-based system was used to map the two-dimensional mean cross-sectional thermal structure of a natural gas flare plume as it dispersed downwind of 0.25- to full-scale flare stacks. These experimental results were compared against a previous plume dispersion model developed for 0.15- to 0.33-scale flare stacks.

The present study was conducted under the following experimental conditions:  $2.0 \text{ m/s} \leq U_{\infty} \leq 8.0 \text{ m/s}$ ,  $0.5 \text{ m/s} \leq V_j \leq 2.0 \text{ m/s}$ ,  $26.9 \text{ mm} \leq d_i \leq 102.3 \text{ mm}$  (0.25- to full-scale),  $0.50 \text{ m} \leq X_o \leq 8.30 \text{ m}$ .

A buoyant plume rise model was used to scale the characteristic dimension of the flare plume,  $d_p^*$ , against the physical parameters crosswind speed ( $U_{\infty}$ ), fuel jet speed ( $V_j$ ), distance downwind from the flare stack axis ( $X_o$ ), and the flare stack inner diameter ( $d_i$ ).  $d_p^*$  was physically defined as the diameter of an ideal circular plume cross-section with area equal to the area contained within the 50 % temperature contour of a plume's mean cross-sectional structure.

The correlation was defined as

$$d_p^* = Ag^{1/3} \frac{V_j^{1/3}}{U_{\infty}} X_o^{2/3} d_i^{2/3} \quad (8.1)$$

The present study found that  $A = 2.34$ . This result was compared with past research conducted by Poudenx (2000). A curve fit to Poudenx's data resulted in  $A = 2.22$ . The coefficient  $A$  in the present study varied by 0.12 (5 %) with the past study by Poudenx.

### 8.1.2 Compositional Structure of Flare Plumes

The mean cross-sectional compositional structure of a flare stack plume was investigated experimentally using an open-loop, low-speed, single-pass wind tunnel. A single-point gas sampling system was used to map the two-dimensional mean cross-sectional compositional structure of a natural gas flare plume as it dispersed downwind of 0.25- to full-scale flare stacks. These experimental results were used to calculate combustion efficiency of the flare, and these calculations were compared against combustion efficiency correlations established for 0.11- to 0.44-scale flare stacks.

The present study was conducted under the following experimental conditions:  $LHV_{mass} = 47.5$  MJ/kg,  $4.0$  m/s  $\leq U_{\infty} \leq 14.0$  m/s,  $0.5$  m/s  $\leq V_j \leq 2.0$  m/s,  $30.0$  mm  $\leq d_o \leq 114.3$  mm (0.25- to full-scale).

A correlation was developed that scaled combustion inefficiency ( $1 - \eta$ ) against the physical parameters crosswind speed ( $U_{\infty}$ ), fuel jet speed ( $V_j$ ), flare stack outer diameter ( $d_o$ ), and lower heating value of the fuel by mass ( $LHV_{mass}$ ). The correlation was made dimensionless using the lower heating value by mass of pure methane ( $LHV_{mass,CH_4}$ ).

The dimensionless correlation was defined as

$$(1 - \eta) \left( \frac{LHV_{mass}}{LHV_{mass,CH_4}} \right)^3 = 5.73 \times 10^{-4} \exp \left( 0.330 \frac{U_{\infty}}{(gV_j)^{1/3} d_o^{1/3}} \right) \quad (8.2)$$

This curve fit was compared with research conducted by Johnson and Kostiuk (2002). His dimensionless curve fit was defined as

$$(1 - \eta) \left( \frac{LHV_{mass}}{LHV_{mass, CH_4}} \right)^3 = 1.25 \times 10^{-3} \exp \left( 0.317 \frac{U_\infty}{(gV_j)^{1/3} d_o^{1/3}} \right) \quad (8.3)$$

Johnson and Kostiuk (2002) observed that if the exponent for  $d_o$  was adjusted to 1/2 the natural gas based data collapsed slightly better. His empirical curve fit with  $d_o^{1/2}$  dependence was defined as

$$(1 - \eta) \left( \frac{LHV_{mass}}{LHV_{mass, CH_4}} \right)^3 = 1.17 \times 10^{-3} \exp \left( 0.175 \frac{U_\infty}{(gV_j)^{1/3} d_o^{1/2}} \right) \quad (8.4)$$

The right side of Eq. 8.4 has the units  $m^{-1/6}$ . An empirical curve fit was made to the present data with  $d_o^{1/2}$  dependence to allow for direct comparison to Johnson and Kostiuk (2002). It was defined as

$$(1 - \eta) \left( \frac{LHV_{mass}}{LHV_{mass, CH_4}} \right)^3 = 5.38 \times 10^{-4} \exp \left( 0.210 \frac{U_\infty}{(gV_j)^{1/3} d_o^{1/2}} \right) \quad (8.5)$$

### 8.1.3 Ceiling and Floor Effects On the Flare, Plume Rise and Combustion Efficiency

A wind tunnel's floor and ceiling effects on the physical dimensions of a flare, as well as on the mean cross-sectional thermal and compositional structure of its plume, were investigated using a 0.25-scale adjustable height flare stack burning natural gas in an open-loop, low-speed, single-pass wind tunnel.

The 0.25-scale flare stack's height was adjusted incrementally to bring the stack tip closer to the ceiling or floor; at each increment, mean cross-sectional compositional and thermal maps were generated. Results were compared to determine possible ceiling and floor effects on plume trajectory and dispersion and flare combustion efficiency. True color images of the flame were captured to investigate ceiling effects on the flame's physical structure. Experimental results for plume trajectory were compared against a plume rise model that incorporated the effect of a wind tunnel ceiling.



### 8.1.3.1 Ceiling Effects on Flame Length and Flame Angle

Using a digital still camera, true color images were captured of natural gas flares issuing from the adjustable height flare stack with the false ceiling installed at 2.74 m above the tunnel floor. Experiments were conducted under the following conditions:

- $U_{\infty} = 4.0$  m/s
- $0.5$  m/s  $\leq V_j \leq 2.0$  m/s
  - $V_j = 0.5$  m/s,  $0.15$  m  $\leq Y_c \leq 0.61$  m
  - $V_j = 1.0$  m/s,  $0.23$  m  $\leq Y_c \leq 0.76$  m
  - $V_j = 2.0$  m/s,  $0.30$  m  $\leq Y_c \leq 0.76$  m
- $d_i = 26.9$  mm (0.25-scale)

where  $Y_c$  is the vertical distance from the flare stack exit to the false ceiling.

Images were captured at 7.6 cm (3 in) increments of  $Y_c$ .

### 8.1.3.2 Ceiling Effects on Plume Rise and Dispersion

A multi-point thermocouple-based system was used to map the two-dimensional mean cross-sectional thermal structure of a natural gas flare plume as it dispersed downstream from the adjustable height flare stack with the false ceiling installed at 2.74 m above the tunnel floor. Experiments were conducted under the following conditions:

- $U_{\infty} = 4.0$  m/s
- $0.5$  m/s  $\leq V_j \leq 2.0$  m/s
  - $V_j = 0.5$  m/s,  $0.31$  m  $\leq Y_c \leq 1.22$  m
  - $V_j = 1.0$  m/s,  $0.38$  m  $\leq Y_c \leq 1.22$  m

- $V_j = 2.0 \text{ m/s}, 0.46 \text{ m} \leq Y_c \leq 1.22 \text{ m}$
- $d_i = 26.9 \text{ mm (0.25-scale)}$
- $X_o = 2.13 \text{ m}$

Thermal maps were generated at 7.6 cm increments of  $Y_c$ .

Centroids were calculated for each of the 20 plumes collected, and the vertical component of each of the centroid locations was used to represent the plume centerline.

#### 8.1.3.3 Ceiling Effects on Combustion Efficiency

A single-point gas sampling system was used to map the two-dimensional mean cross-sectional compositional structure of a natural gas flare plume as it dispersed downstream from the adjustable height flare stack with the false ceiling installed at 2.74 m above the tunnel floor. Experiments were conducted under the same conditions as in section 8.3.2. Maps were generated at 7.6 cm increments of  $Y_c$ .

#### 8.1.3.4 Floor Effects on Plume Rise and Dispersion

A multi-point thermocouple-based system was used to map the two-dimensional mean cross-sectional thermal structure of a natural gas flare plume as it dispersed downstream from the adjustable height flare stack. Experiments were conducted under the following conditions:

- $U_\infty = 4.0 \text{ m/s}$
- $0.5 \text{ m/s} \leq V_j \leq 2.0 \text{ m/s}$ 
  - $31 \text{ cm} \leq Y_f \leq 69 \text{ cm}$
- $d_i = 26.9 \text{ mm (0.25-scale), 1.52 m traversing flare stack}$
- $X_o = 2.13 \text{ m}$

where  $Y_f$  is the vertical distance from the flare stack exit to the floor. Maps were generated at 7.6 cm (3 in) increments of  $Y_f$ .

Using the centroid analysis technique in section 8.3.2, the vertical component of the centroid location represented the centerline of the plume.

#### 8.1.3.5 Floor Effects on Combustion Efficiency

A single-point gas sampling system was used to map the two-dimensional mean cross-sectional compositional structure of a natural gas flare plume as it dispersed downstream from the adjustable height flare stack. Experiments were conducted under the same conditions as in section 8.3.5. Maps were generated at 7.6 cm increments of  $Y_c$ .

## 8.2 Conclusions

### 8.2.1 Thermal Structure and Trajectory of Flare Plumes

The curve fits applied to both sets of data compare well with each other, showing that the characteristic dimension ( $d_p^*$ ) of the mean cross-sectional thermal structure of the plume is scalable over the full range of flare stack scales investigated,  $16.7 \text{ mm} \leq d_i \leq 102.3 \text{ mm}$  (0.15- to full-scale).

The scaling parameter  $d_p^*$  originated from a buoyant plume rise model that was derived based on the Richardson Number, which assumes that the buoyancy of the combustion products and the momentum of the crosswind are the dominant forces in the flow. Richardson Numbers are well-defined for non-reacting flows, and the results in this study indicate that a flare stack plume behaves similarly to a non-reacting buoyant jet over the wide range of flare stack scales investigated.

### 8.2.2 Compositional Structure of Flare Plumes

The curve fits applied to both sets of data for  $n = 1/3$  (Eq. 8.2 and 8.3) compare well with each other. The present study is significant in that it provides the first known

scientific confirmation that the overall combustion inefficiency of a flare stack is scalable over the wide range of flare stack sizes studied.

Curve fits made on Johnson's data and the present data for  $d_o^n$  with  $n = 1/3$  and  $n = 1/2$  dependence indicate that the overall combustion inefficiency of a flare plume is scalable over the full range of flare stack scales investigated,  $12.1 \text{ mm} \leq d_o \leq 114.3 \text{ mm}$  (0.11- to full-scale). The coefficient  $n = 1/3$  is the correct value to be used, as this results in a dimensionless correlation.

### 8.2.3 Ceiling and Floor Effects On the Flare, Plume Rise and Combustion Efficiency

#### 8.2.3.1 Ceiling Effects on Flame Length and Flame Angle

It was determined that for the given experimental conditions, the proximity of the false ceiling had no discernible effect on the approximate flame length,  $L_f$ , or flame angle,  $\theta_f$ .

#### 8.2.3.2 Ceiling Effects on Plume Rise and Dispersion

It was determined for plumes whose cores were not found in the false ceiling's turbulent boundary layer, the proximity of the ceiling to the plume had no important effects on plume rise. However, the presence of the ceiling did have a significant effect upon the local rate of plume rise.

A corrected buoyant plume rise model was developed to incorporate the effects of a ceiling. The resulting model was solved numerically for three cases of fuel jet speeds  $V_j = 0.5, 1.0, \text{ and } 2.0 \text{ m/s}$  at set values of  $Y_c$ . In all cases the theoretical plume rise model agreed with collected experimental data concerning the vertical component of plume centroids.

The model made use of a constant known as the displaced airflow factor,  $f_{daf}$ . Although  $f_{daf}$  varied between 0.006 and 0.008 for the cases presented, it was found that

setting  $f_{daf}$  to 0.007 incurred errors of less than 1 % in the maximum attained plume rise,  $h_{b,actual}$ , for the cases  $V_j = 0.5$  and 2.0 m/s. Hence,  $f_{daf}$  can be considered a constant with the value 0.007 for the cases presented in this study,  $V_j = 0.5, 1.0$  and 2.0 m/s.

#### 8.2.3.3 Ceiling Effects on Combustion Efficiency

It was found that combustion inefficiency of the  $d_o = 26.9$  mm flare stack remained relatively constant as the stack exit was moved closer to the false ceiling, indicating that the proximity of the false ceiling had no significant impact on combustion inefficiency of the flare stack.

#### 8.2.3.4 Floor Effects on Plume Rise and Dispersion

It was found that as the flare stack exit moved closer to the floor, the plume trajectory was deflected downwards. The effect appeared strongest for downwashed plumes with a strong recirculation region downstream of the flare stack, such as for  $V_j = 0.5$  m/s.

The fluid dynamics near the floor could be visualized theoretically by positioning a counter-rotating mirror image recirculation region “under” the floor (similar to the image plume concept employed in section 7.1.2.1), which would act to increase overall circulation observed near the flare stack. However, this image source does not adequately simulate how the real, solid stack alters the floor’s turbulent boundary layer. There is in fact a complex interaction between the vortices oriented perpendicular to the crosswind in the floor’s turbulent boundary layer and the solid flare stack. As these vortices meet the flare stack, they bend and distort themselves around the stack’s shape, resulting in very complicated and chaotic flow structures.

The manner in which a plume entrains ambient air at a fixed position downstream can provide an alternate and simpler explanation. The pair of counter-rotating vortices in a bent-over buoyant plume act to entrain ambient air from the plume’s underside at an entrainment speed  $u_e = \beta U_\infty$ . The entrainment coefficient  $\beta$  can be considered to be a

constant, which also means that the flux of ambient air into the plume's underside at that position is a constant. This produces a low-pressure region below the buoyant plume, as air is rushing to that location to enter the plume's volume. As a plume nears the floor, there becomes less air between the underside of the plume and the floor, and since the rate of air entrainment is a constant, ambient air must move faster to the underside of the plume in order to maintain the rate of flux of entrained air. This causes the pressure on the underside of the plume to drop.

Assuming the above explanation holds true for all positions downstream of the flare stack, pressure beneath the length of the plume will be lower than for a plume that is far above the floor, and since a higher, unchanged pressure still exists on the topside of the plume, the buoyant plume's centerline trajectory will be deflected downwards.

#### 8.2.3.5 Floor Effects on Combustion Efficiency

For the cases  $V_j = 1.0$  and  $2.0$  m/s, combustion inefficiency of the  $d_o = 26.9$  mm flare stack remained relatively constant as the stack exit was moved closer to the floor. However, for the case  $V_j = 0.5$  m/s, flare stack combustion inefficiency was observed to decrease as the adjustable stack height was decreased.

An explanation for this can be made using the fuel stripping mechanism identified by Johnson et al. (2001b) and how it may interact with the floor. This mechanism consists of the flare stack's downstream recirculation region and the vortices shedding from the flare stack, and how they affect the flare. The coherent, shedding vortices act to open intermittent holes in the flame, allowing bursts of unburned hydrocarbons to be pulled from the flame by the downstream recirculation region. These bursts of unburned hydrocarbons are then ejected from the reacting jet, resulting in combustion inefficiency.

The floor's turbulent boundary layer may be interfering with the formation of coherent vortices shedding from the flare stack, essentially reducing the frequency of holes in the flame, and thus increasing the combustion efficiency of the flare. Combining this argument with the one presented in section 7.2.1 concerning plume rise, it may be concluded that by increasing flare downwash (or reducing a plume's buoyancy) and

moving a flare stack exit closer to the floor of a wind tunnel, plume rise is deflected downwards and the flame burns more efficiently.

### 8.3 Future Work

It was observed that current and past combustion inefficiency correlations collapsed slightly better using the coefficient  $n = 1/2$ , resulting in the dimension  $m^{-1/6}$  on the right hand side of the empirical curve fit. This suggests that there may be underlying mechanisms influencing inefficiencies in combustion other than the crosswind momentum flux and jet buoyancy. One proposed method, a fuel stripping mechanism for wake-stabilized jet diffusion flames in crosswind, has been discussed and studied by Johnson et al. (2001b). Further study should be devoted to exploring the fluid dynamics of this proposed fuel stripping mechanism, through experimental study and perhaps numerical simulation.

The corrected buoyant plume rise model developed for this study to incorporate the presence of a wind tunnel's ceiling made use of a parameter known as the displaced airflow factor,  $f_{daf}$ . It found that  $f_{daf}$  was a constant with the value 0.007 for the cases presented in this study,  $V_j = 0.5, 1.0, \text{ and } 2.0 \text{ m/s}$ . Further work on this topic would consist determining whether  $f_{daf}$  remains a constant for other values of  $V_j$  not explored in this study, or developing alternate plume rise models to account for the presence of a ceiling.

## REFERENCES

1. A.D. Birch, D.R. Brown, M. Fairweather, G.K. Hargrave (1989) "An Experimental Study of a Turbulent Natural Gas Jet in a Cross-Flow", *Combustion Science and Technology*, Vol. 66, pp. 217-232.
2. C.H. Bosanquet and J.L. Pearson (1936) "The Spread of Smoke and Gases from Chimneys", *Transactions of the Faraday Society*, Vol. 32, pp. 1249-1264.
3. P.E. Botros and T.A. Brzustowski (1978) "An Experimental and Theoretical Study of the Turbulent Diffusion Flame in Cross-Flow", 17<sup>th</sup> International Symposium on Combustion, pp. 389-397.
4. G.A. Briggs (1975) "Plume Rise Predictions", Chapter 3 of *Lectures on Air Pollution and Environmental Impact Analyses*, American Meteorological Society, pp. 59-111.
5. S. Djurfors and D. Netterville (1977) "Buoyant Plume Rise in Non-Uniform Wind Conditions", Syncrude Canada Ltd. Professional Paper 1977-3, *Journal of the Air Pollution Control Association*, Vol. 28, No. 8, pp. 780-784.
6. Energy Utilities Board (2001) *EUB Statistical Series 2002-60B: Upstream Petroleum Industry Flaring and Venting Report*, 2001, pp. 2-4.
7. S.R. Gollahalli, T.A. Brzustowski and H.F. Sullivan (1975) "Characteristics of a Turbulent Propane Diffusion Flame in a Cross-Wind", *Transactions of the Canadian Society of Mechanical Engineering*, Vol. 3, No. 4, pp. 205-214.
8. S.R. Gollahalli and B. Nanjundappa (1995) "Burner Wake Stabilized Gas Jet Flames in Cross-Flow" *Combustion Science and Technology*, Vol. 109, pp. 327-346.
9. T.A. Hewett, J.A. Fay and D.P. Hoult (1971) "Laboratory Experiments of Smokestack Plumes in a Stable Atmosphere", *Atmospheric Environment*, Vol. 5, pp. 767-789.
10. V.O. Hoehne and R.G. Luce (1992) "The Effect of Velocity, Temperature, and Molecular Weight on Flammability Limits in Wind-Blown Jets of Hydrocarbon Gases", *American Petroleum Institute* 56-70, pp. 1057-1073.
11. J.T. Houghton, L.G. Meira Filho, B.A. Callander, N. Harris, A. Kateenger and K. Marshall (1996) "Climate Change 1995: The Science of Climate Change",



Intergovernmental Panel on Climate Change (IPCC), Cambridge University Press, Cambridge, U.K., p. 572.

12. R.F. Huang and J.M. Chang (1994) "The Stability and Visualized Flame and Flow Structures of a Combusting Jet in Cross Flow", *Combustion and Flame*, Vol. 98, pp. 267-278.
13. R.F. Huang and S.M. Wang (1999) "Characteristic Flow Modes of Wake-Stabilized Jet Flames in a Transverse Air Stream", *Combustion and Flame*, Vol. 117, pp.59-77.
14. R.F. Huang and M.J. Yang (1996) "Thermal and Concentration Fields of Burner-Attached Jet Flames in Cross Flow", *Combustion and Flame*, Vol. 105, pp. 211-224.
15. F.P. Incropera and D.P. DeWitt (1996) "Introduction to Heat Transfer", John Wiley & Sons, Inc., 3<sup>rd</sup> Ed., p. 349.
16. M.R. Johnson, L.W. Kostiuk (2000) "Efficiencies of Low-Momentum Jet Diffusion Flames in Crosswinds", *Combustion and Flame*, Vol. 123, pp. 189-200.
17. M.R. Johnson, L.W. Kostiuk (2002) "Experimental Modeling of the Efficiency of Flares in a Crosswind, submitted to the 29<sup>th</sup> International Combustion Symposium, Sapporo, Japan, July 21-26, 2002.
18. M.R. Johnson, L.W. Kostiuk and J.L. Spangelo (2001a) "A Characterization of Solution Gas Flaring in Alberta", *Journal of the Air and Waste Management Association*, Vol. 51, pp. 1167-1177.
19. M.R. Johnson, D.J. Wilson and L.W. Kostiuk (2001b) "A Fuel Stripping Mechanism for Wake-Stabilized Jet Diffusion Flames in Crossflow", *Combustion Science and Technology*, Vol. 169, pp. 155-174.
20. C.R. Johnston and D.J. Wilson (1997) "A Vortex Pair Model for Plume Downwash into Stack Wakes", *Atmospheric Environment*, Vol. 31, No.1 pp. 13-20.
21. D. Joseph, J. Lee, C. McKinnon, R. Payne and J. Pohl (1983) "Evaluation of the Efficiency of Industrial Flares: Background – Experimental Design – Facility", Environmental Protection Agency Report EPA-600/2-83-070, Washington D.C.
22. G.T. Kalghatgi (1983) "The Visible Shape and Size of a Turbulent Hydrocarbon Jet Diffusion Flame in Cross-wind", *Combustion and Flame*, Vol. 52, pp. 91-106.

23. D.M. Leahey and M.J.E. Davies (1984) "Observations of Plume Rise from Sour Gas Flares", *Atmospheric Environment*, Vol. 18, No. 5, pp. 917-922.
24. A.J. Majeski, D.J. Wilson, L.W. Kostiuk (2000) "Measuring and Predicting the Length of a Propane Jet Diffusion Flame", presented at the Spring 2000 Technical Meeting of the Combustion Institute, Canadian Section, Ottawa, Ontario, May 15-17, 2000, Paper #7, 6 pages.
25. R.J. Margason (1993) "Fifty Years of Jet in Cross Flow Research", AGARD Conference Proceedings, pp. 1-1 1-48.
26. B.R. Morton, G.I. Taylor and J.S. Turner (1956) "Turbulent gravitational convection from maintained and instantaneous sources", *Proc. Roy. Soc. (London)*, Ser. A, 234, pp. 1-23
27. D. Netterville (1979) "Concentration Fluctuations in Plumes", Syncrude Canada Ltd. Environmental Affairs Department.
28. G. Ooms (1972) "A New Method for the Calculation of the Plume Path of Gases Emitted by a Stack", *Atmospheric Environment*, Vol. 6, pp. 899-909.
29. R.L. Panton (1996) "Incompressible Flow", John Wiley & Sons, Inc., 2<sup>nd</sup> Ed., pp. 471-545.
30. J.H. Pohl and N.R. Soelberg (1985) "Evaluation of the Efficiency of Industrial Flares: Flares Head Design and Gas Composition", Environmental Protection Agency Report EPA-600/2-85-106, Washington D.C.
31. J.H. Pohl, J. Lee and R. Payne (1986) "Combustion Efficiency of Flares", *Combustion Science and Technology*, Vol. 50, pp. 217-231.
32. P.D. Poudenx, L.W. Howell, D.J. Wilson, L.W. Kostiuk (2004) "Downstream Similarity of Thermal Structure in Plumes from Jet Diffusion Flames in a Crossflow", *Combustion Science and Technology*, Vol. 176, pp. 409-435.
33. P.D. Poudenx, M.R. Johnson, D.J. Wilson, L.W. Kostiuk (2000) "Local Combustion Efficiency Measurements of Gas Flares", presented at the Spring 2000 Technical Meeting of the Combustion Institute, Canadian Section, Ottawa, Ontario, May 15-17, 2000, Paper #11, 6 pages.
34. R.A. Prybysh, M.D. Checkel, L.W. Kostiuk (2000) "Collection and Analysis of Solid-Phase Emissions from Continuous Flares", presented at the Spring 2000 Technical Meeting of the Combustion Institute, Canadian Section, Ottawa, Ontario, May 15-17, 2000, Paper #21, 5 pages.
35. R.R. Romano (1983) "Control Emissions with Flare Efficiency", *Hydrocarbon Processing*, Vol. 62, No. 10, pp. 78-80.

36. J. Shwartz and M.P. Tulin (1972) "Chimney Plumes in Neutral and Stable Surroundings", *Atmospheric Environment*, Vol. 6, pp. 19-35.
37. K. D. Siegel (1980), "Über den Umsatzgrad von Fackelgas in Raffineriehochfackeln", Report on BMI-BMFT-DGMK-Gemeinschaftsprojekt 135-02, Ph.D. Dissertation, University of Karlsruhe.
38. SKM Consulting Ltd. (1988) "Review and Assessment of Current Flaring Technology", Environment Canada Western and Northern Region, Report CP(EP) WNR-87/88-5.
39. P.R. Slawson and G.T. Csanady (1967) "On the Mean Path of Buoyant, Bent-Over Chimney Plumes", *Journal of Fluid Mechanics*, Vol. 28, part 2, pp. 311-322.
40. S.H. Smith and M.G. Mungal (1998) "Mixing, Structure and Scaling of the Jet in Crossflow", *Journal of Fluid Mechanics*, Vol. 357, pp. 83-122.
41. M. Strosher (1996) "Investigations of Flare Gas Emissions in Alberta", Alberta Research Council Environmental Technologies.
42. T.H. Toften, A.E. Holdo and D.Kapfer (1993) "Effects of Free-Stream Turbulence on a Jet in a Cross Flow", AGARD Conference Proceedings, pp. 35-1 35-10.
43. J.C. Weil (1977) "Plume Rise", Chapter 3 of *Lectures in Air Pollution Modeling*, A. Venkatram and J.C. Wyngaard eds., American Meteorological Society, pp. 119-166.
44. F.M. White (1999) "Fluid Mechanics", The McGraw-Hill Companies, Inc., 4<sup>th</sup> Ed., p. 428.
45. S.J. Wright (1977) "Mean Behavior of Buoyant Jets in a Crossflow", *Journal of the Hydraulics Division*, No. 5, pp. 499-513.

## APPENDIX A: Derivation of the Plume Entrainment Model

The following provides the theoretical basis for the derivation of the plume entrainment model, shown in Figure A.1. The radius of the plume,  $R_p$ , will be expressed as a function of the fuel jet radius,  $R_j$  (where  $R_j = d_i/2$ ), the fuel jet velocity,  $V_j$ , the crosswind speed,  $U_\infty$ , and the distance downstream from the stack,  $X_o$ . Lastly, it will be shown how this equation defining  $R_p$  is used to create the correlation for the characteristic dimension,  $d_p^*$ .

### A.1 Buoyancy Flux

The rise of a buoyant plume, with  $\rho_s$  less than  $\rho_\infty$  (where  $\rho_s$  denotes the density of the stoichiometric products of combustion originating from the point source), depends on the initial flux of buoyancy force from an idealized point source. The conventional definition of buoyancy flux,  $F_b$ , is as follows,

$$F_b = g \left( \frac{\rho_\infty - \rho_s}{\rho_\infty} \right) V_j R_j^2 \quad (\text{A.1})$$

This flux is predominantly positive for reacting plumes associated with natural gas flares, meaning the plume will naturally rise and gradually gain upward momentum. We can further simplify this equation and remove any ambiguity concerning an appropriate value for  $\rho_s$  by using the ideal gas law,

$$P = \rho \bar{R} T \quad (\text{A.2})$$

where

$\bar{R}$  = specific gas constant

$P$  = pressure

$T$  = temperature

By using Eq. A.2 we assume that the source gas has essentially the same molecular weight as air. Eq. A.1 then becomes

$$F_b = g \left( \frac{T_s - T_\infty}{T_s} \right) V_j R_j^2 \quad (\text{A.3})$$

Buoyancy flux can also be expressed in terms of the heat release rate,  $H_s$ , which is defined as

$$H_s = \pi R_j^2 V_j \rho_s C_{p\infty} (T_s - T_\infty) \quad (\text{A.4})$$

where

$C_{p\infty}$  = specific heat capacity of the ambient air

Rearranging this equation can produce an expression for the heating value of the gas source.

$$Q_{hv} = \frac{H_s}{\pi R_j^2 V_j \rho_j} = C_{p\infty} (T_s - T_\infty) \quad (\text{A.5})$$

Combining Eq. A.3 and A.5,

$$F_b = g \frac{Q_{hv}}{T_s C_{p\infty}} V_j R_j^2 \quad (\text{A.6})$$

## A.2 Buoyant Plume Trajectory

To obtain a closed-form solution for the trajectory of a buoyant jet one must make the following assumptions.

- Crosswind speed,  $U_\infty$ , is constant with height.

- The plume is fully bent-over for its entire length, so entrainment velocity is  $u_e = \beta U_\infty$  at all times.  $\beta$  is the plume entrainment coefficient.
- The Boussinesq approximation can be applied (i.e. density differences between the plume and ambient air are negligible).

For a purely buoyant plume with no momentum and an effective ideal point source diameter equal to zero ( $R_o = 0$ ), the buoyant plume rise (Weil, 1977) is given by

$$h_b = \left( \frac{3}{2\beta^2} \right)^{1/3} \frac{F_b^{1/3}}{U_\infty} X_o^{2/3} \quad (\text{A.7})$$

Combining Eq. A.6 and A.7,

$$h_b = \left( \frac{3}{2\beta^2} \right)^{1/3} \frac{g^{1/3} Q_{hv}^{1/3} R_j^{2/3} V_j^{1/3}}{T_s^{1/3} C_{p\infty}^{1/3} U_\infty} X_o^{2/3} \quad (\text{A.8})$$

Morton et al. (1956) determined a hypothesis that the radius of the plume could be defined in the following manner,

$$R_p = \beta h_b \quad (\text{A.9})$$

Substituting Eq. A.8 into A.9, the radius of the plume may be defined as

$$R_p = \left( \frac{3\beta Q_{hv}}{2T_s C_{p\infty}} \right)^{1/3} g^{1/3} R_j^{2/3} \frac{V_j^{1/3}}{U_\infty} X_o^{2/3} \quad (\text{A.10})$$

Finally, we may define the characteristic dimension,  $d_p^*$ , which is the square root of the area contained within the 50 % temperature contour of a plume's mean cross-sectional structure.

$$d_p^* = (\pi)^{1/2} \left( \frac{3\beta Q_{hv}}{2T_s C_{p\infty}} \right)^{1/3} g^{1/3} d_i^{2/3} \frac{V_j^{1/3}}{U_\infty} X_o^{2/3} \quad (\text{A.11})$$

The collection of terms  $(\pi)^{1/2} (3\beta Q_{hv} / 2T_s C_{p\infty})^{1/3}$  is a constant when fuel composition remains the same, combustion is almost complete ( $\eta \approx 1$ ) and ambient pressure is constant. Finally, the characteristic dimension of the plume is

$$d_p^* \propto g^{1/3} \frac{V_j^{1/3}}{U_\infty} X_o^{2/3} d_i^{2/3} \quad (\text{A.12})$$

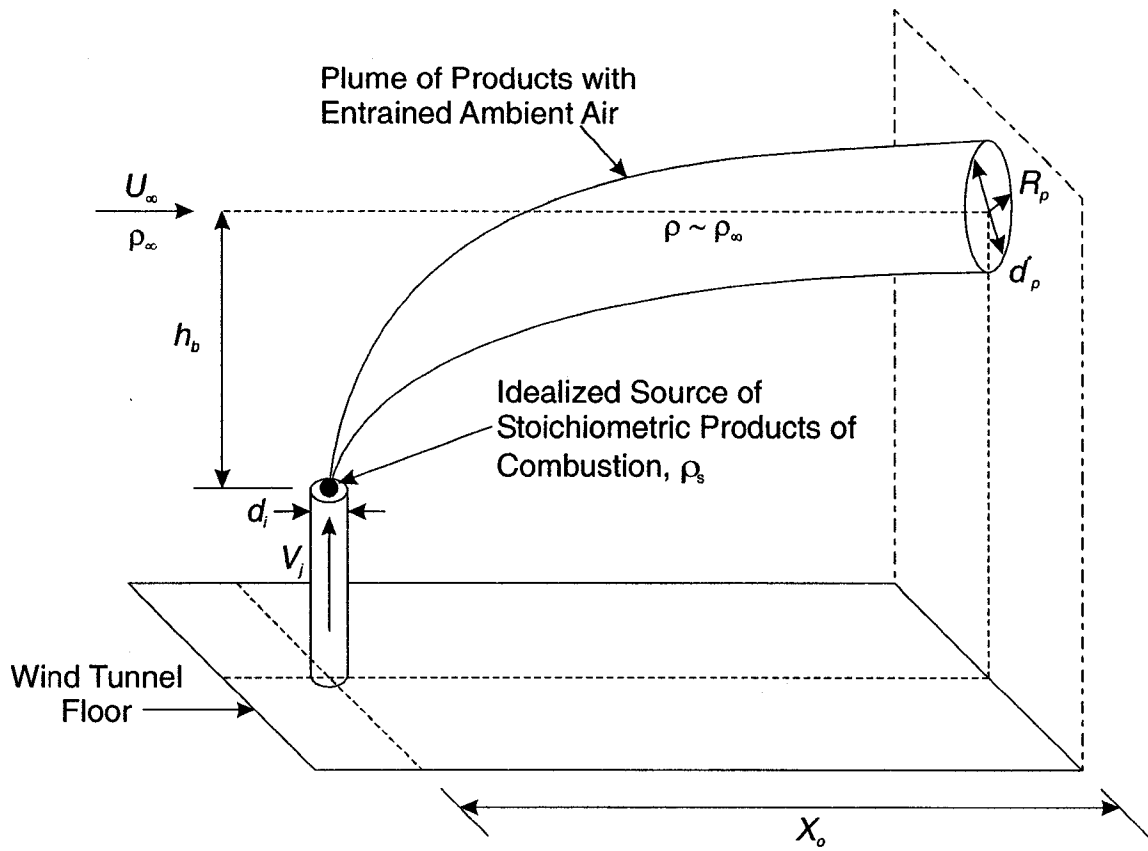


**Figure A.1: Model of a non-reacting buoyant plume in crosswind**



## APPENDIX B: Sensitivity and Uncertainty Analysis

### B.1 Sensitivity Analysis

Recalling the definition of the local combustion efficiency calculation as derived in Chapter 3,

$$\eta = \frac{[CO_2]_p}{[CO_2]_p + [CO]_p + [CH_4]_p} \quad (B.1)$$

where

$[A]_p$  = concentration of molecule A in products of combustion

In reference to the variables defined in Chapter 3 (with subscripts S and E denoting concentrations of the sample gas and the entrained air, respectively), the concentrations of chemical species in the products of combustion may be rewritten as

$$[CO_2]_p = \frac{[CO_2]_s - (1 - \alpha_L)[CO_2]_E}{\alpha_L} \quad (B.2)$$

$$[CO]_p = \frac{[CO]_s - (1 - \alpha_L)[CO]_E}{\alpha_L} \quad (B.3)$$

$$[CH_4]_p = \frac{[CH_4]_s - (1 - \alpha_L)[CH_4]_E}{\alpha_L} \quad (B.4)$$

where

$$\alpha_L = 1 - \frac{[O_2]_s}{[O_2]_E} = \text{local volume fraction of products in the gas sample} \quad (B.5)$$

Using Eq. B.2 to B.5, B.1 may be rewritten as

$$\eta = \frac{[CO_2]_S - \left(\frac{[O_2]_S}{[O_2]_E}\right)[CO_2]_E}{[CO_2]_S + [CO]_S + [CH_4]_S - \left(\frac{[O_2]_S}{[O_2]_E}\right)([CO_2]_E + [CO]_E + [CH_4]_E)} \quad (B.6)$$

So, the combustion efficiency calculation is based on the measurement of 8 separate chemical species' concentrations. This analysis will determine how sensitive the above equation is to slight changes in the values of the 8 variables.

The first part of this analysis will investigate the sensitivity of Eq. B.6 for two separate cases. The first case will be for a gas sample taken from a flame with very high combustion efficiency, the second case for a gas sample taken from a lower efficiency flame. Both cases will have measured values for the 8 chemical species' concentrations. Each of these 8 concentrations will have its value increased by + 5 % and the effect on the calculated combustion efficiency will be observed.

The second part of this analysis will study 5 cases to determine how the sensitivity of Eq. B.6 changes as the calculated combustion inefficiency ( $1 - \eta$ ) increases.

Tables B.1 and B.2 display the concentrations of the 8 chemical species for each case.

Efficiency	99.04	%
[CO <sub>2</sub> ] <sub>S</sub>	3000	ppm
[CO <sub>2</sub> ] <sub>E</sub>	300	ppm
[CO] <sub>S</sub>	10	ppm
[CO] <sub>E</sub>	1	ppm
[CH <sub>4</sub> ] <sub>S</sub>	20	ppm
[CH <sub>4</sub> ] <sub>E</sub>	3	ppm
[O <sub>2</sub> ] <sub>S</sub>	20	%
[O <sub>2</sub> ] <sub>E</sub>	21	%

**Table B.1: Case 1, measured values for chemical species' concentrations**

Efficiency	87.57	%
[CO <sub>2</sub> ] <sub>S</sub>	3500	ppm
[CO <sub>2</sub> ] <sub>E</sub>	300	ppm
[CO] <sub>S</sub>	60	ppm
[CO] <sub>E</sub>	1	ppm
[CH <sub>4</sub> ] <sub>S</sub>	400	ppm
[CH <sub>4</sub> ] <sub>E</sub>	3	ppm
[O <sub>2</sub> ] <sub>S</sub>	20	%
[O <sub>2</sub> ] <sub>E</sub>	21	%

**Table B.2: Case 2, measured values for chemical species' concentrations**

Figures B.1 and B.2 indicate that the two measurements that have the most significant impact on the calculation of combustion efficiency are [CO<sub>2</sub>]<sub>S</sub> and [CH<sub>4</sub>]<sub>S</sub>, the concentrations of carbon dioxide and methane in the sample gas. In both cases the effect on the final calculation is a difference of less than 1 %. Measurements of gas concentrations in the entrained air do not appear to have a strong effect on the combustion efficiency calculation.

A flare's performance may be expressed at times in terms of combustion *inefficiency* ( $1 - \eta$ ), rather than combustion efficiency. In this case, the sensitivity of the combustion inefficiency calculation is significantly amplified, since inefficiency values are much lower than their complement efficiency values (i.e. 0.96 % for 99.04 %, 12.43 % for 87.57 %). Now, a + 5 % change in the measurement of [CO<sub>2</sub>]<sub>S</sub> results in a 5.21 % and 4.83 % change in ( $1 - \eta$ ) for case 1 and 2, respectively. The effects from all other variables are observed to increase or decrease slightly, retaining their relative effects on the calculation.

Figure B.3 is a plot displaying the effect of increasing combustion inefficiency on the absolute difference in the combustion inefficiency calculation for a + 5 % change in each variable. Five cases are presented using typical values for chemical species' concentrations. For + 5 % increases in [CO<sub>2</sub>]<sub>S</sub> and [CH<sub>4</sub>]<sub>S</sub>, it is seen that the absolute difference in the combustion inefficiency calculation increases in a linear fashion with

increasing combustion inefficiency. The absolute differences due to + 5 % changes in all other variables remain relatively static and insignificant.

### B.1.1 Conclusions

- The combustion efficiency ( $\eta$ ) calculation was most sensitive to slight changes in measurements of  $[\text{CO}_2]_s$  and  $[\text{CH}_4]_s$ . However, the absolute difference in the combustion efficiency calculation for both cases was less than 1 %. This means that Eq. B.6 is very insensitive to slight changes in measured species' concentrations.
- If a flare's performance is expressed in terms of combustion *inefficiency* ( $1 - \eta$ ), then the sensitivity of the combustion inefficiency calculation is significant. A + 5 % change in  $[\text{CO}_2]_s$  results in an absolute difference in the combustion inefficiency of 5.21 % and 4.83 % for case 1 and 2, respectively.
- The sensitivity of the combustion *inefficiency* ( $1 - \eta$ ) calculation increases as combustion inefficiency increases. +5 % changes in  $[\text{CO}_2]_s$  and  $[\text{CH}_4]_s$  have the strongest effect on the calculated combustion inefficiency.

## B.2 Uncertainty Analysis

This analysis will determine how reliable the results are that one obtains from the local combustion efficiency calculation defined by Eq. 3.28. Each of the 8 variables in Eq. B.6 has an uncertainty attributed to the accuracy of the 4 gas analysers used in this study.

The uncertainty,  $\varepsilon_\eta$ , of the combustion efficiency,  $\eta$ , is expressed by

$$\varepsilon_\eta = \sum_{i=1}^{\text{tot}} \left( \frac{\partial \eta}{\partial x_i} \right)^2 \varepsilon_{x_i}^2 \quad (\text{B.7})$$

where

$x_i$  = variable in the combustion efficiency Eq. B.6

$\varepsilon_{x_i}$  = uncertainty of variable  $x_i$

$tot$  = total number of variables (i.e. 8)

Table B.3 presents typical values for each variable for the case  $\eta = 95.5 \%$ .

Variable	Range	Uncertainty	Typical Value	Units
[CO <sub>2</sub> ] <sub>S</sub>	0-10 000	100	2000	ppm
[CO <sub>2</sub> ] <sub>E</sub>	0-10 000	100	400	ppm
[CO] <sub>S</sub>	0-200	2	30	ppm
[CO] <sub>E</sub>	0-200	2	1	ppm
[CH <sub>4</sub> ] <sub>S</sub>	0-500	2.5	100	ppm
[CH <sub>4</sub> ] <sub>E</sub>	0-500	2.5	3	ppm
[O <sub>2</sub> ] <sub>S</sub>	0-25	0.25	20	%
[O <sub>2</sub> ] <sub>E</sub>	0-25	0.25	21	%

**Table B.3: Typical concentration values and associated uncertainties for  $\eta = 95.5 \%$**

The product of each partial derivative using the above values is as follows.

$$\begin{aligned} \frac{\partial \eta}{\partial CO_{2S}} &= 41.430 & \frac{\partial \eta}{\partial CO_{2E}} &= -39.457 & \frac{\partial \eta}{\partial CO_S} &= -531.558 & \frac{\partial \eta}{\partial CO_E} &= 506.245 \\ \frac{\partial \eta}{\partial CH_{4S}} &= -531.558 & \frac{\partial \eta}{\partial CH_{4E}} &= 506.245 & \frac{\partial \eta}{\partial O_{2S}} &= -0.069 & \frac{\partial \eta}{\partial O_{2E}} &= 0.066 \end{aligned}$$

According to Eq. (B.7), this results in  $\varepsilon_\eta = 0.0062$  for  $\eta = 95.5 \%$ . This means that for this typical value of efficiency,

$$\frac{\varepsilon_\eta}{\eta} = 0.65 \% \quad (B.8)$$

Therefore, for this case the result can be stated as

$$\eta = 95.5 \pm 0.7\% \quad (\text{B.9})$$

Or,

$$94.8\% \leq \eta \leq 96.2\% \quad (\text{B.10})$$

In terms of combustion *inefficiency*,

$$3.8\% \leq (1 - \eta) \leq 5.2\% \quad (\text{B.11})$$

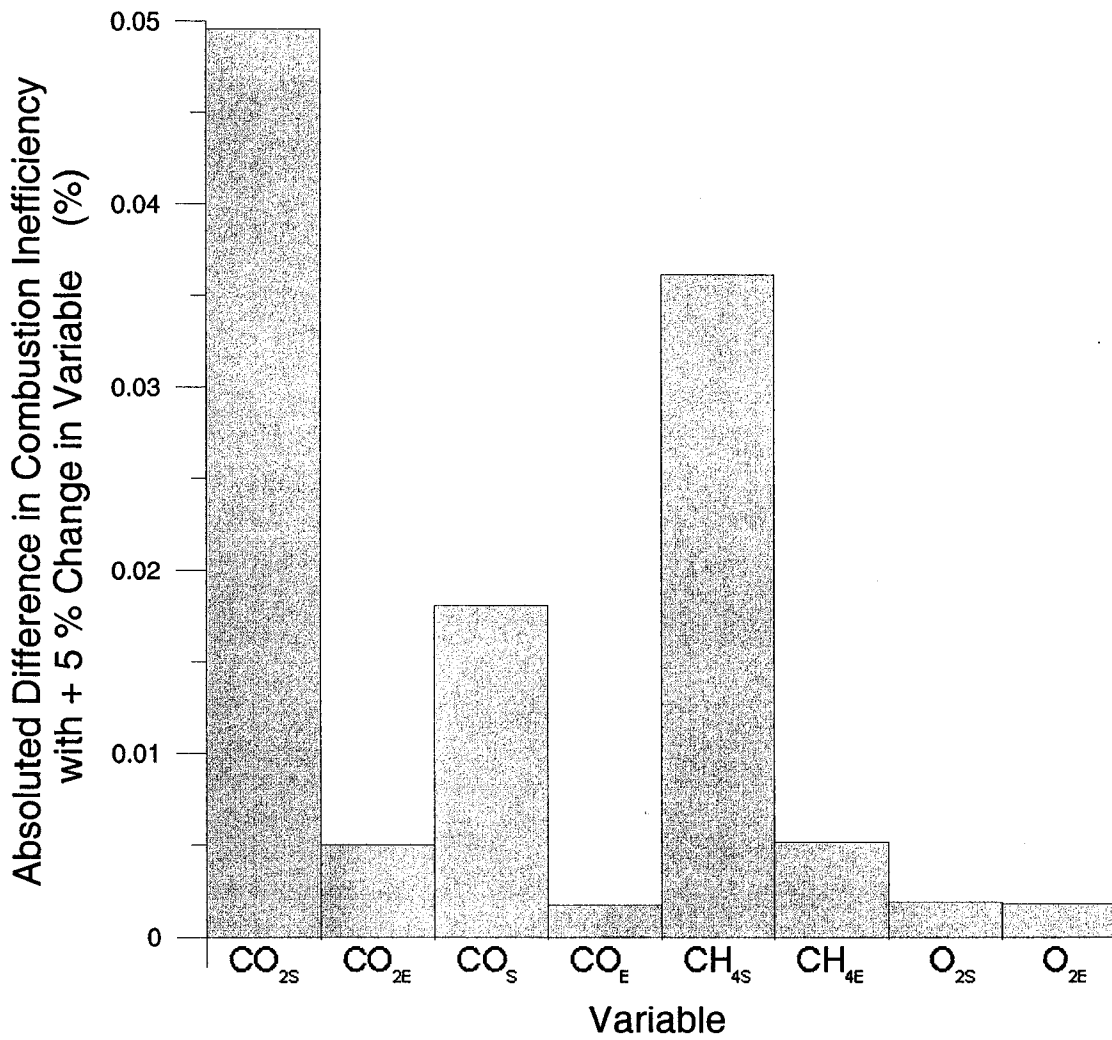


**Figure B.1: Case 1, sensitivity of Eq. B.6 to a + 5 % change in a variable**

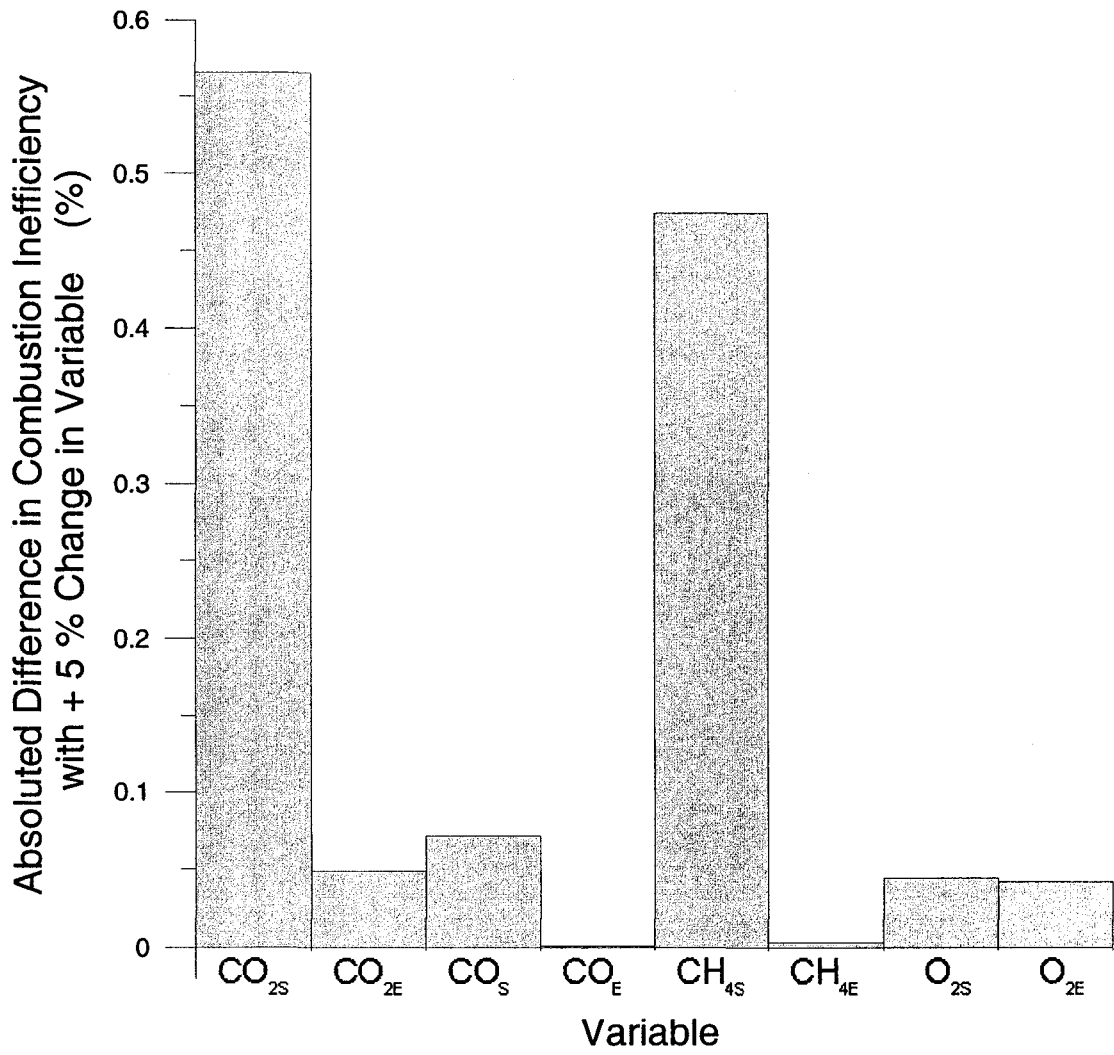
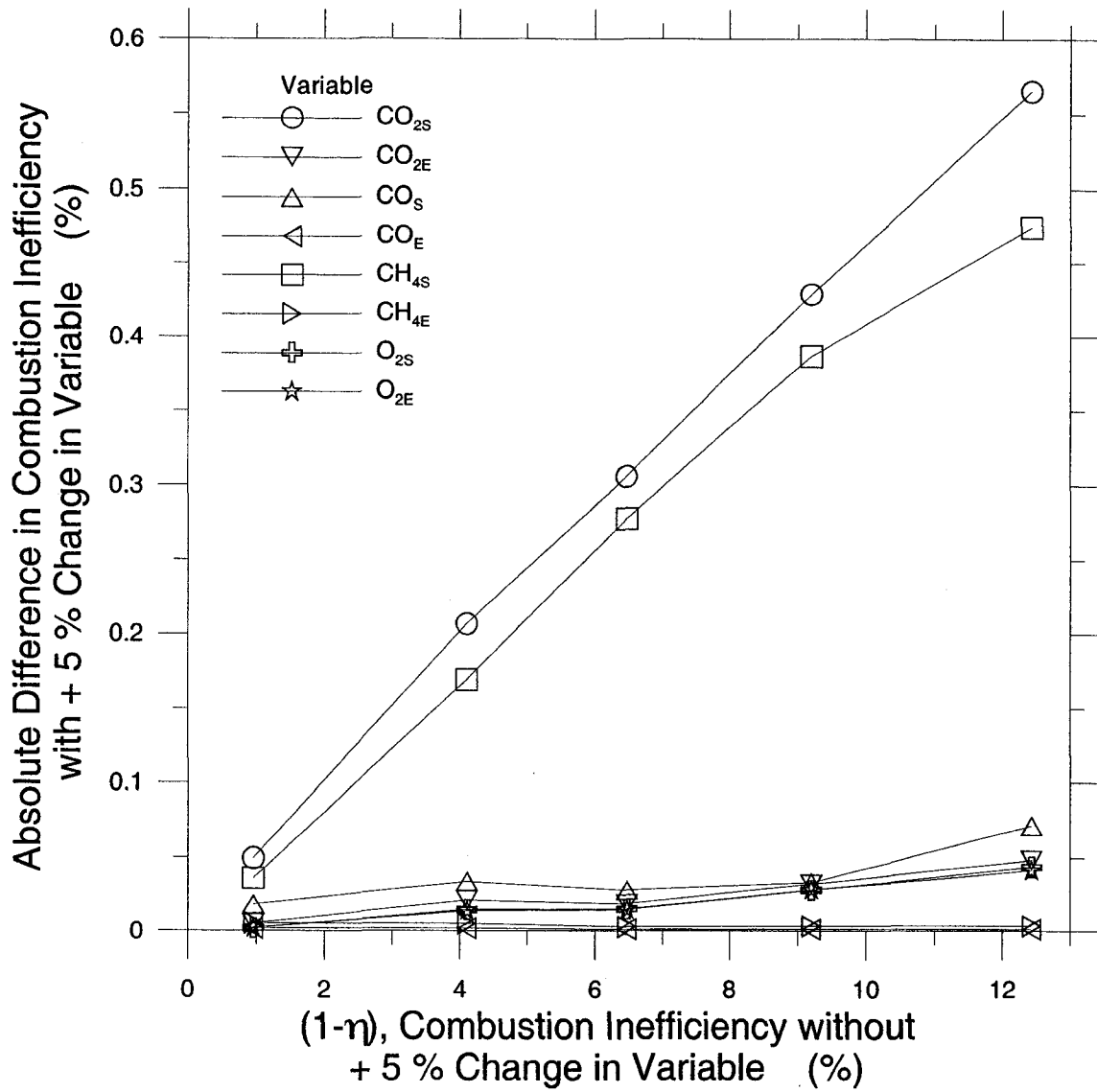


Figure B.2: Case 2, sensitivity of Eq. B.6 to a + 5 % change in a variable





**Figure B.3: Sensitivity of Eq. B.6 to a + 5 % change in a variable with increasing combustion inefficiency**

## APPENDIX C: Corrected Plume Rise Model

The following provides the derivation of the corrected plume rise model. This model accounts for the ceiling that limits the upward displacement and the velocity of the rising plume. Figure C.1 displays a plume rise model without a ceiling. There is an idealized point of oxidation reaction at the exit of the stack that produces the hot products. Complete combustion is assumed to take place, producing stoichiometric products. Figure C.2 displays a comparison between plume rise models with and without the ceiling.

The upward plume velocity, assuming the plume is advected downstream with a constant velocity  $U_\infty$ , is given by

$$W_p = \frac{\partial h_b}{\partial t} = \frac{\partial h_b}{\partial X_o} \frac{\partial X_o}{\partial t} = U_\infty \frac{\partial h_b}{\partial X_o} \quad (\text{C.1})$$

The buoyant plume rise model proposed by Weil (1977),

$$h_b = \left( \frac{3}{2\beta^2} \right)^{1/3} \frac{F_b^{1/3}}{U_\infty} X_o^{2/3} \quad (\text{C.2})$$

The distance between the corrected plume centerline and the ceiling is defined as

$$s_{actual} = Y_c - h_{b,actual} \quad (\text{C.3})$$

The buoyancy flux,  $F_b$ , must be defined in order to complete Eq. C.2. Derivation of this equation is found in Appendix A.

$$F_b = g \left( \frac{T_s - T_\infty}{T_s} \right) V_j R_j^2 \quad (\text{C.4})$$

The definition of the heat release rate at the source,

$$H_s = \pi R_j^2 V_j \rho_s C_{p\infty} (T_s - T_\infty) \quad (\text{C.5})$$

may be substituted into Eq. C.4 to obtain the following.

$$F_b = g \frac{H_s}{\pi \rho_s C_{p\infty} T_s} \quad (\text{C.6})$$

Using the ideal gas law,  $\rho_s T_s = \rho_\infty T_\infty = \frac{P_\infty}{R_\infty}$ , Eq. C.6 becomes,

$$F_b = H_s \left( \frac{g \bar{R}_\infty}{\pi C_{p\infty} P_\infty} \right) \quad (\text{C.7})$$

Substituting Eq. C.7 into Eq. C.2,

$$h_b = \left( \frac{3}{2\beta^2} \right)^{1/3} \left( \frac{g \bar{R}_\infty}{\pi C_{p\infty} P_\infty} \right)^{1/3} \frac{H_s^{1/3} X_o^{2/3}}{U_\infty} \quad (\text{C.8})$$

Setting  $K_h = \left( \frac{3}{2\beta^2} \right)^{1/3} \left( \frac{g \bar{R}_\infty}{\pi C_{p\infty} P_\infty} \right)^{1/3}$  to simplify Eq. C.8,

$$h_b = K_h \frac{H_s^{1/3} X_o^{2/3}}{U_\infty} \quad (\text{C.9})$$

Now, substituting Eq. C.9 into Eq. C.1 and taking the derivative gives the upward plume speed,

$$W_p = \frac{2}{3} K_h \left( \frac{H_s}{X_o} \right)^{1/3} \quad (\text{C.10})$$

A buoyant rising plume may be idealized as a rising solid cylinder with an expanding radius of  $R_p$ , so  $W_p$  may be derived in another manner that makes use of

potential flow theory (Panton, 1996, pp. 471-545). Figure C.3 presents this idealized situation.

Referring to Figure C.3, the velocity induced by the rising cylinder,  $W$ , may be defined by the following.

$$W = W_p \left( \frac{R_p}{Y} \right)^2 \quad (\text{C.11})$$

Using the above equations, one may derive a corrected plume rise model by placing an image flare stack and plume on the opposite side of the wind tunnel ceiling. Figure C.4 demonstrates this concept, with the subscripts ( $j$ ) and ( $j-1$ ) denoting the index of the data point along the plume centerline. Using Eq. C.11, the downward velocity induced by the corrected image plume on the corrected real plume may be defined as

$$W_{\text{image at plume, actual}(j-1)} = f_{\text{daf}} W_{p, \text{actual}(j-1)} \left( \frac{R_{p(j-1)}}{2S_{\text{actual}(j-1)}} \right)^2 \quad (\text{C.12})$$

where

$$R_{p(j-1)} = \beta h_{b(j-1)} = \frac{\beta K_h H_s^{1/3}}{U_\infty} X_{o(j-1)}^{2/3} \quad (\text{C.13})$$

In Eq. C.12 the displaced airflow factor,  $f_{\text{daf}}$ , is meant to account for the ambient air that is not entrained into the plume cylinder as it rises. The inertia of this non-entrained air must be overcome and its mass must be “pushed-aside” by the rising cylinder, thus decreasing the magnitude of  $W_{p, \text{actual}}$  imposed on the real plume by the image plume.

Using a backward difference method, the corrected plume centerline may be calculated.

$$h_{b,actual(j)} = h_{b,actual(j-1)} + (W_{p,actual(j-1)} - W_{image\ at\ plume,actual(j-1)})\Delta t \quad (C.13)$$

$$\text{where } \Delta t = \frac{\Delta X_o}{U_\infty}$$

Buoyant plume entrainment can be used to find the corrected upward plume velocity,  $W_{p,actual}$ .

$$W_{p,actual(j-1)} = W_{p,actual(j-2)} + \left( \frac{\partial W_{p(j-1)}}{\partial t} \right) \Delta t \quad (C.14)$$

$$\text{where } \Delta t = \frac{\Delta X_o}{U_\infty}$$

The two right hand terms in Eq. (C.14) are defined as

$$W_{p,actual(j-2)} = \frac{h_{b,actual(j-1)} - h_{b,actual(j-2)}}{\Delta t} \quad (C.15)$$

$$\frac{\partial W_{p(j-1)}}{\partial t} = \frac{\partial W_p}{\partial X_o} \frac{\partial X_o}{\partial t} \Bigg|_{(j-1)} = -\frac{2}{9} K_h H_s^{1/3} U_\infty X_o^{-4/3} \quad (C.16)$$

Referring to Figure C.4, care should be taken when employing the above equations so that the dashed image plume centerline is used to correct the dashed real plume centerline.

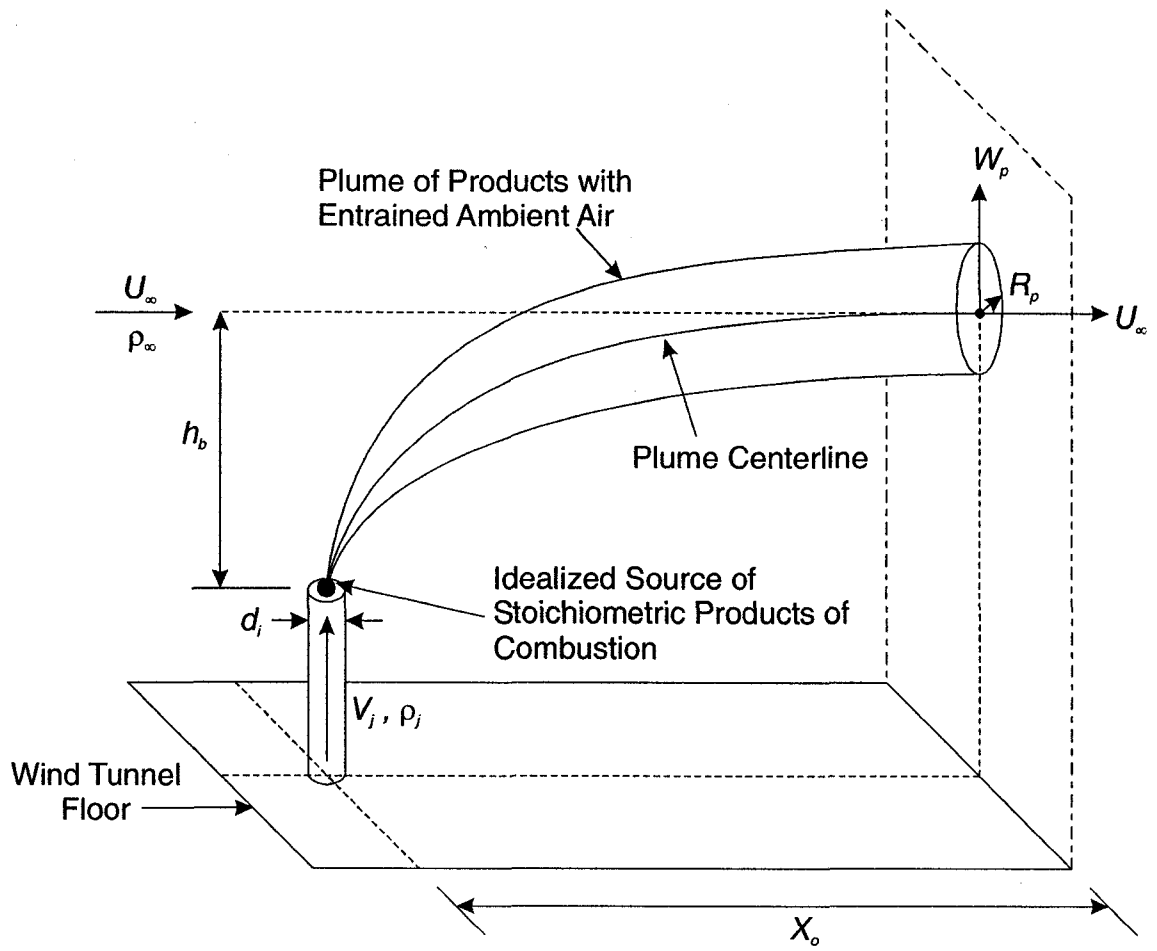


**Figure C.1: Model for a non-reacting buoyant plume in crosswind**

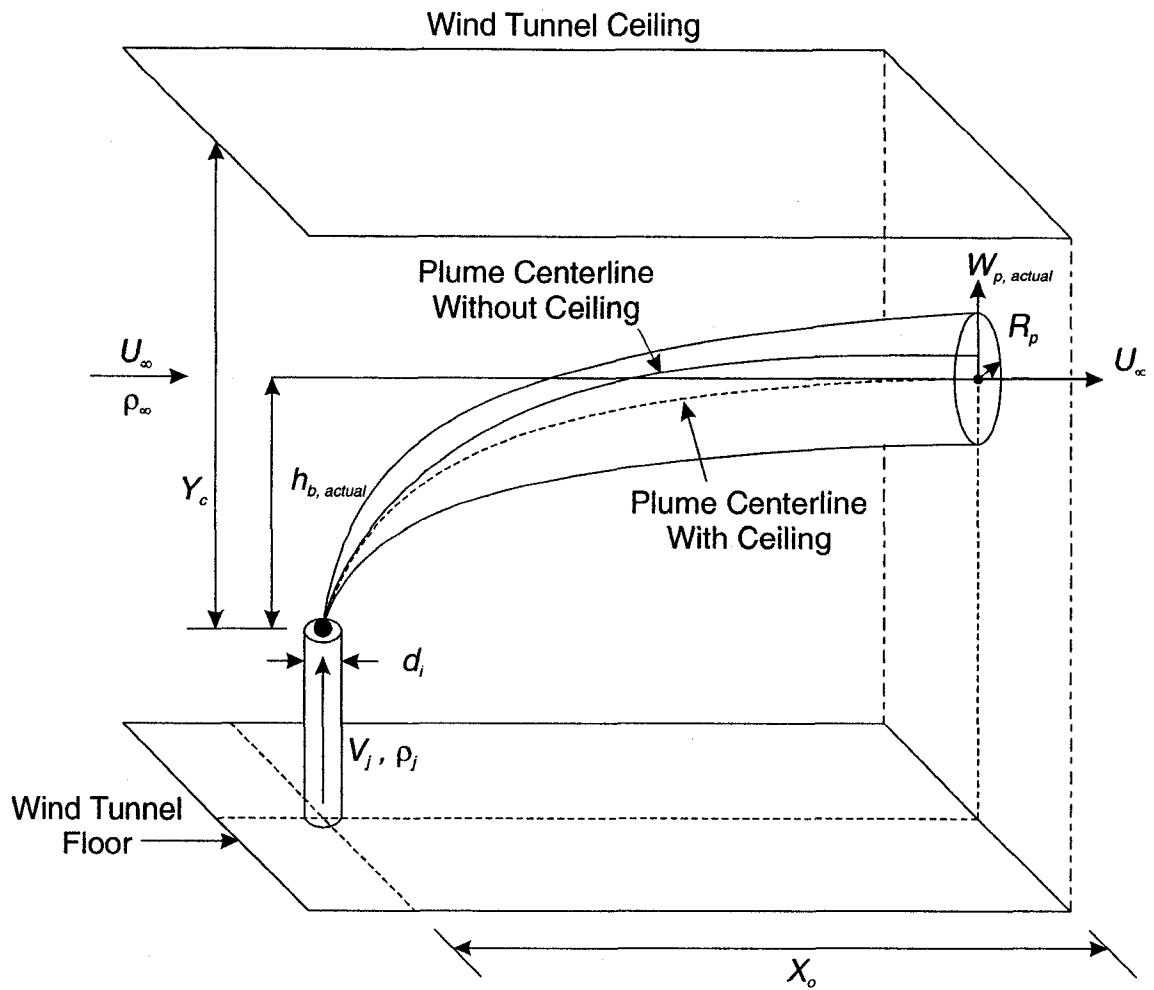


**Figure C.2: Comparison between buoyant plume rise models with and without a ceiling**

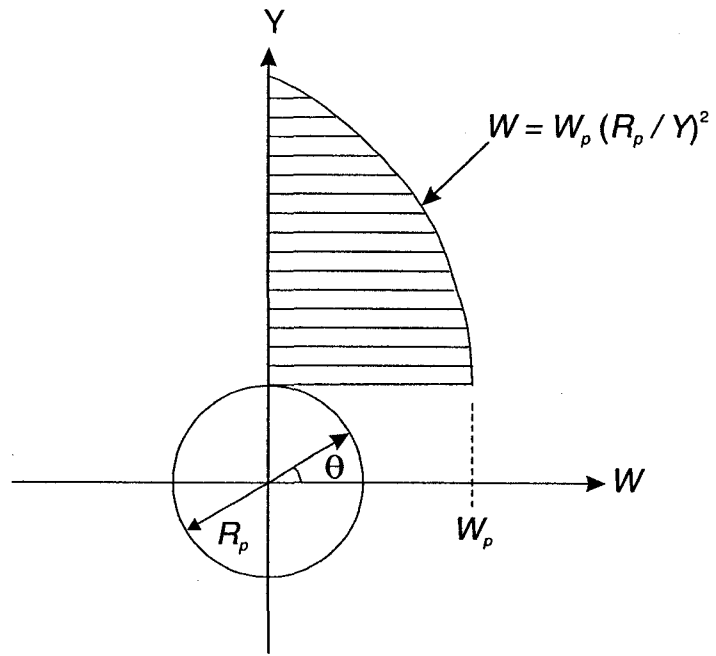


**Figure C.3: Idealized cross-section of buoyant plume structure. Rising cylinder induces velocity  $W$  as a function of  $Y$**



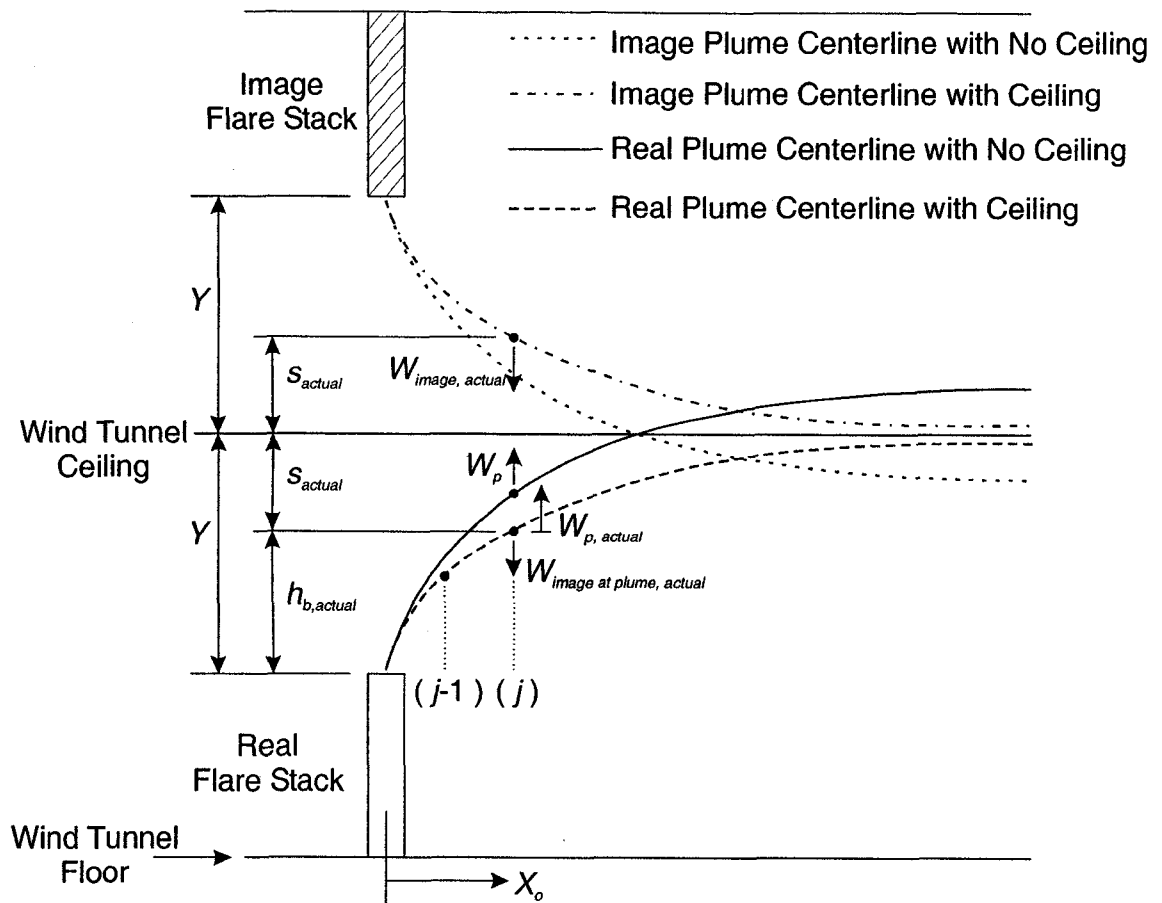


**Figure C.4: Corrected and uncorrected real and image plume centerline trajectories**

## APPENDIX D: Radiation Effects On Type E Thermocouples

The following provides a detailed energy balance calculation for a type E thermocouple subjected to convection and maximum expected radiation effects in the NRC open-loop low-speed wind tunnel facility. It will be shown that radiation heat flux from the flare has a negligible effect on temperature measurements. To demonstrate this point the experimental conditions were as follows.

- Fuel: sales grade natural gas (see Table 3.1), energy density is  $37.5 \text{ MJ/m}^3$
- $d_i = 102.3 \text{ mm}$  (full-scale)
- $V_j = 2.0 \text{ m/s}$ , corresponding to a fuel flow rate of  $920 \text{ l/min}$  ( $0.0153 \text{ m}^3/\text{s}$ )
- $U_\infty = 4 \text{ m/s}$
- $T_{\text{max}} = 450 \text{ K}$  ( $\sim 175 \text{ }^\circ\text{C}$ )
- $T_\infty = 293 \text{ K}$  ( $20 \text{ }^\circ\text{C}$ )

Figure D.1 represents this situation.

Flame radiation on thermocouple TC1 can be calculated using Eq. D.1 from Joseph et al. (1983). To simplify the thermal flux calculation, the flame was approximated by an equivalent radiating point source assumed to be at the geometric centre of the flame. Upon visual inspection, it was concluded that the approximate geometric centre of the flame (represented by a cross in Figure D.1) for the above experimental conditions was located at  $R_z = 0.4Z_{TC} = 2.1 \text{ m}$  relative to the nearest thermocouple, TC1.

$$q'' = \frac{\epsilon_{ng} Q}{4\pi R_z^2} \quad (D.1)$$

where

$q''$  = radiation heat flux

$\epsilon_{ng}$  = emissivity of the natural gas flame, assume 0.2

$Q$  = total heat content of flared gas

The total heat content of the flared gas was calculated using the energy density and volumetric flow rate.

$$Q = 37.5 \text{ MJ/m}^3 (0.0153 \text{ m}^3/\text{s}) = 575 \text{ kJ/s} \quad (D.2)$$

Solving Eq. D.1,

$$q'' \cong 2000 \text{ W/m}^2 \quad (D.3)$$

The thermocouple of interest, TC1, extended 4 cm from the tip of the steel tubing in which it was housed. The junction for TC1 was approximately 2 mm in diameter.

Treating TC1 as a cylindrical object, the exposed surface area ( $A_{TC}$ ) can be calculated.

$$A_{TC} = 2.54 \times 10^{-4} \text{ m}^2 \quad (D.4)$$

To simplify the problem, TC1 was idealized as a spatially isothermal sphere with the same  $A_{TC}$  subjected to convection and radiation heat transfer under steady-state conditions (Figure D.2).

Since  $A_{TC}$  is known,

$$R_s = 4.5 \times 10^{-3} \text{ m} \quad (D.5)$$

Performing an energy balance on the closed system shown in Figure D.2,

Rate energy in = Rate energy out

$$q'' + \bar{h}(T_{\max} - T_{TC}) = \varepsilon_{TC} \sigma (T_{TC}^4 - T_o^4) \quad (D.6)$$

where

$\bar{h}(T_{\max} - T_{TC})$  = convection heat transfer from ambient air to TC1

$\bar{h}$  = mean convection coefficient

$\varepsilon_{TC} \sigma (T_{TC}^4 - T_o^4)$  = radiation heat transfer from TC1 to surroundings

$\varepsilon_{TC}$  = emissivity of TC1, assume 0.9

$\sigma$  = Stefan-Boltzmann constant =  $5.67 \times 10^{-8}$  W/m<sup>2</sup>.K

To solve Eq. D.6, the mean convection coefficient,  $\bar{h}$ , must be calculated. The following equation posed by Incropera and DeWitt (1996, p. 349) can be applied.

$$\overline{Nu}_D = 2 + (0.4 Re_D^{1/2} + 0.06 Re_D^{2/3}) Pr^{0.4} \left( \frac{\mu}{\mu_s} \right)^{1/4} \quad (D.7)$$

where

$$Re_D = \frac{U_{\infty} D}{\nu} \quad (D.8)$$

$$D = 2R_s$$

$\nu$  = kinematic viscosity of air at 1 atm, 450 K =  $32.39 \times 10^{-6}$  m<sup>2</sup>/s

Pr = Prandtl number of air at 1 atm, 450 K = 0.686

$\mu$  = viscosity of air at 1 atm, 450 K =  $250.7 \times 10^{-7}$  N.s/m<sup>2</sup>

$\mu_s$  = viscosity of air at surface of TC1  $\cong \mu$  (assume  $T_{TC} \cong T_{\max}$ )

Once  $\overline{Nu}_D$  is calculated,  $\overline{h}$  may be found.

$$\overline{h} = \overline{Nu}_D \frac{k}{D} \quad (D.9)$$

where

$k$  = thermal conductivity of air at 1 atm, 450 K

$$k = 37.3 \times 10^{-3} \text{ W/m.K}$$

Substituting in all required values and solving Eq. D.9 yields

$$\overline{h} = 79 \text{ W/m}^2.\text{K} \quad (D.10)$$

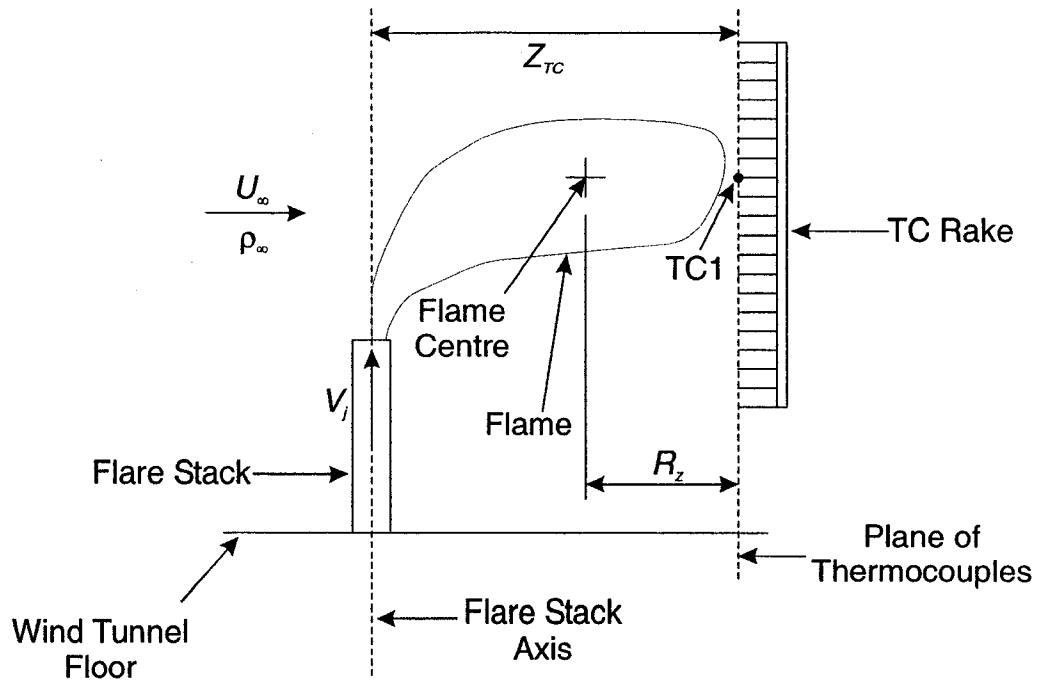
Finally, the difference  $T_{TC} - T_{\max}$  may be solved using Eq. D.6.

$$T_{TC} - T_{\max} = 4 \text{ K} \quad (D.11)$$

Considering the maximum plume temperature measured in this situation was 450 K (~175 °C), an incurred error of 4 K can be considered acceptable. This corresponds to a percent error in measured temperature difference ( $\epsilon_{\Delta T}$ ) of

$$\epsilon_{\Delta T} = \left( \frac{T_{TC} - T_{\max}}{T_{\max} - T_{\infty}} \right) (100\%) = \left( \frac{4K}{450K - 293K} \right) (100\%) = 2.5\% \quad (D.12)$$

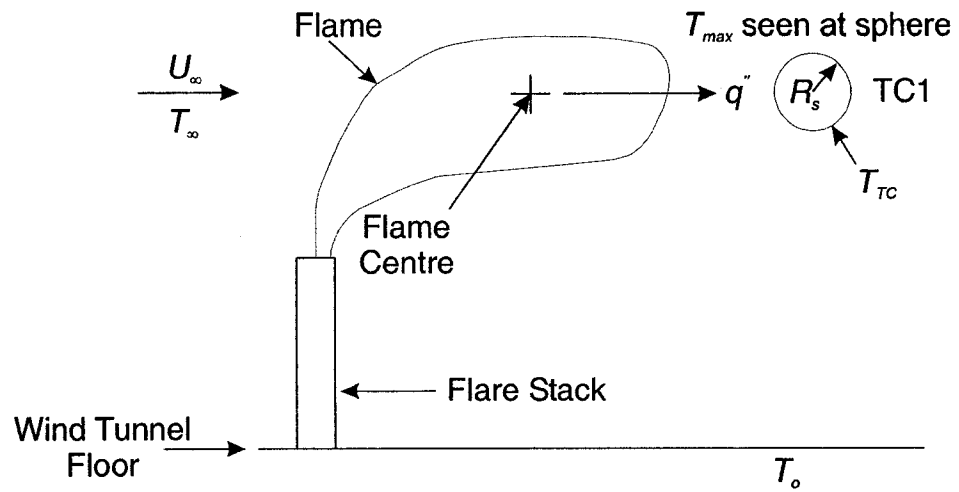
One can conclude that for all other thermal plume mappings, heat flux resulting from flare radiation incurred an error in temperature measurements of less than 4 K.



$Z_{TC}$  = perpendicular distance from flare stack axis to plane of thermocouples

$R_z$  = perpendicular distance from approximate geometric centre of flame to plane of thermocouples

**Figure D.1: Position of TC rake relative to flare stack flame for above experimental conditions**



$R_s$  = radius of TC1 sphere

$T_{TC}$  = surface temperature of TC1 sphere

$T_o$  = temperature of surroundings

**Figure D.2: One-dimensional convection and radiation heat transfer model for TC1 idealized as a spatially isothermal sphere under steady-state conditions**